Scleral Biomechanics in the Normal, Glaucomatous and Aging Eye

An Abstract

Submitted On The Fifth Day Of November, 2008

To The Department Of Biomedical Engineering

In Partial Fulfillment Of The Requirements

Of The Graduate School

Of Tulane University

For The Degree

Of

Doctor Of Philosophy

By

_____

Michaël Julien Alexandre Girard

Approved: _____
J. Crawford Downs, Ph.D.,
Co-Chairman

_____
J-K. Francis Suh, Ph.D.,
Co-Chairman

_____
Claude F. Burgoyne, M.D.,
Co-Chairman

_____
Ronald C. Anderson, Ph.D.

_____
Donald P. Gaver, Ph.D.

Abstract

Glaucoma is the second leading cause of blindness worldwide and is characterized by an irreversible damage to the retinal ganglion cell axons within the optic nerve head (ONH). Once thought to only occur at elevated levels of intraocular pressure (IOP), glaucoma can develop at normal levels without distinct etiology. Since IOP alone cannot explain the development and progression of the disease, we have theorized that the biomechanics of the ONH plays a central role in driving several pathologic mechanisms that can lead to the neuropathy.

The ONH is embedded within the posterior scleral shell – the white outer coat of the eye. From a biomechanical perspective, the sclera directly transmits IOP-induced stress and strain to the ONH, and we therefore hypothesize that the biomechanical behavior of the sclera contributes to the development and progression of glaucoma.

Our objective is to use state-of-the-art experimental and computational tools to characterize scleral biomechanics in normal and glaucomatous monkey eyes. Because the prevalence of glaucoma increases exponentially with age, we additionally characterize scleral biomechanics in the aging monkey eye to investigate the underlying mechanisms for the age-related increased susceptibility to glaucoma.

We introduce a constitutive model for the posterior sclera that includes stretch-induced stiffening and multi-directionality of the collagen fibers. Application of this

model to an idealized eye geometry shows that scleral collagen fibers have a strong impact on ONH deformations. By experimentally measuring IOP-induced 3-D scleral deformations, and regional variations in scleral topography and thickness, we characterize the mechanical properties of individual scleral shells using an inverse finite element (FE) method. We show that monkey posterior sclera 1) is a nonlinear, anisotropic, inhomogeneous tissue, 2) stiffens with age, 3) is biomechanically altered in some, but not all, glaucomatous eyes. In normal eyes, we suggest that the sclera shields the ONH from biomechanical insult by resisting large deformations (nonlinearity), and scleral canal expansion (anisotropy). We suggest that age-related scleral stiffening could dramatically impact the homeostasis of the ONH. Finally, we suggest that scleral remodeling occurs in glaucomatous eyes to prevent further increase in ONH deformations and thus inhibits progression of the disease.

Scleral Biomechanics in the
Normal, Glaucomatous and Aging Eye

A Dissertation

Submitted On The Fifth Day Of November, 2008

To The Department Of Biomedical Engineering

In Partial Fulfillment Of The Requirements

Of The Graduate School

Of Tulane University

For The Degree

Of

Doctor Of Philosophy

By

_____

Michaël Julien Alexandre Girard

Approved: _____

J. Crawford Downs, Ph.D.,
Co-Chairman

_____

J-K. Francis Suh, Ph.D.,
Co-Chairman

_____

Claude F. Burgoyne, M.D.,
Co-Chairman

_____

Ronald C. Anderson, Ph.D.

_____

Donald P. Gaver, Ph.D.

Salvador Dalí, 1944
Study for the Dream Sequence in *Spellbound,* movie directed by Alfred Hitchcock
Oil on panel (58.7 × 84 cm)
Private collection
© 2008 Salvador Dalí, Fundació Gala-Salvador Dalí/Artists
Right Society (ARS), New York

Acknowledgement

I wish to express my sincere gratitude to my advisors Crawford Downs, Francis Suh and Claude Burgoyne for their support, encouragement, and guidance throughout my graduate studies. I am greatly in debt to Crawford Downs, who taught me invaluable experimental techniques for soft-tissues and was always ready to assist me with either work-related or personal issues, and helped me built my confidence about my work. I am greatly in debt to Francis Suh, one of my favorite teachers at Tulane University, who greatly strengthened my knowledge in finite element analysis, introduced me to the basics and advanced aspects of soft-tissue biomechanics, supervised my work, and provided great insight into fiber-based constitutive modeling. I am greatly in debt to Claude Burgoyne who provided funding for this project, put his trust in me, taught me a great deal about glaucoma, and always reminded me about the clinical importance of my work. I enjoyed all the discussions I shared with Claude as they greatly helped me maintain focus and made my work, not just a mathematical gibberish, but something accessible to clinicians.

Thanks to my committee members, Don Gaver and Ron Anderson, who provided insightful suggestions and comments, and took the time to read this thesis. Thanks also to the co-authors of my manuscripts: Michael Bottlang for his precious help with the ESPI sensor and Richard Hart who provided useful suggestions, followed my work very closely, and also taught me the finite element method.

Guillaume, Julien, Pierrot, Benoit, Youssef, Sabine, Sebastian and all the others. Finally, I give my special thanks to Xiao, the love of my life, who always stood near me during the good, the bad and the ugly times.

Table of Contents

List of Figures

List of Tables

List of Symbols

Conventions

$a, A, \alpha, b, B, \beta$	0th order tensors (scalars)
$\mathbf{a}, \mathbf{b}, \mathbf{c}$	1st order tensors (vectors)
$\mathbf{A}, \mathbf{B}, \mathbf{C}$	2nd order tensors (dyadics)
$\mathbb{A}, \mathbb{B}, \mathbb{C}$	4th order tensors (tetradics)

Chapter 2

Symbol	Definition	Units
c	Relaxation ratio, $c = G(0)/G(\infty) - 1$	-
E_0	Instantaneous elastic modulus, $E_0 = \sigma_0 / \varepsilon_0$	MPa
E_∞	Equilibrium elastic modulus, $E_\infty = E_0 / (1 + c)$	MPa
G	Reduced relaxation function	-
t	Time	s
z	Logarithm of relaxation time ratio, $z = \log(\tau/\tau_m)$	-
β	Half-width of the Gaussian distribution	-
ε_0	Constant strain value	-
Φ	Log-normal distribution function	-
σ	Stress, $\sigma(\varepsilon_0, t) = G(t) \cdot \sigma^e(\varepsilon_0)$	MPa
σ_0	Peak stress	MPa
σ^e	Instantaneous tensile stress, $\sigma^e(\varepsilon_0) = E_0 \varepsilon_0$	MPa
τ	Relaxation time	s

| τ_m | Mean relaxation time | s |

Chapter 3

Symbol	Definition	Units
a_i	Interpolation coefficients, $i \in [\![1,8]\!]$	-
$\mathbf{b}$	Vector containing temporal derivatives of the intensity	-
I_k	Pixel intensity of an RGB image, $k \in [\![1,3]\!]$	-
$\mathbf{M}$	Matrix containing spatial derivatives of the intensity	-
R	Region of interest	pixel^2
t	Time	s
u_x	x-pixel displacement	pixel
u_{Cx}	x-pixel displacement of a marker's centroid	pixel
u_y	y-pixel displacement	pixel
u_{Cy}	y-pixel displacement of a marker's centroid	pixel
v_x	x-pixel velocity	pixel/s
v_y	y-pixel velocity	pixel/s
x	x-pixel coordinate	pixel
X_C	x-spatial coordinate of a marker's centroid	mm
y	y-pixel coordinate	pixel
Y_C	y-spatial coordinate of a marker's centroid	mm

Chapter 4

Symbol	Definition	Units
$\mathbf{a}_0$	Local fiber direction in the undeformed configuration	-
$\mathbf{a}$	Local fiber direction in the deformed configuration	-

$\mathbf{B}$, $\tilde{\mathbf{B}}$	Left Cauchy-Green deformation tensors	-
c_1	First Mooney-Rivlin coefficient	kPa
c_3	Fiber stress coefficient	kPa
c_4	Fiber uncrimping rate coefficient	-
$\mathbf{C}$, $\tilde{\mathbf{C}}$	Right Cauchy-Green deformation tensors	-
$\mathbb{C}$	Spatial elasticity tensor	MPa
$\mathbb{C}$	Material elasticity tensor	MPa
$\mathbf{F}$, $\tilde{\mathbf{F}}$	Deformation gradient tensors	-
I_0	Modified Bessel function (1st kind, order 0)	-
I_1, $\tilde{I}_1$	First invariants of $\mathbf{C}$ and $\tilde{\mathbf{C}}$	-
I_4, $\tilde{I}_4$	Squared fiber stretches (4th invariants)	-
$\mathbf{I}$	Second order unit tensor, $\mathbf{I}_{ij} = \delta_{ij}$	-
$\mathbb{I}$	Fourth order unit tensor, $\mathbb{I}_{ijkl} = \delta_{ik}\delta_{jl}$	-
J	Jacobian of the deformation	-
k	Fiber concentration factor	-
K	Bulk modulus	GPa
p	Hydrostatic pressure	kPa
P	Statistical distribution function	-
$\mathbb{P}$	Spatial projection tensor	-
$\mathbb{P}$	Material projection tensor	-
$\mathbf{S}$	Second Piola-Kirchhoff stress tensor	kPa
$\mathbb{S}$	Fourth order unit tensor, $\mathbb{S}_{ijkl} = \frac{1}{2}\left(\delta_{ik}\delta_{jl} + \delta_{il}\delta_{jk}\right)$	-
W	Strain energy function	kPa
$\tilde{W}$	Isochoric strain energy function	kPa
W_{vol}	Volumetric strain energy function	kPa
λ, $\tilde{\lambda}$	Fiber stretches	-
σ	Cauchy stress tensor	kPa
θ_p	Preferred fiber orientation	°

Tensor Rule	Order
$(\mathbf{A} \cdot \mathbf{B})_{ij} = \mathbf{A}_{ik}\mathbf{B}_{kj}$	2
$\mathbf{A} : \mathbf{B} = \mathbf{A}_{ij}\mathbf{B}_{ij}$	0
$(\mathbb{A} : \mathbf{B})_{ij} = \mathbb{A}_{ijkl}\mathbf{B}_{kl}$	2
$(\mathbb{B} : \mathbb{A})_{ijkl} = \mathbb{B}_{ijmn}\mathbb{A}_{mnkl}$	2
$(\mathbf{A} \otimes \mathbf{B})_{ijkl} = \mathbf{A}_{ij}\mathbf{B}_{kl}$	4
$(\mathbf{A} \underline{\otimes} \mathbf{B})_{ijkl} = \mathbf{A}_{ik}\mathbf{B}_{jl}$	4
$\left(\dfrac{\partial \mathbf{A}}{\partial \mathbf{A}}\right)_{ijkl} = \mathbb{I}_{ijkl} = \delta_{ik}\delta_{jl}$	4
$\left(\dfrac{\partial \mathbf{A}^{-1}}{\partial \mathbf{A}}\right)_{ijkl} = -\left(\mathbf{A}^{-1} \odot \mathbf{A}^{-1}\right)_{ijkl} = -\dfrac{1}{2}\left(\mathbf{A}_{ik}^{-1}\mathbf{A}_{jl}^{-1} + \mathbf{A}_{il}^{-1}\mathbf{A}_{jk}^{-1}\right)$	4
$\mathbf{A} : (\mathbf{B} \otimes \mathbf{C}) = (\mathbf{A} : \mathbf{B})\mathbf{C}$	2
$\mathbb{A} : (\mathbf{B} \otimes \mathbf{C}) = (\mathbb{A} : \mathbf{B}) \otimes \mathbf{C}$	2
$\dfrac{\partial \mathbf{A}}{\partial \mathbf{A}} : \mathbf{B} = \mathbf{B} : \dfrac{\partial \mathbf{A}}{\partial \mathbf{A}} = \mathbf{B}$	2

Chapter 5

Symbol	Definition	Units
$\mathbf{a}$	Transformation matrix	-
c_1	First Mooney-Rivlin coefficient	kPa
c_3	Fiber stress coefficient	kPa
c_4	Fiber uncrimping rate coefficient	-
$\mathbb{C}$	Spatial elasticity tensor	MPa
$\mathbb{C}'_{1111}$	Tangent modulus along the preferred fiber orientation	MPa
$\mathbb{C}'_{2222}$	Tangent modulus perpendicular to the preferred fiber orientation	MPa
d_i	Scleral thickness at location i, $i \in [\![1,20]\!]$	μm

E_{ONH}	ONH elastic modulus	MPa
k	Fiber concentration factor	-
K	Bulk modulus	GPa
n	Surface node number	-
N	Total number of surface nodes	-
p	IOP level	mmHg
P	Total number of IOP levels	-
S_1	Structural stiffness along the preferred fiber orientation	kN/m
S_2	Structural stiffness perpendicular to the preferred fiber orientation	kN/m
t_i	Echo time	μs
T	Local scleral thickness	μm
v_{sclera}	Speed of sound in the sclera (value: 1,597)	m/s
$x^e_{n,p}$	x experimental displacement component (node n and IOP p)	μm
$x^m_{n,p}$	x model displacement component (node n and IOP p)	μm
$y^e_{n,p}$	y experimental displacement component (node n and IOP p)	μm
$y^m_{n,p}$	y model displacement component (node n and IOP p)	μm
$z^e_{n,p}$	z experimental displacement component (node n and IOP p)	μm
$z^m_{n,p}$	z model displacement component (node n and IOP p)	μm
ε	Cost function	μm
θ_p	Preferred fiber orientation	°

Chapter 6

Symbol	Definition	Units
c_1	First Mooney-Rivlin coefficient	kPa
c_3	Fiber stress coefficient	kPa
c_4	Fiber uncrimping rate coefficient	-

k	Fiber concentration factor	-
θ_p	Preferred fiber orientation	°

Chapter 7

Symbol	Definition	Units
c_1	First Mooney-Rivlin coefficient	kPa
c_3	Fiber stress coefficient	kPa
c_4	Fiber uncrimping rate coefficient	-
k	Fiber concentration factor	-
θ_p	Preferred fiber orientation	°

1   **Introduction**

1.1. **Background and Significance**

Brief Anatomy and Physiology of the Eye

The human eye functions similarly to a digital camera (Smith 1997). In both systems, light is focused with a lens assembly and converges to an imaging sensor that captures light information, which is then transformed into electric signals. In the normal eye (Figure 1.1.1), light focusing is performed mainly by the cornea, a transparent soft tissue of relatively fixed curvature, and also by the lens, an adaptive, biconvex and transparent soft tissue that can adapt its shape and curvature through a process called accommodation (Abolmaali *et al.* 2007). In the eye, the iris (a terminology also used for digital cameras) is responsible for regulating the amount of light exposed to the lens by changing the diameter of the pupil (*i.e.* the iris opening). In a digital camera, light information is captured by an imaging sensor: a 2-D matrix of photodiodes (one photodiode per picture element or *pixel*). Similarly, in the eye, light is captured by cells from the retina organized in an hexagonal mosaic. The retina is the inner layer of the eye, and can be considered as the eye's imaging sensor. However, the retina is an extremely

complex structure stratified in ten cellular layers, in which 80% of the sensory input of the human body takes place (Sharma and Ehinger 2003).
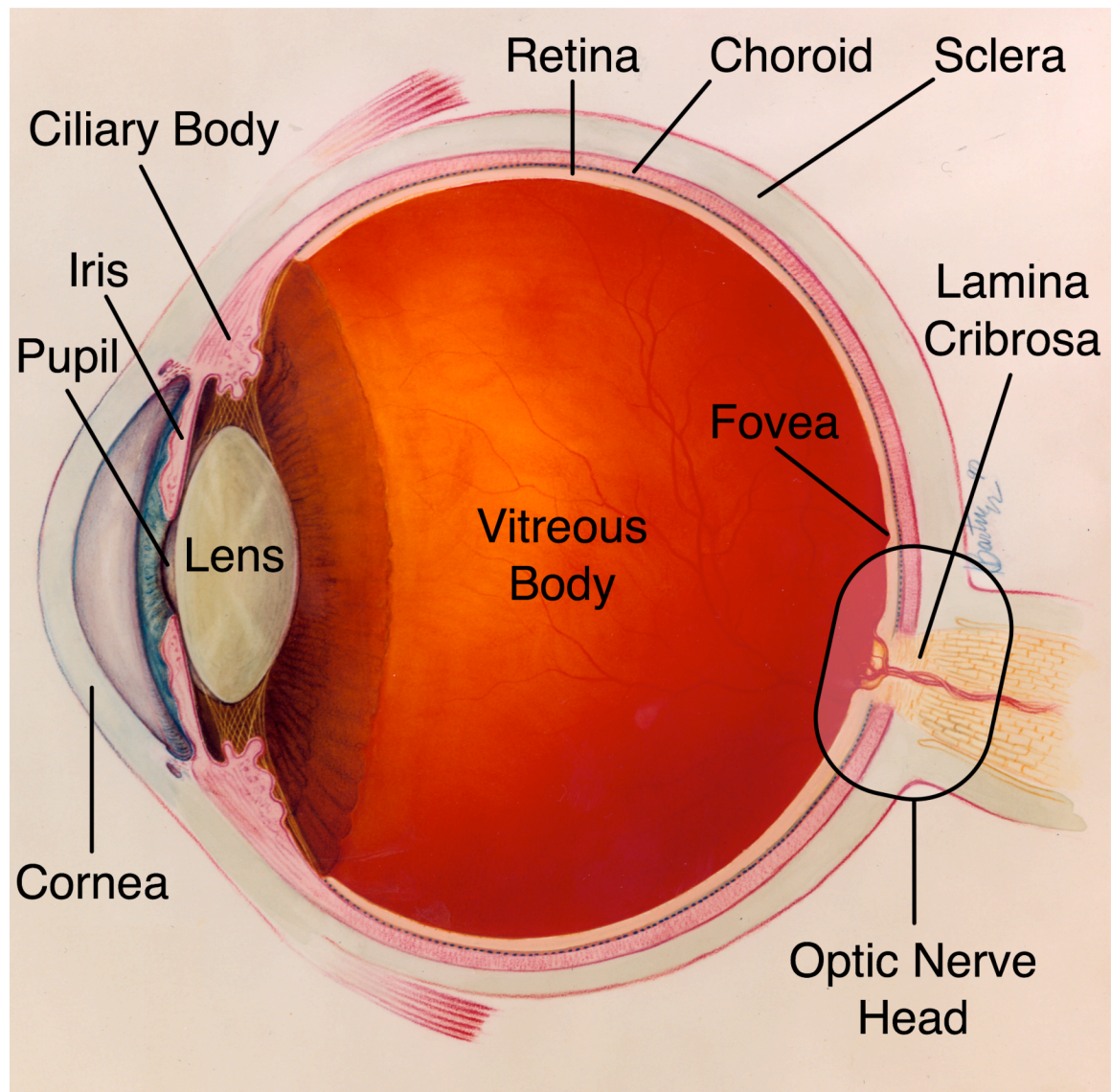
Figure 1.1.1. Anatomy of the human eye. Adapted from the photograph provided by the National Eye Institute and National Institutes of Health, http://www.nei.nih.gov/photo/.

In the retina, photoreceptors are the cells responsible for converting light into electric signals (or nerve signals) through a process called phototransduction. Photoreceptors cover the outermost layer of the retina called the retinal pigment epithelium. From the photoreceptors, nerve signals are passed to second-order cells, then to ganglion cells,

which form the ganglion cell layer of the retina. Retinal ganglion cells are neurons, whose axons form the innermost layer of the retina called the nerve fiber layer. Oxygen and nutrients are supplied to the retinal photoreceptors by the choroid, a highly vascularized and pigmented layer that lies between the retina and the sclera and forms the ciliary body in the anterior chamber of the eye as shown in Figure 1.1.1. The sclera is the white outer coat of the eye and is principally composed of Type-I collagen fibers. The sclera and the cornea form the corneo-scleral shell envelope that provides necessary mechanical strength to sustain intraocular pressure (IOP), and constant protection to the adjacent intraocular tissues. Within the posterior portion of the sclera there is an opening called the scleral canal through which the retinal ganglion cell axons pass on their path to the brain. The optic nerve head (ONH), which consists of connective tissues (peripapillary sclera, scleral canal wall, and lamina cribrosa), neural tissues (retinal ganglion cell axons), and cells (astrocytes, glial cells, endothelial cells, and pericytes) includes the scleral canal and its encapsulating tissues (Burgoyne *et al.* 2005). Figure 1.1.2 shows a sagittal section of a monkey ONH.
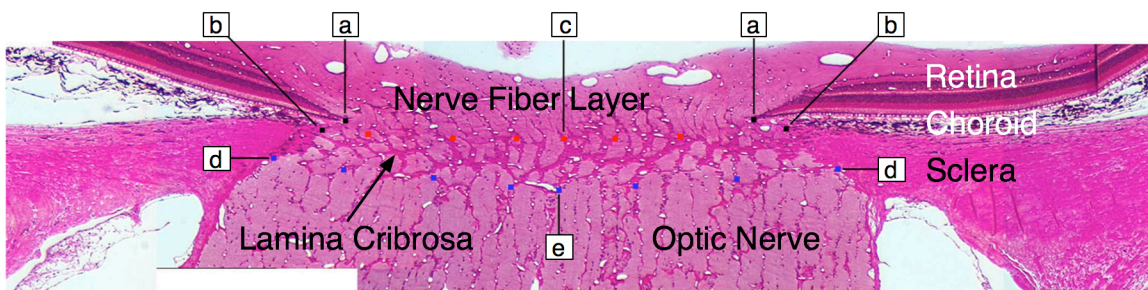
Figure 1.1.2. Sagittal section of a monkey ONH obtained from histology. **(a)** Bruch's membrane opening, **(b)** anterior scleral canal opening, **(c)** anterior edge of the lamina cribrosa in red, **(d)** posterior scleral canal opening, and **(e)** posterior edge of the lamina cribrosa in blue. Adapted from (Bellezza *et al.* 2003b).

In the human and monkey eye, approximately one million retinal ganglion cell axons (Sanchez *et al.* 1986; Mikelberg *et al.* 1991; Jonas *et al.* 1992; Levin 2003) converge to the ONH and exit the eye through a hole in the peripapillary sclera (*i.e.* the sclera adjacent to the ONH) known as the scleral canal. The latter is spanned by the lamina cribrosa, a fenestrated connective tissue structure, which is similar in appearance to the trabecular meshwork in cancellous bone. The lamina cribrosa inserts deeply into the peripapillary sclera and is anchored peripherally to a ring of elastin and collagen fibers within the peripapillary sclera known as the laminar scleral ring (Hernandez *et al.* 1987; Quigley *et al.* 1991a; Tektas and Lutjen-Drecoll 2008). The laminar trabeculae (or laminar beams) provide nutrients, from capillaries that run within them, to the retinal ganglion cell axons as they continue their journey to the brain by passing through the laminar pores. Basement membranes, made primarily of collagen Type-IV, coat both the capillary endothelial cells and the laminar beams, and modulate filtration for nutrient supply (Morrison *et al.* 1988). Collagen Type-IV is thought to be generated by astrocytes, a type of glial cell that surrounds the laminar beams within the basement membrane, also responsible for maintaining ionic homeostasis and providing nutrients to the retinal ganglion cell axons through processes that extend toward the laminar capillaries (Hernandez 2000). Laminar beams additionally provide mechanical and structural support. Figure 1.1.3 shows the laminar beams and pores of a 3-D anatomically-accurate reconstruction of a monkey lamina cribrosa.
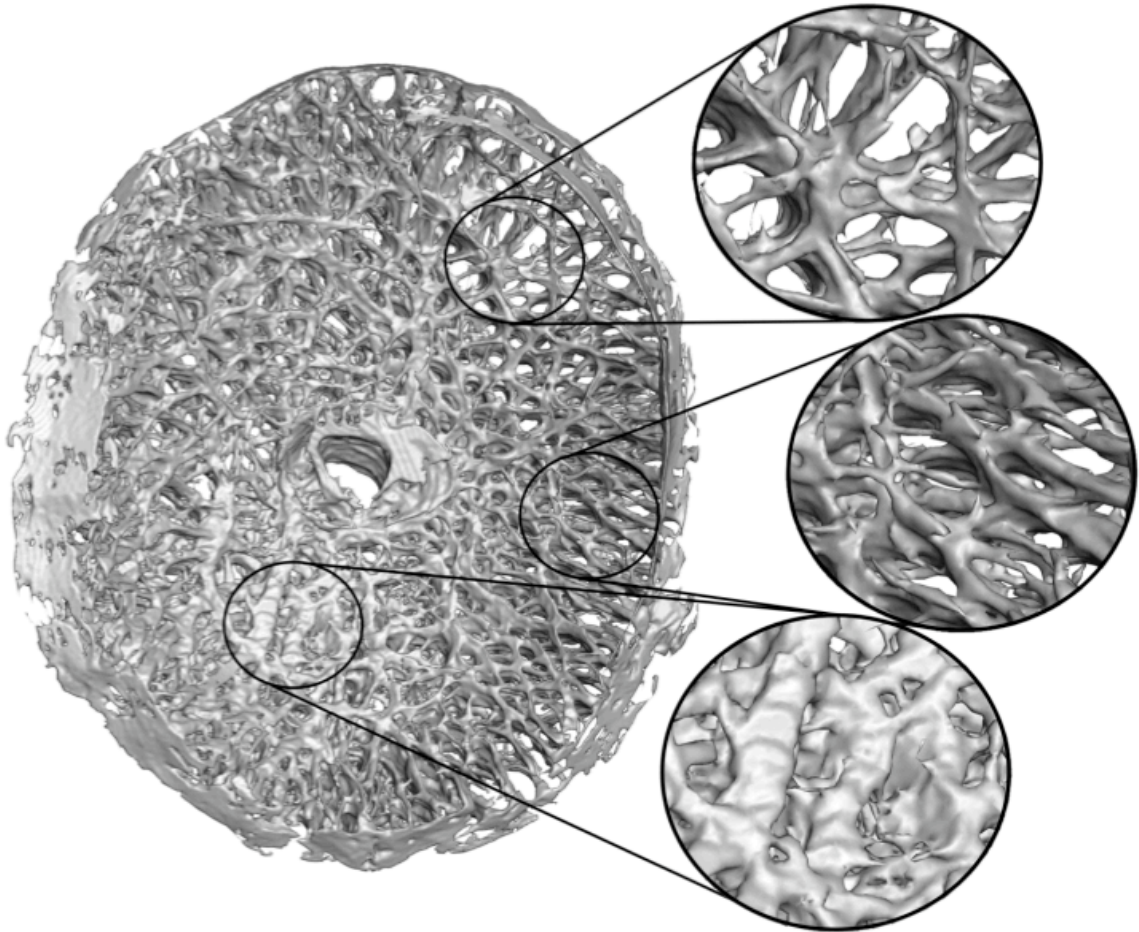
Figure 1.1.3. 3-D anatomically-accurate reconstruction of a monkey lamina cribrosa. Note the regional variations in laminar beam thickness and orientation, and laminar pore size. Within the laminar beams run capillaries that provide nutrients to the retinal ganglion cell axons as they pass through the laminar pores. Figure obtained from (Sigal *et al.* 2009).

After passing through the lamina cribrosa, the retinal ganglion cell axons gather together to form the optic nerve (Figure 1.1.2), which leads to the brain. One main target of the retinal ganglion cell axons is the lateral geniculate nucleus, a part of the brain where the processing of visual information starts (Levin 2003). Diseases that severely damage the retinal ganglion cell axons in the retina, ONH, or optic nerve, are common causes of blindness.

Glaucoma

A recent study estimated that there were 37 million blind people and 124 million with low vision in the 2002 world population (Resnikoff *et al.* 2004). Of those 37 million, 82 % (~30.3 million) are over the age of 50, and 12 % (~ 4.4 million) are blind from glaucoma (Figure 1.1.4), an ocular neuropathy and second leading cause of blindness behind cataract (Foster and Resnikoff 2005). While cataract can be treated, and much effort is needed to prevent this ocular disease in developing countries, glaucoma remains incurable. Another recent work predicted that there will be 60.5 million people with glaucoma in the 2010 world population, of which 8.4 million will be bilaterally blind, and 79.6 million in the 2020 world population, of which 11.1 million will be bilaterally blind (Quigley and Broman 2006). According to these estimates and predictions, there is an ongoing need to understand the causes of glaucoma. The work presented in this thesis is expected to provide insights toward the understanding of the pathophysiology of glaucoma.

Figure 1.1.4. Simulation of glaucoma, a blinding ocular disorder, using virtual reality. By the time a patient experiences visual field loss, irreversible damage to the retinal ganglion cell axons has already occurred. Figure obtained from (Jin *et al.* 2005).

Glaucoma is characterized by an irreversible damage to the retinal ganglion cell axons accumulated over long periods of time at the site of the ONH (Quigley and Anderson 1976; Quigley and Addicks 1980; Quigley *et al.* 1981) and is clinically manifested by cupping of the ONH. Glaucoma was first documented by Hippocrates in 400 BC and was described as a blinding disease common in the elderly. However, much controversy today exists as to whether the description made by the ancient Greeks referred to cataract or glaucoma as no clear distinctions were made between the two (Tsatsos and Broadway 2007). Currently, knowledge of the disease has evolved and glaucoma can be categorized into two main types, even though clear definitions are still lacking as much remains to be understood. Open-angle glaucoma, originally thought to only occur in eyes with elevated IOP (Levene 1980; Quigley 1993), is characterized by open angles in the anterior chamber and can occur at all levels of IOP (*i.e.* normal and elevated). Clinically, open-angle glaucoma is distinguished between normal-tension glaucoma (IOP range: 10 – 21 mm Hg) and high-tension glaucoma (IOP > 21 mm Hg), even though no evidence suggests different etiologies associated with both appellations (Quigley 2005; Leske 2007; Drance 2008). Angle-closure glaucoma, being almost as prevalent as open-angle glaucoma (Quigley and Broman 2006), is the result of narrow or closed angles in the anterior chamber blocking the normal fluid drainage pathway of the eye, thus leading to IOP spikes that may damage the retinal ganglion cell axons (Saw *et al.* 2003). To date, it is clear that increased IOP is associated with increased prevalence (Sommer *et al.* 1991) and incidence (Le *et al.* 2003; Nemesure *et al.* 2007; Leske *et al.* 2008) of glaucoma. IOP is the only major risk factor for glaucoma that can be controlled. Reduction in IOP, either through pharmacological or surgical treatment, has been proven

beneficial in arresting the progression of the disease (Collaborative Normal-Tension Glaucoma Study Group 1998; Heijl *et al.* 2002; Maier *et al.* 2005). However, reduction in IOP is not always successful, as progressive damage to the retinal ganglion cell axons persists approximately 50 % of the time even after treatment (Leske *et al.* 2003). Moreover, some drugs (*e.g.* Latanoprost) have been shown to directly impact the biochemical composition of the anterior and posterior sclera with an increase in glycosaminoglycans (Trier and Ribel-Madsen 2004). These changes in scleral composition have unknown consequences.

It should also be emphasized that some patients with elevated IOP never seem to develop glaucoma, a condition characterized as ocular hypertension and usually not considered a disease per se. In some populations, ocular hypertension is almost as prevalent as open-angle glaucoma (Varma *et al.* 2004). Adding the fact that open-angle glaucoma occurs nearly as often in patients with normal levels of IOP (Bengtsson 1981; Quigley 2005) as in those with elevated levels, and is the most prevalent type of glaucoma in Japan (Shiose *et al.* 1991; Iwase *et al.* 2004), it is clear that factors other than IOP must play important roles in the development and progression of this disease (Drance 1972; Drance *et al.* 1973; Leske *et al.* 2008). In our opinion, the effects of IOP cannot be evaluated by examining the level or changes in IOP alone, since IOP may serve as an indirect cause of glaucoma by deforming the ocular soft tissues (acute effects) and/or by modifying ocular soft tissue properties and geometry (chronic effects).

Specifically, in the following sections, we will argue that the eye is a biomechanical structure, and as a consequence, it is influenced by the baseline level of IOP level as well as both acute and chronic changes in IOP. We suggest that the IOP-

induced biomechanical response of an individual eye is essential in the development and progression of glaucoma.

Ocular Biomechanics in Glaucoma

Biomechanics helps us understand the effects of external and internal forces on living systems (Fung 1993). In the eye, biomechanics is not usually thought to play an important role, yet its application to ocular soft tissues considerably enriches our understanding of the physiology and pathophysiology of the eye (Ethier *et al.* 2004). Over the past two decades, we witnessed the emergence of several areas of research related to the biomechanics of ocular soft tissues. While most of these areas are outside the scope of this thesis, we should acknowledge the following works: aqueous humor and Schlemm's canal biomechanics (Johnson and Kamm 1983; Ethier 2002), corneal biomechanics (Pinsky *et al.* 2005; Elsheikh *et al.* 2008; Nguyen *et al.* 2008), iris biomechanics (Heys and Barocas 1999), lens biomechanics (Pedrigi *et al.* 2007), ONH biomechanics (see this section), orbital fat and ocular muscles biomechanics (Schutte *et al.* 2006), scleral biomechanics (see later sections), and vitreous humor biomechanics (Lee *et al.* 1992; David *et al.* 1998). Note that this reference list is by no means complete as other researchers have greatly contributed to the field of ocular biomechanics.

In this thesis, we propose that the ONH (the principal site of damage in glaucoma) which includes the peripapillary sclera, can be represented as a biomechanical structure and that all ONH tissue are constantly exposed to substantial levels of IOP-induced stress and strain. We also propose that IOP-induced stress and strain levels within the ONH tissues are highly eye-specific (or individual-specific) and can be substantial at low,

normal, or elevated levels of IOP, and depend on the ONH's biomechanical features, such as mechanical properties and geometry. Our long-term goal is to explain the pathophysiology of glaucoma in terms of biomechanics and account for cases in which glaucoma develops at normal levels of IOP (normal tension glaucoma) but also never appears even at elevated levels of IOP (ocular hypertension). The fact that the ONH tissues are affected by IOP-induced strain and stress levels that may correlate with retinal ganglion cell axon death is often referred to as the *mechanical theory* or *IOP-related theory* (Quigley *et al.* 1980; Fechtner and Weinreb 1994; Hernandez 2000; Burgoyne *et al.* 2005). An additional theory, namely the *vasogenic theory* (Fechtner and Weinreb 1994), states that the impairment of the blood flow within the microvasculature of the ONH (Figure 1.1.5) can cause retinal ganglion cell axon loss mainly through ischemia (Hayreh 2001). It should be noted that the *vasogenic* and *mechanical theories* are not mutually exclusive and glaucomatous optic neuropathy can be a result of simultaneous ischemic and IOP-induced mechanical insults for an individual patient. In our opinion, the *vasogenic theory* can also be thought as a mechanical theory considering that the study of blood flow is a biofluid mechanics problem, the potential IOP-induced constrictions of blood vessels is a fluid-structure interaction problem, and the altered nutrient-delivery to the retinal ganglion cell axons is a biotransport problem. Therefore, in this thesis we will argue that the *mechanical theory*, in its broader definition, also includes the *vasogenic theory*. However, as a first step toward our understanding of ONH biomechanics, we will exclude the study of the ONH in glaucoma as a biofluid mechanics problem without disregarding the importance of ONH blood flow. We will mainly consider the study of the ONH in glaucoma as a biosolid mechanics problem.
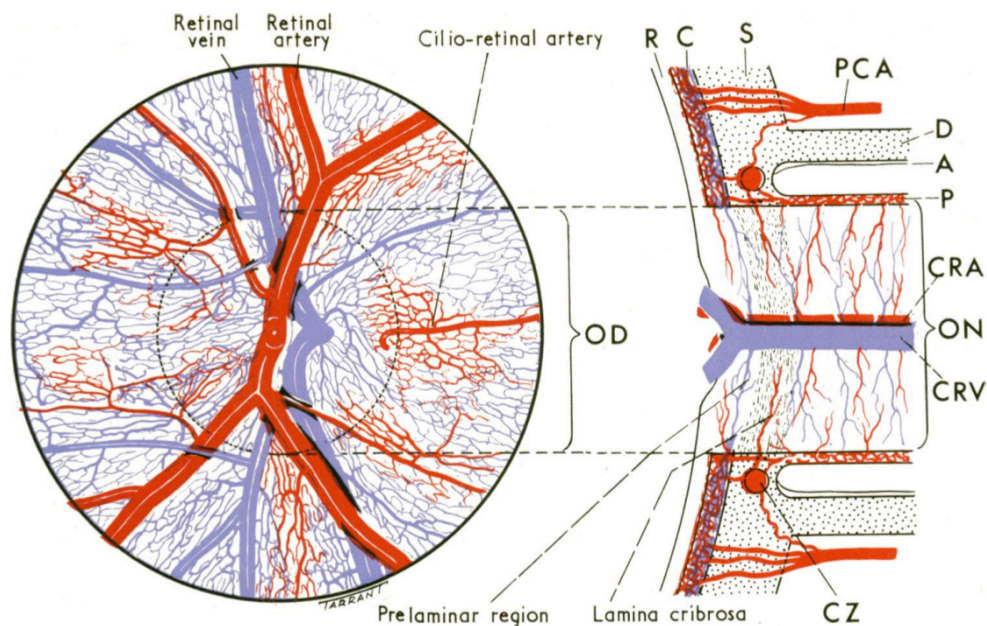
Figure 1.1.5. Schematic of ONH blood supply. Figure obtained from (Hayreh 1969). (**A**) Arachnoid, (**C**) Choroid, (**CRA**) Central Retinal Artery, (**CRV**) Central Retinal Vein, (**CZ**) Circle of Zinn and Haller, (**D**) Dura, (**OD**) Optic Disc, (**ON**) Optic Nerve, (**P**) Pia, (**PCA**) Posterior Ciliary Arteries, (**R**) Retina, (**S**) Peripapillary Sclera.

To date, it is clear that the lamina cribrosa, as well as other ONH tissues, deforms in response to acute elevation of IOP and several investigators have experimentally measured either posterior laminar deformation in humans (Levy and Crapps 1984; Yan *et al.* 1994) and monkeys (Levy *et al.* 1981), or anterior laminar deformation in humans (Albon *et al.* 2000b) and monkeys (Bellezza *et al.* 2003a). These studies were performed either through direct measurements in cadaver eyes or through traditional histology. The lamina cribrosa deforms, but it is still unclear as to whether it moves posteriorly or anteriorly as IOP increases, which might be explained by the use of different IOP ranges and species in these studies.

Axonal transport, defined as the movement of axoplasm and organelles along the axons either toward the synapses (orthograde transport) or toward the cell body

(retrograde transport), has been shown to be blocked at the site of the ONH in both directions due to acute and chronic elevations of IOP (Anderson and Hendrickson 1974; Minckler *et al.* 1977). To explain this phenomenon, Quigley and coworkers proposed that IOP-induced deformations of the lamina cribrosa are directly responsible for interfering with the normal activities of the retinal ganglion cell axons, thus leading to axonal transport blockage. Their theory is as follows: (1) retinal ganglion cell axons can be compressed in the anterior region of the lamina cribrosa due to IOP-induced laminar bowing (Figure 1.1.6a), (2) retinal ganglion cell axons can be compressed in the periphery of the laminar pores due to enlargement of the pores along a preferred orientation (Figure 1.1.6b), and (3) retinal ganglion cell axons can bend due to shearing of the lamina cribrosa with respect to its surface (Figure 1.1.6c).
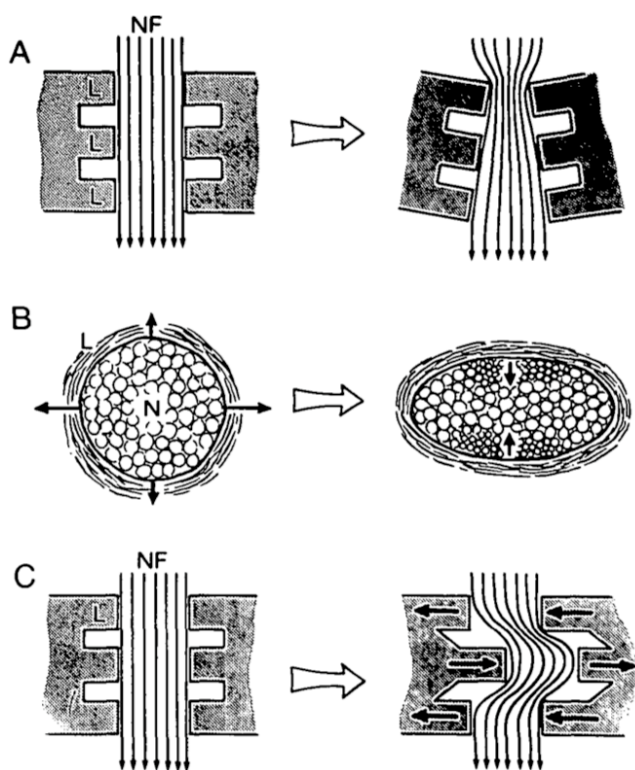
Figure 1.1.6. Different types of retinal ganglion cell damage that could occur with lamina cribrosa deformations as a result of increased IOP as suggested by Quigley and coworkers. (**L**) Laminar beams, (**NF**) Nerve fibers. (**A**) Posterior bowing of the lamina cribrosa could result in nerve fiber damage through compression in the anterior region of the lamina cribrosa. (**B**) Elongation of laminar pores in one direction could result in compression of the nerve fibers in the perpendicular direction. (**C**) Shear with respect to the laminar surface could distort the nerve fibers. Figure obtained from (Quigley *et al.* 1980).

To date, it is still unclear if these types of deformation ever occur in an individual lamina cribrosa. Recent evidence suggests that laminar pores located in the periphery of the nerve collapse under acute elevations of IOP while those in the central region enlarge (Brown *et al.* 2007), which supports one type of IOP-induced laminar deformation. The theory proposed by Quigley and coworkers has yet to be validated, but it strongly reinforces our idea that IOP-induced laminar deformations could have a direct impact on retinal ganglion cell axons, and this independently of connective tissue damage. Moreover, axonal transport blockage could directly lead to retinal ganglion cell death, but this remains to be seen.

Interestingly, in the earliest stage of glaucoma, retinal ganglion cell axon loss occurs at the inferior and superior regions of the optic nerve (Quigley and Green 1979), following a so-called hourglass pattern. This pattern is highly correlated with the structure of the human lamina cribrosa, in which larger pores and thinner beams are found in both the inferior and superior ONH quadrants (Quigley and Addicks 1981; Brown *et al.* 2007). Together, these results suggest a potential weakening of the laminar structure in the inferior and superior regions of the ONH that may correlate with retinal ganglion cell death and emphasizes a need to understand the biomechanics of ONH connective tissues.

Connective tissues of the ONH are also altered with the development and progression of glaucomatous optic neuropathy. In the human lamina cribrosa, Quigley and coworkers reported a decrease in total collagen content, but not in elastin content (Quigley *et al.* 1991b). However, they reported a disorganization of the elastin fibers where those appeared more buckled and disinserted from other constituents depending on

the stage of glaucomatous damage as shown in Figure 1.1.7 (Quigley *et al.* 1991a). Hernandez and coworkers also reported a disorganization of elastin, however, it was accompanied with a clear loss of elastin fibers. In addition, they showed a considerable increase in collagen Type-IV, which acted as extra wrapping material covering the laminar beams and extended into the laminar pores (Hernandez *et al.* 1990). The latter are known to be solely occupied by retinal ganglion cell axons in the normal eye. Morrison and coworkers confirmed the apparition of collagen Type-IV material within the laminar pores and laminar beams, but also acknowledged that it was accompanied with collagen Type-I and Type-III within the laminar pores (Morrison *et al.* 1990). While there are slight discrepancies between these studies, it should be noted that they are not necessarily inconsistent because different types of extracellular matrix alteration could occur at different stages of glaucomatous damage.
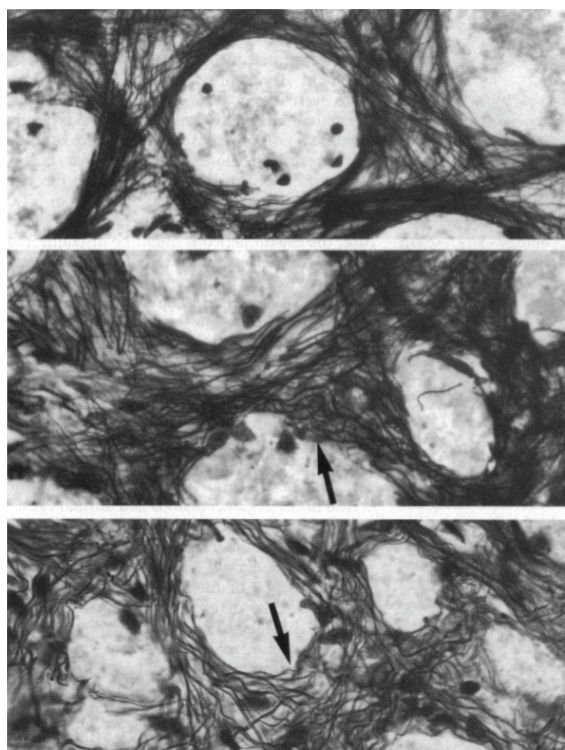
Figure 1.1.7. Human laminar beams stained for elastin at different stage of glaucomatous damage. Elastin fibers are shown as normal (**Top**), mildly damaged (**Middle**) and severely damaged (**Bottom**), which is correlated with the stage of glaucomatous damage. Note that as glaucoma progresses, the elastin fibers appear more buckled and disinserted from other constituents. Elastin content was not measured in this study. Figure obtained from (Quigley *et al.* 1991a).

In the earliest stage of glaucomatous damage, Burgoyne and coworkers reported morphologic changes in the monkey ONH including permanent posterior deformation and thickening of the lamina cribrosa (Burgoyne *et al.* 2004). Yang and coworkers reported thickening of the prelaminar tissues (Yang *et al.* 2007a) and lamina cribrosa as well as mild thinning of the peripapillary sclera (Yang *et al.* 2007b). Roberts and coworkers reported an increase in connective tissue volume and an increase in the total number of laminar beams through the thickness of the lamina cribrosa (Roberts *et al.* 2008). In humans, Quigley and coworkers and Jonas and coworkers reported considerable thinning and permanent deformation of the lamina cribrosa in mild to severe stages of glaucomatous damage (Quigley *et al.* 1983; Jonas *et al.* 2003).

Whether changes in composition and morphology of the lamina cribrosa extracellular matrix results from dying axons or is a cause for axonal death remains to be determined. In this study, we hypothesize that IOP-induced stress and strain are responsible for the reorganization of the lamina cribrosa extracellular matrix that includes disinsertion, failure, and generation of protein fibers (mainly elastin and collagen). We therefore assume that IOP-induced stress and strain directly affect the mechanical behavior of the lamina cribrosa by altering its mechanical properties and geometry. To date, it is still unclear if the lamina cribrosa will stiffen or soften with glaucomatous damage. While Zeimer and coworkers suggested a stiffening of the lamina cribrosa as a function of the stage of glaucomatous damage based on laser Doppler velocimetry measurements (Zeimer and Ogura 1989), Bellezza and coworkers suggested that the lamina cribrosa is hypercompliant (*i.e.* softer) in the earliest stage of glaucomatous damage based on traditional histology measurements (Bellezza *et al.* 2003b). Both

studies are not necessary inconsistent, as the mechanical behavior of the lamina cribrosa could in fact evolve differently depending on the stage of glaucomatous damage. In our opinion, changes in composition and morphology of the lamina cribrosa extracellular matrix could precipitate retinal ganglion axon death either through (1) direct effects such as an increase in IOP-induced strain or stress that eventually leads to more mechanical damage as well as an increase in glial cell response, or (2) indirect effects such as the blockage of nutrient delivery to the retinal ganglion cell axons due to the alterations in blood flow, and/or the capillary and astrocyte basement membranes.

Understanding the biomechanics of living tissues under normal and pathophysiologic conditions is a considerable achievement considering that (1) tissue properties are highly complex, and subject to constant remodeling *in vivo*, (2) inter-individual variations in tissue properties may be large, and (3) alterations in tissue properties with the development and progression of a pathophysiology, if present, may be difficult to detect.

Characterizing the biomechanical properties of a living tissue at the macroscopic level is usually performed in a two-step process. The first step is the development of an experimental mechanical test (*in vivo* or *ex vivo* usually performed in animal models) to measure the deformational behavior of the tissue of interest as it is subjected to load. The second step is the development of a constitutive theory (*i.e.* a stress/strain relationship using principles of continuum solid mechanics) to estimate biomechanical properties and stress levels for the tissue of interest based on the experimental observations. It should be noted that constitutive theories are usually combined with numerical methods (*e.g.* the finite element (FE) method) when the tissue of interest has a complex geometry, which is

often encountered in biological systems. This general approach is the one we will pursue to study ocular biomechanics in glaucoma. Our long term goal is to build eye-specific biomechanical models of the posterior hemisphere of the eye to estimate IOP-induced stress and strain levels within the ONH and understand the pathophysiology of glaucoma. This requires accurate geometry and biomechanical properties for the ONH, and the peripapillary and posterior sclera.

The lamina cribrosa and the peripapillary and posterior sclera are the principal load-bearing tissues of the posterior hemisphere of the eye, while the retina is generally thought to carry minimal IOP-induced loads due to its large cellular content. The lamina cribrosa was once thought to be similar to the sclera in composition and simply an extension of the sclera. Today, evidence suggests that the lamina cribrosa is more compliant and very different in composition than the adjacent posterior sclera making the study of ocular biomechanics in glaucoma a fascinating problem. First, the lamina cribrosa is a highly porous structure, which allows for the passage of the retinal ganglion cell axons through the scleral canal (Figure 1.1.3). The sclera is not porous on the macro-scale. Second, the lamina cribrosa contains large amounts of collagen Type-IV and elastin, some collagen Type-III, but relatively little collagen Type-I (Hernandez *et al.* 1987) although there is some controversy on the real amount of collagen Type-I and Type-III (Morrison *et al.* 1989). Conversely, the posterior sclera is principally composed of collagen Type-I (Edelhauser and Ubels 2003). The higher percentages of elastin and collagen Type-IV within the lamina cribrosa should result in a more compliant tissue. Third, the collagen fibers of the lamina cribrosa have smaller diameters than those of the peripapillary and posterior sclera (Quigley *et al.* 1991b) which is consistent with higher

compliance as well. Fourth, Woo and coworkers provided the first estimate of the mechanical properties of the human ONH and showed that the ONH elastic modulus was 4.4 to 7.5 times lower than that of the posterior sclera (Woo *et al.* 1972). Fifth, using uniaxial testing, Spoerl and coworkers found that the human lamina cribrosa elastic modulus (at 20 % strain) was 2.2 times lower than that of the peripapillary sclera (Spoerl *et al.* 2005).

It should be pointed out that the data reported by Woo and coworkers (Woo *et al.* 1972) and Spoerl and coworkers (Spoerl *et al.* 2005) are crude estimates of the biomechanical behavior of the ONH. In fact, the diameter of the scleral canal is small (*i.e.* anterior scleral canal opening in Figure 1.1.2) as it is 1.5 mm on average in humans (Jonas *et al.* 1991), which makes the measurement of the IOP-induced deformational-behavior of the ONH by means of experimental techniques incredibly challenging. However, *in vivo* and *ex vivo* technologies are currently being developed and appear highly promising such as optical coherence tomography imaging (Guo *et al.* 2005; Burgoyne *et al.* 2008; Kagemann *et al.* 2008; Srinivasan *et al.* 2008), second harmonic imaging microscopy (Brown *et al.* 2007; Lomb 2007), and magnetic resonance imaging (Sadun *et al.* 2002; Rausch *et al.* 2007). These new techniques will likely drive our knowledge of ONH biomechanics forward as work progresses. It should be noted that the latest estimate of the lamina cribrosa elastic modulus was reported by Lomb using second harmonic imaging and was found to be in the 0.4 – 2.2 MPa range for porcine eyes (Lomb 2007).

Because strong evidence suggests that lamina cribrosa is more compliant than the adjacent peripapillary and posterior sclera, the biomechanics of the ONH has been

compared to the engineering problem of a circular or elliptical hole within an infinite thin plate that is under uniaxial (Greene 1980; Bellezza *et al.* 2000) or biaxial (Sander *et al.* 2006) tension. The stress concentration factors (uniaxial and biaxial cases) reported in these studies provide an estimation of the stress levels that are present at the scleral-laminar boundary. In these cases, they only depend on the idealized geometry of the canal, which is a gross approximation and insufficient to understand the complexity of ONH biomechanics.

More recently, ONH biomechanics has been studied with the FE method to estimate the IOP-induced stress and strain levels within the posterior sclera and the ONH tissues. Bellezza and coworkers generated the first idealized FE models of the posterior hemisphere of the normal human eye using linear elastic isotropic theory (Bellezza *et al.* 2000). They concluded that IOP-induced stress levels were significantly higher than IOP (6 to $122 \times$ IOP) in the load bearing tissues of the eye, at all levels of IOP, and that IOP-induced stress levels highly depend on the scleral canal size, scleral canal eccentricity and scleral thickness. Sigal and coworkers generated idealized axisymmetric and individual-specific FE models of the posterior hemisphere of the normal human eye using linear elastic isotropic theory (Sigal *et al.* 2004; Sigal *et al.* 2005; Sigal *et al.* 2008a; Sigal *et al.* 2008b). They reported stress levels in the 0.1 to $12 \times$ IOP range, depending on the tissue considered, and concluded that the elastic modulus of the sclera and eye size were the major determinants of strain in the lamina cribrosa. The fact that the elastic modulus of the sclera has a high influence on ONH biomechanics is a major motivation for this work. Downs and coworkers and Roberts and coworkers generated individual-specific FE models of the posterior hemisphere of the normal and early-glaucomatous monkey eye

using linear orthotropic theory for the lamina cribrosa and linear isotropic theory for sclera (Downs *et al.* 2007; Roberts *et al.* 2007). They found that the lamina cribrosa was a highly anisotropic and inhomogeneous soft tissue based on 3-D histologic reconstructions and that the early glaucomatous lamina cribrosa exhibited less stress but more strain than its contralateral normal. Their work suggests a weakening of the laminar structure in the earliest stage of glaucoma through remodeling of the connective tissues.

While these studies were major contributions to the field of ocular biomechanics, the presented FE models are still in their infancy, and are still lacking experimental validation. Therefore, all results from these studies must be taken with caution. Moreover, the posterior sclera has been modeled as a linear isotropic material, which is an oversimplification for this soft tissue. The principal goal of our study is to estimate the mechanical properties of the peripapillary and posterior sclera with state-of-the-art computational and experimental tools. Specifically, we will characterize scleral biomechanics in the normal and glaucomatous eye as to refine our current estimates of IOP-induced stress and strain levels within the ONH, and understand the interactions between the ONH tissues and the posterior sclera that could lead to glaucomatous optic neuropathy.

The Importance of the Peripapillary and Posterior Sclera in Glaucoma

As previously mentioned, the sclera is the outer shell and principal load-bearing tissue of the eye. Consisting primarily of collagen fibers and essentially avascular, it provides constant protection for the adjacent intraocular tissues. Ninety percent of the scleral collagen fibers are Type-I (Edelhauser and Ubels 2003), which provides the majority of the tissue's mechanical integrity and tensile strength (Fung 1993) to resist acute and chronic changes in IOP, as well as mechanical stress from the extraocular muscles.

The sclera has been recognized to exhibit complex anisotropic characteristics, which are a consequence of the multi-directional arrangement of collagen fibers that run in directions parallel to the scleral surface (Watson and Young 2004). Collagen fibers within the sclera are highly variable in their diameters and are organized into irregularly arranged and interwoven lamellae (Komai and Ushiki 1991; Watson and Young 2004) as shown in Figure 1.1.8. Collagen fiber diameters vary between 25 and 300 nm within the different scleral lamellae (Quantock and Meek 1988; Komai and Ushiki 1991) and are on average smaller in the peripapillary region than in the equatorial region (Quigley *et al.* 1991b). The scleral lamellae also vary greatly in thickness and in preferred orientation (Watson and Young 2004; Rada *et al.* 2006). The overall organization of the collagen fibers in the sclera is more random than that in the cornea (Teng *et al.* 2006), which makes the sclera a white opaque tissue.
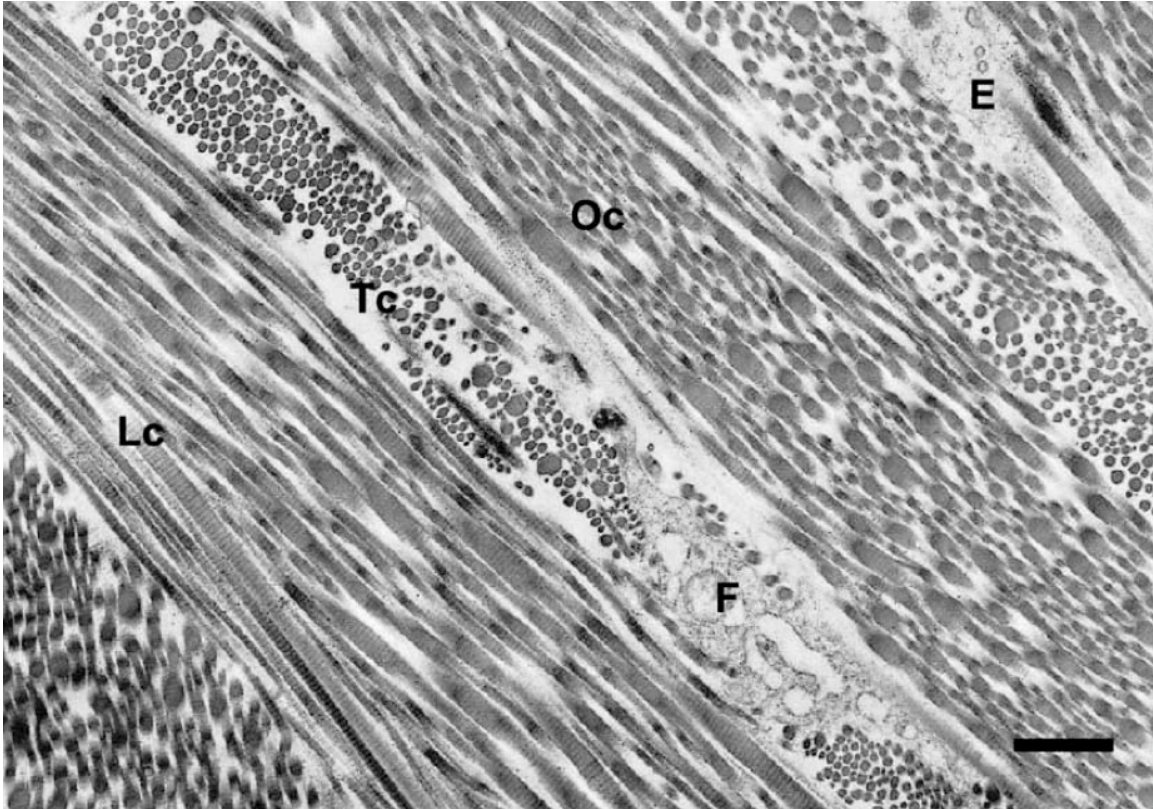
Figure 1.1.8. Scleral lamellar organization of the collagen fibers from a human eye showing the wide variations in lamella preferred fiber orientation and collagen fiber diameters. (**Lc**) Longitudinal fibers, (**Tc**) transverse fibers, and (**Oc**) Oblique fibers with respect to the section plane. Note that fibroblasts (**F**) and elastin (**E**) are also present. The bar located at the bottom right corner represent an approximate length of 1.5 μm. All collagen fibers are perpendicular to the transmural direction of the tissue. Figure obtained from (Watson and Young 2004), reproduced from (Bron *et al.* 1997).

It has been shown that the collagen fibers of the sclera are more organized in the immediate peripapillary region and oriented circumferentially to the ONH (Kokott 1934; Greene 1980; Hernandez *et al.* 1987). In our opinion, the collagen fibers within the peripapillary sclera region have a protective role with respect to the ONH connective and axonal tissues, and that the anisotropy of the sclera exists to provide functions such as limiting stress concentration at the scleral-laminar junction. Two extraocular muscles (the inferior oblique and the superior oblique muscles) are directly attached to the sclera in the

posterior portion of the eye. Where these muscles attach, the scleral collagen fibers orient

perpendicularly to their insertions as shown in Figure 1.1.9.
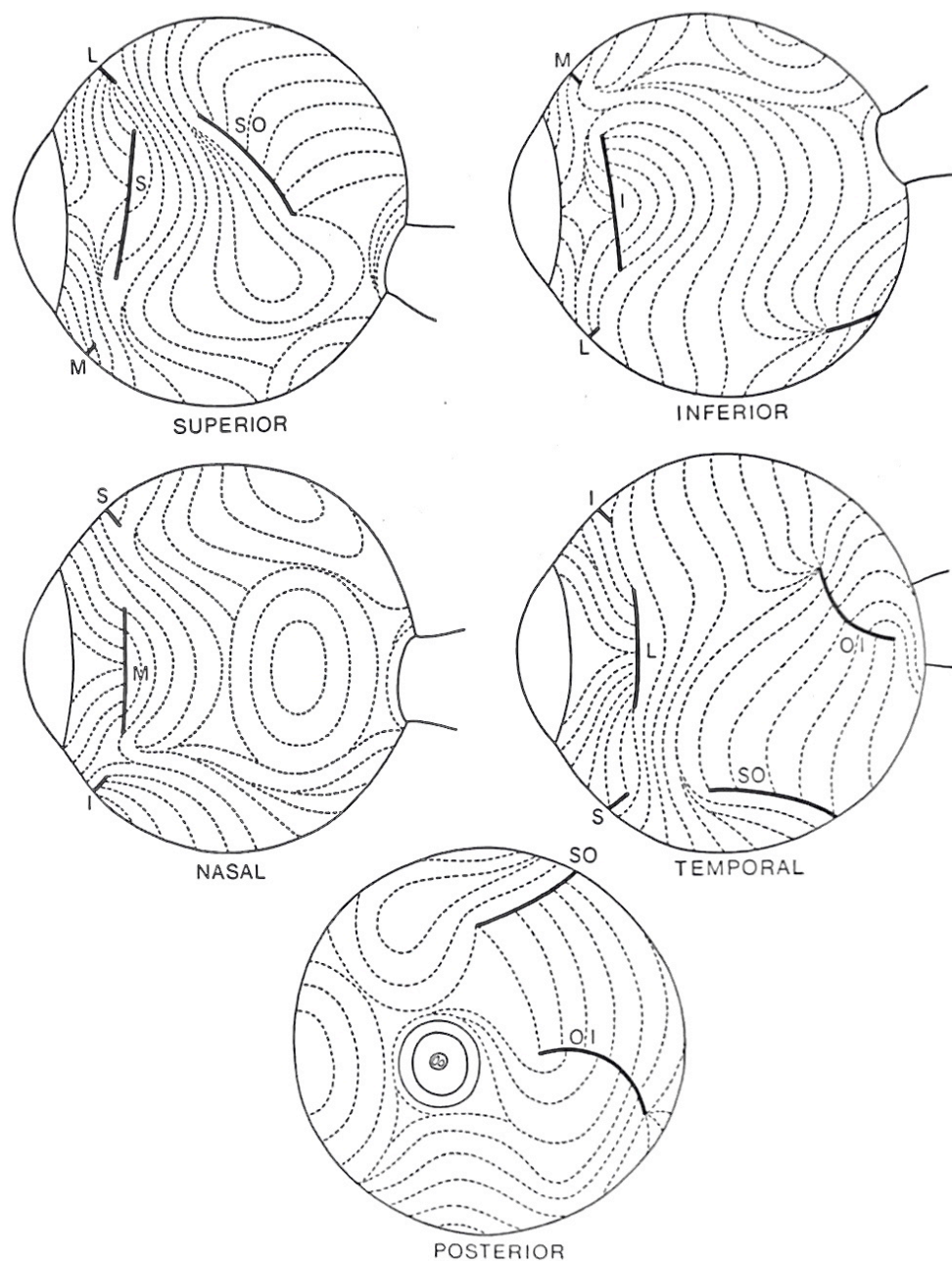
Figure 1.1.9. Gross representation of the preferred collagen fiber orientation in the sclera of a human eye based on traditional histology. A circumferential organization is emphasized near the ONH, and collagen fibers are oriented perpendicularly to the inferior and superior oblique muscle insertions. Muscle insertions: (**OI**) inferior oblique, (**SO**) superior oblique, (**L**) lateral rectus, (**M**) medial rectus, (**S**) superior rectus, (**I**) inferior rectus. Figure obtained from (Hogan 1971) which was reproduced from (Kokott 1934).

The inferior and superior oblique muscles have the potential to generate large stress and strain levels within the sclera during eye movements, which are experienced during normal activities such as reading. Therefore, it seems reasonable that the scleral collagen fibers are oriented perpendicular to the inferior and superior oblique muscle insertions to limit large deformations of the scleral shell. The inferior oblique muscle insertion is located close to the infero-temporal region of the ONH (within ~ 3 mm), which is one of the regions of greatest susceptibility to glaucomatous retinal ganglion cell axon loss (Quigley and Green 1979). Stress and strain levels generated at the Inferior oblique muscle insertion during eye movements (no relationship to IOP) may eventually prove to be substantial and propagate toward the ONH.

Scleral thickness is not uniform. In fact, it varies significantly from the limbus to the peripapillary region (Figure 1.1.10). The sclera is thinnest near the equator of the eye and becomes thickest in the peripapillary region. This trend has been reported in humans (Avetisov *et al.* 1983; Olsen *et al.* 1998), monkeys (Downs *et al.* 2001) and pigs (Olsen *et al.* 2002). Porcine sclera is as thick as human sclera but monkey posterior sclera is about half as thick as human sclera. In the peripapillary region, the sclera is thinner near the scleral canal opening (Figure 1.1.2) and thinnest in the nasal quadrant (Downs *et al.* 2002). Evidence suggests that the monkey peripapillary and posterior sclera thins in eyes exposed to chronic IOP elevations (Downs *et al.* 2001; Yang *et al.* 2007b). A decrease in scleral thickness, separate from a change in mechanical properties, will be associated with an increase in IOP-induced stress levels at the scleral-laminar boundary (Bellezza *et al.* 2000). Therefore, scleral thickness is likely an important factor that should be monitored during the development and progression of glaucomatous optic neuropathy. In

fact, scleral thickness has been considered the fifth most important determinant of ONH biomechanics (Sigal *et al.* 2005). A decrease in scleral thickness is often a characteristic of myopia (Phillips and McBrien 1995) and some evidence suggests that highly myopic eyes are more susceptible to glaucomatous damage than normal eyes (Mitchell *et al.* 1999; Jonas *et al.* 2004; Jonas and Budde 2005), but this remains controversial. One important aspect of our work will be to understand the potential interactions between scleral thickness and mechanical properties in normal and glaucomatous eyes.
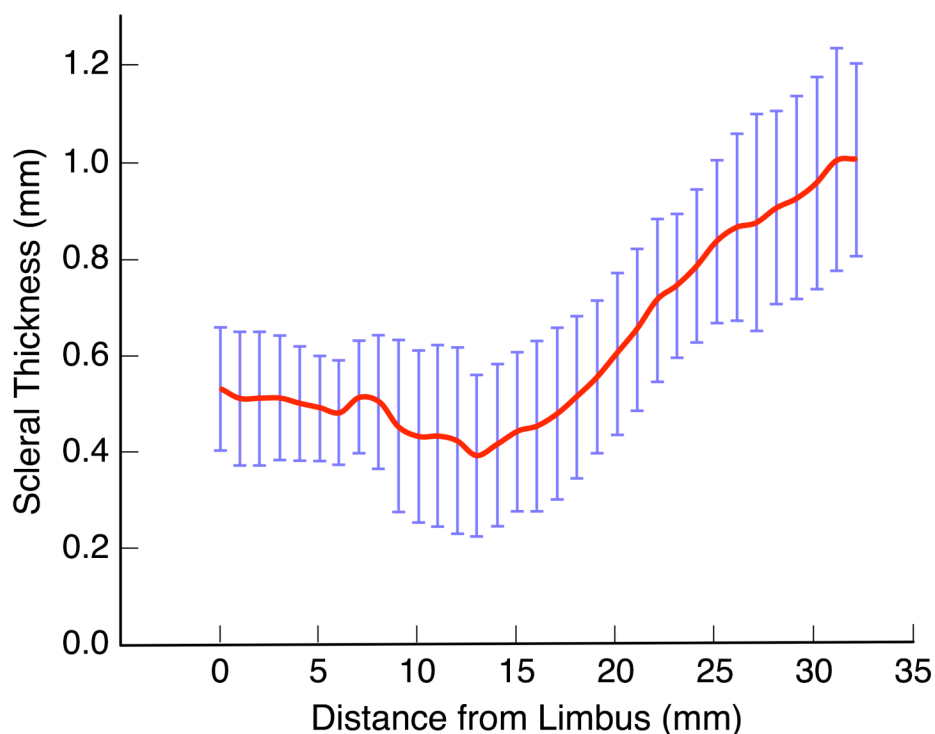
Figure 1.1.10. Human scleral thickness (mean ± standard deviation) versus the distance from the surgical Limbus (*i.e.* scleral corneal boundary) toward the ONH. Redrawn from (Olsen *et al.* 1998).

The remodeling process that is involved during the development and progression of glaucomatous optic neuropathy within the load-bearing tissues of the eye, including the sclera, remains poorly understood. The term remodeling is broad and can represent

changes in shape (morphogenesis), mass (growth), collagen fiber alignment (reorientation), collagen fiber diameter, protein content and protein type. Changes in mass and shape will have a direct impact on soft tissue geometries, while changes in collagen fiber orientation, fiber diameter, protein content and type will directly affect soft tissue mechanical properties at the macroscopic level.

Both biochemical and biomechanical stimuli have been proposed to play a role in inducing extracellular matrix remodeling in soft tissues (Streuli 1999). In the sclera, fibroblasts located between lamellae (Figure 1.1.8) are believed to be exclusively responsible for the synthesis of the scleral extracellular matrix (Rada *et al.* 2006). In the field of biomechanics, two theories have been proposed to explain the remodeling process occurring in collagenous soft tissue. The first theory assumes that collagen fibers will align along positive principal strain directions and that fiber content will increase as fiber strain increases (Driessen *et al.* 2003). In other words, remodeling is triggered by the macroscopic deformations that the collagenous soft tissue experiences. This approach is commonly used for the study of bones (Roberts and Hart 2005). In many cases, fiber reorientation is a process optimized to protect biological structures by minimizing deformations and providing strength. For example, ligaments that have a longitudinal arrangement of collagen fibers are highly optimized for axial loading.

The second theory states that stress, not strain, is the driving mechanism that will lead to fiber reorientation and tissue growth (Taber and Humphrey 2001; Hariton *et al.* 2007a). Hariton and coworkers recently proposed a stress-driven remodeling theory to explain the collagen fiber architecture in arterial walls (Hariton *et al.* 2007a) and in carotid bifurcations (Hariton *et al.* 2007b). Using this theory, they were able to simulate

similar collagen fiber orientations to those observed histologically and concluded that collagen fibers are configured to optimize stress levels within arterial walls and carotid bifurcations.

It is somewhat disconcerting to see that remodeling in soft tissues cannot be explained with a single unified theory that is either strain- or stress-driven. Recently, Humphrey gently reminded biomechanicists that the cells responsible for triggering a remodeling response sense neither stress nor strain as they are both macroscopic constructs (Humphrey 2001). Macroscopic stress and strain do not inform us about the microscopic behavior of cells and molecules, and it seems merely convenient to wonder if remodeling is correlated with those macroscopic constructs. That said, nothing precludes different types of cells sensing mechanical stimuli through different mechanisms, which requires different remodeling theories for different soft tissues.

In the case of the sclera, a variety of studies have reported a correlation between mechanical strain and scleral fibroblast cellular response. Mechanical strain applied to a thin membrane on which scleral fibroblasts were grown resulted in the suppression of TIMP-1 (0.45 % cyclic strain in humans (Yamaoka *et al.* 2001)), in changes in gene expression (4 % constant strain in humans (Cui *et al.* 2004)), in the production of MMP-2 and suppression of TIMP-2 (15 % cyclic strain in humans (Shelton and Rada 2007)), and in enhanced expression of both MMP-2 and TIMP-2 mRNA (20 % cyclic strain in chicks (Fujikura *et al.* 2002)). According to these studies, a wide range of strain levels (0.45 % to 20 %) has the capacity to trigger remodeling of the scleral extracellular matrix which could result in thinning or thickening, and/or softening or stiffening of the sclera. It will

eventually become important to understand these phenomena, because changes in scleral material properties can have a major impact on ONH deformations.

Studies have shown that collagen content in the peripapillary sclera was significantly lower in glaucomatous human eyes when compared to normal human eyes, however, these changes were not observed in monkey eyes (Quigley *et al.* 1991b). A decrease in collagen content should result in a lower elastic modulus, assuming there is no change in fiber diameter, which was also reported. Downs and coworkers reported that the instantaneous and equilibrium elastic moduli of monkey peripapillary sclera were significantly higher in glaucomatous monkey eyes than in normal monkey eyes (Downs *et al.* 2005). To resolve such discrepancy, it is important to provide a higher-level material description for the sclera based upon its internal constitution and organization. Furthermore, the use of an anisotropic material description for the posterior and peripapillary sclera, with incorporation of regional variations in thickness, will potentially allow us to detect more subtle differences between glaucomatous and normal monkey eyes. To our knowledge, nobody has yet provided a constitutive description for the posterior sclera that is based upon collagen fiber behavior. Because the lamina cribrosa inserts deeply into the peripapillary sclera and because the elastic modulus of the sclera has been shown to be the largest single determinant of strains within the lamina cribrosa (Sigal *et al.* 2005), the sclera is likely to play an important role in the development and progression of glaucomatous optic neuropathy (Ethier 2006). Therefore it is crucial to understand scleral biomechanics with improved experimental and computational tools.

Measurement of Scleral Deformations

Data from mechanical testing on biological soft tissues are important for deriving proper constitutive equations that will help us predict and understand their mechanical behaviors in physiological environments. It is also important to respect the physiological loading that biological soft tissues will encounter through life. Most membranous pressure vessels, such as eyes, experience mostly tension in their physiological environment.

To understand the mechanical behavior of soft tissues, biomechanicists started mechanical testing with uniaxial tests, during which the force and the associated stretch were measured in one unique direction. Most mechanical tests that have been performed on the sclera were uniaxial tests of scleral strips that were harvested from the eye at different locations (Curtin 1969; Friberg and Lace 1988; Phillips and McBrien 1995; Siegwart and Norton 1999; Downs *et al.* 2003; Wollensak and Spoerl 2004; Downs *et al.* 2005; Girard *et al.* 2007; Schultz *et al.* 2008; Weiyi *et al.* 2008). Uniaxial deformation data are easier to obtain, but cannot be generalized to describe the mechanical behavior of a membranous soft tissue in multi-axial loading conditions. Working with passive cardiac tissue (composed of muscle, collagen and elastin fibers), Humphrey and Yin demonstrated that mechanical properties determined from uniaxial testing could result in gross underestimates of the actual stresses within the tissue (Humphrey and Yin 1987).

Lanir and Fung were among the first investigators to test biological soft tissues biaxially (Lanir and Fung 1974a; Lanir and Fung 1974b). In their experiments, a square piece of rabbit skin was stretched in two perpendicular directions simultaneously. Deformations that arise from biaxial testing are commonly recorded with optical tracking

techniques, in which markers or microspheres are glued to the tissue surface and tracked over time (Hoffman and Grigg 1984; Humphrey *et al.* 1987; Billiar and Sacks 2000b). Biaxial tests provide a way to determine the complete three-dimensional constitutive relationships for biological soft tissues if one assumes incompressibility. It should be noted that the posterior sclera has recently been tested biaxially (Olesen *et al.* 2007). However, in pressure vessels such as the eye, the specimens have to be flattened prior testing, meaning that the curved anatomical geometry cannot be maintained and hence unwanted residual stresses can be generated within the tissue. In terms of experiments on the sclera specifically, several investigators have considered pressure loading as appropriate by either clamping the scleral shell at the equator on a pressure chamber (Woo *et al.* 1972; Smolek 1988), or by keeping the globe intact and inserting a cannula within the anterior chamber for pressure control (Greene and McMahon 1979). Greene and Woo were able to track several markers located on the scleral shell surface but were unable to generate the full 3-D displacement maps that are necessary for the derivation of a constitutive theory.

In the field of biomechanics, it is usually difficult to find inexpensive high-resolution technologies to generate 3-D deformation data. Nevertheless, measurement systems based on holographic and speckle interferometry technologies (Jones and Wykes 1989) are currently used in biomechanics research for *in vitro* mechanical testing (Charette *et al.* 1997; Erne *et al.* 2005; Kessler *et al.* 2006). In this study, we used electronic speckle pattern interferometry (ESPI) to measure the 3-D surface deformation of posterior scleral shells loaded via a custom-built pressurization apparatus. By measuring the surface deformation patterns of the posterior sclera at various pressures,

we are able to determine its local stiffness and also develop corresponding constitutive theories. By incorporating these new data into our models, we will enhance the accuracy of our IOP-induced stress and strain predictions within the load-bearing tissues of the eye.

A Constitutive Theory for the Peripapillary and Posterior Sclera

Constitutive theories are fundamental to specify the mechanical properties of materials based upon their internal constitution (Mase and Mase 1999). The sclera has often been described as a thin-walled pressure vessel, which obeys the analytical constitutive equation known as Laplace's law (Cahane and Bartov 1992). Laplace's law is defined as $\sigma = PR/2t$, where σ is the hoop stress, P is the pressure inside the spherical vessel, R is the radius of the vessel and t is the thickness of the wall. Laplace's law provides a gross estimation of the state of stress within the sclera, because this equation is only valid for isotropic spherical vessels with uniform wall thickness and does not take into account the discontinuity that exists within the sclera due to the presence of the scleral canal. If the lamina cribrosa is more compliant than the corneo-scleral shell, we would expect large IOP-induced stress concentrations near the scleral canal (Bellezza *et al.* 2000; Sigal *et al.* 2004). Therefore Laplace's law should always be avoided for predicting scleral stresses in the eye.

Many investigators have reported a single elastic modulus for the sclera (Battaglioli and Kamm 1984; Friberg and Lace 1988; Smolek 1988; Avetisov *et al.* 2003; Pierscionek *et al.* 2007). It has been well established that collagen fibers are the source of the sclera's tensile strength. They exhibit a characteristic nonlinear stress-strain curve

consisting of the initial *toe region* of increasing elastic modulus and the subsequent *linear region* of constant but higher elastic modulus (Fung 1993). The *toe region* is usually associated with the range of stress and strain the tissue experiences under its physiological environment. In an unstretched state, corresponding to the zero stress-strain point, collagen fibers are buckled. As they are stretched along their axis, fibers become uncrimped and move up to the initial *toe region* in the stress-strain curve, hence increasing their stiffness. At the end of the *toe region*, it has been shown that all fibers straighten and enter the *linear region* (Kastelic *et al.* 1978). A single elastic modulus is therefore insufficient to fully describe the nonlinear mechanical behavior of the sclera and it is more appropriate to employ the terminology of *tangent modulus*, in which *tangent* simply refers to the tangent of the nonlinear stress-strain curve at a given point. The tangent modulus is not a unique quantity but varies with the deformations experienced by the tissue. Many investigators have measured the nonlinear behavior of the sclera experimentally and reported tangent modulus estimates (Woo *et al.* 1972; Phillips and McBrien 1995; Siegwart and Norton 1999; Wollensak and Spoerl 2004; Spoerl *et al.* 2005; Olesen *et al.* 2007; Schultz *et al.* 2008; Weiyi *et al.* 2008). However, they were unable to translate these observations into a proper 3-D constitutive theory that is necessary to fully predict the mechanical behavior of the sclera. In this thesis, we propose a constitutive theory that incorporates the 3-D mechanical behavior of the collagen fibers, and we hypothesize that the sclera becomes stiffer with IOP.

The sclera has been modeled as a viscoelastic material by Downs and coworkers (Downs *et al.* 2003; Downs *et al.* 2005). They reported three viscoelastic parameters from uniaxial testing using linear isotropy. However, while viscoelasticity plays a role in the

eye's response to IOP fluctuations, it is currently unknown if the viscous behavior of the posterior sclera is important in the development of chronic diseases such as glaucoma.

The ultrastructure of soft tissues can significantly influence overall tissue mechanical behavior, so current material descriptions for the sclera are simplistic. Relating material properties to tissue ultrastructure is a field that is growing in importance, and several investigators have realized the value of deriving fiber-based theories for anisotropic soft tissues (Lanir 1983; Humphrey *et al.* 1990; Ault and Hoffman 1992; Weiss *et al.* 1996; Billiar and Sacks 2000a; Holzapfel *et al.* 2000; Zulliger *et al.* 2004; Pinsky *et al.* 2005; Gasser *et al.* 2006; Driessen *et al.* 2008; Nguyen *et al.* 2008). Note that this reference list is by no means complete as many other investigators have provided 3-D constitutive theories to describe collagenous soft tissues. These models are strain energy-based, meaning that stresses are derived from a potential function, and rely on a mechanical theory known as fiber-reinforced composite theory (Spencer 1974) that is suitable for large deformations (Green 1970). The theory states that the fibers should be long compared to their diameters and the fiber spacings, and should form a substantial proportion of the composite (> 50%).

The two main types of extracellular protein fibers in membranous soft tissues are elastin and collagen. Because collagen is organized into long and dense fibrous bundles and is responsible for most of the tensile strength, and elastin is organized in "noodle-like" cross-linked coil, it is often common to treat collagen as the primary biomechanical element. Hence, collagen fibers are mathematically isolated and all the other tissue components such as elastin, proteoglycans, glycosaminoglycans, fibroblasts and tissue fluid are included in the ground substance matrix (Weiss 1994). Because it has been

shown that the collagen fibers of the sclera are locally parallel in distinct layers, and their preferred orientations change throughout the layers (Figure 1.1.8), we propose to model the sclera with multi-directional fibers at local material points as performed for other soft tissues (Billiar and Sacks 2000a; Driessen *et al.* 2003; Freed *et al.* 2005; Pinsky *et al.* 2005; Gasser *et al.* 2006; Nguyen *et al.* 2008). By taking this approach, we will greatly improve our knowledge of scleral biomechanics and improve our estimates of IOP-induced stress and strain levels at the scleral-laminar boundary.

Summary of Previous Studies on Scleral Biomechanics

Table 1.1.1 shows a summary of previous work that has been performed to characterize scleral biomechanics. It should be noted that wide ranges for scleral mechanical properties are observed depending on the species, the experimental techniques used, and the constitutive theories applied.

Author	Year	Species	Region	Experiment	Theory	Material Parameters	Value (MPa)
Curtin	1969	Human	Anterior Equator Posterior	1D Tension	NA	Tangent Modulus (73 kPa stress)	Anterior: 5.0 − 12.2 Equator: 4.2 − 12.7 Posterior: 1.1 − 3.9
Curtin	1969	Porcine	Anterior Equator Posterior	1D Tension	NA	Tangent Modulus (73 kPa stress)	Anterior: 3.3 − 4.2 Equator: 6.2 − 15.6 Posterior: 1.4 - 3.0
Woo	1972	Human	Posterior	Pressurization	Trilinear Elasticity	Tangent Modulus	0.9 − 2.7
Greene	1979	Rabbit	Posterior	Pressurization	NA	NA	NA
Avetisov	1984	Human	Posterior	1D Tension	Linear Elasticity	Elastic Modulus	Anterior: 15 − 30 Posterior: 5 − 15
Battaglioli	1984	Bovine	Anterior	Compression	Linear Elasticity	Compressive Modulus	0.00121 − 0.0019
Battaglioli	1984	Human	Anterior	Compression	Linear Elasticity	Compressive Modulus	0.0027 − 0.0041
Smolek	1988	Bovine	Posterior	Pressurization	Linear elasticity	Elastic Modulus	3.9 − 9.0
Friberg	1988	Human	Anterior Posterior	1D Tension	Linear Elasticity	Elastic Modulus	1.3 − 3.5
Phillips	1995	Tree Shrew	Posterior	1D Tension	Nonlinear Elasticity	Tangent Modulus (1.5 % strain)	2.28 − 3.44
Siegwart	1999	Tree Shrew	Posterior	1D Tension	Trilinear Elasticity	Tangent Modulus	0.69 − 18.1
Downs	2003	Rabbit	Peripapillary	1D Tension	Linear Viscoelasticity	Instantaneous Modulus (1% strain) Equilibrium Modulus	9.6 − 13.3 0.54 − 0.91
Downs	2003	Monkey	Peripapillary	1D Tension	Linear Viscoelasticity	Instantaneous Modulus Equilibrium Modulus	25.3 − 34.3 2.91 − 5.51
Wollensak	2004	Porcine	Sagital	1D Tension	Nonlinear Elasticity	Tangent Modulus (8% strain)	5.95
Wollensak	2004	Human	Sagital	1D Tension	Nonlinear Elasticity	Tangent Modulus (8% strain)	22.82
Spoerl	2005	Human	Peripapillary	1D Tension	Nonlinear Elasticity	Tangent Modulus (20% strain)	28.5 − 36.0
Girard	2007	Rabbit	Peripapillary	1D Tension	Linear Viscoelasticity	Instantaneous Modulus (1% strain) Equilibrium Modulus	23.0 − 30.3 2.7 − 3.8
Olesen	2007	Human	Posterior	2D Tension	Nonlinear Elasticity	Tangent Modulus	2.5 − 14
Pierscionek	2007	Porcine	Posterior	Pressurization	Linear Elasticity	Elastic Modulus	0.2 − 0.5
Girard	2008	Porcine	Peripapillary	Pressurization	NA	NA	NA
Weiyi	2008	Rabbit	Ante − Post	1D Tension	Nonlinear Elasticity	Tangent Modulus	0.35 − 1.08
Schultz	2008	Porcine	Posterior	1D Tension	Nonlinear Elasticity	Tangent Modulus (1% strain)	0.65 ± 0.53
Schultz	2008	Human	Posterior	1D Tension	Nonlinear Elasticity	Tangent Modulus (1% strain)	2.60 ± 2.13
Girard	2008	Monkey	Posterior	Pressurization	Anisotropic Nonlinear Elasticity	Tangent Modulus (30 mm Hg IOP) Peripapillary Sclera	Young Normal 8.3 − 8.7
Girard	2008	Monkey	Posterior	Pressurization	Anisotropic Nonlinear Elasticity	Tangent Modulus (30 mm Hg IOP) Peripapillary Sclera	Young: 5.6 − 22.1 Old: 19.1 − 41.3
Girard	2008	Monkey	Posterior	Pressurization	Anisotropic Nonlinear Elasticity	Tangent Modulus (30 mm Hg IOP) Peripapillary Sclera	Normal: 11.1 − 30.3 EG: 10.9 − 31.5 MG: 15.1 − 49.7

Table 1.1.1. Summary of previous work on scleral biomechanics showing experimental techniques, constitutive theories and mechanical property estimates. Note that Curtin did not report tangent modulus values and these were calculated from the experimental data that were reported. (**EG**) Early glaucoma, (**MG**) Moderate glaucoma.

Age as a Risk Factor in Glaucoma

Strong evidence suggests that ONH tissues become more susceptible to progressive glaucomatous damage with age. Recently, the Eye Disease Prevalence Research Group summarized prevalence estimates of open-angle glaucoma by age groups from eight population-based studies that were performed in the United States, Australia, and in Europe (Friedman *et al.* 2004). These data are summarized in Figure 1.1.11.
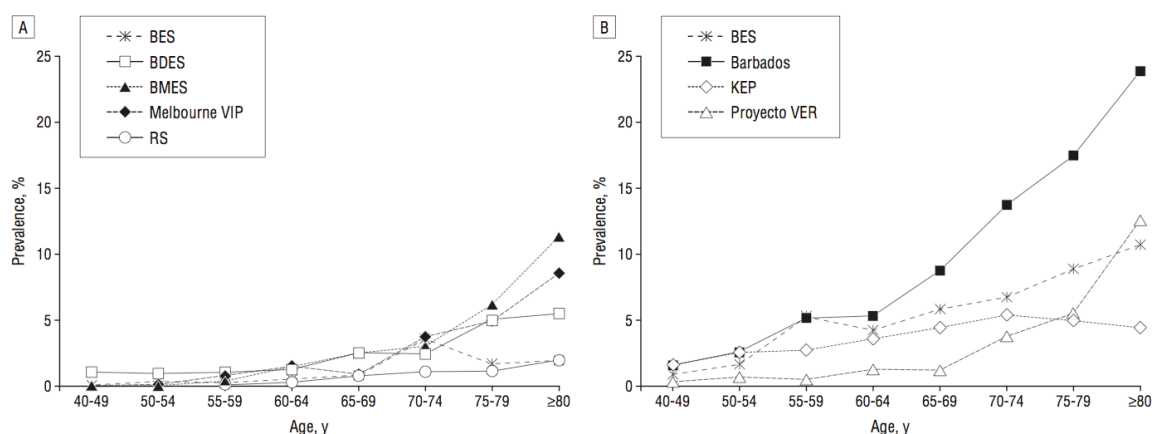
Figure 1.1.11. Prevalence of open-angle glaucoma in white (**A**), black and Hispanic (**B**) subjects. (**BES**) Baltimore Eye Survey (Tielsch *et al.* 1991), (**BDES**) Beaver Dam Eye Study (Klein *et al.* 1992), (**BMES**) Blue Mountain Eye Study (Mitchell *et al.* 1996), (**Melbourne VIP**) Melbourne Visual Impairment Project (Wensor *et al.* 1998), (**RS**) Rotterdam Study (Wolfs *et al.* 2000), (**Barbados**) Barbados Eye Study (Leske *et al.* 1994), (**KEP**) Kongwa Eye Project (Buhrmann *et al.* 2000), (**Proyecto VER**) Vision Evaluation Research (Quigley *et al.* 2001). Figure obtained from (Friedman *et al.* 2004).

In almost all populations, it is apparent that the prevalence of open-angle glaucoma significantly increases with age, which confirms that open-angle glaucoma is a disease of the elderly. Moreover, pediatric glaucoma has been described as relatively rare, even though there is a lack of epidemiologic data regarding this condition (Papadopoulos *et al.* 2007). Some investigators have found that IOP does not vary with age (Rochtchina *et al.* 2002), while others have found only slight variations: a 1 mm Hg increase per decade

from forty to eighty years old in black patients (Leske *et al.* 1997), and a 1 mm Hg decrease from forty to eighty years old in Japanese patients (Nomura *et al.* 2002). All together, these results suggest that glaucomatous damage in the elderly is likely caused by a greater susceptibility to IOP or other non IOP-related factors rather than increasing IOP.

In this study, we hypothesize that age-related changes in ONH and scleral biomechanics underlie the increased susceptibility to glaucomatous damage in the elderly. There is substantial evidence that the connective tissues of the lamina and sclera are altered with age, which in turn alters their biomechanical behavior. Age-related changes in the human lamina cribrosa have been associated with increased collagen and elastin content as well as increased collagen and elastin cross-links (Hernandez *et al.* 1989; Albon *et al.* 1995; Albon *et al.* 2000a). Collagen cross-linking is a characteristic of aging soft tissues (Bailey *et al.* 1998), which results in an increase of stiffness at the tissue level (Spoerl *et al.* 2005), accompanied with an increase in failure stress (more brittle collagen fibers) and a decrease in failure strain (Bailey *et al.* 1998). Several studies using uniaxial tensile testing of scleral strips from tree shrew (Siegwart and Norton 1999) and human (Curtin 1969; Avetisov *et al.* 1983; Friberg and Lace 1988) eyes concluded that the stiffness of the sclera increases with age. However, none of these studies used either a 3-D characterization of scleral biomechanics in the aging eye or fiber-reinforced composite theory. By ultimately building FE models of the ONH and scleral shell from young and old eyes, we hope to elucidate the underlying mechanisms of how and why aging can become a risk factor for the development of glaucoma. These models will require a proper characterization of scleral biomechanics in the aging eye, which will be

undertaken in this study. We hope to eventually understand if there is a predictable pattern of damage to the load-bearing tissues of the ONH that is related to IOP-induced stress and strain.

The Monkey Model of Glaucoma

The non-human primate is one of the few animals in which IOP elevation can be used to create an optic neuropathy that is clinically and histologically indistinguishable from human glaucoma (Gaasterland and Kupfer 1974; Gaasterland *et al.* 1978; Quigley and Addicks 1980). In each individual monkey, the trabecular meshwork of one eye is photocoagulated, creating a chronic IOP elevation that eventually leads to retinal ganglion cell axon damage. The contralateral eye, being untreated, is used as a control. To detect alterations attributed to chronic IOP elevation, between eye differences in the lasered monkeys must exceed inter-eye physiologic differences in well characterized groups of normal monkeys. This model provides an efficient way to evaluate the risk factors for retinal ganglion cell axon damage such as connective tissue architecture and stiffness by comparing the lasered eye to its contralateral control. In this thesis, we will study scleral biomechanics in the normal, glaucomatous, and aging monkey eye.

1.2. Hypotheses and Specific Aims

The goal of this study is to characterize peripapillary and posterior scleral biomechanics in the normal, glaucomatous and aging monkey eye using both state-of-the-art experimental and computational protocols. Mechanical properties of the peripapillary and posterior sclera are considered a major determinant of the levels of deformation in

the ONH (the principal site of damage in glaucoma) exposed to acute elevations of IOP. This emphasizes the importance of the sclera as a load-bearing tissue in glaucoma. Here, we aim to provide a better understanding of the 3-D mechanical behavior of the peripapillary and posterior sclera due to acute elevations of IOP, which has never been characterized previously. We also aim to investigate how the mechanical properties, thickness, and fibrous architecture of the peripapillary and posterior sclera can potentially play a role, and be altered by, the development and progression of glaucoma. In addition, because glaucoma is primarily a disease of the elderly, we hope to provide insight into whether age-related changes in scleral biomechanics can contribute to the initiation or progression of the disease.

To begin this investigation, we will provide a series of experimental tools to measure 1-D (uniaxial test and extensometer), 2-D (pressurization test and planar optical tracking) and 3-D (pressurization test and 3-D electronic speckle pattern interferometry) scleral deformations, as well as scleral topography (3-D digitizer) and scleral thickness (ultrasound transducer). To mathematically model scleral biomechanics, we will develop: 1) a new viscoelastic constitutive model, 2) a preprocessing FE software to generate anatomically-accurate posterior scleral geometries, 3) a new anisotropic hyperelastic constitutive model for soft tissues with multi-directional fibers, as well as its FE implementation, and 4) a postprocessing FE software to visualize scleral displacement, strain, stress and preferred fiber orientation. Finally, we will develop an inverse FE method to extract scleral mechanical properties based on experimental observations of IOP-induced 3-D scleral displacements.

We state the following hypotheses:

Hypothesis 1. Scleral biomechanics is unaltered for at least 72 hours after enucleation if sclera is stored in phosphate buffered saline.

Hypothesis 2. The posterior sclera is a highly nonlinear, anisotropic, and inhomogeneous tissue, is optimized to limit IOP-induced mechanical insult to the ONH, and can be modeled as an hyperelastic material.

Hypothesis 3. The posterior sclera is considerably stiffer in older eyes.

Hypothesis 4. Chronic IOP elevations lead to posterior scleral remodeling, including changes in scleral thickness, mechanical properties and collagen fiber organization.

In order to test these hypotheses, the following specific aims are proposed:

Specific Aim 1. To evaluate the effects of post-mortem storage time on the mechanical properties of rabbit peripapillary sclera after enucleation, using uniaxial testing and linear viscoelastic theory.

Specific Aim 2. To develop experimental methods to measure 2-D and 3-D monkey posterior scleral deformations due to acute elevations in IOP, as well as regional variations in scleral thickness and topography.

Specific Aim 3. To develop a 3-D constitutive model for the posterior sclera based on fiber-reinforced composite theory, and its corresponding FE implementation. The sclera will be modeled as a nonlinear, anisotropic and inhomogeneous material using hyperelasticity.

Specific Aim 4. To develop an inverse FE method to extract nonlinear, anisotropic, inhomogeneous mechanical properties (Aim 3) for the posterior sclera based on experimental observations (Aim 2). Scleral biomechanics will be characterized for

normal (young and old) monkey eyes and for monkey eyes exposed to chronic IOP elevations (*i.e.* experimental glaucoma).

1.3. Format of the Following Chapters

This section provides details of the work I have conducted during my PhD thesis and a brief summary of the following Chapters. Chapter 2 contains all work related to the viscoelastic characterization of rabbit peripapillary sclera according to different post-mortem storage time. I started this work as a first year graduate student in the department of Biomedical Engineering at Tulane University in the Summer of 2003. I used the uniaxial testing apparatus Crawford Downs designed during his PhD training, which was mounted on a highly accurate testing frame provided by Francis Suh. In the Fall of 2003, I had the chance to develop a new viscoelastic constitutive model that did a wonderful job in fitting the uniaxial data obtained from experiments. This part of work addresses Aim 1.

Chapter 3 contains all work related to the 2-D optical tracking of porcine peripapillary scleral deformations. This work was initated in the Spring of 2004 during which I developed a new experimental protocol to measure *ex-vivo* scleral deformations. A pressurization apparatus was built to inflate posterior scleral shells of different sizes and in the Summer of 2004, I started to develop a method to track microspheres attached to the scleral shell surface based on the optical flow algorithm. This work addresses part of Aim 2.

Chapter 4 contains all work concerning the development of anisotropic hyperelastic constitutive model for the posterior sclera. This work was started during the

Spring of 2005 and thanks to Francis Suh, I had the chance to obtain the source code of the nonlinear FE software Nike3d. I was able to learn from Jeffrey Weiss' excellent work on tendons and ligaments as Jeffrey Weiss implemented a module for transversely isotropic hyperelastic materials within Nike3d. Using this module, combined with what I learned from the experimental study on porcine eyes, I improved the code to allow for incorporation of multi-directional collagen fibers at local material points. This part of work addresses Aim 3.

Chapter 5 contains all work concerning the development of experimental methods to measure scleral thickness, topography and 3-D deformations and the development of an inverse FE method to extract mechanical properties according to the experimental observations. This Chapter is the core of this thesis as it combines 3-D experimental and computational protocols to characterize scleral biomechanics. In August of 2005, New Orleans, LA was severely hit by hurricane Katrina, and I followed Claude Burgoyne and Crawford Downs and relocated to Portland, OR to continue my PhD work. Most of the experimental equipments that was designed at Tulane University was brought with us. I also had the chance to collaborate with Michael Bottlang in Portland, thanks to Crawford Downs. I was able to use his wonderful ESPI sensor to measure 3-D scleral deformations due to acute elevations of IOP, and this was started in the Fall of 2005. The measurement of scleral thickness and topography was started at Tulane University, initially on porcine eyes, and carried on in Portland, OR. After much hard work, the complete method to extract mechanical properties for the posterior sclera (including the inverse FE method) was ready in the Fall of 2006 and was applied to fresh porcine and monkey eyes. This part of work addresses Aims 2 and 3.

Chapter 6 contains all work related to scleral biomechanics in the aging monkey eye using the method described in Chapter 5. I started performing experiments on both eyes of sixteen monkeys (four young, four old, four early glaucoma, and four moderate glaucoma) in the Spring of 2007 and extracted mechanical properties for young and old monkeys in the Fall of 2007. This part of work addresses Aim 4.

Chapter 7 contains all work related to scleral biomechanics in the normal and glaucomatous monkey eye using the method described in Chapter 5. Computational simulations to extract mechanical properties for normal and glaucomatous eyes were started in the Spring of 2008. This part of work addresses Aim 4.

Chapter 8 summarizes the principal findings of my PhD thesis, provides conclusions and important remarks, as well as future work that should be performed in order to gain more understanding about the relationship between ocular biomechanics and glaucoma. In addition, Appendix A documents the fully-detailed experimental protocols to perform 3-D mechanical testing on posterior sclera and anterior chambers, as well as additional protocols to extract 3-D displacements, reconstruct anatomically accurate posterior scleral geometries, and perform inverse FE simulations in order to extract mechanical properties. Appendix B contains all user manuals for the main codes I have written during my PhD thesis, including: 1) Eyemesh, which is a preprocessing FE software, 2) the FE implementation of the anisotropic hyperelastic constitutive model, 3) the inverse FE method and 4) Eyeview, which is a postprocessing FE software. It should be noted that I have also performed mechanical experiments on both corneas from the same sixteen monkeys, but none of these data will be presented in this thesis and this study will be reserved for a later time.

2   Effects of Storage Time on Scleral Biomechanics[1]

2.1. Abstract

In the field of biomechanics, little research has been performed to evaluate the effects of storage time on the material properties of ocular tissues. Twenty-four rabbit eyes were divided into six groups with storage times from 3 to 72 hours. A tensile specimen was prepared from the inferior quadrant of each sclera, and was subjected to a stress relaxation test. The data were analyzed using linear viscoelastic theory and a newly implemented Gaussian spectrum yielding four material parameters (E_0: instantaneous elastic modulus, E_∞: equilibrium elastic modulus, β: half-width of the Gaussian distribution, τ_m: mean relaxation time). No statistically significant differences were found in the material properties of each group, which suggests that sclera can be stored up to three days without risking mechanical deterioration.

---

[1]This chapter was submitted partially to Current Eye Research on November 22nd, 2006 as "Effects of Storage Time on the Mechanical Properties of Rabbit Peripapillary Sclera after Enucleation" and published in May 2007.

2.2. Introduction

Glaucomatous optic neuropathy is one of the three leading causes of blindness in the U.S (Leske 1983). While intraocular pressure (IOP) plays a central role in the development of glaucomatous vision loss, other factors such as age, ischemia and inflammation are likely important in the disease (Burgoyne *et al.* 2005; Burgoyne and Downs 2008).

In order to evaluate the effect of elevated IOP on the connective tissues of the posterior pole and optic nerve head, computational biomechanical models of the posterior pole of the eye are currently under construction in our laboratory (Downs *et al.* 2007; Roberts *et al.* 2007). Our goal is to fully characterize the biomechanical behavior of each tissue within and around the optic nerve head (ONH). To build these models, accurate values for material properties of the load-bearing tissues are necessary. Preliminary work has been done on the material properties of monkey and rabbit peripapillary sclera (Downs *et al.* 2003; Downs *et al.* 2005).

The sclera is the outer shell and principal load-bearing tissue of the eye. Consisting primarily of collagen fibers (Edelhauser and Ubels 2003) and essentially avascular, it provides constant protection for the adjacent intraocular tissues. 90 % of the sclera collagen fibers are collagen type I fibers, which provides the majority of the tissue's mechanical integrity and tensile strength.

The posterior sclera, just nasal to the fovea, contains the scleral canal which is spanned by a fenestrated connective tissue structure known as the lamina cribrosa. The retinal ganglion cell axons that transmit visual signals from the retina to the brain pass through these fenestrations. The mechanical properties of the sclera immediately adjacent

to this canal (the peripapillary sclera) likely influence the biomechanics of the optic nerve head and are therefore very important in engineering models used to determine to which extent the ONH will deform under changing IOP.

Most mechanical testing experiments on biologic soft tissues are conducted just after death to ensure the results reflect the specimen's original physiological state as closely as possible. Human donor eyes are usually stored in phosphate buffered saline (PBS) before they are released for research, however the effect of post-enucleation storage time on the material properties of the load-bearing ocular tissues has not been rigorously characterized. The purpose of this study was to investigate the effects of post-enucleation storage time on the mechanical properties of rabbit peripapillary sclera using linear-viscoelastic theory.

2.3. Experimental Setup and Testing Protocol

Twelve mature New Zealand white rabbits were anesthetized with an intramuscular injection of ketamine/xylazine, and sacrificed with an intravenous sodium pentobarbital injection. After enucleation, eyes were randomly divided into six groups (four samples per group) according to the post-enucleation time (3, 8, 24, 36, 48 and 72 hours), cleaned from extra-orbital tissues, and stored in a PBS solution at 4 °C. Human donor eyes are generally available within 48 hours postmortem, therefore 72 hours was chosen as the maximum time limit. Other time points were added at 3, 8, 24, 36, and 48 hours to ensure that the time course of changes in the mechanical response of sclera, should they occur, would be detected. The sample size of four animals per group was identified in a power analysis as the minimum number of samples necessary to achieve statistical significance if changes in material properties were present (Downs *et al.* 2005).

For each eye, the anterior chamber, vitreous, retina and choroid of each eye were removed in order to isolate the sclera. Each scleral shell was then mounted on a fixed, 15-mm-diameter polyethylene sphere, and a custom-built cutting die (three mating stainless steel parts that compress two flexible razor blades into a precise dog-bone shape) was rotated over the surface of each scleral shell to generate a tensile test specimen (Figure 2.3.1). A detailed description of the tensile specimen preparation protocol has been reported previously (Downs *et al.* 2003).
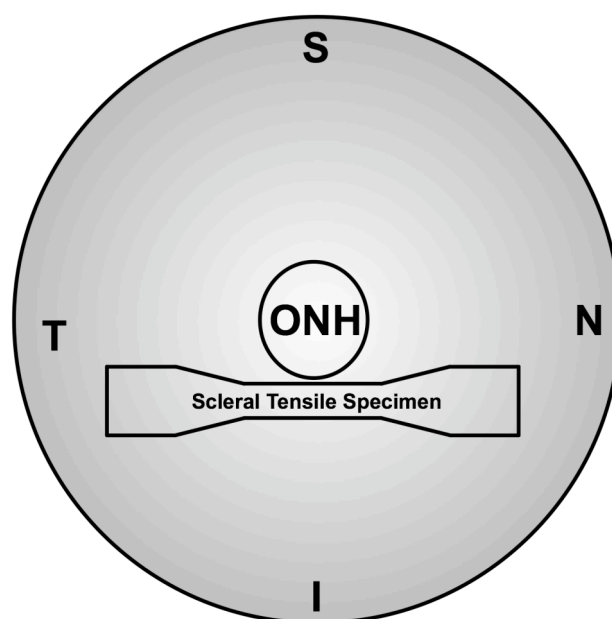
Figure 2.3.1. Posterior view of the scleral shell of a left rabbit eye showing the position of the gauge length of a scleral tensile specimen harvested from the inferior quadrant. Redrawn from Crawford Downs (Downs 2002).

Each scleral specimen, generated with a gauge length of 8 mm, a gauge width of 3 mm and an averaged thickness of 750 μm, was prepared from the inferior quadrant of the sclera with its center tangent to the optic nerve head (Figure 2.3.1). The specimen was then clamped via custom-built soft tissue grips within an environment chamber maintained at 37 °C and kept moist with an isotonic saline mist [3]. The sample was then

slowly preloaded to 0.08 N using a material testing machine (Renew 1122, MTS, Eden Prairie, MN) equipped with a 2,000 gram load cell. A double-armed, soft-contact extensometer (Biomedical extensometer Model 632.32F, MTS, Eden Prairie MN) was then applied to the central 5 mm of the specimen in order to measure the actual strain of the peripapillary sclera in the gauge section.

After extensometer placement, the specimen was subjected to a uniaxial preconditioning in tension, consisting of ten cycles from 0 to a maximum of 1 % strain at a rate of 1 % per second. The specimen was allowed to recover for 360 seconds, and then a stress relaxation test was performed as follows. A 1 %/sec strain ramp to 1 % strain was applied to the tissue and the stress relaxation behavior was recorded while displacement was held constant for 1,000 seconds (Figure 2.3.2). We based this strain range on our estimate that the posterior sclera shell experiences a strain on the order of 1 % under normal physiological conditions according to thin-walled, spherical pressure vessel theory (Timoshenko 1970). Furthermore, our previous studies (Downs *et al.* 2003; Downs *et al.* 2005) have shown that a stress relaxation test is appropriate because sclera's mechanical behavior under uniaxial tension can be accurately described with a time-dependent mathematical theory (i.e. linear viscoelastic theory).
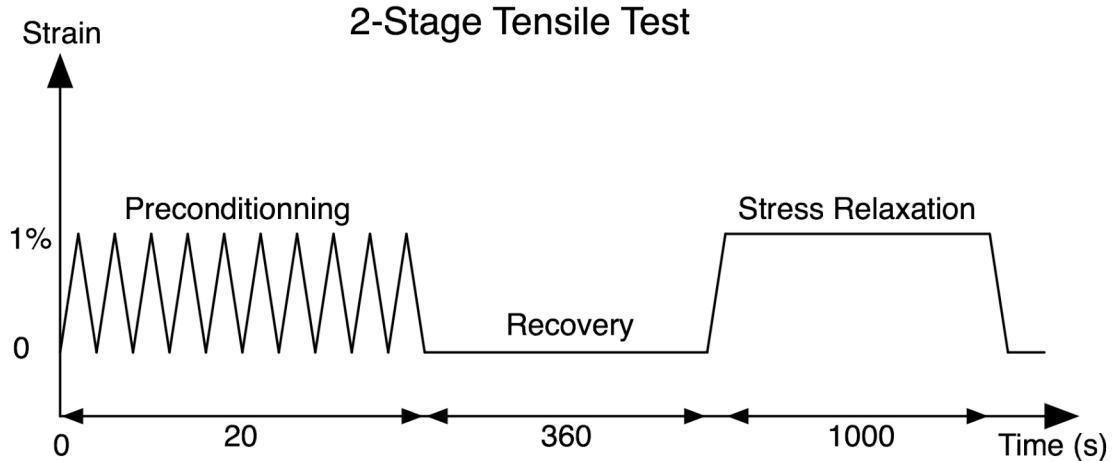
Figure 2.3.2. Diagram showing the time course of the 2-stage, uniaxial tensile testing protocol. Redrawn from Crawford Downs (Downs 2002).

2.4. Viscoelastic Constitutive Model

In order to quantify the relaxation phenomenon of the peripapillary sclera, we used linear viscoelastic theory, which was initially described by Fung (Fung 1993). The model states that a viscoelastic material when subjected to a constant strain ε_0 exhibits a stress relaxation response (Figure 2.4.1) that can be expressed as

$$\sigma(\varepsilon_0, t) = G(t) \cdot \sigma^e(\varepsilon_0) \tag{2.4.1}$$

in which G is the reduced relaxation function, a normalized function of time, and σ^e is the elastic response function of the applied strain, ε_0. $\sigma^e(\varepsilon_0)$ can be described as the tensile stress instantaneously generated in the material when a step function of strain, ε_0, is applied to the specimen, so $\sigma^e(\varepsilon_0) = E_0 \varepsilon_0$, with E_0 being the instantaneous elastic modulus of the material.
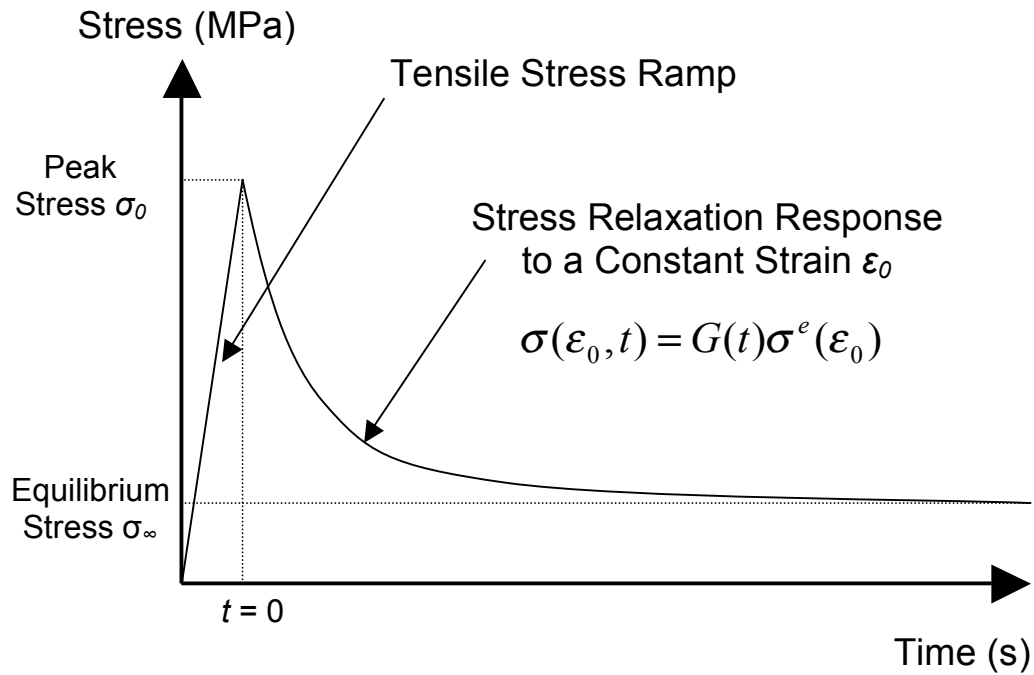
Figure 2.4.1. A typical stress relaxation response of soft tissue. In this study, the specimen was stretched at a strain rate of 1%/sec to the peak strain of 1%. At time $t = 0$, the displacement was fixed (no further stretching of the specimen), and the stress monitored until the specimen reached stress equilibrium (1,000 s).

The function G, which satisfies $G(0) = 1$, can be expressed as

$$G(t) = \frac{1 + c \int\limits_{-\infty}^{+\infty} \Phi(\log \tau) \exp(-\frac{t}{\tau}) d \log \tau}{1 + c \int\limits_{-\infty}^{+\infty} \Phi(\log \tau) d \log \tau} \tag{2.4.2}$$

in which c is a relaxation ratio determined by $c = G(0)/G(\infty) - 1$, τ is the relaxation time, and Φ is the log distribution function of the relaxation time (Nowick and Berry 1961) which satisfies

$$\int\limits_{-\infty}^{+\infty} \Phi(\log \tau) d \log \tau = 1 \tag{2.4.3}$$

We chose a log-normal distribution function for $\Phi(\log \tau)$ (Gaussian distribution) (Olberding and Suh 2006) which can be expressed as

$$\Phi\left(\log \tau\right) = \frac{1}{\beta\sqrt{\pi}} \exp\left(-\frac{\left(\log \tau - \log \tau_m\right)^2}{\beta^2}\right) \tag{2.4.4}$$

where β is the half-width of the Gaussian distribution, and τ_m is the mean relaxation time constant (i.e. the most probable value of τ).

As suggested by Wagner (Wagner 1913), the variable $z = \log\left(\tau/\tau_m\right)$ can be introduced in Eq. (2.4.4) and satisfies $dz = d\log\tau$. After simplification, the stress relaxation response can be written as

$$\sigma\left(t\right) = \frac{\sigma_0}{1+c}\left(1 + \frac{c}{\beta\sqrt{\pi}} \int_{-\infty}^{+\infty} \exp\left(-\frac{z^2}{\beta^2} - \frac{t}{\tau_m 10^z}\right) dz\right) \tag{2.4.5}$$

where σ_0 is defined as the peak stress (Figure 2.4.1) and is directly obtained from the experimental data.

A genetic optimization algorithm known as differential evolution (Price *et al.* 2005) was employed to curve-fit the stress calculation of Eq. (2.4.5) with the experimental data, thus leading to unique estimates of the three model parameters: β, τ_m and c. Examples of stress relaxation responses and their corresponding model predictions are shown in Figure 2.4.2. Excellent agreements between the experimentally-measured and model-predicted stresses can be observed.
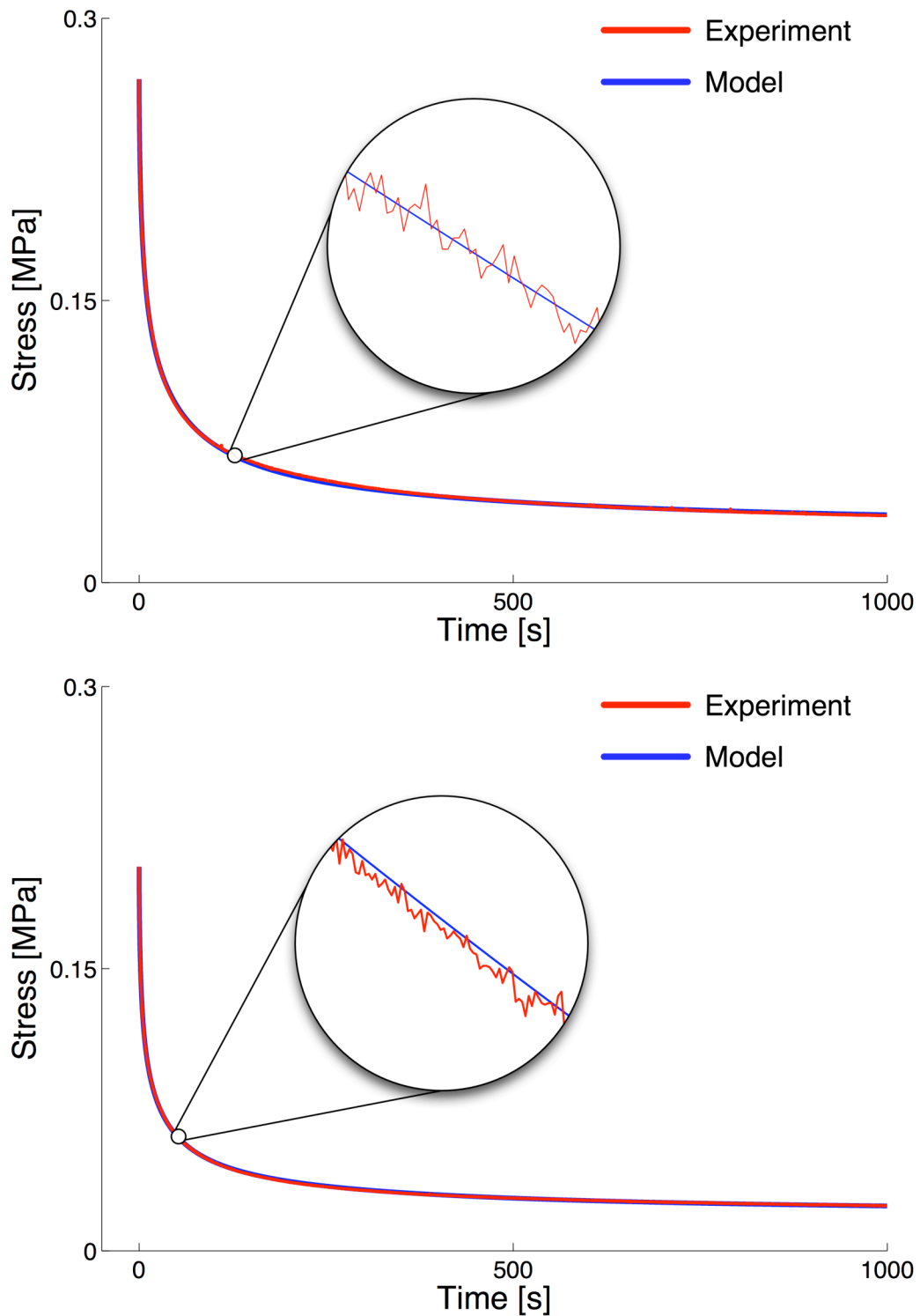
Figure 2.4.2. Examples of stress relaxation responses of two randomly-chosen rabbit eyes (in red) and their corresponding model-predictions (in blue). Note the excellent agreements between the experimentally-measured and model-predicted stresses. Excellent agreements were obtained for all tested eyes.

From the estimated model parameters, two elastic moduli, the instantaneous elastic modulus E_0 and the equilibrium elastic modulus E_∞, were determined as follows

$$E_0 = \frac{\sigma_0}{\varepsilon_0} \qquad\qquad (2.4.6)$$

$$E_\infty = \frac{E_0}{1+c} \qquad\qquad (2.4.7)$$

2.5 Statistical Analysis and Results

An analysis of variance (ANOVA) was employed to compare the four material parameters (β, τ_m, E_0 and E_∞) among the six groups (n=4 each for postmortem times of 3, 8, 24, 36, 48, and 72 hours) and to determine the effects of post-enucleation storage time on the mechanical properties of rabbit peripapillary sclera.

Mean stress relaxation curves were plotted for each group (Figure 2.5.1) (n=4 samples per group). Mean value ± standard deviation of each of the four material parameters (E_0: instantaneous elastic modulus, E_∞: equilibrium elastic modulus, β: half-width of the Gaussian distribution, τ_m: mean relaxation time) are shown in Table 2.5.1. By ANOVA, no statistically significant difference was detected in the material properties of the peripapillary sclera between the groups ($P > 0.05$ for each of the four parameters).

Postmortem Storage Time (hours)	E_o (MPa)	E_∞ (MPa)	β (-)	τ_m (s)
3	28.7 ± 7.1	3.3 ± 0.4	1.5 ± 0.2	14.5 ± 4.0
8	24.4 ± 7.5	3.8 ± 1.1	1.6 ± 0.3	20.8 ± 10.9
24	30.3 ± 6.9	3.2 ± 1.3	1.4 ± 0.2	12.0 ± 5.2
36	25.7 ± 3.9	3.0 ± 0.9	1.6 ± 0.2	10.3 ± 3.4
48	23.0 ± 7.6	2.7 ± 1.8	1.5 ± 0.1	18.8 ± 14.6
72	29.3 ± 3.8	3.2 ± 0.5	1.3 ± 0.1	16.3 ± 9.4

Table 2.5.1. Material properties of rabbit peripapillary sclera listed by postmortem group (mean value ± standard deviation).
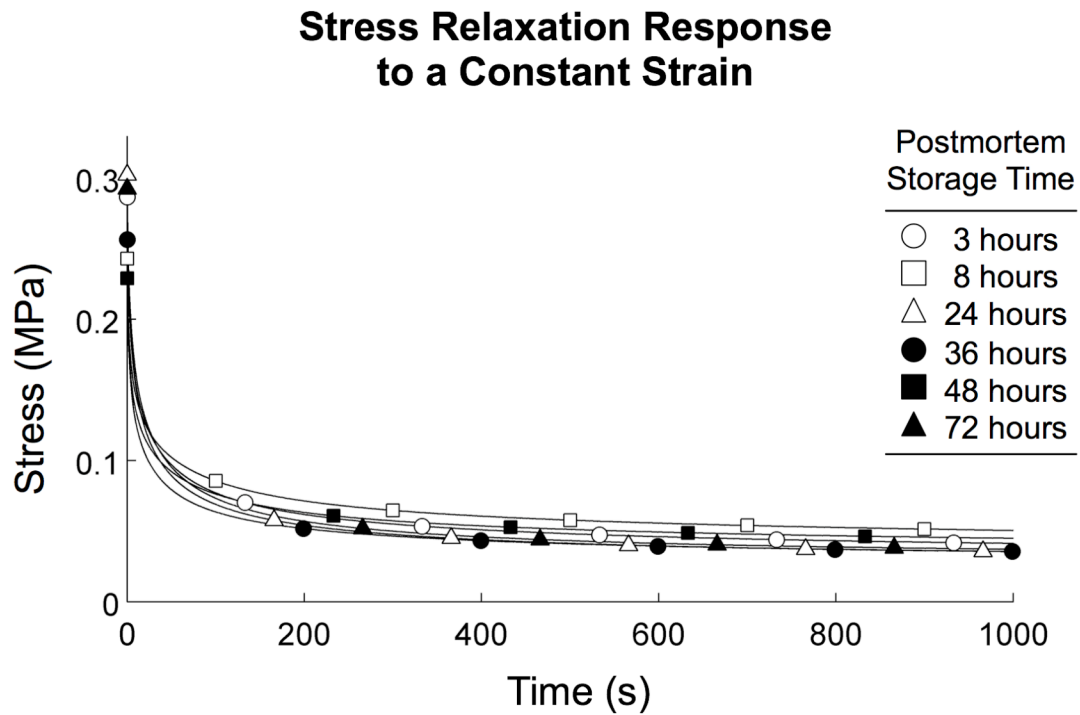
Figure 2.5.1. Average stress relaxation responses of rabbit peripapillary sclera (inferior quadrant only) for postmortem storage times of 3, 8, 24, 36, 48, and 72 hours.

2.6. Discussion

In this report, we quantified the viscoelastic behavior of rabbit peripapillary sclera by using four viscoelastic parameters. Eyes were divided into 6 groups according to the time separating the animal sacrifice from the beginning of the test (postmortem time of 3, 8, 24, 36, 48, and 72 hours). No significant differences in the viscoelastic properties of rabbit peripapillary sclera from each group were detected, which indicates that rabbit sclera can be stored in PBS at 4 °C for up to 72 hours without causing any detectible change in its mechanical properties.

One of the possible explanations for this result is that sclera is predominantly avascular, has a low cell density, and consists mainly of collagen fibers (75 to 80% of its dry weight (Edelhauser and Ubels 2003)). Due to the preponderance of extracellular matrix (ECM), the necrosis of scleral cells (mainly fibroblasts) is unlikely to affect the mechanical properties of the tissue. While this is likely true for the sclera, prolonged storage time might have an impact on highly perfused tissues with a high cell density, such as retina, choroid, nerve fiber layer, blood vessels and musculature. In such tissues, the anchoring junctions mechanically joining these cells could deteriorate rapidly due to postmortem cell necrosis, which could disturb the integrity of the tissue and result in a change of mechanical properties (Alberts *et al.* 2008).

It has been shown that sclera from humans and rabbits have similar organic composition and similar proteoglycan content and collagen organization (Young 1985). As a result, mechanical testing of ocular load-bearing tissues from human donor eyes that have been collected and stored in PBS for up to 72 hours should yield reliable material property data. There have also been some studies that relied on histomorphometric

measures of IOP-induced tissue deformation in human donor eyes that were fixed at pressure via cannulation (Sigal *et al.* 2004). Our results suggest that as long as the fixation was performed within 72 hours postmortem, the results from these studies should provide insight into the true deformation of the load-bearing tissues.

Downs (Downs *et al.* 2003) reported both rabbit peripapillary sclera instantaneous and equilibrium elastic moduli to be 11.6 MPa and 0.79 MPa in average, respectively. These values are about three times lower than the values obtained in this study and these differences likely arise from the improvement of both experimental protocol and computational fitting of the material parameters that have been used in this study. First, the tensile tests were performed on a much more accurate test frame fitted with a high-sensitivity, low-noise load cell, which yielded improved stress relaxation curves with a significantly higher signal-to-noise ratio. Second, an improved relaxation spectrum (Eq. (2.4.4)) was employed to estimate the viscoelastic stress relaxation, which produced a stress relaxation curve that more closely matched the experimental data, resulting in better estimates of material property parameters.

Several limitations warrant further discussion. First, the initial strain ramp phase (1 second) used in the stress relaxation experiment was excluded in the model simulation. As in similar experiments of this kind, stress relaxation can take place during the initial strain ramp phase, which likely results in an error in the instantaneous elastic modulus reported in Table 2.5.1. We investigated the effects of including the initial ramp phase in the model and found that the computed peak stress (at $t = 0$ in Figure 2.4.1) showed an error as large as 25% when compared with the experimental peak stress value (data not

shown). We believe that ignoring the tensile ramp phase in the computational fitting of parameters provides the best estimate for the material parameters.

Second, the scleral thickness was assumed to be uniform at 750 μm for all specimens (Downs *et al.* 2003). The potential variation in the scleral thickness in each sample could introduce errors in the stress calculation, which would likely affect the reported values of the elastic moduli, E_0 and E_∞. To minimize the effects of varying scleral thickness on our results, all scleral samples were harvested from the inferior quadrant of the posterior pole, and were randomized to treatment. Previous histomorphometric characterizations of scleral thickness have indicated that the sclera is composed of two principle layers: the dense lamellar load-bearing sclera, and the loose, disorganized episclera (Downs *et al.* 2001; Downs *et al.* 2002). Only the dense scleral tissue should be attributed thickness for the purpose of material property determination through mechanical testing. Unfortunately, these layers are inseparable via dissection in fresh sclera, and it remains unclear how one might measure the thickness of the load-bearing layer alone in fresh tissues.

Third, the sclera has complex anisotropic characteristics produced from the multi-directional arrangement of collagen fibers embedded in the ground substance (Komai and Ushiki 1991; Watson and Young 2004). It has been shown that the collagen and elastin fibers of the sclera are predominantly oriented circumferentially to the ONH in the immediate peripapillary region (Hernandez *et al.* 1987). As our specimens were harvested from the immediate peripapillary region (Figure 2.3.1), it is likely that the load-bearing fibers in the gauge section of our tested samples were predominantly oriented along the axial direction of the tensile test in the study. Therefore, the data presented here

likely represent the mechanical properties of the sclera in the direction of the collagen fibers. A multi-axial mechanical testing protocol is necessary to describe the 3-D behavior of sclera with a multi-directional arrangement of collagen fibers, and this approach will be the topic of the following Chapters.

Finally, the rabbit eyes in this study were enucleated, placed in PBS, and stored at 4°C within two hours after death. However, in the case of human cadaver eyes, it is most common for 6 to 48 hours to pass between the time of death and the time of enucleation. Our study was not designed to test the effect of post-mortem time prior enucleation, during which the tissue may undergo undetermined degradation. Future studies will be required to understand if the initial stage of decomposition can impact the mechanical properties of the sclera.

Biomechanical testing and modeling of the human sclera will contribute to our understanding of glaucomatous optic nerve head damage, myopia, and a host of other ocular disorders. The results from this study suggest that for human cadaver eyes obtained soon after death, scleral viscoelastic material properties should be stable for postmortem storage times (in PBS) of up to 72 hours.

3   2-D Optical Tracking of Scleral Deformations[1]

3.1. Abstract

The purpose of this study was to experimentally characterize 2-D surface mapping of the deformation pattern of porcine peripapillary sclera following acute elevations of intraocular pressure (IOP) from 5 to 45 mm Hg. Four porcine eyes were obtained within 48 hours post mortem and dissected to the sclera. After the anterior chamber was removed, each posterior sclera shell was individually mounted at the equator on a custom-built pressurization device, which internally pressurize the scleral samples with isotonic saline at 22°C. Black polystyrene microspheres (10 μm in diameter) were randomly scattered and attached to the scleral surface. IOP was incrementally increased from 5 to 45 mm Hg (± 0.15 mm Hg), and the surface deformation of the peripapillary sclera immediately adjacent to the dural insertion was optically tracked at a resolution of 2 μm/pixel one quadrant at a time, for each of four quadrants (superior, nasal, inferior, and temporal). The 2-D displacement data of the

microsphere markers were extracted using the optical flow equation, smoothed with a thin-plate B-spline, and converted to the corresponding Lagrangian finite surface strain. In all four quadrants of each eye, the principal strain was highest and primarily circumferential immediately adjacent to the scleral canal. Average maximum Lagrangian strain across all quadrants for all eyes was 0.013 ± 0.005 from 5 to 10 mm Hg, 0.014 ± 0.004 from 10 to 30 mm Hg and 0.004 ± 0.001 from 30 to 45 mm Hg, demonstrating the nonlinearity in the IOP-strain relationship. For each scleral shell, the observed surface strain mapping implied that the scleral stiffness was relatively low between 5 and 10 mm Hg, but dramatically increased for each IOP elevation increment beyond 10 mm Hg. Peripapillary deformation following an acute IOP elevation may be governed by the underlying scleral collagen microstructure and is likely in the high-stiffness region of the scleral stress-strain curve when IOP is above 10 mm Hg.

3.2. Introduction

Glaucomatous optic neuropathy is one of the three leading causes of blindness in the U.S (Leske 1983). We hypothesize that the mechanical properties of peripapillary and posterior sclera are altered during the disease and play a significant role in the development and progression of glaucomatous damage to the neural and connective tissues within the optic nerve head (ONH) (Burgoyne *et al.* 2005).

In order to evaluate the effect of elevated intraocular pressure (IOP) on the connective tissues of the posterior pole and ONH, finite element models of the posterior pole of the eye are being constructed in our laboratory (Downs *et al.* 2007; Roberts *et al.* 2007). The ultimate goal of our work is to fully characterize the mechanical behavior of

each tissue within and around the ONH, and to investigate how the mechanical environment in the ONH influences the onset and progression of glaucoma. To build these models, accurate characterization of the material properties of the load-bearing tissues is necessary. Preliminary work has been done on the material properties of monkey and rabbit peripapillary sclera using uniaxial tensile testing (Downs *et al.* 2003; Downs *et al.* 2005; Girard *et al.* 2007), and this study extends those methodologies to pressure testing techniques.

The sclera is the outer shell and principal load-bearing tissue of the eye, which consists primarily of avascular lamellae of collagen fibers (Edelhauser and Ubels 2003). Ninety percent of the collagen fibers in the sclera are Type I, which provide mechanical integrity and tensile strength. The posterior sclera contains the scleral canal, which is spanned by a fenestrated connective tissue structure known as the lamina cribrosa. The retinal ganglion cell axons that transmit visual signals from the retina to the brain pass through these fenestrations. This region is known as the ONH, and is the principal site of damage in glaucoma (Quigley and Anderson 1976; Quigley and Addicks 1980). We believe that ONH biomechanics plays a significant role in the development and progression of glaucoma, and the mechanical properties of the peripapillary sclera determine the extent to which the scleral canal deforms in response to elevated IOP.

In our previous studies (Downs *et al.* 2003; Downs *et al.* 2005; Girard *et al.* 2007), experimental and mathematical models were used to determine the uniaxial mechanical properties of the sclera, and the tissue was assumed to be linearly viscoelastic and isotropic. While this was a good first step, the sclera is a complex structure with varying collagen fiber orientation (Kokott 1934; Greene 1980; Komai and Ushiki 1991; Rada *et al.* 2006), so its mechanical behavior under IOP-induced mechanical stress is

likely to be anisotropic and nonlinear. Hence, uniaxial testing is likely to be insufficient to predict the mechanical behavior of the tissue *in vivo*, and a more physiological testing protocol is necessary to fully describe the 3-D behavior of the sclera in response to IOP elevations.

This Chapter presents a method to experimentally characterize the surface deformation pattern of porcine peripapillary sclera exposed to IOP ranging from 5 to 45 mm Hg. The method described herein can be applied to thin soft-tissues that are mechanically loaded with uni- and multi-axial testing protocols.

3.3. Experimental Setup and Testing Protocol

Four porcine eyes were harvested from a slaughterhouse and stored in a phosphate buffered saline solution (PBS) at 4°C for 48 hours until the experiments were conducted. In Chapter 3, we reported that donor eyes can be stored up to 72 hours at 4°C in PBS without risking deterioration of the uni-axial mechanical behavior of the sclera (Girard *et al.* 2007).

At the time of experiments, the anterior chamber, vitreous, retina and choroid of each eye were removed in order to isolate the posterior half of the sclera, which was then mounted and clamped at the equator on a custom-built pressurization apparatus (Figures 3.3.1 and 3.3.2).

Pneumatic control of saline inflow and outflow was driven by a pressure regulator (Model 81, Fairchild, Winston-Salem, NC), which allowed each posterior scleral sample to be pressurized with a resolution of 0.15 mm Hg. Before the experiment, each pressurized scleral sample was quickly blotted with a gauze pad, and black dyed

microspheres (10-µm-diameter Polybead Polystyrene Microspheres, Polysciences, Inc,

Warrington, PA), dissolved in a 70% ethanol solution, were randomly scattered onto the

tissue surface. The microspheres were allowed to adhere to the scleral surface for 5

minutes while the ethanol dried and were used as surface markers for the optical tracking

method described below. All tissue samples were then kept moist with drops of PBS

applied throughout the entire experiment, which only minimally affected the optical

tracking of the surface marker position.
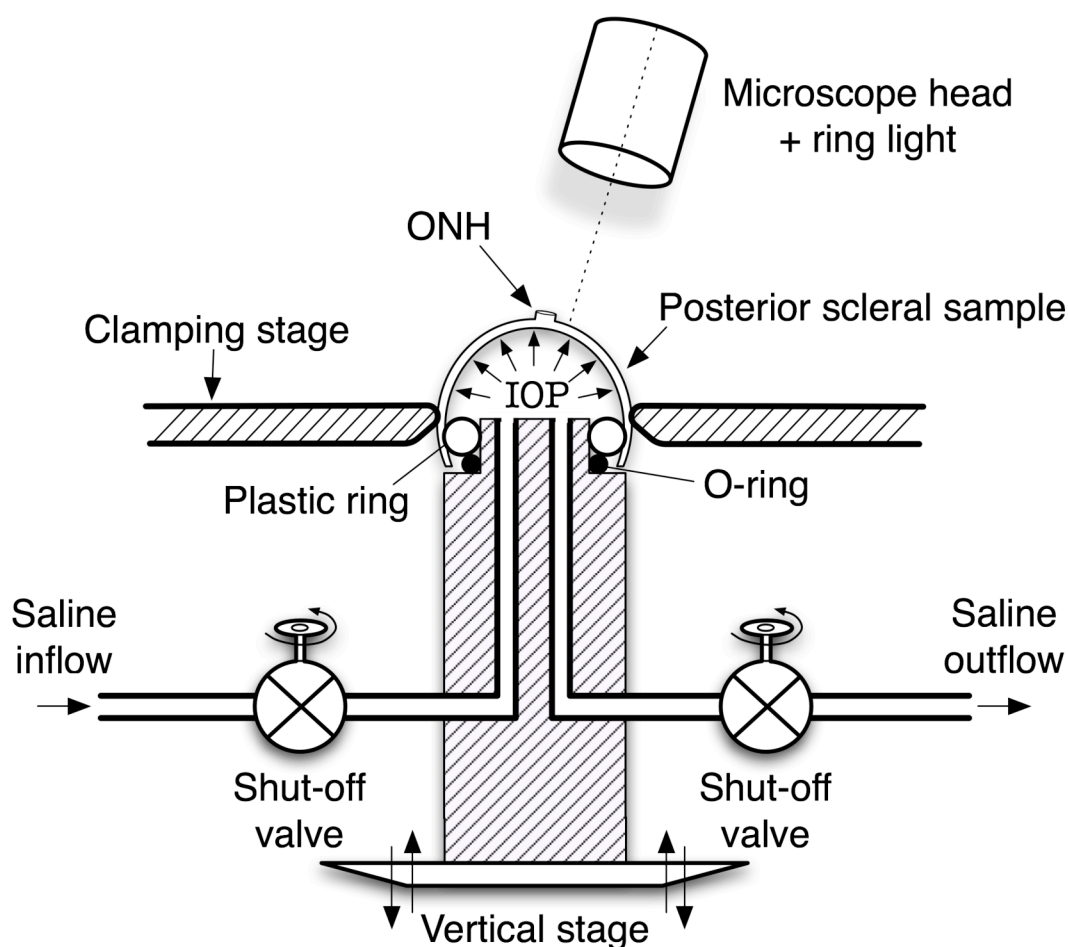
Figure 3.3.1. Schematic showing a cross-section of the custom-built pressurization apparatus. The posterior scleral shell was first mounted onto the plastic ring, and then clamped at the equator by moving the vertical stage toward the clamping stage. The saline outflow was interrupted after saline filled the posterior shell cavity and IOP reached 5 mm Hg. The scleral surface was imaged as IOP was increased from 5 to 45 mm Hg with an increment of 1 mm Hg.
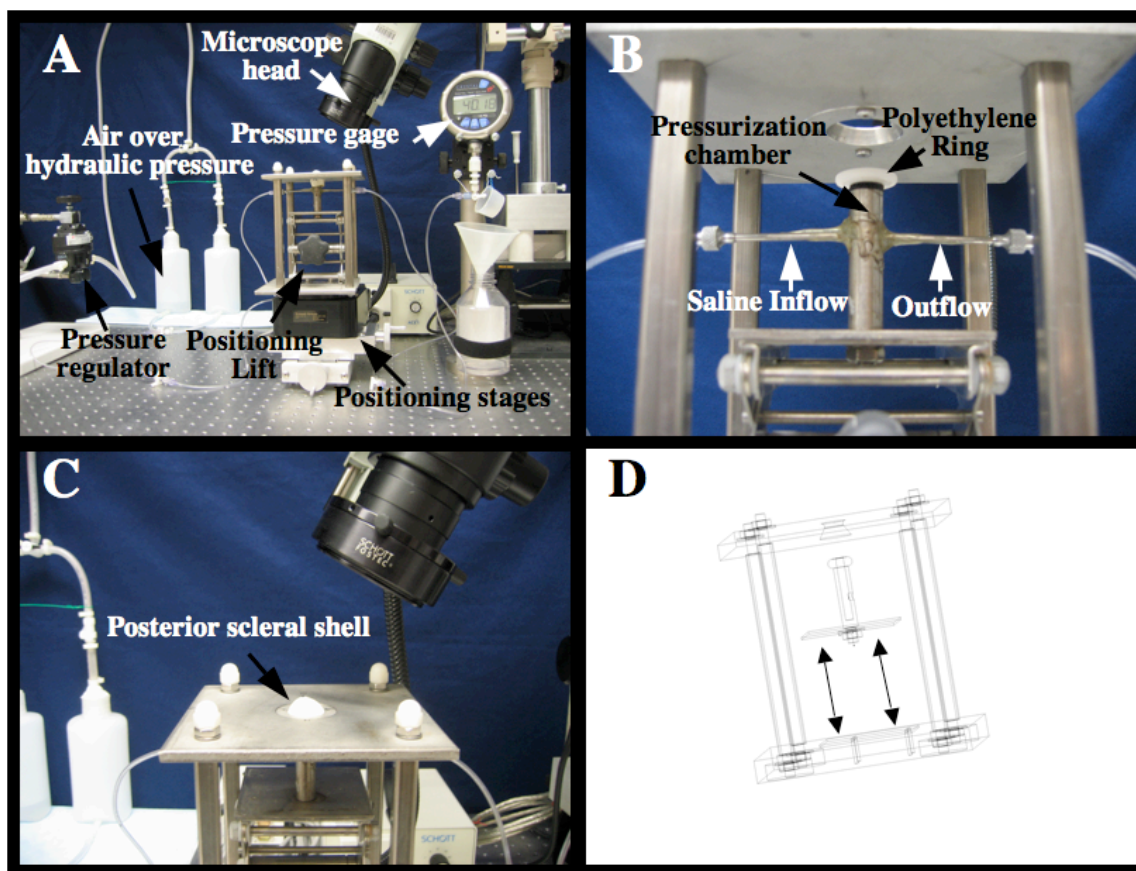
Figure 3.3.2. (A) Photograph of the pressurization apparatus. **(B)** Photograph showing the clamping system used to mount the posterior scleral shells. **(C)** Photograph showing a clamped and pressurized porcine scleral shell. **(D)** Initial CAD drawing of the pressurization apparatus.

Each scleral shell was subjected to IOP preconditioning, consisting of 20 IOP cycles from 5 mm Hg to a maximum of 15 mm Hg at a rate of 5 mm Hg per second, and then allowed to recover for 360 seconds.

An optical measurement system, consisting of a high-resolution microscope (SZX-12, Olympus, Center Valley, PA) and a high-resolution digital camera (MicroFire, Optronics, Goleta, CA) was employed to capture images of the markers at a resolution of 2 μm/pixel within a 4 mm ×4 mm region of sclera. These images were acquired for each of the four quadrants of the peripapillary sclera around the ONH, in the following

sequence: superior (S), nasal (N), inferior (I), and temporal (T) (Figure 3.3.3A). Pixel resolution was calibrated using a slide mounted micrometer scale, and the sclera was illuminated using a fiber optic ring light to ensure even illumination.

For each scleral shell, pressure was slowly increased by incremental steps of 1 mm Hg, from 5 mm Hg to 45 mm Hg, and images were generated for the inferior quadrant only. Each scleral shell was then depressurized from 45 to 5 mm Hg until equilibrium was reached, and the process of image acquisition was repeated three times for the three other (temporal, nasal, and superior) quadrants. Each image was post processed with a sharpening filter to increase the contrast of the surface marker image, then a contour was defined for each marker, and its centroid was calculated (Figure 3.3.3B).

Based on the set of images generated for each quadrant, the 2-D displacement field was extracted using the optical flow equation as described below, which allowed accurate tracking of the markers for each 1 mm Hg elevation of IOP.
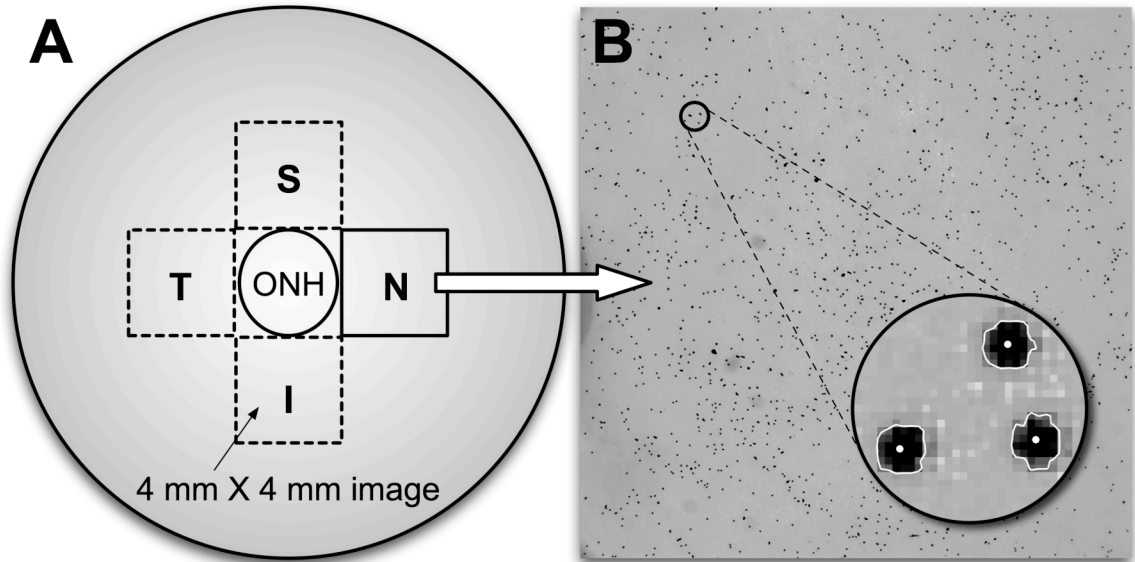
Figure 3.3.3. (A) Diagram of the posterior scleral shell of a left eye (OS) showing the position of the 4 fields of view within which 2-D scleral deformation patterns were determined. Each field of view is 4 mm × 4 mm with a single image resolution of 2 μm per pixel. **(B)** Image of a nasal quadrant with microsphere markers present on the surface of the shell and a magnified view of three microspheres showing their contours and centroids.

3.4. Optical Flow Algorithm for Marker Tracking

Manually tracking the movements of hundreds of markers in each image is a daunting and time-consuming process. This study, therefore, utilized RGB digital images of markers and an optical flow algorithm to automate the tracking of marker movements, from which the pixel displacement of each marker could be determined.

It was assumed that scleral illumination was uniform and the intensity of the markers did not change with motion from one image to the next. Considering the pixel intensity I_k of an RGB image, the previous assumption can be mathematically transcribed to

$$dI_k = 0, \quad k \in [\![1,3]\!] \tag{3.4.1}$$

Here, the index k ranges from 1 to 3 corresponding to the three components of an RGB image (i.e. red, green, and blue). The pixel intensity I_k of the 2-D image of the marker can be expressed as a function of space and time, $I_k(x,y,t)$, in which x and y represent the pixel coordinates. Taylor's first order approximation of Eq. (3.4.1) can be rewritten as

$$\frac{\partial I_k(x,y,t)}{\partial t} \cdot dt + \frac{\partial I_k(x,y,t)}{\partial x} \cdot dx + \frac{\partial I_k(x,y,t)}{\partial y} \cdot dy = 0, \quad k \in [\![1,3]\!], \tag{3.4.2}$$

or

$$\frac{\partial I_k(x,y,t)}{\partial t} + \frac{\partial I_k(x,y,t)}{\partial x} \cdot v_x + \frac{\partial I_k(x,y,t)}{\partial y} \cdot v_y = 0, \quad k \in [\![1,3]\!], \tag{3.4.3}$$

where v_x and v_y are defined as the pixel velocity components. Equation (3.4.3) is known as the color optical flow equation (Barron and Klette 2002) and can be applied to two 2-D color pixel images taken at two consecutive time points.

A large body of work has been done to solve the optical flow equation using numerical approximations. Barron (Barron *et al.* 1994) summarized and evaluated the most commonly used optical flow algorithms and their performance. For the present study, we chose to adopt the Lucas-Kanade algorithm (Lucas and Kanade 1981) as described below because our preliminary comparative study found this reliable for RGB images (Barron and Klette 2002).

If each image is captured at a physical equilibrium state, the time variable becomes secondary in Eq. (3.4.2). It is then reasonable to approximate Eq. (3.4.2) with $dx = u_x$ and $dy = u_y$, where u_x and u_y are defined as the pixel displacements. In the Lucas-Kanade approximation (Lucas and Kanade 1981), the displacement field can be

assumed to be smooth over a region of interest, R, such that for each pixel, the adjacent pixels are subjected to the same displacement field. As a result, if R is a square patch of 3×3 pixels with the pixel of interest in the center of that region, it requires a total of 9 equations to be solved for each color channel (Red, Green and Blue) for the center pixel of R. This results in an over-determined system of 27 equations with 2 unknowns to be solved for the center pixel, which can be rearranged in a matrix equation form:

$$\underbrace{\begin{pmatrix} \dfrac{\partial I_1(x_1,y_1)}{\partial x} & \dfrac{\partial I_1(x_1,y_1)}{\partial y} \\ \dfrac{\partial I_2(x_1,y_1)}{\partial x} & \dfrac{\partial I_2(x_1,y_1)}{\partial y} \\ \vdots & \vdots \\ \dfrac{\partial I_3(x_9,y_9)}{\partial x} & \dfrac{\partial I_3(x_9,y_9)}{\partial y} \end{pmatrix}}_{\mathbf{M}} \begin{pmatrix} u_x \\ u_y \end{pmatrix} = -\underbrace{\begin{pmatrix} \dfrac{\partial I_1(x_1,y_1)}{\partial t} \\ \dfrac{\partial I_2(x_1,y_1)}{\partial t} \\ \vdots \\ \dfrac{\partial I_3(x_9,y_9)}{\partial t} \end{pmatrix}}_{\mathbf{b}} dt \qquad (3.4.4)$$

where (x_i,y_i) *for* $i \in [1,9]$ are the pixel-coordinates of the region of interest R, and I_k *for* $k \in [1,3]$ are the corresponding RGB pixel intensities.

Using the least square minimization method, Eq. (3.4.4) can be left-multiplied by the matrix transpose of $\mathbf{M}$

$$\mathbf{M}^\mathbf{T} \cdot \mathbf{M} \cdot \begin{pmatrix} u_x \\ u_y \end{pmatrix} = \mathbf{M}^\mathbf{T} \cdot \mathbf{b} \qquad (3.4.5)$$

For each pixel, therefore, the displacements can be simply expressed as

$$\begin{pmatrix} u_x \\ u_y \end{pmatrix} = \left(\mathbf{M}^\mathbf{T} \cdot \mathbf{M}\right)^{-1} \cdot \mathbf{M}^\mathbf{T} \cdot \mathbf{b} \qquad (3.4.6)$$

The solution of Eq. (3.4.6) was computed for each pixel and repeated over the entire pixel domain in the two consecutive images taken before and after each 1 mm Hg

IOP increment. The partial derivatives $\dfrac{\partial I_k}{\partial x}, \dfrac{\partial I_k}{\partial y}$ in Eq. (3.4.4) were estimated using a 7-

point rule, and the term $\dfrac{\partial I_k}{\partial t} \cdot dt$, with a 2-point rule.

Using the aforementioned optical flow algorithm, Eqs. (3.4.3)-(3.4.6), the spatial coordinates $X_C(i)$ and $Y_C(i)$ of the centroid of each surface marker were processed to estimate its pixel displacement vector $\{u_{Cx}(i), u_{Cy}(i)\}$ after the incremental IOP increase. Once the pixel displacement of a marker centroid was estimated by the aforementioned optical flow algorithm, a small circular area around the estimated centroid location $\{X_C(i) + u_{Cx}(i), Y_C(i) + u_{Cy}(i)\}$ with a diameter of two-pixels was searched to locate any marker centroid in the second image, as shown in Figure 3.4.1. This newly located marker centroid was then registered as the true marker centroid after the deformation. This step was repeated for each particle in the image, for each 1 mm Hg pressure increment, and summed over an IOP elevation from 5 to 45 mm Hg. Hence, the actual displacement vector was accurately determined for the IOP elevations from 5 to 10 mm Hg, from 10 to 30 mm Hg, and from 30 to 45 mm Hg.
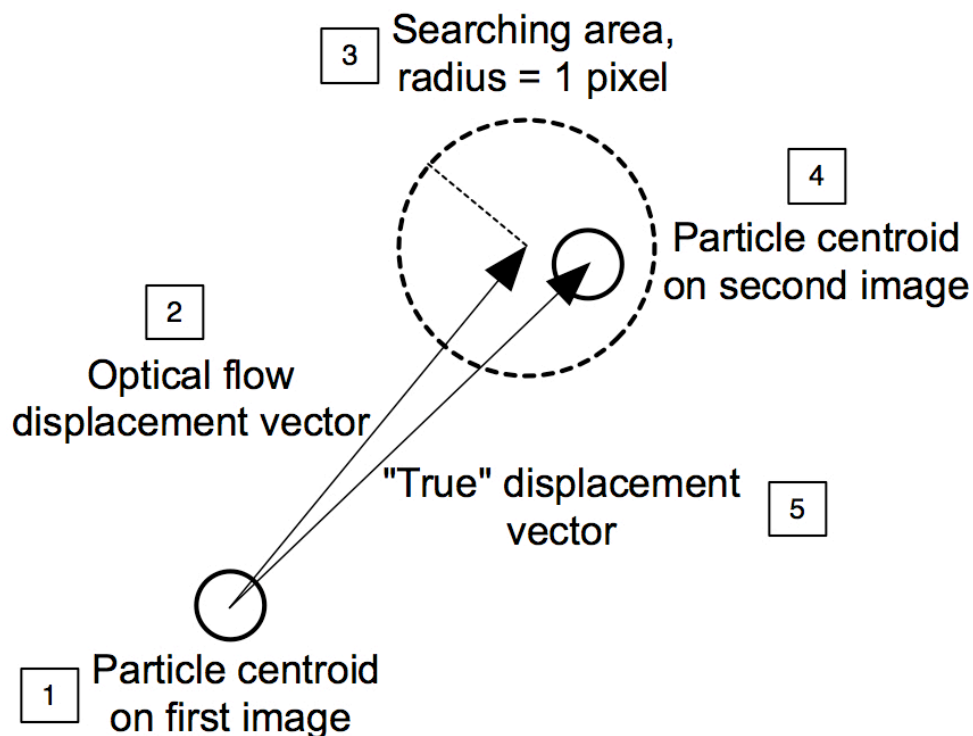
Figure 3.4.1. The optical flow displacement vector was used as an initial guess to derive the true displacement vector. The steps were as follows and were repeated for each 1 mm Hg IOP increase: **1.** The coordinates of the particle centroids were determined on the first image; **2.** The optical flow algorithm was executed to derive the predicted displacements; **3.** For each particle, the optical flow displacement vector was added to the particle centroid coordinates, and a 2-pixel-diameter search area was created; **4.** The matching particle centroid on the second image was found in the search area; **5.** For each particle, subtracted centroid coordinates yielded the true displacement vector.

3.5. Preliminary Validation of the Tracking Method Using a Rubber Balloon

The experimental protocol and the optical flow algorithm method were validated using a half-spherical rubber balloon mounted and imaged as described previously, for incremental pressures increases from 70 to 80 mm Hg. The images were acquired within a 4 mm × 4 mm region located midway between the equator and the pole of the balloon. The displacement field vector was generated for each 1 mm Hg pressure increment using

the optical flow algorithm method. Since rubber is an isotropic, homogeneous elastic material, and the balloon wall is of relatively constant thickness, the resulting 2-D displacement vector field as observed from the camera should be radial from the center of the image field.

Balloon experimental displacement field
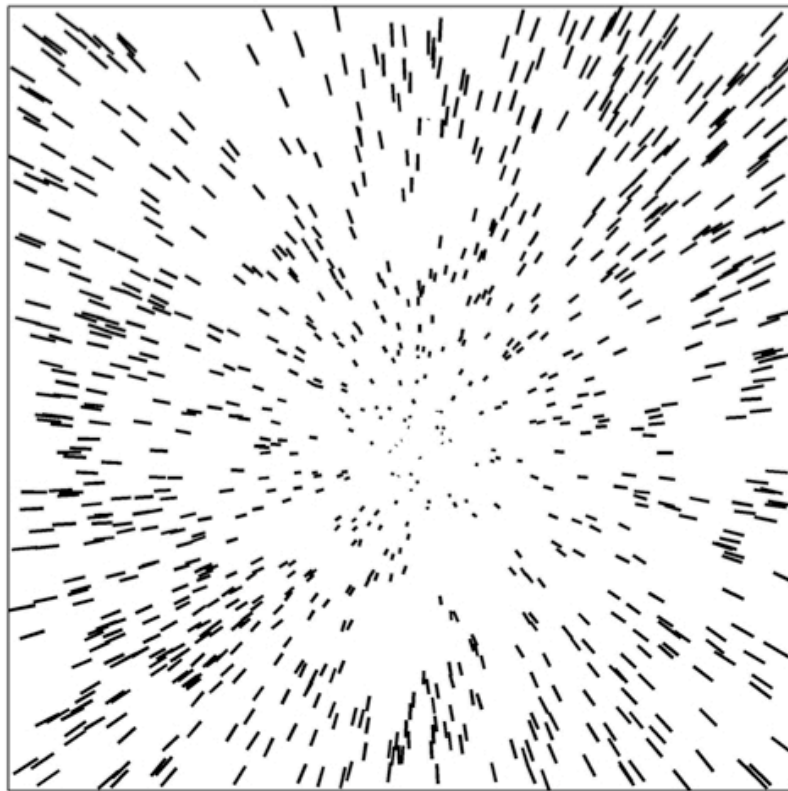
Figure 3.5.1. Experimental displacement field for a 4 mm by 4 mm square location at the surface of a spherical rubber balloon. The microscope head was oriented perpendicular to the balloon surface and the displacement field was generated for a pressure ranging from 70 to 80 mm Hg.

The experimental displacement field obtained from a rubber balloon as a part of validation process of the optical flow method is shown in Figure 3.5.1. The pattern of the displacement field was radial, and was qualitatively very similar to that of an isotropic,

homogeneous spherical pressure vessel. For the entire 4 mm $\times$ 4 mm region, displacement components u and v were well fitted with two surface planes.

The Lagrangian strain tensor was calculated according to Eq. (3.6.3), and its maximum and minimum principal strains were found to be 0.90 % and 0.79 %, respectively. Although the maximum and minimum principal strains obtained for the rubber balloon were not exactly identical, they were close enough so that the rubber material could be assumed to be quasi-isotropic.

3.6. Determination of Scleral Lagrangian Strains

After the displacement vector field was determined by the optical flow algorithm, the Lagrangian strain field on the scleral surface was calculated. To accomplish this, the 4 mm $\times$ 4 mm domain in each field image was first meshed with equal sized 4-noded quadrilateral finite elements, and the nodal displacements were smoothed from the above displacement vector field using the thin plate smoothing spline method (Matlab, The Mathworks, Nattick, MA). For each quadrilateral element, a continuous displacement field function was then approximated by a bilinear interpolation function as

$$\begin{cases} u_x(x,y) = a_1 + a_2 x + a_3 y + a_4 xy \\ u_y(x,y) = a_5 + a_6 x + a_7 y + a_8 xy \end{cases} \tag{3.6.1}$$

in which the coefficients, a_i, could be determined from the nodal displacement values. The Lagrangian strain tensor $\mathbf{E}$ was calculated at Gaussian points in each quadrilateral element as

$$\mathbf{E}(x,y) = \frac{1}{2}\left(\mathbf{F}^{\mathrm{T}}(x,y)\cdot\mathbf{F}(x,y) - \mathbf{I}\right) \tag{3.6.2}$$

where $\mathbf{F}$ is the deformation gradient tensor expressed as

$$\mathbf{F}(x,y) = \begin{bmatrix} \dfrac{\partial u_x}{\partial x} + 1 & \dfrac{\partial u_x}{\partial y} \\[2ex] \dfrac{\partial u_y}{\partial x} & \dfrac{\partial u_y}{\partial y} + 1 \end{bmatrix} \tag{3.6.3}$$

The magnitudes and directions of the corresponding principal Lagrangian strain were also obtained by calculating the eigenvalues and eigenvectors of the Lagrangian strain tensor shown in Eq. (3.6.2), respectively. It should be noted that the posterior scleral geometry pressurized to 5 mm Hg was chosen as the reference configuration. Therefore all Lagrangian strains mentioned in this study were computed from this reference configuration.

Figures 3.6.1 and 3.6.2 illustrate that the maximum principal strain was highest and primarily circumferential in trajectory in the peripapillary scleral region (immediately adjacent to the scleral canal). All four porcine eyes tested showed this specific pattern. However, the strain pattern was nonspecific in the peripheral scleral region further away from the scleral canal. Maximum increase of the principal Lagrangian strain for each IOP increase was averaged for all quadrants and for all specimen, and was found to be 0.013 ± 0.005 for an IOP elevation from 5 to 10 mm Hg (ΔIOP=5 mm Hg), 0.014 ± 0.004 for an IOP elevation from 10 to 30 mm Hg (ΔIOP=20 mm Hg), and 0.004 ± 0.001 for an IOP elevation from 30 to 45 mm Hg (ΔIOP=15 mm Hg). This result shows that the additional strain per unit increase in IOP was significantly lower at higher IOPs, demonstrating a high degree of nonlinearity in the IOP-maximum principal strain relationship. For each posterior scleral shell, this surface strain mapping also implied that

the scleral stiffness was relatively low for low IOPs (<10 mm Hg), but dramatically

increased at higher IOPs (>10 mm Hg), as shown in Figure 3.6.3.

Figure 3.6.1. Principal direction associated with maximum principal strain for a porcine scleral shell (OS) due to an IOP increase from 10 to 30 mm Hg. All four porcine eyes that were tested showed the same specific patterns, for all four quadrants, and for all IOP ranges (i.e. 5 to 10 mm Hg, 10 to 30 mm Hg and 30 to 45 mm Hg).

Maximum Principal Strain Magnitude
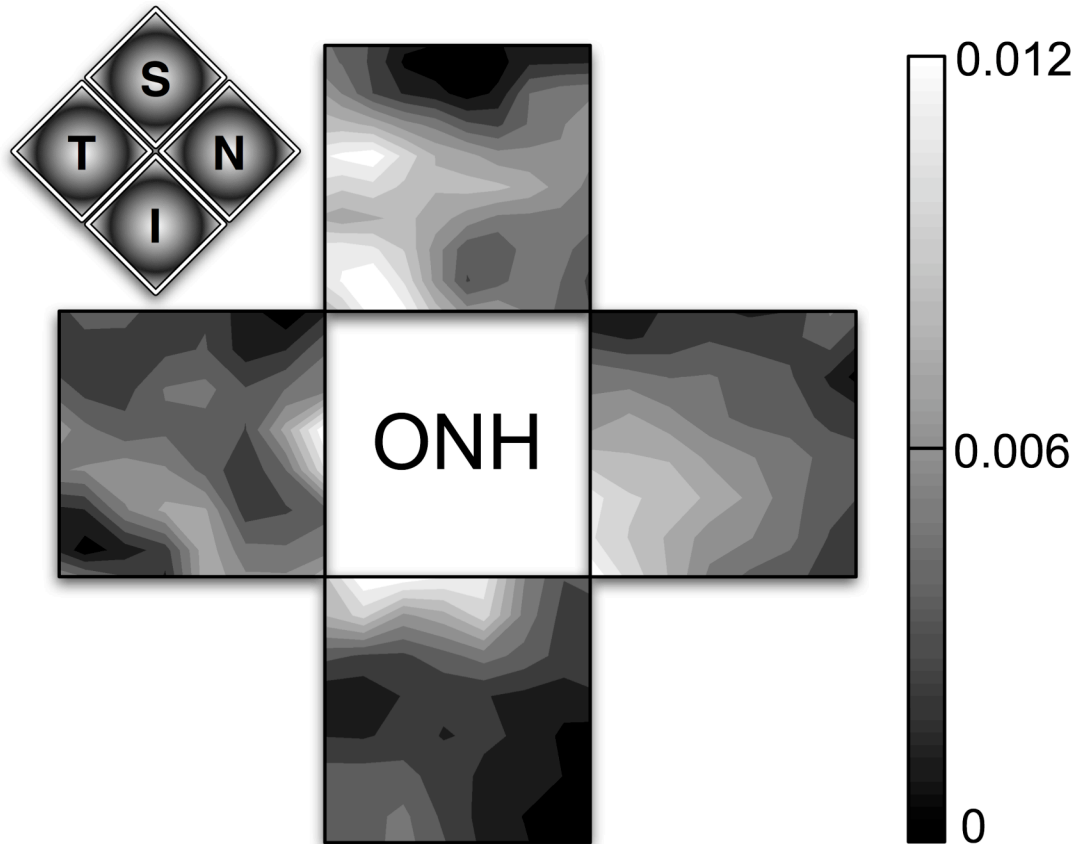
Figure 3.6.2. Maximum principal strain magnitude for a porcine scleral shell (OS) due to an IOP increase from 10 to 30 mm Hg. All four porcine eyes that were tested showed the same specific patterns, for all four quadrants, and for all IOP ranges (i.e. 5 to 10 mm Hg, 10 to 30 mm Hg and 30 to 45 mm Hg).
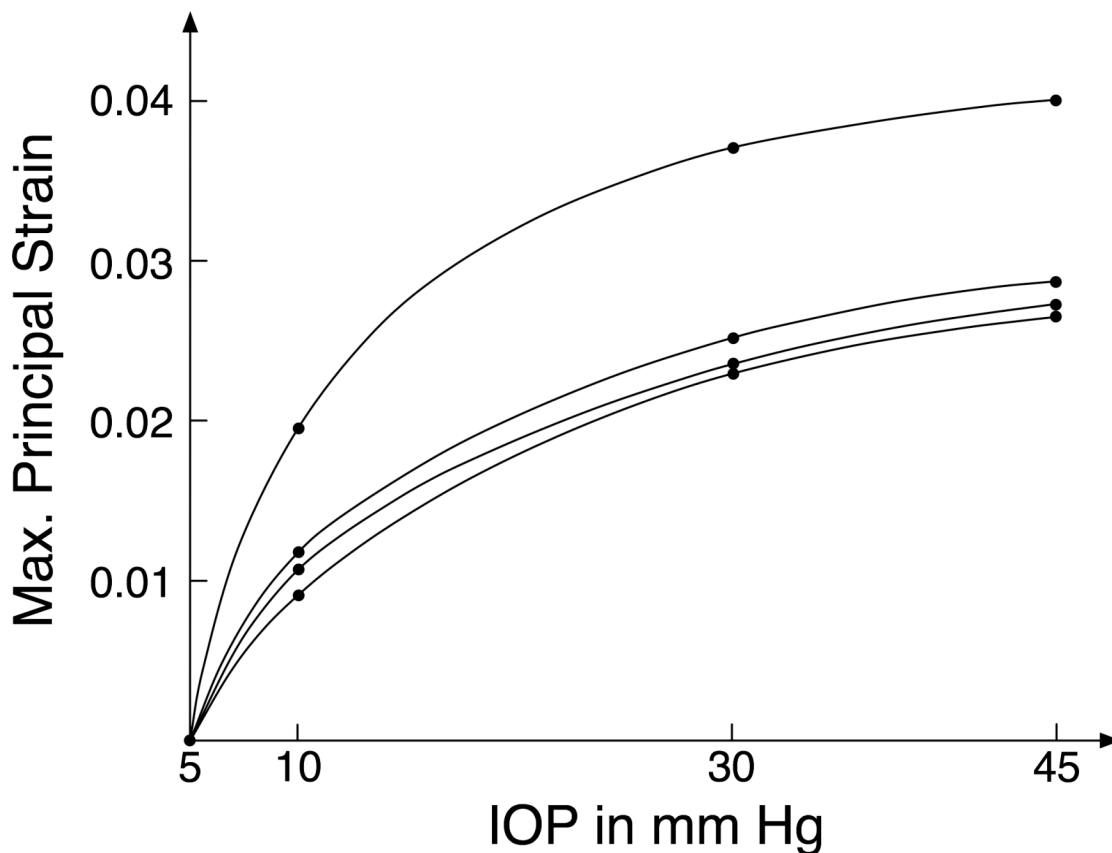
Figure 3.6.3. Mean maximum increase of the maximum principal strain as a function of IOP for each of the four porcine eyes, showing the high degree of nonlinearity in the response. For each eye, means were calculated for all four quadrants pooled together. As IOP increases, porcine sclera becomes considerably stiffer.

3.7. Discussion

In this Chapter, a new experimental method was developed to measure the surface strain in thin materials. This methodology has wide applicability to uni- and multi-axial mechanical testing of thin soft tissues. In this study, we performed mechanical testing of porcine peripapillary sclera using a pressurization apparatus to induce elevations of IOP from 5 to 45 mm Hg. For the 4 porcine scleral shells that were tested, the maximum principal strain magnitude was a nonlinear function of the applied IOP. The maximum

principal strain was highest in magnitude and was circumferential in trajectory in the peripapillary region immediately adjacent to the scleral canal.

The nonlinear IOP-sclera strain relationship may be due to collagen fibers in the sclera. It is well known that, under tension, collagen fibers exhibit a characteristic nonlinear stress-strain curve consisting of the initial 'toe' region of low elastic modulus and the subsequent 'linear' region of higher elastic modulus (Fung 1993). Our data would suggest that collagen fibers in the porcine sclera could have been in the linear elastic region when IOP is beyond 30 mm Hg. Additional experiments that consider a broader IOP range (e.g. 5 to 100 mm Hg) will eventually be needed as to obtain a better characterization of the nonlinear-linear transition if shown to exist.

The sclera also exhibits complex anisotropic characteristics as a result of the multi-directional arrangement of collagen fibers embedded in the proteoglycan-based ground substance matrix (Komai and Ushiki 1991; Watson and Young 2004). Collagen fibers in the sclera have a large distribution of diameters and are formed into irregularly arranged, multi-layered lamellae, with each lamella having different principal fiber orientation and thickness (Rada *et al.* 2006). Previous studies have found that scleral collagen fibers in the immediate peripapillary region are more organized and oriented predominantly in the circumferential direction relative to the scleral canal (Kokott 1934; Greene 1980).

Our results suggest a possible correlation between the fiber orientation and the principal directions associated with the maximum principal strain in the region adjacent to the scleral canal (the peripapillary sclera). Other studies have shown that soft tissue structures within the ONH (e.g. neural tissue, lamina cribrosa) are considerably weaker than the surrounding sclera tissue (Woo *et al.* 1972; Sigal *et al.* 2004; Spoerl *et al.* 2005),

which would likely cause the maximum principal stress/strain to orient along the tangent to the scleral canal (Bellezza *et al.* 2000; Sander *et al.* 2006). A remodeling theory for living soft tissues has been proposed that postulates that the ultrastructural organization of the collagen fibers is likely to be dictated by the direction and magnitude of the maximum principal strain (Driessen *et al.* 2003). According to this theory, it is likely that there would be strong correlation between the collagen fiber orientation and the direction of the maximum principal strain in the peripapillary sclera. In fact, maximum principal strain is oriented circumferentially around the scleral canal, and the collagen fibers are predominantly oriented circumferentially as well (Kokott 1934; Greene 1980). Overall, the collagen ultrastructure in the peripapillary sclera could be optimized to withstand IOP-related stress concentrations resulting from the geometry of the scleral canal. This is likely protective of the delicate lamina cribrosa that spans the scleral canal and the axons that pass through the canal at the ONH.

In this study, several limitations warrant further discussion. This technique is limited to the 2-D surface strain on planar specimens, and ignores the remaining three components of the 3-D finite strain tensor, the radial strain and the two transverse shearing strains. This limitation is acceptable for a thin-walled isotropic pressure vessel, in which the principal loading axes are tangent to the material surface (Timoshenko 1970), and can also be acceptable with a moderate confidence for scleral tissue, because the collagen fibers are mostly aligned tangent to the material surface. Therefore, we believe our 2-D optical measurement system composed of a high-resolution digital camera and microscope is sufficiently accurate to extract the principal components of scleral surface strain. It should be noted that the field of view in the 2-D optical measurement has to be sufficiently small compared to the diameter of the eye in order to

minimize the optical error due to the out-of-focus marker images. The field of view in the current study was chosen to be a 4 mm $\times$ 4 mm in size, and the diameter of each porcine eye was approximately 25 mm. Using a 2-D experimental method to describe the behavior of a 3-D soft tissue structure is a first step toward understanding ocular mechanics and its possible implications in glaucomatous damage to the ONH. In Chapter 5, we will develop an optical method to evaluate the full 3-D displacement field of monkey posterior sclera under IOP, which will allow us to confirm the presented results.

It is also important to note that the pixel displacement vector obtained from the optical flow algorithm is only an approximation of the actual 2-D displacement vector of each marker centroid, and that the predicted pixel displacement vector is likely contaminated by an error (Fig. 3). This is due to the inaccuracy of the Lucas-Kanade approximation as well as to the noise in the marker images. Although this error should be small in each incremental increase of IOP (1 mm Hg), the error could be accumulated to become unacceptably large over multiple incremental steps from 5 mm Hg up to 45 mm Hg. However, our method only used the Lucas-Kanade algorithm to provide a first estimation of marker displacement, so that optical flow errors did not affect the final displacement fields. It should be noted that the optical flow algorithm has been shown to perform well for qualitative purposes but will perform less accurately for quantitative purposes (Verri and Poggio 1987).

Finally, the sclera was assumed to be purely elastic, as the process of increasing IOP from 5 to 45 mm Hg was repeated four times (one for each quadrant of the eye). As this study was aimed at visualizing surface strains of porcine peripapillary sclera, not at determining scleral stiffness, we concluded that this assumption was a good first

approximation. Our new experimental protocol will allow us to measure 3-D displacements from the whole posterior scleral shell in a single pressurization cycle.

Mechanical testing and modeling of ocular soft tissues will contribute to our understanding of glaucomatous ONH (Bellezza *et al.* 2003; Burgoyne *et al.* 2004; Burgoyne *et al.* 2005) and peripapillary scleral (Downs *et al.* 2005) damage, myopia (Rada *et al.* 2006), and a host of other ocular disorders. Since the peripapillary sclera determines the levels of strain and stress placed on the contained ONH, and has been demonstrated to be altered in early experimental glaucoma (Downs *et al.* 2005) it is likely to play an important role in glaucomatous damage and warrants further investigation.

4   Development of an Anisotropic Hyperelastic Constitutive Model[1]

4.1. Abstract

The sclera is the white outer shell and principal load-bearing tissue of the eye as it sustains the intraocular pressure. We have hypothesized that the mechanical properties of the posterior sclera play a significant role in, and are altered by the development of glaucoma – an ocular disease manifested by structural damage to the optic nerve head. An anisotropic hyperelastic constitutive model is presented to simulate the mechanical behavior of the posterior sclera under acute elevations of intraocular pressure. The constitutive model is derived from fiber-reinforced composite theory, and incorporates stretch-induced stiffening of the reinforcing collagen fibers. Collagen fiber alignment was assumed to be multi-directional at local material points, confined within the plane tangent to the scleral surface, and described by the semi-circular von-Mises distribution. The introduction of a model parameter, namely the fiber concentration factor, was used to control collagen fiber alignment along a preferred fiber orientation. To investigate the

---

effects of scleral collagen fiber alignment on the overall behaviors of the posterior sclera and optic nerve head, finite element simulations of an idealized eye were performed. The four output quantities analyzed were the scleral canal expansion, the scleral canal twist, the posterior scleral canal deformation and the posterior laminar deformation. A circumferential fiber organization in the sclera restrained scleral canal expansion but created posterior laminar deformation, whereas the opposite was observed with a meridional fiber organization. Additionally, the fiber concentration factor acted as an amplifying parameter on the considered outputs. The present model simulation suggests that the posterior sclera has a large impact on the overall behavior of the optic nerve head. It is therefore primordial to provide accurate mechanical properties for this tissue. In the next chapter, we present a method to measure the 3-D deformations of monkey posterior sclera and extract mechanical properties based on the proposed constitutive model with an inverse finite element method.

4.2. Introduction

The sclera is the outer shell and principal load-bearing tissue of the eye, which consists primarily of avascular lamellae of collagen fibers (Edelhauser and Ubels 2003). Ninety percent of the collagen fibers in the sclera are Type I, which provide the eye with necessary mechanical strength (Fung 1993) to sustain the intraocular pressure (IOP). Within the posterior portion of the scleral shell, there is a fenestrated canal, called the optic nerve head (ONH), through which the retinal ganglion cell axons pass transmitting visual signals from the retina to the brain. The meshwork of connective tissue beams which span this opening are collectively called the lamina cribrosa.

Glaucomatous optic neuropathy is one of the three leading causes of blindness in the US (Leske 1983), and is manifested by a structural damage of the ONH under all levels (normal and elevated) of IOP (Burgoyne *et al.* 2005). We hypothesize that the mechanical properties of the posterior sclera are altered during the disease and play a significant role in the development and progression of glaucomatous damage to the lamina cribrosa and ganglion cell axons within the ONH (Burgoyne *et al.* 2005). In order to evaluate the effect of IOP on the connective tissues of the ONH, finite element (FE) models of the eye are being studied by our group (Bellezza *et al.* 2000; Downs *et al.* 2007; Roberts *et al.* 2007) and others (Sigal *et al.* 2005; Sigal *et al.* 2008). Our goal is to fully characterize the mechanical behavior of tissue structures around and within the ONH, and to investigate how the mechanical environment in the ONH influences the onset and progression of glaucoma. To build these models, accurate characterization of the mechanical properties of the load-bearing tissues is necessary.

In our previous studies (Downs *et al.* 2003; Downs *et al.* 2005; Girard *et al.* 2007), experimental and mathematical models were used to determine the uniaxial mechanical properties of the sclera under the assumption of isotropic, linear viscoelasticity. Sigal et al. have used a simplified FE model of the posterior sclera with linear elasticity to determine that the elastic modulus of the sclera would be the largest single determinant of strain in the ONH (Sigal *et al.* 2005; Sigal *et al.* 2008). While this was a good first step, the sclera is a complex structure with varying collagen fiber orientation (Kokott 1934; Greene 1980; Komai and Ushiki 1991; Rada *et al.* 2006), so its mechanical behavior under IOP- induced mechanical stress is likely to be anisotropic and nonlinear. Therefore, new testing and modeling protocols, with anisotropic and nonlinear

mechanical characteristics, are necessary to fully describe the 3-D behavior of the sclera in response to IOP elevations.

This Chapter considers the development of an anisotropic hyperelastic constitutive model, with application to an idealized posterior eye geometry. In Chapter 5, we present a method to experimentally characterize the 3-D deformation pattern of monkey posterior sclera due to acute elevation of IOP from 5 to 45 mm Hg, and use an inverse FE method to extract mechanical properties for the entire posterior sclera. The methods described in Chapters 4 and 5 can be applied to determine the mechanical properties of thin soft tissues that act as pressure vessels and are mechanically loaded in 3-D.

4.3. Anisotropic Hyperelastic Constitutive Model

For most soft-tissues, collagen is often considered as the primary biomechanical element as it provides tensile strength (Fung 1993), arising from its long and dense fibrous bundle organization. Accordingly, soft-tissues can be presented as fiber-reinforced composites, and modeled as hyperelastic materials that are characterized by a strain energy function W. An example of such strain energy function has been described in Weiss (Weiss *et al.* 1996) to model ligaments. It is defined as

$$W = W_{matrix} + W_{fiber},$$
(4.3.1)

where W_{matrix} is an isotropic contribution from the ground substance matrix which contains the elastin fibers, proteoglycans, fibroblasts, tissue fluid and all other tissue constituents except collagen; W_{fiber} is an anisotropic contribution from the reinforcing collagen fiber family. In (Weiss *et al.* 1996), the collagen fibers were aligned along a

single direction at local material points to represent transverse isotropy. Moreover, W_{fiber} was expressed as a nonlinear function of the fourth invariant I_4 (Spencer 1985) defined as

$$I_4 = \mathbf{a}_0 \cdot \mathbf{C} \cdot \mathbf{a}_0, \tag{4.3.2}$$

where $\mathbf{a}_0$ is a unit vector representing the local fiber direction in the undeformed configuration, and $\mathbf{C}$ is the right Cauchy-Green deformation tensor. Here, notice the link between I_4 and the fiber stretch λ. The latter can be expressed as

$$\lambda \mathbf{a} = \mathbf{F} \cdot \mathbf{a}_0, \tag{4.3.3}$$

where $\mathbf{a}$ is a unit vector representing the local fiber direction in the deformed configuration, and $\mathbf{F}$ is the deformation gradient tensor. Since $\mathbf{C} = \mathbf{F}^{\mathbf{T}} \cdot \mathbf{F}$, the fourth invariant I_4 is equivalent to the squared fiber stretch

$$I_4 = \mathbf{a}_0 \cdot \mathbf{C} \cdot \mathbf{a}_0 = \mathbf{a}_0 \cdot \mathbf{F}^{\mathbf{T}} \cdot \mathbf{F} \cdot \mathbf{a}_0 = \lambda^2. \tag{4.3.4}$$

For many soft-tissues, the collagen fiber alignment is multi-directional at local material points (Driessen *et al.* 2003; Pinsky *et al.* 2005), instead of being uni-directional. In the case of the posterior sclera, the collagen fibers have a large variation in their diameters and are formed into irregularly arranged, multi-layered lamellae, with each lamella having different preferred fiber orientation and thickness (Greene 1980; Komai and Ushiki 1991; Rada *et al.* 2006). To allow for multi-directionality at local material points, we assumed that the scleral collagen fiber alignment is confined within a plane tangent to the scleral surface, following a 2-D statistical distribution function P defined as

$$P(\theta) = \frac{1}{\pi I_0(k)} \exp\left(k \cos\left(2\left(\theta - \theta_p\right)\right)\right). \tag{4.3.5}$$

P is known as the semi-circular Von-Mises distribution (Fisher 1993) and I_0 is the modified Bessel function of the first kind (order 0),

$$I_0(k) = \frac{1}{\pi} \int_0^\pi \exp(k\cos(x))dx .$$
(4.3.6)

θ_p is the preferred fiber orientation relative to a local coordinate system, and *k* is the fiber concentration factor. Note that *P* satisfies the normalization condition

$$\int_{\theta_p - \pi/2}^{\theta_p + \pi/2} P(\theta)d\theta = 1 .$$
(4.3.7)

Figure 4.3.1. depicts the variations of *P* for $\theta_p = 0$ with different magnitude of *k*. $k = 0$ represents a case of planar isotropy, whereas a larger *k* represents a fiber distribution relative to θ_p. Note that the statistical distribution *P* was chosen for its simplicity as it can describe collagen fiber alignment with two parameters.
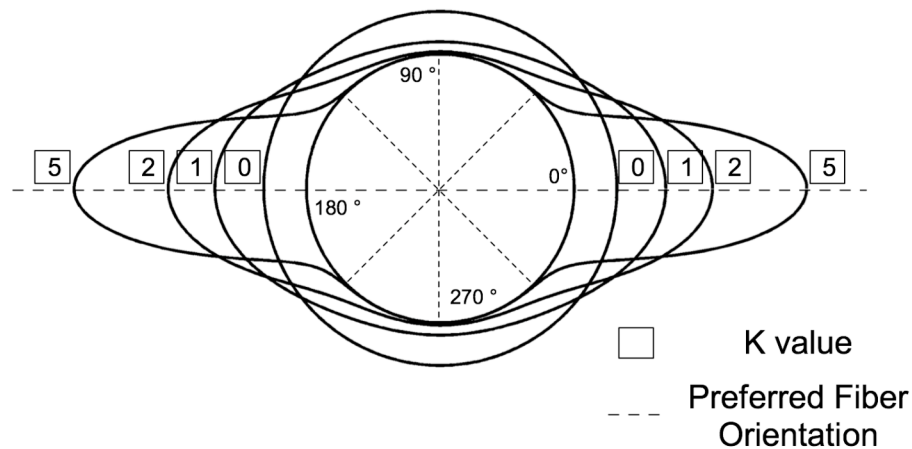
Figure 4.3.1. Polar representation of the semi-circular Von Mises distribution describing in-plane collagen fiber alignment. In this case, the preferred fiber orientation θ_p is equal to zero degrees. When the fiber concentration factor *k* is equal to zero, the collagen fibers have an isotropic distribution in a plane tangent to the scleral wall. As *k* increases, the collagen fibers align along the preferred fiber orientation θ_p. Note that the distributions were plotted on a circle of unit one to ease visualization.

Using Eq. (4.3.1), we propose the scleral strain energy function to be

$$W = W_{matrix} + \int_{\theta_p - \pi/2}^{\theta_p + \pi/2} P(\theta) W_{fiber} \circ I_4(\theta) d\theta \tag{4.3.8}$$

where the following notation was used: $f \circ g(x) = f[g(x)]$. Here, $W_{fiber} \circ I_4$ is the strain energy associated with the collagen fiber family aligned in the orientation of θ. Thus I_4 becomes a function of θ, such as

$$I_4(\theta) = \mathbf{a}_0(\theta) \cdot \mathbf{C} \cdot \mathbf{a}_0(\theta) = \lambda^2(\theta). \tag{4.3.9}$$

To represent tissue nonlinearity, the strain energy associated with the collagen fiber family was defined for each θ orientation such that

$$\lambda(\theta) \frac{\partial W_{fiber} \circ I_4(\theta)}{\partial \lambda(\theta)} = c_3 \left(\exp\left(c_4 \left(\lambda(\theta) - 1\right)\right) - 1 \right), \quad \forall \lambda(\theta) \in \mathbb{R}, \tag{4.3.10}$$

where c_3 is the exponential fiber stress coefficient and c_4 is the rate of uncrimping collagen fibers (Weiss *et al.* 1996). Finally, the ground substance matrix of the sclera was modeled as a Neo-Hookean material such that

$$W_{matrix} = c_1 (I_1 - 3), \tag{4.3.11}$$

where I_1 is the first invariant of the right Cauchy-Green deformation tensor ($I_1 = \mathrm{tr}(\mathbf{C})$), and c_1 is the first Mooney-Rivlin coefficient also equivalent to the matrix shear modulus divided by two.

4.4. Finite Element Implementation

The proposed constitutive model was implemented within the nonlinear FE code Nike3d (Hallquist 1984) that was provided by the Lawrence Livermore National

Laboratory. Modifications were made to the modules for a transversely isotropic, hyperelastic material with near-incompressibility (Weiss 1994). A multiplicative decomposition (Simo and Taylor 1991; Weiss *et al.* 1996; Bonet and Wood 1997; Holzapfel 2000) was applied to the deformation gradient tensor $\mathbf{F}$ and the right Cauchy-Green deformation tensor $\mathbf{C}$ such as

$$\mathbf{F} = J^{1/3}\tilde{\mathbf{F}}, \quad \mathbf{C} = J^{2/3}\tilde{\mathbf{C}}, \tag{4.4.1}$$

where $J = \det(\mathbf{F})$ is the Jacobian of the deformation; $\tilde{\mathbf{F}}$ and $\tilde{\mathbf{C}} = \tilde{\mathbf{F}}^{\mathrm{T}} \cdot \tilde{\mathbf{F}}$ are both tensors associated with a volume-preserving (isochoric) deformation since from Eq. (4.4.1), $\det(\tilde{\mathbf{F}}) = 1$. Accordingly, the strain energy function W was decoupled into two parts: isochoric ($\tilde{W}$) and volumetric (W_{vol}), such as

$$W(\mathbf{C}) = W_{vol}(J) + \tilde{W}(\tilde{\mathbf{C}}). \tag{4.4.2}$$

The material invariants of $\tilde{\mathbf{C}}$ are defined as

$$\begin{aligned}
\tilde{I}_1 &= \mathrm{tr}(\tilde{\mathbf{C}}) = J^{-2/3}\mathrm{tr}(\mathbf{C}) \\
\tilde{I}_4(\theta) &= \mathbf{a}_0(\theta) \cdot \tilde{\mathbf{C}} \cdot \mathbf{a}_0(\theta) = J^{-2/3}\mathbf{a}_0(\theta) \cdot \mathbf{C} \cdot \mathbf{a}_0(\theta)
\end{aligned} \tag{4.4.3}$$

The second Piola-Kirchhoff stress tensor $\mathbf{S}$ is derived from the strain energy function W as

$$\mathbf{S} = 2\frac{\partial W(\mathbf{C})}{\partial \mathbf{C}} = 2\frac{\partial W_{vol}(J)}{\partial \mathbf{C}} + 2\frac{\partial \tilde{W}(\tilde{\mathbf{C}})}{\partial \mathbf{C}}, \tag{4.4.4}$$

where $\tilde{W}$ for the sclera is defined from Eq. (4.3.8) as

$$\tilde{W} = \tilde{W}_{matrix} + \int_{\theta_p - \pi/2}^{\theta_p + \pi/2} P(\theta)\tilde{W}_{fiber} \circ \tilde{I}_4(\theta)d\theta. \tag{4.4.5}$$

Using the chain rule, the first right-hand term in Eq. (4.4.4) becomes

$$\frac{\partial W_{vol}(J)}{\partial \mathbf{C}} = \frac{\mathrm{d}W_{vol}(J)}{\mathrm{d}J}\frac{\partial J}{\partial \mathbf{C}}, \tag{4.4.6}$$

where $\dfrac{\partial J}{\partial \mathbf{C}} = \dfrac{1}{2}J\mathbf{C}^{-1}$, and $\dfrac{\mathrm{d}W_{vol}(J)}{\mathrm{d}J}$ is the hydrostatic pressure p.

The second right-hand term in Eq. (4.4.4) can be expressed as

$$\frac{\partial \tilde{W}(\tilde{\mathbf{C}})}{\partial \mathbf{C}} = \frac{\partial \tilde{W}(\tilde{\mathbf{C}})}{\partial \tilde{\mathbf{C}}} : \frac{\partial \tilde{\mathbf{C}}}{\partial \mathbf{C}}, \tag{4.4.7}$$

where

$$\begin{aligned}
\frac{\partial \tilde{\mathbf{C}}}{\partial \mathbf{C}} &= \frac{\partial \left(J^{-2/3}\mathbf{C}\right)}{\partial \mathbf{C}} = J^{-2/3}\frac{\partial \mathbf{C}}{\partial \mathbf{C}} + \mathbf{C} \otimes \frac{\partial J^{-2/3}}{\partial \mathbf{C}} \\
&= J^{-2/3}\left(\mathbb{I} - \frac{1}{3}\mathbf{C}\otimes\mathbf{C}^{-1}\right) = J^{-2/3}\underbrace{\left(\mathbb{I} - \frac{1}{3}\tilde{\mathbf{C}}\otimes\tilde{\mathbf{C}}^{-1}\right)}_{\mathbb{P}^{\mathbf{T}}}.
\end{aligned} \tag{4.4.8}$$

Here, $\mathbb{I}$ is a 4$^{\text{th}}$ order unit tensor ($\mathbb{I}_{ijkl} = \delta_{ik}\delta_{jl}$) and $\mathbb{P}_{ijkl} = \mathbb{I} - \dfrac{1}{3}\mathbf{C}^{-1}\otimes\mathbf{C}$ is referred to as

the material projection tensor. Also note that $\dfrac{\partial J^{-2/3}}{\partial \mathbf{C}} = -\dfrac{1}{3}J^{-2/3}\mathbf{C}^{-1}$. Therefore, the

isochoric part of the second Piola-Kirchhoff tensor can be rewritten as

$$\begin{aligned}
2\frac{\partial \tilde{W}(\tilde{\mathbf{C}})}{\partial \mathbf{C}} &= 2J^{-2/3}\frac{\partial \tilde{W}(\tilde{\mathbf{C}})}{\partial \tilde{\mathbf{C}}} : \mathbb{P}^{\mathbf{T}} = 2J^{-2/3}\mathbb{P} : \frac{\partial \tilde{W}(\tilde{\mathbf{C}})}{\partial \tilde{\mathbf{C}}} \\
&= 2J^{-2/3}\left(\frac{\partial \tilde{W}(\tilde{\mathbf{C}})}{\partial \tilde{\mathbf{C}}} - \frac{1}{3}\left(\frac{\partial \tilde{W}(\tilde{\mathbf{C}})}{\partial \tilde{\mathbf{C}}} : \tilde{\mathbf{C}}\right)\tilde{\mathbf{C}}^{-1}\right).
\end{aligned} \tag{4.4.9}$$

By using $\tilde{W}$ from Eq. (4.4.5), it can be shown that

$$\frac{\partial \tilde{W}}{\partial \tilde{\mathbf{C}}} = c_1 \frac{\partial}{\partial \tilde{\mathbf{C}}} \left(\tilde{I}_1 - 3 \right) + \frac{\partial}{\partial \tilde{\mathbf{C}}} \left(\int_{\theta_p - \pi/2}^{\theta_p + \pi/2} P(\theta, k) \tilde{W}_{fiber} \circ \tilde{I}_4(\theta) d\theta \right)$$

$$= c_1 \frac{\partial \tilde{I}_1}{\partial \tilde{\mathbf{C}}} + \int_{\theta_p - \pi/2}^{\theta_p + \pi/2} P(\theta, k) \frac{\partial \tilde{W}_{fiber} \circ \tilde{I}_4(\theta)}{\partial \tilde{I}_4(\theta)} \frac{\partial \tilde{I}_4(\theta)}{\partial \tilde{\mathbf{C}}} d\theta$$

(4.4.10)

where

$$\frac{\partial \tilde{I}_1}{\partial \tilde{\mathbf{C}}} = \frac{\partial \tilde{\mathbf{C}} : \mathbf{I}}{\partial \tilde{\mathbf{C}}} = \mathbf{I} : \frac{\partial \tilde{\mathbf{C}}}{\partial \tilde{\mathbf{C}}} = \mathbf{I} : \mathbb{I} = \mathbf{I}, \text{ and}$$

(4.4.11)

$$\frac{\partial \tilde{I}_4(\theta)}{\partial \tilde{\mathbf{C}}} = \mathbf{a_0}(\theta) \otimes \mathbf{a_0}(\theta).$$

(4.4.12)

From Eq. (4.3.10), we now define $\tilde{W}_4$ as

$$\tilde{W}_4(\theta) = \frac{\partial \tilde{W}_{fiber} \circ \tilde{I}_4(\theta)}{\partial \tilde{I}_4(\theta)} = \frac{c_3}{2\tilde{\lambda}(\theta)^2} \left\{ \exp\left(c_4 \left[\tilde{\lambda}(\theta) - 1 \right] \right) - 1 \right\},$$

(4.4.13)

and therefore Eqn (4.4.10) becomes

$$\frac{\partial \tilde{W}}{\partial \tilde{\mathbf{C}}} = c_1 \mathbf{I} + \int_{\theta_p - \pi/2}^{\theta_p + \pi/2} P(\theta, k) \tilde{W}_4(\theta) \mathbf{a_0}(\theta) \otimes \mathbf{a_0}(\theta) d\theta.$$

(4.4.14)

Using Eq. (4.4.4), (4.4.6), and (4.4.14), the final form of the 2nd Piola Kirchhoff stress tensor $\mathbf{S}$ can be written as

$$\boxed{\begin{aligned} \mathbf{S} = pJ\mathbf{C}^{-1} + 2J^{-2/3} &\left[c_1 \left(\mathbf{I} - \frac{1}{3} \tilde{I}_1 \tilde{\mathbf{C}}^{-1} \right) \right. \\ &+ \left. \int_{\theta_p - \pi/2}^{\theta_p + \pi/2} P(\theta, k) \tilde{W}_4(\theta) \left(\mathbf{a_0}(\theta) \otimes \mathbf{a_0}(\theta) - \frac{1}{3} \tilde{I}_4(\theta) \tilde{\mathbf{C}}^{-1} \right) d\theta \right] \end{aligned}}$$

(4.4.15)

The Cauchy stress tensor σ is derived from the 2nd Piola Kirchhoff stress tensor $\mathbf{S}$ with the following equation

$$\sigma = \frac{1}{J} \mathbf{F} \cdot \mathbf{S} \cdot \mathbf{F}^{\mathrm{T}}.$$

(4.4.16)

Using Eq. (4.4.14), we derive

$$\tilde{\mathbf{F}} \cdot \frac{\partial \tilde{W}}{\partial \tilde{\mathbf{C}}} \cdot \tilde{\mathbf{F}}^{\mathrm{T}} = c_1 \tilde{\mathbf{B}} + \int_{\theta_p - \pi/2}^{\theta_p + \pi/2} P(\theta,k) \tilde{W}_4(\theta) \tilde{I}_4(\theta) \mathbf{a}(\theta) \otimes \mathbf{a}(\theta) d\theta, \qquad (4.4.17)$$

where $\tilde{\mathbf{B}} = \tilde{\mathbf{F}} \cdot \tilde{\mathbf{F}}^{\mathrm{T}}$ is the Left Cauchy-Green deformation tensor associated with the isochoric deformation. Showing that

$$\mathbf{F} \cdot pJ\mathbf{C}^{-1} \cdot \mathbf{F}^{\mathrm{T}} = p\mathbf{I}, \qquad (4.4.18)$$

we can then provide the final form of the Cauchy stress tensor as

$$\boxed{\begin{aligned} \sigma = p\mathbf{I} + \frac{2}{J}\Bigg[& c_1\left(\tilde{\mathbf{B}} - \frac{1}{3}\tilde{I}_1\mathbf{I} \right) \\ & + \int_{\theta_p - \pi/2}^{\theta_p + \pi/2} P(\theta,k)\tilde{W}_4(\theta)\tilde{I}_4(\theta)\left(\mathbf{a}(\theta) \otimes \mathbf{a}(\theta) - \frac{1}{3}\mathbf{I} \right)d\theta \Bigg] \end{aligned}} \qquad (4.4.19)$$

The material elasticity tensor $\mathbb{C}$ is expressed as

$$\mathbb{C} = 4\frac{\partial^2 W(\mathbf{C})}{\partial \mathbf{C}\partial \mathbf{C}} = 2\frac{\partial \mathbf{S}(\mathbf{C})}{\partial \mathbf{C}}, \qquad (4.4.20)$$

and we recall that the 2$^{\mathrm{nd}}$ Piola Kirchhoff stress tensor was expressed as

$$\mathbf{S} = pJ\mathbf{C}^{-1} + 2J^{-2/3}\left(\frac{\partial \tilde{W}}{\partial \tilde{\mathbf{C}}} - \frac{1}{3}\left(\frac{\partial \tilde{W}}{\partial \tilde{\mathbf{C}}} : \tilde{\mathbf{C}} \right)\tilde{\mathbf{C}}^{-1} \right). \qquad (4.4.21)$$

Therefore we have

$$\mathbb{C} = 2\frac{\partial \left(pJ\mathbf{C}^{-1} \right)}{\partial \mathbf{C}} + 4\frac{\partial}{\partial \mathbf{C}}\left(J^{-2/3}\left(\frac{\partial \tilde{W}}{\partial \tilde{\mathbf{C}}} - \frac{1}{3}\left(\frac{\partial \tilde{W}}{\partial \tilde{\mathbf{C}}} : \tilde{\mathbf{C}} \right)\tilde{\mathbf{C}}^{-1} \right) \right). \qquad (4.4.22)$$

The first right-hand term of Eqn (4.4.22) is expanded as

$$2\frac{\partial\left(pJ\mathbf{C}^{-1}\right)}{\partial\mathbf{C}} = 2\mathbf{C}^{-1}\otimes\frac{\partial(pJ)}{\partial\mathbf{C}} + 2pJ\frac{\partial\mathbf{C}^{-1}}{\partial\mathbf{C}}$$

$$= 2\mathbf{C}^{-1}\otimes\left(p\frac{\partial J}{\partial\mathbf{C}} + J\frac{\partial p}{\partial\mathbf{C}}\right) + 2pJ\frac{\partial\mathbf{C}^{-1}}{\partial\mathbf{C}}$$

$$= 2\mathbf{C}^{-1}\otimes\left(p\frac{\partial J}{\partial\mathbf{C}} + J\frac{\mathrm{d}p}{\mathrm{d}J}\frac{\partial J}{\partial\mathbf{C}}\right) + 2pJ\frac{\partial\mathbf{C}^{-1}}{\partial\mathbf{C}} \qquad, \qquad (4.4.23)$$

$$= 2\mathbf{C}^{-1}\otimes\frac{\partial J}{\partial\mathbf{C}}\left(p + J\frac{\mathrm{d}p}{\mathrm{d}J}\right) + 2pJ\frac{\partial\mathbf{C}^{-1}}{\partial\mathbf{C}}$$

$$= J\mathbf{C}^{-1}\otimes\mathbf{C}^{-1}\left(p + J\frac{\mathrm{d}p}{\mathrm{d}J}\right) + 2pJ\frac{\partial\mathbf{C}^{-1}}{\partial\mathbf{C}}$$

$$= pJ\left(\mathbf{C}^{-1}\otimes\mathbf{C}^{-1} - 2\mathbf{C}^{-1}\odot\mathbf{C}^{-1}\right)$$

where $\mathrm{d}p/\mathrm{d}J$ was assumed to be zero and the operator $\odot$ was defined such that

$$\frac{\partial\mathbf{C}^{-1}}{\partial\mathbf{C}} = -\mathbf{C}^{-1}\odot\mathbf{C}^{-1}. \qquad (4.4.24)$$

The second right-hand term of Eqn (4.4.22) becomes

$$4\frac{\partial}{\partial\mathbf{C}}\left(J^{-2/3}\left(\frac{\partial\tilde{W}}{\partial\tilde{\mathbf{C}}} - \frac{1}{3}\left(\frac{\partial\tilde{W}}{\partial\tilde{\mathbf{C}}}:\tilde{\mathbf{C}}\right)\tilde{\mathbf{C}}^{-1}\right)\right)$$

$$= 4\left(\frac{\partial\tilde{W}}{\partial\tilde{\mathbf{C}}} - \frac{1}{3}\left(\frac{\partial\tilde{W}}{\partial\tilde{\mathbf{C}}}:\tilde{\mathbf{C}}\right)\tilde{\mathbf{C}}^{-1}\right)\otimes\frac{\partial J^{-2/3}}{\partial\mathbf{C}} \qquad (4.4.25)$$

$$+ 4J^{-2/3}\frac{\partial}{\partial\mathbf{C}}\left(\frac{\partial\tilde{W}}{\partial\tilde{\mathbf{C}}} - \frac{1}{3}\left(\frac{\partial\tilde{W}}{\partial\tilde{\mathbf{C}}}:\tilde{\mathbf{C}}\right)\tilde{\mathbf{C}}^{-1}\right)$$

From the previous equation, we can derive

$$4\left(\frac{\partial\tilde{W}}{\partial\tilde{\mathbf{C}}} - \frac{1}{3}\left(\frac{\partial\tilde{W}}{\partial\tilde{\mathbf{C}}}:\tilde{\mathbf{C}}\right)\tilde{\mathbf{C}}^{-1}\right)\otimes\frac{\partial J^{-2/3}}{\partial\mathbf{C}}$$

$$= -\frac{4}{3}J^{-2/3}\left(\frac{\partial\tilde{W}}{\partial\tilde{\mathbf{C}}} - \frac{1}{3}\left(\frac{\partial\tilde{W}}{\partial\tilde{\mathbf{C}}}:\tilde{\mathbf{C}}\right)\tilde{\mathbf{C}}^{-1}\right)\otimes\mathbf{C}^{-1} \qquad, \qquad (4.4.26)$$

$$= -\frac{4}{3}J^{-4/3}\left(\frac{\partial\tilde{W}}{\partial\tilde{\mathbf{C}}} - \frac{1}{3}\left(\frac{\partial\tilde{W}}{\partial\tilde{\mathbf{C}}}:\tilde{\mathbf{C}}\right)\tilde{\mathbf{C}}^{-1}\right)\otimes\tilde{\mathbf{C}}^{-1}$$

and

$$4J^{-2/3}\frac{\partial}{\partial \mathbf{C}}\left(\frac{\partial \tilde{W}}{\partial \tilde{\mathbf{C}}} - \frac{1}{3}\left(\frac{\partial \tilde{W}}{\partial \tilde{\mathbf{C}}}:\tilde{\mathbf{C}}\right)\tilde{\mathbf{C}}^{-1}\right)$$

$$= 4J^{-2/3}\frac{\partial}{\partial \tilde{\mathbf{C}}}\left(\frac{\partial \tilde{W}}{\partial \tilde{\mathbf{C}}} - \frac{1}{3}\left(\frac{\partial \tilde{W}}{\partial \tilde{\mathbf{C}}}:\tilde{\mathbf{C}}\right)\tilde{\mathbf{C}}^{-1}\right):\frac{\partial \tilde{\mathbf{C}}}{\partial \mathbf{C}}$$, (4.4.27)

$$= 4J^{-4/3}\left(\frac{\partial^2 \tilde{W}}{\partial \tilde{\mathbf{C}}\partial \tilde{\mathbf{C}}} - \frac{1}{3}\frac{\partial}{\partial \tilde{\mathbf{C}}}\left[\left(\frac{\partial \tilde{W}}{\partial \tilde{\mathbf{C}}}:\tilde{\mathbf{C}}\right)\tilde{\mathbf{C}}^{-1}\right]\right):\left(\mathbb{I} - \frac{1}{3}\mathbf{C}\otimes \mathbf{C}^{-1}\right)$$

with

$$\frac{\partial}{\partial \tilde{\mathbf{C}}}\left[\left(\frac{\partial \tilde{W}}{\partial \tilde{\mathbf{C}}}:\tilde{\mathbf{C}}\right)\tilde{\mathbf{C}}^{-1}\right] = \left(\frac{\partial \tilde{W}}{\partial \tilde{\mathbf{C}}}:\tilde{\mathbf{C}}\right)\frac{\partial \tilde{\mathbf{C}}^{-1}}{\partial \tilde{\mathbf{C}}} + \tilde{\mathbf{C}}^{-1}\otimes \frac{\partial}{\partial \tilde{\mathbf{C}}}\left(\frac{\partial \tilde{W}}{\partial \tilde{\mathbf{C}}}:\tilde{\mathbf{C}}\right)$$

$$= J^{4/3}\left(\frac{\partial \tilde{W}}{\partial \tilde{\mathbf{C}}}:\tilde{\mathbf{C}}\right)\frac{\partial \mathbf{C}^{-1}}{\partial \mathbf{C}} + \tilde{\mathbf{C}}^{-1}\otimes\left(\frac{\partial \tilde{W}}{\partial \tilde{\mathbf{C}}}:\frac{\partial \tilde{\mathbf{C}}}{\partial \tilde{\mathbf{C}}} + \tilde{\mathbf{C}}:\frac{\partial^2 \tilde{W}}{\partial \tilde{\mathbf{C}}\partial \tilde{\mathbf{C}}}\right)$$. (4.4.28)

$$= -J^{4/3}\left(\frac{\partial \tilde{W}}{\partial \tilde{\mathbf{C}}}:\tilde{\mathbf{C}}\right)\mathbf{C}^{-1}\odot \mathbf{C}^{-1} + \tilde{\mathbf{C}}^{-1}\otimes\frac{\partial \tilde{W}}{\partial \tilde{\mathbf{C}}} + \tilde{\mathbf{C}}^{-1}\otimes\left(\tilde{\mathbf{C}}:\frac{\partial^2 \tilde{W}}{\partial \tilde{\mathbf{C}}\partial \tilde{\mathbf{C}}}\right)$$

Therefore the material elasticity tensor $\mathbb{C}$ becomes

$$\mathbb{C} = pJ\left(\mathbf{C}^{-1}\otimes \mathbf{C}^{-1} - 2\mathbf{C}^{-1}\odot \mathbf{C}^{-1}\right) + \frac{4}{3}\left(\frac{\partial \tilde{W}}{\partial \tilde{\mathbf{C}}}:\tilde{\mathbf{C}}\right)\left(\mathbf{C}^{-1}\odot \mathbf{C}^{-1} - \frac{1}{3}\mathbf{C}^{-1}\otimes \mathbf{C}^{-1}\right)$$

$$-\frac{4}{3}J^{-4/3}\left[\tilde{\mathbf{C}}^{-1}\otimes\left(\frac{\partial \tilde{W}}{\partial \tilde{\mathbf{C}}} - \frac{1}{3}\left(\frac{\partial \tilde{W}}{\partial \tilde{\mathbf{C}}}:\tilde{\mathbf{C}}\right)\tilde{\mathbf{C}}^{-1}\right) + \left(\frac{\partial \tilde{W}}{\partial \tilde{\mathbf{C}}} - \frac{1}{3}\left(\frac{\partial \tilde{W}}{\partial \tilde{\mathbf{C}}}:\tilde{\mathbf{C}}\right)\tilde{\mathbf{C}}^{-1}\right)\otimes \tilde{\mathbf{C}}^{-1}\right]$$

$$+4J^{-4/3}\frac{\partial^2 \tilde{W}}{\partial \tilde{\mathbf{C}}\partial \tilde{\mathbf{C}}} - \frac{4}{3}J^{-4/3}\left[\left(\frac{\partial^2 \tilde{W}}{\partial \tilde{\mathbf{C}}\partial \tilde{\mathbf{C}}}:\tilde{\mathbf{C}}\right)\otimes \tilde{\mathbf{C}}^{-1} + \tilde{\mathbf{C}}^{-1}\otimes\left(\tilde{\mathbf{C}}:\frac{\partial^2 \tilde{W}}{\partial \tilde{\mathbf{C}}\partial \tilde{\mathbf{C}}}\right)\right]$$, (4.4.29)

$$+\frac{4}{9}J^{-4/3}\left(\tilde{\mathbf{C}}:\frac{\partial^2 \tilde{W}}{\partial \tilde{\mathbf{C}}\partial \tilde{\mathbf{C}}}:\tilde{\mathbf{C}}\right)\tilde{\mathbf{C}}^{-1}\otimes \tilde{\mathbf{C}}^{-1}$$

which when expressed in a shorter form

$$\boxed{\begin{aligned}\mathbb{C} &= pJ\left(\mathbf{C}^{-1}\otimes \mathbf{C}^{-1} - 2\mathbf{C}^{-1}\odot \mathbf{C}^{-1}\right) + 4J^{-4/3}\mathbb{P}^{\mathbf{T}}:\frac{\partial^2 \tilde{W}}{\partial \tilde{\mathbf{C}}\partial \tilde{\mathbf{C}}}:\mathbb{P}\\ &\quad -\frac{4}{3}J^{-4/3}\left[\tilde{\mathbf{C}}^{-1}\otimes\left(\mathbb{P}:\frac{\partial \tilde{W}}{\partial \tilde{\mathbf{C}}}\right) + \left(\mathbb{P}:\frac{\partial \tilde{W}}{\partial \tilde{\mathbf{C}}}\right)\otimes \tilde{\mathbf{C}}^{-1}\right]\\ &\quad +\frac{4}{3}\left(\frac{\partial \tilde{W}}{\partial \tilde{\mathbf{C}}}:\tilde{\mathbf{C}}\right)\left(\mathbf{C}^{-1}\odot \mathbf{C}^{-1} - \frac{1}{3}\mathbf{C}^{-1}\otimes \mathbf{C}^{-1}\right)\end{aligned}}$$. (4.4.30)

The spatial elasticity tensor $\mathbb{c}$ is derived from the material elasticity tensor $\mathbb{C}$ as

$$\mathbb{c} = \frac{1}{J}\left(\mathbf{F} \underline{\otimes} \mathbf{F}\right):\mathbb{C}:\left(\mathbf{F}^{\mathbf{T}} \underline{\otimes} \mathbf{F}^{\mathbf{T}}\right), \tag{4.4.31}$$

where the operator $\underline{\otimes}$ is defined such that $\left(\mathbf{F} \underline{\otimes} \mathbf{F}\right)_{ijkl} = \mathbf{F}_{ik}\mathbf{F}_{jl}$.

Using Einstein's notation we will consider the following derivations:

- 4th order tensor $\mathbf{C}^{-1} \otimes \mathbf{C}^{-1}$

$$
\begin{aligned}
&\left[\left(\mathbf{F} \underline{\otimes} \mathbf{F}\right):\mathbf{C}^{-1} \otimes \mathbf{C}^{-1}:\left(\mathbf{F}^{\mathbf{T}} \underline{\otimes} \mathbf{F}^{\mathbf{T}}\right)\right]_{ijkl} \\
&= \left(\mathbf{F} \underline{\otimes} \mathbf{F}\right)_{ijmn}\left(\mathbf{C}^{-1} \otimes \mathbf{C}^{-1}\right)_{mnop}\left(\mathbf{F}^{\mathbf{T}} \underline{\otimes} \mathbf{F}^{\mathbf{T}}\right)_{opkl} \\
&= \mathbf{F}_{im}\mathbf{F}_{jn}\mathbf{C}^{-1}{}_{mn}\mathbf{C}^{-1}{}_{op}\mathbf{F}^{\mathbf{T}}{}_{ok}\mathbf{F}^{\mathbf{T}}{}_{pl} \\
&= \mathbf{F}_{im}\mathbf{F}_{jn}\mathbf{F}^{-1}{}_{mq}\mathbf{F}^{-\mathbf{T}}{}_{qn}\mathbf{F}^{-1}{}_{or}\mathbf{F}^{-\mathbf{T}}{}_{rp}\mathbf{F}^{\mathbf{T}}{}_{ok}\mathbf{F}^{\mathbf{T}}{}_{pl} \\
&= \mathbf{F}_{im}\mathbf{F}_{jn}\mathbf{F}^{-1}{}_{mq}\mathbf{F}^{-1}{}_{nq}\mathbf{F}^{-1}{}_{or}\mathbf{F}^{-1}{}_{pr}\mathbf{F}_{ko}\mathbf{F}_{lp} \\
&= \delta_{iq}\delta_{jq}\delta_{kr}\delta_{lr} \\
&= \delta_{ij}\delta_{kl} \\
&\Rightarrow \left(\mathbf{F} \underline{\otimes} \mathbf{F}\right):\mathbf{C}^{-1} \otimes \mathbf{C}^{-1}:\left(\mathbf{F}^{\mathbf{T}} \underline{\otimes} \mathbf{F}^{\mathbf{T}}\right) = \mathbf{I} \otimes \mathbf{I}
\end{aligned}
\tag{4.4.32}
$$

- 4th order tensor $\mathbf{C}^{-1} \odot \mathbf{C}^{-1} = J^{-4/3}\tilde{\mathbf{C}}^{-1} \odot \tilde{\mathbf{C}}^{-1}$

$$
\begin{aligned}
&\left[\left(\mathbf{F} \underline{\otimes} \mathbf{F}\right):\mathbf{C}^{-1} \odot \mathbf{C}^{-1}:\left(\mathbf{F}^{\mathbf{T}} \underline{\otimes} \mathbf{F}^{\mathbf{T}}\right)\right]_{ijkl} \\
&= \left(\mathbf{F} \underline{\otimes} \mathbf{F}\right)_{ijmn}\left(\mathbf{C}^{-1} \odot \mathbf{C}^{-1}\right)_{mnop}\left(\mathbf{F}^{\mathbf{T}} \underline{\otimes} \mathbf{F}^{\mathbf{T}}\right)_{opkl} \\
&= \frac{1}{2}\mathbf{F}_{iI}\mathbf{F}_{jJ}\mathbf{F}_{kK}\mathbf{F}_{lL}\left(\mathbf{C}^{-1}{}_{IK}\mathbf{C}^{-1}{}_{JL}+\mathbf{C}^{-1}{}_{IL}\mathbf{C}^{-1}{}_{JK}\right) \\
&= \frac{1}{2}\mathbf{F}_{iI}\mathbf{F}_{jJ}\mathbf{F}_{kK}\mathbf{F}_{lL}\left(\mathbf{F}_{IM}{}^{-1}\mathbf{F}_{KM}{}^{-1}\mathbf{F}_{JN}{}^{-1}\mathbf{F}_{LN}{}^{-1} + \mathbf{F}_{IO}{}^{-1}\mathbf{F}_{LO}{}^{-1}\mathbf{F}_{JP}{}^{-1}\mathbf{F}_{KP}{}^{-1}\right) \\
&= \frac{1}{2}\left(\delta_{iM}\delta_{kM}\delta_{jN}\delta_{lN} + \delta_{iO}\delta_{lO}\delta_{jP}\delta_{kP}\right) \\
&= \frac{1}{2}\left(\delta_{ik}\delta_{jl} + \delta_{il}\delta_{jk}\right) \\
&= \mathbb{S}_{ijkl} \\
&\Rightarrow \left(\mathbf{F} \underline{\otimes} \mathbf{F}\right):\mathbf{C}^{-1} \odot \mathbf{C}^{-1}:\left(\mathbf{F}^{\mathbf{T}} \underline{\otimes} \mathbf{F}^{\mathbf{T}}\right) = \mathbb{S}
\end{aligned}
\tag{4.4.33}
$$

- Scalar $\dfrac{\partial \tilde{W}}{\partial \tilde{\mathbf{C}}} : \tilde{\mathbf{C}} = \tilde{\mathbf{F}} \dfrac{\partial \tilde{W}}{\partial \tilde{\mathbf{C}}} \tilde{\mathbf{F}}^{\mathbf{T}} : \mathbf{I}$

$$
\begin{aligned}
\frac{\partial \tilde{W}}{\partial \tilde{\mathbf{C}}} : \tilde{\mathbf{C}} &= \left(\frac{\partial \tilde{W}}{\partial \tilde{\mathbf{C}}} \right)_{ij} \tilde{\mathbf{C}}_{ij} = \left(\frac{\partial \tilde{W}}{\partial \tilde{\mathbf{C}}} \right)_{ij} \tilde{\mathbf{F}}^{\mathbf{T}}_{iK} \tilde{\mathbf{F}}_{Kj} \\
&= \left(\frac{\partial \tilde{W}}{\partial \tilde{\mathbf{C}}} \right)_{ij} \tilde{\mathbf{F}}_{Ii} \tilde{\mathbf{F}}_{Jj} \delta_{IK} \delta_{JK} = \tilde{\mathbf{F}}_{Ii} \tilde{\mathbf{F}}_{Jj} \left(\frac{\partial \tilde{W}}{\partial \tilde{\mathbf{C}}} \right)_{ij} \delta_{IJ} \qquad (4.4.34) \\
&\Rightarrow \frac{\partial \tilde{W}}{\partial \tilde{\mathbf{C}}} : \tilde{\mathbf{C}} = \tilde{\mathbf{F}}^{\mathbf{T}} \frac{\partial \tilde{W}}{\partial \tilde{\mathbf{C}}} \tilde{\mathbf{F}} : \mathbf{I}
\end{aligned}
$$

- 4th order tensor $\mathbf{C}^{-1} \otimes \dfrac{\partial \tilde{W}}{\partial \tilde{\mathbf{C}}}$

$$
\begin{aligned}
\mathbf{F}_{iI} \mathbf{F}_{jJ} \mathbf{F}_{kK} \mathbf{F}_{lL} \left(\mathbf{C}^{-1} \otimes \frac{\partial \tilde{W}}{\partial \tilde{\mathbf{C}}} \right)_{IJKL} &= \mathbf{F}_{iI} \mathbf{F}_{jJ} \mathbf{F}_{kK} \mathbf{F}_{lL} \mathbf{C}_{IJ}^{-1} \left(\frac{\partial \tilde{W}}{\partial \tilde{\mathbf{C}}} \right)_{KL} \\
&= \mathbf{F}_{iI} \mathbf{F}_{jJ} \mathbf{F}_{kK} \mathbf{F}_{lL} \mathbf{F}_{IM}^{-1} \mathbf{F}_{JM}^{-1} \left(\frac{\partial \tilde{W}}{\partial \tilde{\mathbf{C}}} \right)_{KL} = \mathbf{F}_{kK} \mathbf{F}_{lL} \delta_{iM} \delta_{jM} \left(\frac{\partial \tilde{W}}{\partial \tilde{\mathbf{C}}} \right)_{KL} \\
&= \delta_{ij} \mathbf{F}_{kK} \mathbf{F}_{lL} \left(\frac{\partial \tilde{W}}{\partial \tilde{\mathbf{C}}} \right)_{KL} = \left(\mathbf{I} \otimes \mathbf{F} \frac{\partial \tilde{W}}{\partial \tilde{\mathbf{C}}} \mathbf{F}^{\mathbf{T}} \right)_{ijkl} \\
&\Rightarrow (\mathbf{F} \underline{\otimes} \mathbf{F}) : \mathbf{C}^{-1} \otimes \frac{\partial \tilde{W}}{\partial \tilde{\mathbf{C}}} : \left(\mathbf{F}^{\mathbf{T}} \underline{\otimes} \mathbf{F}^{\mathbf{T}} \right) = \mathbf{I} \otimes \mathbf{F} \frac{\partial \tilde{W}}{\partial \tilde{\mathbf{C}}} \mathbf{F}^{\mathbf{T}}
\end{aligned}
$$

$$(4.4.35)$$

Finally, we can express the spatial elasticity tensor $\mathbb{C}$ as

$$
\boxed{
\begin{aligned}
\mathbb{C} = {}& p(\mathbf{I} \otimes \mathbf{I} - 2\mathbb{S}) - \frac{2}{3}\left[\mathbf{I} \otimes \mathbb{P} : \boldsymbol{\sigma} + \mathbb{P} : \boldsymbol{\sigma} \otimes \mathbf{I} \right] \\
& + \frac{4}{3J} \left(\frac{\partial \tilde{W}}{\partial \tilde{\mathbf{C}}} : \tilde{\mathbf{C}} \right) \left(\mathbb{S} - \frac{1}{3} \mathbf{I} \otimes \mathbf{I} \right) \\
& + \frac{4}{J} \left(\tilde{\mathbf{F}} \underline{\otimes} \tilde{\mathbf{F}} \right) : \frac{\partial^2 \tilde{W}}{\partial \tilde{\mathbf{C}} \partial \tilde{\mathbf{C}}} : \left(\tilde{\mathbf{F}}^{\mathbf{T}} \underline{\otimes} \tilde{\mathbf{F}}^{\mathbf{T}} \right) \\
& - \frac{4}{3J} \left[\tilde{\mathbf{F}} \cdot \left(\frac{\partial^2 \tilde{W}}{\partial \tilde{\mathbf{C}} \partial \tilde{\mathbf{C}}} : \tilde{\mathbf{C}} \right) \cdot \tilde{\mathbf{F}}^{\mathbf{T}} \otimes \mathbf{I} + \mathbf{I} \otimes \tilde{\mathbf{F}} \cdot \left(\frac{\partial^2 \tilde{W}}{\partial \tilde{\mathbf{C}} \partial \tilde{\mathbf{C}}} : \tilde{\mathbf{C}} \right) \cdot \tilde{\mathbf{F}}^{\mathbf{T}} \right] \\
& + \frac{4}{9J} \left(\tilde{\mathbf{C}} : \frac{\partial^2 \tilde{W}}{\partial \tilde{\mathbf{C}} \partial \tilde{\mathbf{C}}} : \tilde{\mathbf{C}} \right) \mathbf{I} \otimes \mathbf{I}
\end{aligned}
}
$$

$$(4.4.36)$$

where $\mathbb{P}$ is the spatial projection tensor ($\mathbb{P} = \mathbb{I} - \dfrac{1}{3}\mathbf{I} \otimes \mathbf{I}$), which, when applied to a 2nd

order tensor, extracts its deviatoric component (Holzapfel 2000).

The terms needed for the spatial elasticity tensor are expressed as follows

$$\frac{\partial \tilde{W}}{\partial \tilde{\mathbf{C}}} : \tilde{\mathbf{C}} = \tilde{\mathbf{F}} \cdot \frac{\partial \tilde{W}}{\partial \tilde{\mathbf{C}}} \cdot \tilde{\mathbf{F}}^{\mathbf{T}} : \mathbf{I} = c_1 \tilde{I}_1 + \int\limits_{\theta_p - \pi/2}^{\theta_p + \pi/2} P(\theta, k) \tilde{W}_4(\theta) \tilde{I}_4(\theta) d\theta \qquad (4.4.37)$$

$$\frac{\partial^2 \tilde{W}}{\partial \tilde{\mathbf{C}} \partial \tilde{\mathbf{C}}} = \int\limits_{\theta_p - \pi/2}^{\theta_p + \pi/2} P(\theta, k) \tilde{W}_{44}(\theta) \mathbf{a_0}(\theta) \otimes \mathbf{a_0}(\theta) \otimes \mathbf{a_0}(\theta) \otimes \mathbf{a_0}(\theta) d\theta \qquad (4.4.38)$$

$$\tilde{\mathbf{F}} \cdot \left(\frac{\partial^2 \tilde{W}}{\partial \tilde{\mathbf{C}} \partial \tilde{\mathbf{C}}} : \tilde{\mathbf{C}} \right) \cdot \tilde{\mathbf{F}}^{\mathbf{T}} = \int\limits_{\theta_p - \pi/2}^{\theta_p + \pi/2} P(\theta, k) \tilde{W}_{44}(\theta) \tilde{I}_4^2(\theta) \mathbf{a}(\theta) \otimes \mathbf{a}(\theta) d\theta \qquad (4.4.39)$$

$$\tilde{\mathbf{C}} : \frac{\partial^2 \tilde{W}}{\partial \tilde{\mathbf{C}} \partial \tilde{\mathbf{C}}} : \tilde{\mathbf{C}} = \int\limits_{\theta_p - \pi/2}^{\theta_p + \pi/2} P(\theta, k) \tilde{W}_{44}(\theta) \tilde{I}_4^2(\theta) d\theta \qquad (4.4.40)$$

$$\left(\tilde{\mathbf{F}} \underline{\otimes} \tilde{\mathbf{F}} \right) : \frac{\partial^2 \tilde{W}}{\partial \tilde{\mathbf{C}} \partial \tilde{\mathbf{C}}} : \left(\tilde{\mathbf{F}}^{\mathbf{T}} \underline{\otimes} \tilde{\mathbf{F}}^{\mathbf{T}} \right)$$

$$= \int\limits_{\theta_p - \pi/2}^{\theta_p + \pi/2} P(\theta, k) \tilde{I}_4^2 \tilde{W}_{44}(\theta) \mathbf{a}(\theta) \otimes \mathbf{a}(\theta) \otimes \mathbf{a}(\theta) \otimes \mathbf{a}(\theta) d\theta \qquad (4.4.41)$$

where $\tilde{W}_{44}$ is calculated from Eqn (4.4.13) as

$$\tilde{W}_{44}(\theta) = \frac{\partial^2 \tilde{W}_{fiber} \circ \tilde{I}_4(\theta)}{\partial \tilde{I}_4(\theta) \partial \tilde{I}_4(\theta)}$$

$$= \frac{1}{4\tilde{\lambda}^3(\theta)} \left[e^{c_4 (\tilde{\lambda}(\theta) - 1)} \left(c_3 c_4 - \frac{c_3}{\tilde{\lambda}(\theta)} - 1 \right) + \frac{c_3}{\tilde{\lambda}(\theta)} + 1 \right] \qquad (4.4.42)$$

The 2nd Piola-Kirchhoff stress tensor from Eqn (4.4.15), the Cauchy stress tensor from Eqn (4.4.19) and the spatial elasticity tensor from Eqn (4.4.36) are the three tensors that were implemented within Nike3d.

4.5. Numerical Considerations

Each integral $\int_{\theta_p - \pi/2}^{\theta_p + \pi/2} (\bullet) d\theta$, present in both stress and elasticity tensors (see previously and Appendixes A & B), was calculated numerically with a ten-points Gaussian quadrature rule applied to each of twelve equally-divided intervals between $\theta_p - \pi/2$ and $\theta_p + \pi/2$. For a large k value (typically $k > 20$), the statistical distribution function is highly concentrated in its preferred orientation θ_p. Therefore, the method was applied to the interval $\left[\theta_p - 12/\sqrt{4k}, \ \theta_p + 12/\sqrt{4k}\right]$ in order to obtain a better accuracy for the numerical integration. Notice that for large k values, the semi-circular version of the Von-Mises distribution converges to the Gaussian distribution with standard deviation $\sigma = 1/\sqrt{4k}$, i.e.

$$P(\theta) \underset{k \gg 1}{\sim} \frac{1}{\sigma\sqrt{2\pi}} e^{-\frac{(\theta - \theta_p)^2}{2\sigma^2}}, \quad \sigma = 1/\sqrt{4k}. \tag{4.5.1}$$

4.6. Model Verification

In order to verify the numerical accuracy of our constitutive model, a biaxial extension test was simulated on an 8-noded hexahedral element and results were compared to analytical solutions for varying levels of k (Figure 4.6.1.). The strain energy function was chosen from Eq. (4.4.5) and the model parameters were defined as ($c_1 = 10$ Pa, $c_3 = 50$ Pa, $c_4 = 5$, $K = 10^6$ Pa), where K is the scleral bulk modulus.

Biaxial Extension Test
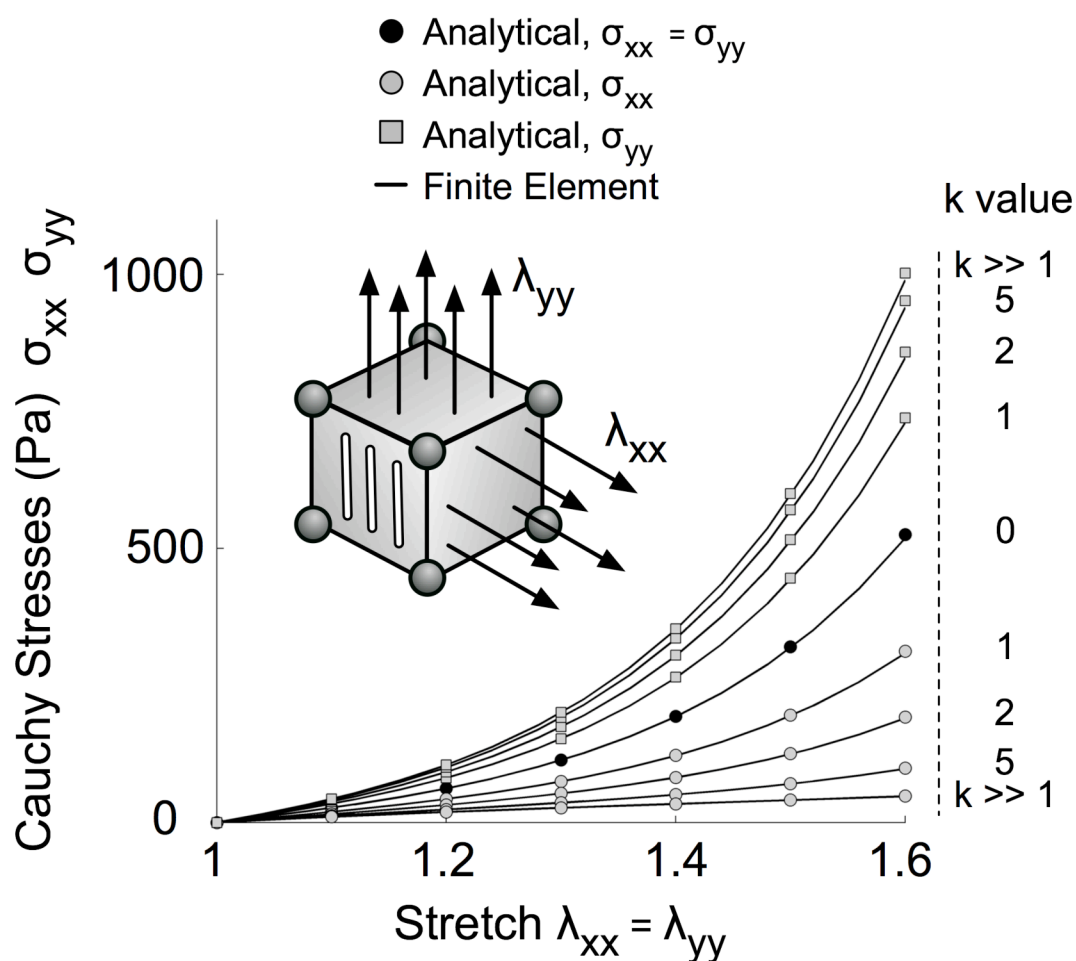
Figure 4.6.1. Model verification for a biaxial extension test on an 8-noded hexahedral element where symmetry conditions were applied. Here, the preferred fiber orientation is aligned along the y-axis and collagen fibers are confined within the xy-plane. When the fiber concentration factor k is equal to zero (isotropy in the xy-plane), Cauchy stresses in x- and y-directions are equal, for both the analytical and finite element solutions. When the fiber concentration factor is large ($k \gg 1$), the sclera behave like a transversely isotropic material. Notice the good agreement between the analytical and finite element solutions.

Figure 4.6.1. demonstrates the excellent agreement between the analytical solutions and

the FE simulations. When the fiber concentration factor k is equal to zero, the collagen

fibers are unorganized and their orientations are random, which corresponds to isotropy

in the xy-plane. Therefore, in Figure 4.6.1., the stresses along the two loading directions (x and y) are identical and nonlinear. As k increases, we observe higher stresses along the y-axis – the axis associated with the preferred fiber orientation. Finally, when k is large, the model exhibits transversely isotropic behavior. In this case the stress reaches its maximum along the preferred fiber orientation (y), whereas the stress is minimum and linear along the second loading direction (x). Note that for $k = \infty$, the statistical distribution function of Eq. (4.3.5) becomes a Dirac delta function

$$P(\theta) \underset{k=\infty}{\sim} \delta(\theta - \theta_p), \tag{4.6.1}$$

which has the following property

$$\int_{\theta_p - \pi/2}^{\theta_p + \pi/2} \delta(\theta - \theta_p) f(\theta) d\theta = f(\theta_p), \tag{4.6.2}$$

where f is any continuous function on the interval $\left[\theta_p - \pi/2, \theta_p + \pi/2\right]$. Accordingly, the isochoric part of the strain energy function (Eq. (4.4.5)) is now that of a transversely isotropic material (Weiss *et al.* 1996), which can be written as

$$\tilde{W} = c_1\left(\tilde{I}_1 - 3\right) + \tilde{W}_{fiber} \circ \tilde{I}_4\left(\theta_p\right) \tag{4.6.3}$$

4.7. Effects of Scleral Collagen Fiber Alignment on Scleral and Optic Nerve Head Mechanics

To investigate the effects of scleral collagen fiber alignment on scleral and ONH mechanics, an idealized FE model of the posterior half of the eye was constructed. The posterior sclera was assumed to be a half-sphere with a radius of 10 mm and a constant thickness of 0.5 mm. The scleral canal was circular with a radius of 0.8 mm. The fiber

orientation was defined such that $\theta_p = 0°$ represents the circumferential orientation (*i.e.*

tangent to the scleral canal boundary) and $\theta_p = 90°$ the meridional orientation (*i.e.*

perpendicular to the scleral canal boundary) as shown in Figure 4.7.1.
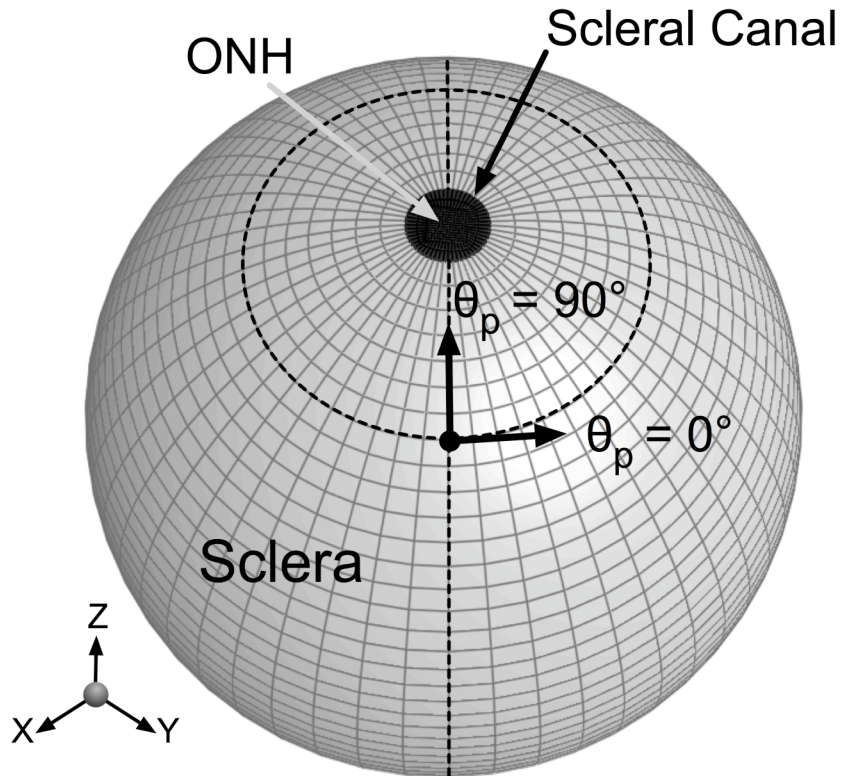
Figure 4.7.1 An idealized FE model of the posterior hemisphere of an eye. The fiber orientation was defined such that θ_p = 0° represents the circumferential orientation (*i.e.* preferred fiber orientation tangent to the scleral canal boundary) and θ_p = 90° the meridional orientation (*i.e.* preferred fiber orientation perpendicular to the scleral canal boundary). The ONH is considered as the posterior hemisphere's pole, which includes the lamina cribrosa and retinal ganglion cell axons.

 Only the fiber alignment parameters (k and θ_p) were allowed to vary, whereas the other

parameters were fixed for all analyses ($c_1 = 100$ kPa , $c_3 = 5$ kPa , $c_4 = 500$,

, $K = 0.1$ GPa), which are typical values for monkey posterior sclera (see Chapter 5).

The ONH was modeled as an incompressible, linear isotropic material with an elastic

modulus fixed to 0.3 MPa (Sigal *et al.* 2005). The nodes at the equator were constrained in all three directions to maintain consistency with the experimental protocol in Chapter 5, and IOP was applied to the inner surface of the shell, then increased from 0 to 45 mm Hg.

We defined four quantities as outputs in order to understand the impact of collagen fiber alignment on scleral and ONH mechanics (Figure 4.7.2.). Scleral canal expansion was the percentage change in scleral canal radius. Scleral canal twist was the amount of rotation that the scleral canal undergoes from its undeformed to its deformed configuration. Posterior laminar deformation was the difference in z-displacements between the center of the ONH and the edge of the scleral canal (posterior surface). Finally, the posterior z-displacement of the scleral canal was also examined.

We chose the following eleven values for the fiber concentration factor k : [0, 0.5, 1, 1.5, 2, 2.5, 3, 3.5, 4, 4.5, 5], and the following ten values for the preferred fiber orientation θ_p : [0, 10, 20, 30, 40, 50, 60, 70, 80, 90]. Therefore, a total of 110 ($= 11 \times 10$) FE runs was performed to assess the effects of collagen fiber alignment on scleral and ONH mechanics.
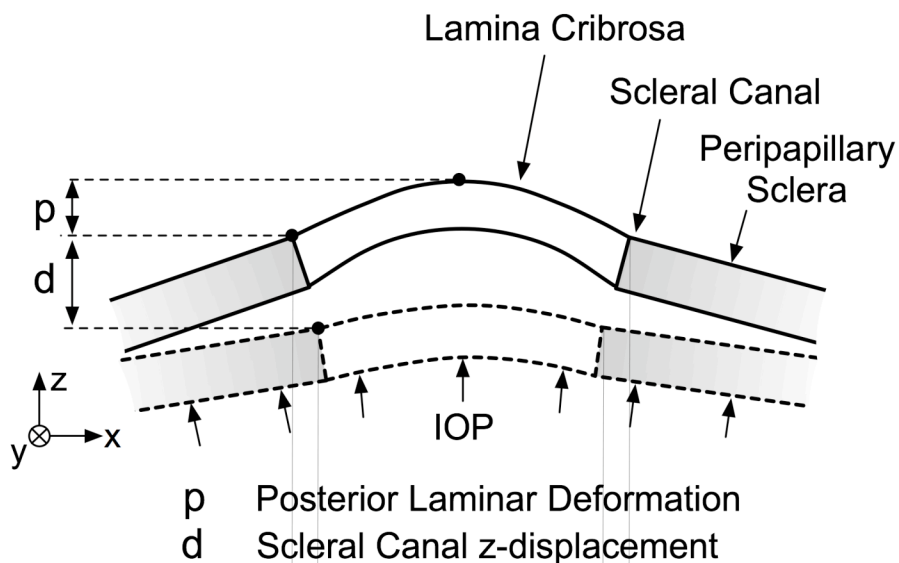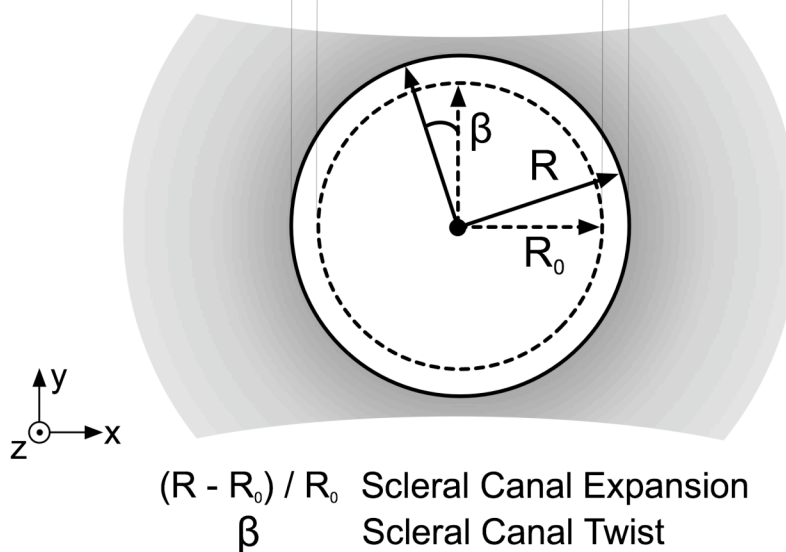
Figure 4.7.2. Schematics of the scleral canal and the ONH in the undeformed and deformed configurations to explain how the four output values were calculated. The four output values considered are scleral canal expansion, scleral canal twist, posterior laminar deformation and scleral canal z-displacement.

Figure 4.7.3. illustrates the effects of collagen fiber alignment on scleral canal expansion and posterior laminar deformation. Small canal expansion occurs when $\theta_p = 0°$, which is associated with large posterior laminar deformation. Conversely, large canal expansion occurs when $\theta_p = 90°$, which is associated with small posterior laminar deformation. It is also observed from Figure 4.7.3. that the fiber concentration factor k acts as an amplifying parameter on the two considered outputs.
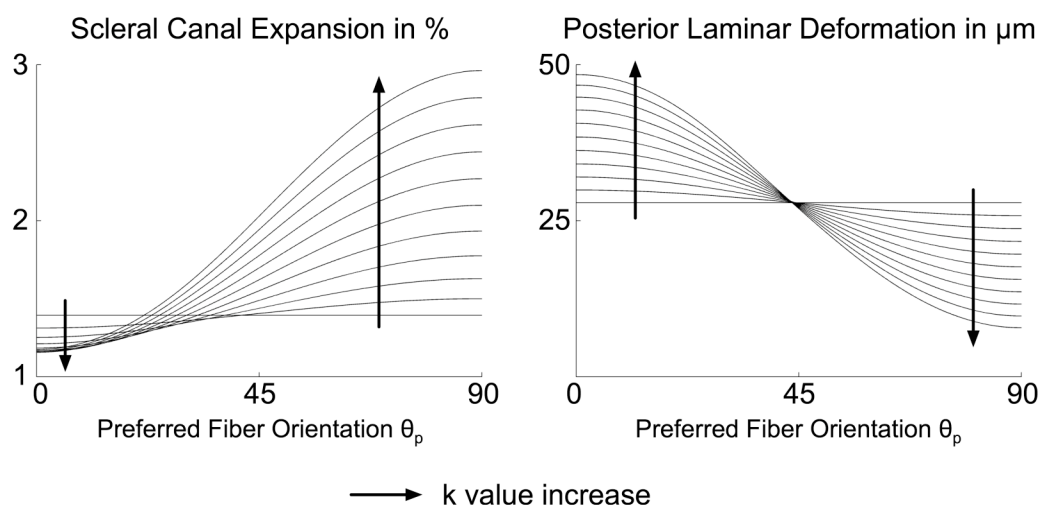
Figure 4.7.3. Effects of the preferred fiber orientation θ_p and fiber concentration factor k on scleral canal expansion and posterior laminar deformation at 45 mm Hg. Each curve has a specific k value, which ranges from 0 to 5 in increments of 0.5.

Figure 4.7.4. illustrates the effects of collagen fiber alignment on scleral canal twist and posterior z-displacement. The maximum amount of scleral canal twist is observed when $\theta_p = 45°$ and increases with the fiber concentration factor k. The maximum posterior z-displacement of the scleral canal occurs when $\theta_p = 0°$ and $k = 5$. In this case, the sclera is reinforced with concentric rings of fibers around the ONH, and the orientation of the maximum principal strains is perpendicular to the scleral canal wall

(not shown), which causes the spherically-shaped sclera to deform into an ellipsoid. For $\theta_p > 45°$, the scleral canal starts to move anteriorly (z-direction), which is especially evident when $\theta_p = 90°$ and $k = 5$. In this case, the orientation of the maximum principal strains is tangent to the scleral canal wall (not shown) and the scleral shell bulges in the mid-periphery, which causes anterior movement of the ONH. For both output values shown in Figure 4.7.4., the fiber concentration factor k also acts as an amplifying parameter, and the effects become more significant for larger k values.
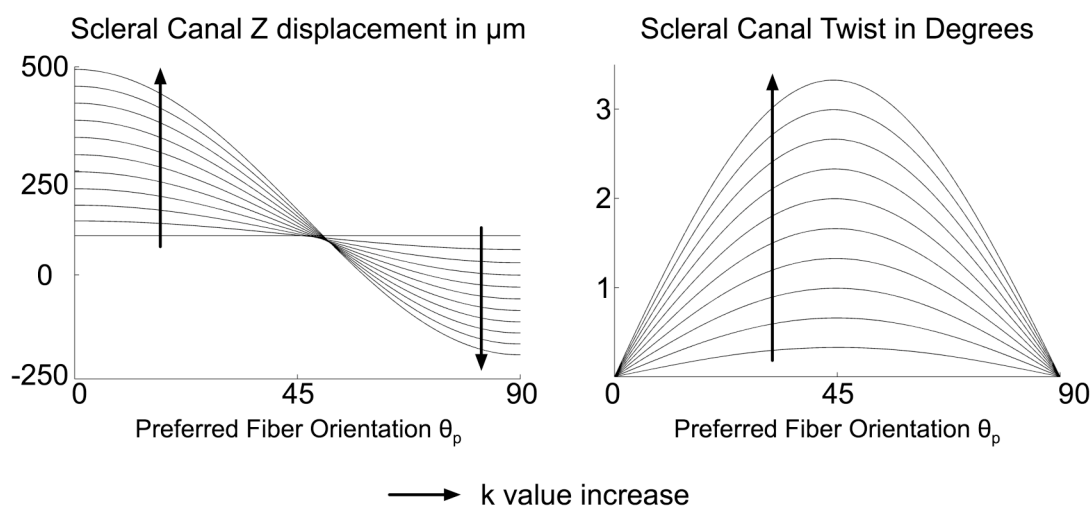
Figure 4.7.4. Effects of the preferred fiber orientation θ_p and fiber concentration factor k on scleral canal z-displacement and scleral canal twist at 45 mm Hg. Each curve has a specific k value, which ranges form 0 to 5 in increments of 0.5.

Finally, deformed scleral shapes can be observed in Figure 4.7.5. for the following three idealized cases ($\theta_p = 0°$, $\theta_p = 45°$, $\theta_p = 90°$) where the fiber concentration factor k was equal to five, to accentuate the scleral deformation patterns.

Idealized Collagen Fiber Alignment (Top View)

Circumferential $\theta_p = 0°$ Helicoidal $\theta_p = 45°$ Meridional $\theta_p = 90°$

Scleral deformation pattern due to IOP increase
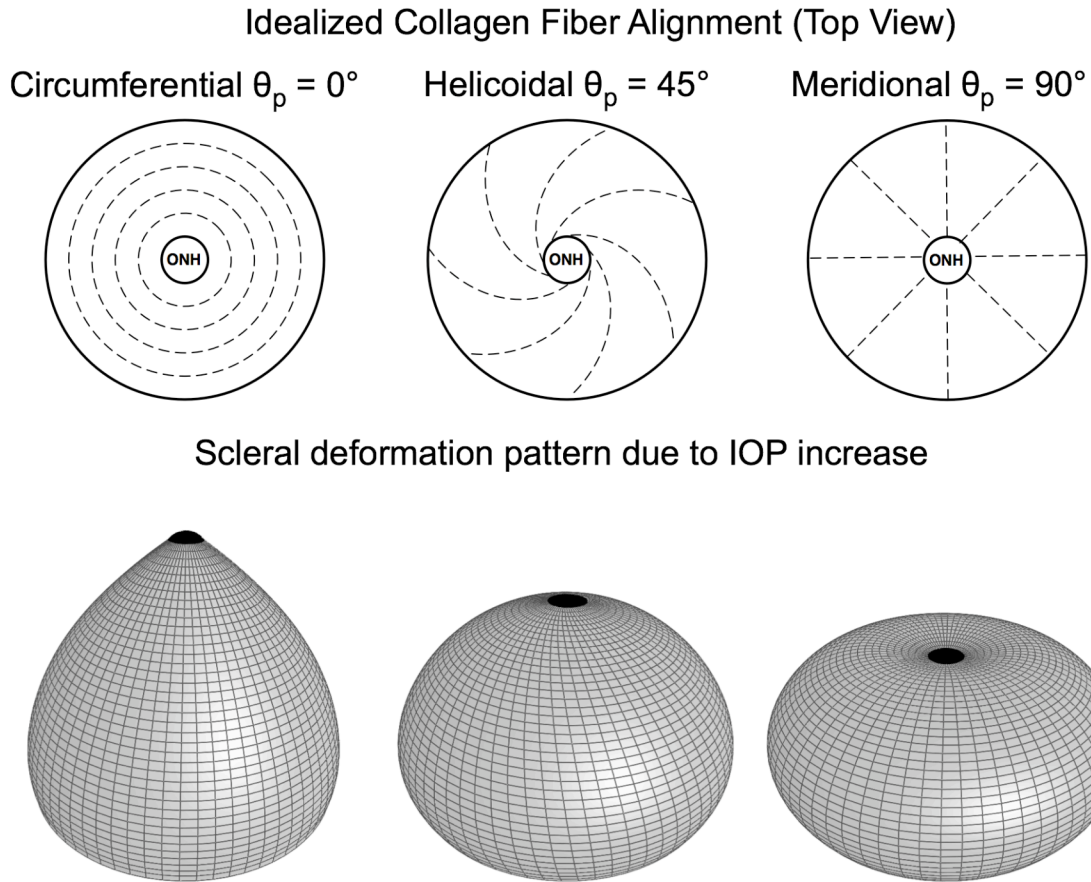
Figure 4.7.5. Effects of the preferred fiber orientation θ_p under acute elevation of IOP. Scleral deformations were displayed for three idealized cases with $\theta_p = 0°$, $\theta_p = 45°$ and $\theta_p = 90°$, respectively. The fiber concentration factor k was equal to five for all three cases, and deformations were exaggerated ten times to emphasize the scleral deformation patterns observed.

4.8. Discussion

In this chapter, an anisotropic hyperelastic constitutive model is presented that can be applied to ocular soft tissues and is especially suitable for the posterior sclera. A new model parameter, the fiber concentration factor k, along with a statistical fiber distribution function, were implemented. k can be considered as an amplifying

parameter for the scleral deformations. To gain a basic knowledge of the constitutive model behavior, effects of the collagen fiber alignment and distribution on scleral deformations due to acute elevations of IOP were analyzed for an idealized posterior scleral shell. Results showed that the observed patterns of the scleral deformation are complex and very different from those of the linear isotropic theory.

Constitutive equations are fundamental to specify the mechanical properties of materials based upon their internal constitution (Holzapfel 2000). The sclera has often been described as a thin-wall pressure vessel, which obeys the analytical constitutive equation known as Laplace's law (Cahane and Bartov 1992). Laplace's law provides a gross estimation of the state of stress within the sclera, because this equation is only valid for isotropic spherical vessels and does not take into account the discontinuity that exists within the sclera due to the presence of the scleral canal.

Current material descriptions for the sclera are simplistic without emphasizing the ultrastructure of the tissue, which, however, can significantly influence the overall tissue behavior under acute elevation of IOP, as observed with our idealized spherical sclera. Several investigators have realized the importance of deriving fiber-based theories for anisotropic biological soft tissues (Ault and Hoffman 1992; Weiss *et al.* 1996; Holzapfel *et al.* 2000; Driessen *et al.* 2003) because most of them are composed of various fiber families. These models are strain energy-based, meaning that stresses are derived from a potential function, and rely on a mechanical theory known as fiber-reinforced composite theory (Spencer 1974).

In this study, we simulated the mechanical behavior of a spherical posterior sclera, with an idealized collagen fiber organization. Although this combination of

idealized geometry and fiber alignment is not physiologic, it is clear from these idealized models that the collagen fiber orientation in the sclera has a large impact on the IOP-induced deformations imparted to the contained ONH. We have previously suggested that the circular arrangement of collagen fibers within the peripapillary sclera could provide a protective mechanism of a more delicate lamina cribrosa which spans the scleral canal (Girard *et al.* 2008). The current model simulations demonstrate that a circular arrangement of collagen fibers significantly limits scleral canal expansion, accompanied by a simultaneous increase in posterior laminar deformation. Whether scleral canal expansion or posterior laminar deformation induce ONH damage in glaucoma remains unknown. Future clinical measurements of those quantities in response to acute IOP elevations will provide more insight into the mechanisms of glaucomatous damage.

Scleral canal twist was also estimated from the model simulations, and is created when $0° < \theta_p < 90°$ and $k \neq 0$. It reaches its maximum for the very specific case of $\theta_p = 45°$, where collagen fibers are running in a helicoidal manner from the eye equator to the ONH pole as shown in Figure 4.7.5. While the magnitude of scleral canal twist shown here may not be physiological, this twisting feature can add complexity to the mechanical behavior of the scleral shell and could be a factor in ONH damage, but this question remains open.

The final output measure that was considered was the posterior z-displacement of the scleral canal. Our models showed that if the sclera is reinforced with fibers running tangent to the scleral canal the scleral canal deforms posteriorly (Figure 4.7.5.), whereas if the fibers are oriented perpendicular to the canal, the canal is anteriorly displaced. This behavior is interesting as it relates to myopia (Greene 1980), in which the sclera

undergoes a large degree of permanent stretching along the anterior/posterior axis.

Several important points warrant further discussions in terms of the difference between the current model and Weiss' previous model for ligaments (Weiss *et al.* 1996). In the later, the behavior of the collagen fibers was described with a total of four independent model parameters: two for the initial nonlinear toe-region (c_3, c_4), one for the upper stretch limit of the toe-region, and one for the slope of the subsequent linear region. As shown in our previous study (Girard *et al.* 2008), porcine posterior sclera exhibits a high degree of nonlinearity for IOPs ranging from 5 to 45 mm Hg, and this behavior has been translated into our constitutive model with a two-parameter fiber strain energy function. Hence, we chose to limit our implementation of fiber nonlinearity to the toe-region to minimize the number of model parameters in our constitutive model, because the sclera is usually subjected to a much lower strain environment than that of tendons and ligaments. The appropriateness of this specification will be confirmed in Chapter 5, wherein we compare model predictions to experimental measurements of scleral deformations.

Additionally, in Weiss implementation, the strain energy function associated with the collagen fibers was chosen to be zero when the fiber stretched was inferior to one. This translates the fact that collagen fibers do not support compressive loads along their long axes, as they tend to buckle under compression. This feature was not considered in our current implementation, mainly because the sclera is a load-bearing structure that essentially behaves in tension with IOP increase.

The two main types of extracellular protein fibers in the sclera are elastin and collagen. Because collagen is organized into long and dense fibrous bundles, but elastin

is organized in "noodle-like" cross-linked coil, it is often common to treat collagen as the only fiber family, as it is thought to be the primary source for tensile strength under acute elevation of IOP. Although, it is well known that elastin fibers are highly present in the peripapillary sclera (Hernandez *et al.* 1987; Quigley *et al.* 1991), which is in close contact with the ONH, our preliminary implementation of anisotropic hyperelasticity did not consider elastin as a separate fiber family for simplicity. A more detailed constitutive model that treats scleral elastin as a separate entity, will eventually become available with our increased knowledge on scleral microstructure.

Our models depict the scleral canal as the center of the posterior scleral shell whereas in most eyes the physiologic center of the posterior globe is the fovea. The fovea is the target structure of the visual axis, contains the greatest density of light-sensitive cells (*i.e.* photoreceptors), and is responsible for the eye's sharpest vision. In most monkey and human eyes, the scleral canal is located 3 to 4 mm away from the fovea along the horizontal midline in the nasal hemisphere of the eye (Levin 2003). For this initial study, we have chosen to locate the scleral canal in the center of the posterior globe to simplify the problem and to establish an initial understanding of the constitutive model presented herein. These initial models concentrate on the effects of scleral mechanical properties, geometry, and collagen fiber organization on the behavior of the sclera and ONH. Because the physiologic shape of the posterior globe and the location of the scleral canal relative to its center may importantly contribute to these behaviors, future models will take these features into consideration.

Modeling and mechanical testing of ocular soft tissues will contribute to our understanding of ONH and peripapillary scleral damage in glaucoma, myopia, and a host

of other ocular disorders. The knowledge gained in this study using our proposed hyperelastic constitutive model will now be used in Chapter 5 to estimate the mechanical properties of monkey posterior sclera.

5 Experimental and Inverse Finite Element Characterization of Scleral Biomechanics[1]

5.1. Abstract

The posterior sclera likely plays an important role in the development of glaucoma and accurate characterization of its mechanical properties is needed to understand its impact on the more delicate optic nerve head – the primary site of damage in the disease. The posterior scleral shells from both eyes of one rhesus monkey were individually mounted on a custom-built pressurization apparatus. Intraocular pressure was incrementally increased from 5 to 45 mm Hg, and the 3-D displacements were measured using electronic speckle pattern interferometry. Finite element meshes of each posterior scleral shell were reconstructed from data generated by a 3D digitizer arm (topography) and a 20 MHz ultrasound transducer (thickness). An anisotropic hyperelastic constitutive model described in Chapter 4, which includes stretch-induced stiffening and multi-directional alignment of the collagen fibers, was applied to each reconstructed mesh. Surface node displacements of each model were fitted to the

experimental displacements using an inverse finite element method, which estimated a unique set of thirteen model parameters. The predictions of the proposed constitutive model matched the 3-D experimental displacements well. In both eyes, the tangent modulus increased dramatically with IOP, which indicates that the sclera is mechanically nonlinear. The sclera adjacent to the optic nerve head, known as the peripapillary sclera, was thickest and exhibited the lowest tangent modulus, which might have contributed to the uniform distribution of the structural stiffness for each entire scleral shell. Posterior scleral deformation following acute IOP elevations appears to be nonlinear and governed by the underlying scleral collagen microstructure as predicted by finite element modeling. The method will be used to characterize posterior scleral mechanics in normal (young and old), early and moderately glaucomatous monkey eyes (Chapters 6 and 7).

5.2. Introduction

This Chapter, together with Chapter 4, propose a strategy to characterize the mechanical behavior of the posterior sclera under acute elevations of intraocular pressure (IOP). To accurately account for scleral anisotropy, we developed an anisotropic hyperelastic model in Chapter 4, which incorporates multi-directional alignment of the collagen fibers at local material points. Application of this model to anatomically accurate geometry of monkey posterior sclera is presented in this Chapter. Scleral mechanical properties are obtained by fitting the model-predicted displacements to the experimentally-measured displacements using an inverse finite-element method.

In literature, estimations of scleral mechanical properties have been limited to nonlinear isotropic analysis based on relatively crude optical tracking of pressurized

shells (Woo *et al.* 1972) and linear and nonlinear isotropic (elastic and viscoelastic) characterization based on uniaxial testing of scleral strips (Curtin 1969; Friberg and Lace 1988; Phillips and McBrien 1995; Siegwart and Norton 1999; Downs *et al.* 2003; Wollensak and Spoerl 2004; Downs *et al.* 2005; Spoerl *et al.* 2005; Girard *et al.* 2007; Schultz *et al.* 2008; Weiyi *et al.* 2008). While these studies made important contributions to our understanding of scleral mechanics, a more comprehensive approach that characterizes the nonlinear, anisotropic nature of the sclera and its inhomogeneous fibrous ultrastructure is necessary. Because the sclera transmits IOP-related deformations to the optic nerve head (ONH) and is altered in early experimental glaucoma (Downs *et al.* 2005), knowledge of scleral mechanics is essential to evaluate how the tissues of the ONH respond to IOP. This information is vital to developing a clear understanding of the role of IOP in the development and progression of glaucoma – an optic neuropathy caused by retinal ganglion cell axon damage at the ONH (Quigley and Anderson 1976; Quigley and Addicks 1980).

5.3. Experimental Setup and Testing Protocol

Specimen Preparation. One male rhesus monkey (2.1 years old) without any apparent optic abnormality was anesthetized with an intramuscular injection of ketamine/xylazine and sacrificed with an intravenous injection of sodium pentobarbital. After enucleation, both eyes were carefully cleaned of extra-orbital tissues and the posterior sclera was separated from the anterior chamber approximately 3 mm anterior to the equator. After removing the iris and the lens, both anterior chambers were stored in a corneal preservation medium (Optisol GS, Bausch & Lomb, Rochester, NY) and reserved

for future mechanical experiments. The retina and choroid were carefully dissected away from the scleral shell except for a 7-mm diameter patch centered on the ONH, which was left intact to prevent fluid leakage from the ONH during pressurization. All ocular tissues were kept moist with phosphate buffered saline (PBS) throughout specimen preparation.
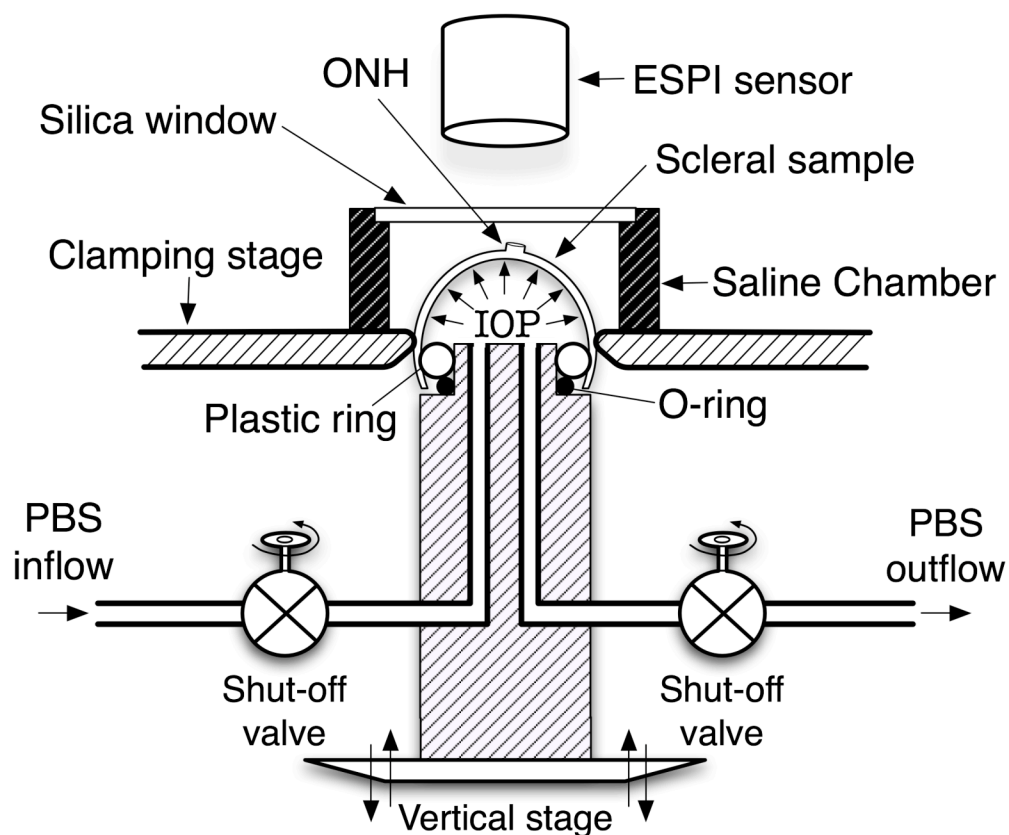
Figure 5.3.1. Schematic showing a cross-section of the custom-built pressurization apparatus. The posterior scleral shell was first mounted onto the plastic ring, then clamped slightly above the equator by moving the vertical stage toward the clamping stage. PBS outflow was interrupted after PBS filled the posterior shell cavity and IOP reached 5 mm Hg. The scleral surface was imaged as IOP was increased from 5 to 45 mm Hg.
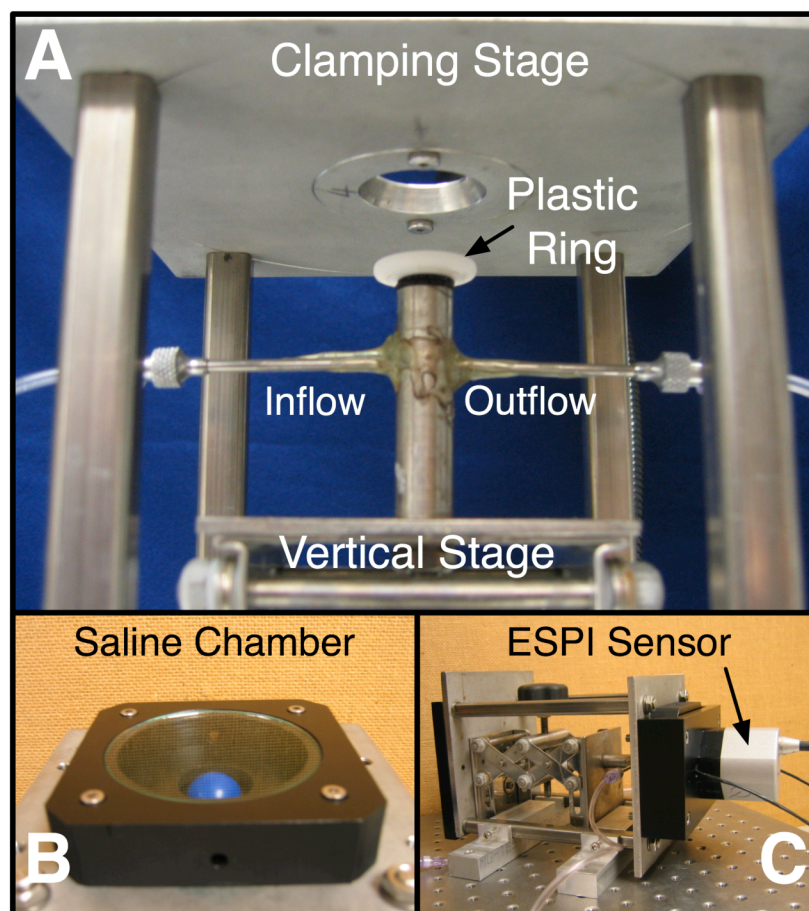
Figure 5.3.2. (A) Photograph of the pressurization apparatus showing the input (PBS inflow) and output (PBS outflow) cannulae, the vertical and clamping stages, and the plastic ring as explained in Figure 5.3.1. **(B)** Photograph of the saline chamber that was mounted on top of a balloon sample (shown in blue), attached to the clamping stage and used to keep the scleral samples hydrated. **(C)** Photograph of the pressurization apparatus showing the ESPI sensor that was positioned above the saline chamber and attached to the clamping stage.

Measurement of Scleral Surface Displacements. The posterior scleral shells from both eyes were individually mounted on a custom-built pressurization apparatus (Figures 5.3.1 and 5.3.2; apparatus adapted from Chapter 3) and internally pressurized using a column of PBS at 22°C. IOP was controlled at a resolution of 0.01 mm Hg by altering the PBS column height with a motor-driven stage (Bislide, Velmex, Bloomfield, NY), and monitored by a digital pressure gauge (X2Pi, Crystal Engineering, San Luis

Obispo, CA). To enhance its optical contrast, each shell surface was blotted dry and treated with white titanium powder (ProCAD Contrast Medium, Ivoclar, Schaan, Lichtenstein) diluted in a 70% ethanol solution. A custom-built chamber was then mounted above the shell and filled with 50 mL of PBS to maintain specimen hydration. The chamber was fabricated with a silica window coated with an anti-reflective film to optimize displacement measurements of the shell surface with an electronic speckle pattern interferometry (ESPI) (Q100, Ettemeyer AG, Germany) sensor (Erne *et al.* 2005). To conduct each experiment, the pressurization apparatus was positioned horizontally as shown in Figure 5.3.2C. This had the advantage of allowing potential air bubbles within the saline chamber to move upward and powder residues within the saline chamber to move downward, thus minimizing noise sources for the ESPI sensor.

Each shell was subjected to IOP preconditioning, consisting of twenty IOP cycles from 5 to 15 mm Hg at a rate of 5 mm Hg per second, and then allowed to recover for 360 seconds. IOP was then increased from 5 to 10 mm Hg in steps of 0.2 mm Hg, from 10 to 30 mm Hg in steps of 0.4 mm Hg, and from 30 to 45 mm Hg in steps of 0.6 mm Hg. Because sclera stiffens with increasing IOP, the IOP step magnitude was increased to keep the resultant displacements within the measurable range of the ESPI sensor. For each IOP step, the ESPI sensor captured laser speckle images over a 35×25 mm^2 area at an equilibrium state. An example of such image is depicted in Figure 5.3.3. Each displacement component (x, y, z) was then computed using speckle image algorithms for each IOP step at a resolution of 0.1 μm, and reported in a 256×256 matrix format that covered the entire measuring area. Finally, each component was summed over the following IOP intervals: 5-7, 5-10, 5-20, 5-30, and 5-45 mm Hg. These IOP intervals

correspond to the physiologic range and were chosen because they are directly comparable to the *in vivo*, image-based ONH compliance testing and perfusion fixation protocols used in our other monkey studies (Bellezza *et al.* 2003; Downs *et al.* 2007). Examples of 3-D displacements using the ESPI sensor are shown in Figure 5.3.3 for a rubber balloon subjected to increasing pressure. 3-D displacements for monkey posterior sclera will be shown in the next sections.
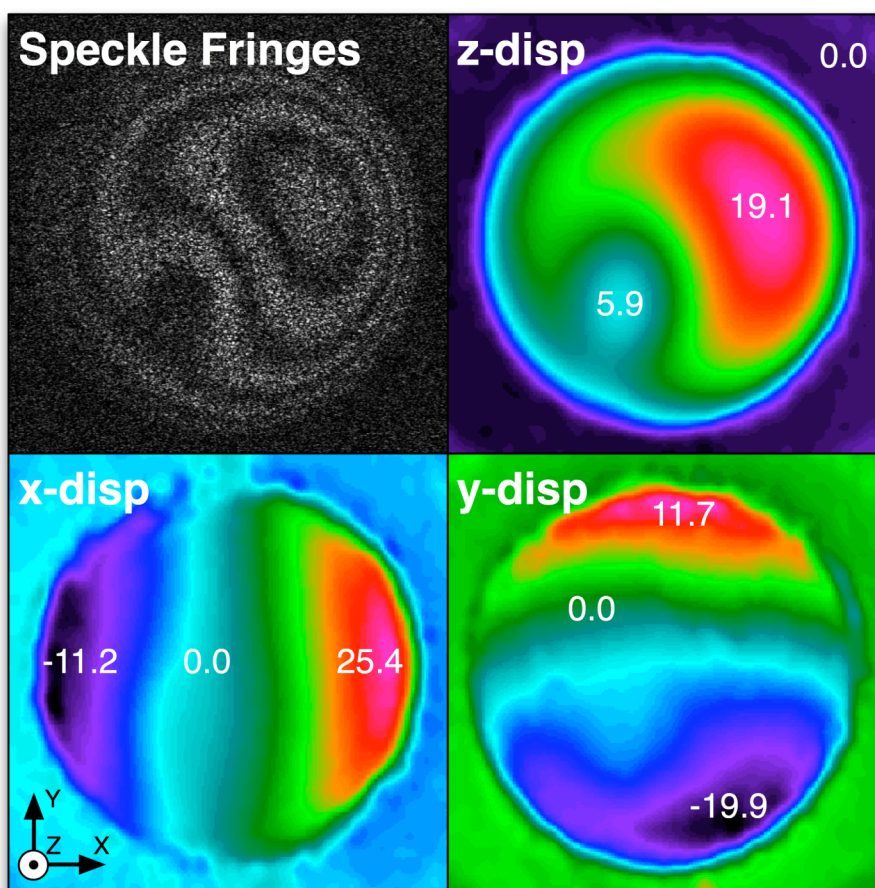
Figure 5.3.3. (Top Left) Example of raw speckle fringes (one of four illumination directions from the ESPI sensor) on a rubber balloon for a pressure increase from 60 to 60.1 mm Hg. The distance between the fringes is proportional to the 3D displacement of the balloon surface. The three other quadrants show the x, y and z components of the 3-D displacement field (in μm) that were extracted using speckle image subtraction and fringe analysis algorithms.

Measurement of Scleral Topography. The following experiment consisted in obtaining the topography of the shell in its reference state (IOP of 5 mm Hg). Once the acquisition of the ESPI images was completed, IOP was lowered from 45 mm Hg to 5 mm Hg, and the shell was allowed to equilibrate. The outer surface geometry of the shell was then manually digitized using a 3-D digitizer arm (MicroScribe G2X, Immersion, San Jose, CA). For each shell, the Cartesian coordinates of one thousand spatial points were recorded to cover the entire scleral surface. The scleral canal and the clamping area were also digitized to provide boundaries for the scleral specimen.

Measurement of Scleral Thickness. Scleral thickness was measured using a 20 MHz ultrasound transducer (PacScan 300P, Sonomed, Inc., Lake Success, NY), combined with a 75 MHz pulser-receiver (5073PR, Olympus NDT, Inc., Waltham, MA) and a 200 MHz digital oscilloscope (TDS2022, Tektronix, Beaverton, OR). This measurement system was able to acquire a minimum thickness of 100 μm at a resolution of 1 μm. Prior to thickness measurements, twenty spatial points were marked on the scleral surface with a fine tip marker (Figure 5.3.4AC) and their Cartesian coordinates were recorded with the 3-D digitizer arm. To enhance acoustic energy reflection at the inner surface of the sclera, the PBS inside the scleral shell was replaced with moist air controlled by a pressure regulator (Model 81, Fairchild, Winston-Salem, NC) and the shell was pressurized to 5 mm Hg. The ultrasound transducer was then positioned perpendicularly to each of the twenty predetermined points and voltage echo signals were collected on the oscilloscope (Figure 5.3.4BD). Scleral thickness, d_i, was calculated at each point according to the following formula

$$d_i = \frac{1}{2} v_{sclera} \cdot t_i, \quad i \in [1,20] \tag{5.3.1}$$

where v_{sclera} is the speed of sound in the sclera, which was set to 1597 m/s (Bereiter-Hahn 1995), and t_i is the echo time, which was determined from the oscilloscope signal (Figure 5.3.4BD). Scleral thickness was calculated for both eyes at each of the twenty predetermined locations and data are shown in Table 5.3.1.
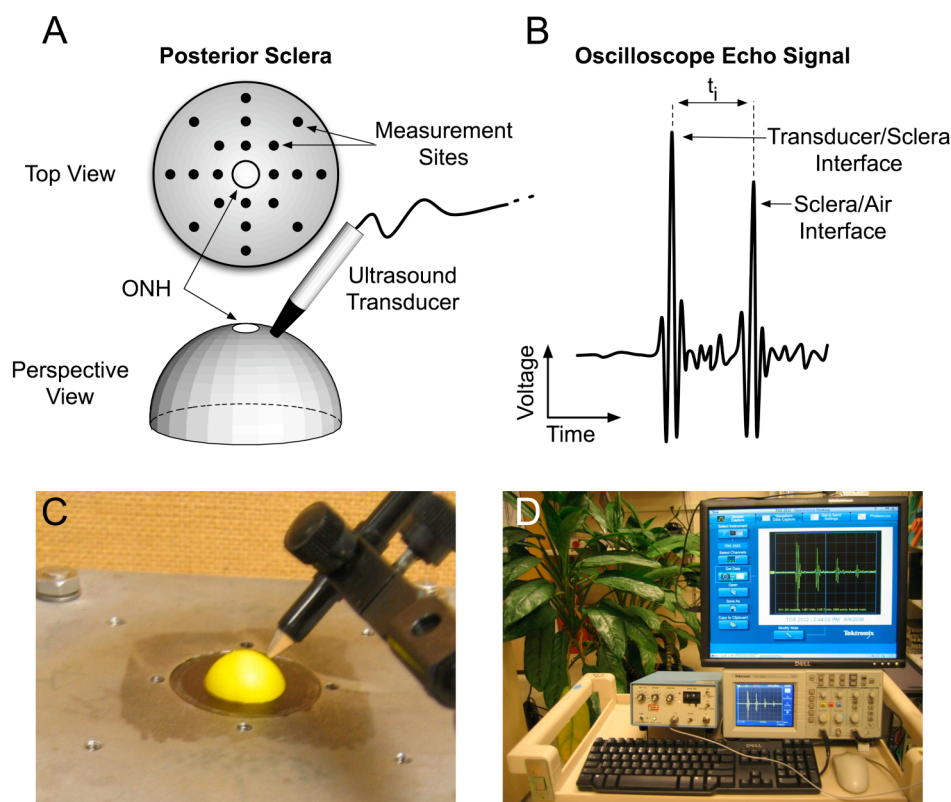
Figure 5.3.4. (A) Location of the twenty thickness measurement sites, shown as black dots on the outer surface of the posterior sclera. For each location, the 20 MHz ultrasound transducer was positioned perpendicularly to the scleral surface, and the corresponding voltage echo signal was recorded in order to extract scleral thickness. **(B)** An example of a voltage echo signal obtained from the oscilloscope for one measurement site. t_i is twice the time taken by an acoustic wave to travel from the transducer/sclera interface to the sclera/air interface. **(C)** Photograph of the ultrasound transducer held by a flexible positioning arm and positioned perpendicularly to the scleral outer surface. **(D)** Photograph of the ultrasound measurement system employed to characterize posterior sclera thickness. The ultrasound transducer was combined with a pulser/receiver (left) and a digital oscilloscope (right). A voltage echo signal is displayed on both the oscilloscope screen and the flat panel monitor.

Region	Right Eye		Left Eye	
	Location	Thickness [μm]	Location	Thickness [μm]
Temporal	1	399	11	372
	2	381	12	218
	3	266	13	205
Superior Temporal	4	484	9	389
	5	272	10	201
Superior	6	458	6	463
	7	398	7	364
	8	225	8	242
Superior Nasal	9	353	4	388
	10	352	5	316
Nasal	11	428	1	522
	12	320	2	290
	13	174	3	288
Inferior Nasal	14	346	19	338
	15	309	20	309
Inferior	16	490	16	425
	17	256	17	302
	18	262	18	209
Inferior Temporal	19	552	14	509
	20	330	15	336

Table 5.3.1. Scleral thickness was calculated at each of the twenty predetermined location for both monkey eyes.

5.4. Finite Element Modeling

Finite Element Mesh. Scleral topography and thickness data were combined to generate a FE mesh of the specimen using the custom-written software Eyemesh, which is fully documented in Appendix B.1. Briefly, the digitized boundaries of the clamp and the scleral canal were fit to a circle and an ellipse, respectively, using a least-square algorithm. The point cloud of the scleral surface was then smoothed using the thin-plate spline method and thickness data were interpolated over the entire scleral surface field. These data were combined to generate a FE mesh with 8-noded hexahedral elements using grid projection methods. The FE mesh was divided into 9 subregions, where regions 1-4 contain the peripheral sclera, regions 5-8 contain the peripapillary sclera, and

region 9 represents the ONH (Figure 5.4.1). A convergence test was performed to assess the numerical accuracy of the FE approximation by increasing the number of nodes. This task was performed with the software Eyemesh by increasing the node density along the meridional, circumferential and transmural directions of the sclera. Adequate numerical accuracy was achieved with 5091 nodes and 3328 elements (Figure 5.4.2).
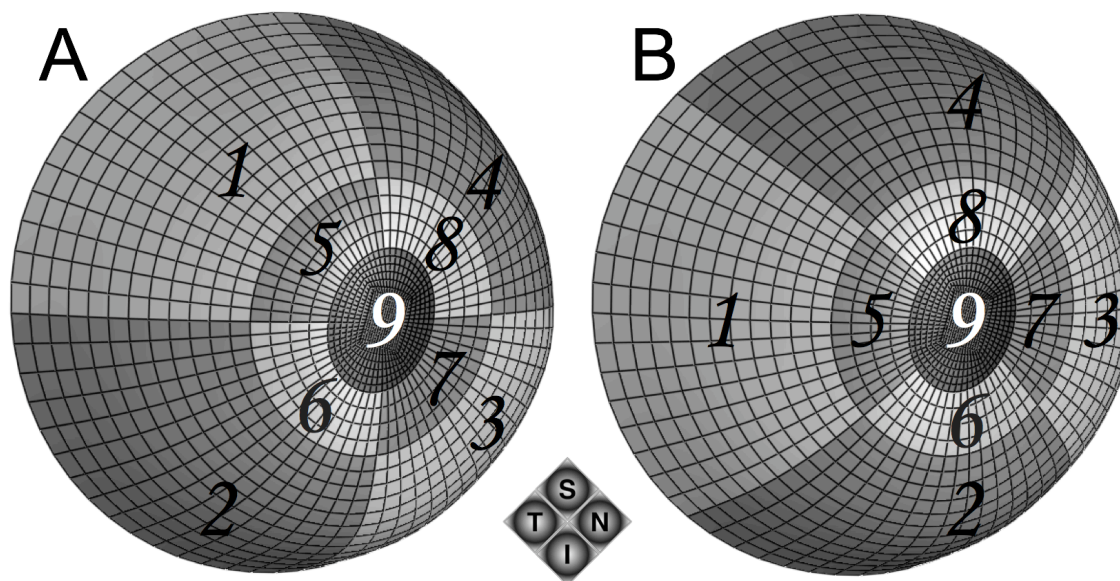
Figure 5.4.1. (A) FE model of the monkey posterior scleral shell of a left eye showing one regionalization pattern. Regions (1-4) are the peripheral sclera, regions (5-8) are the peripapillary sclera, and region (9) is the ONH. **(B)** Same FE mesh as (A), but with a different regionalization pattern. S, superior; N, nasal; I, inferior; T, temporal.
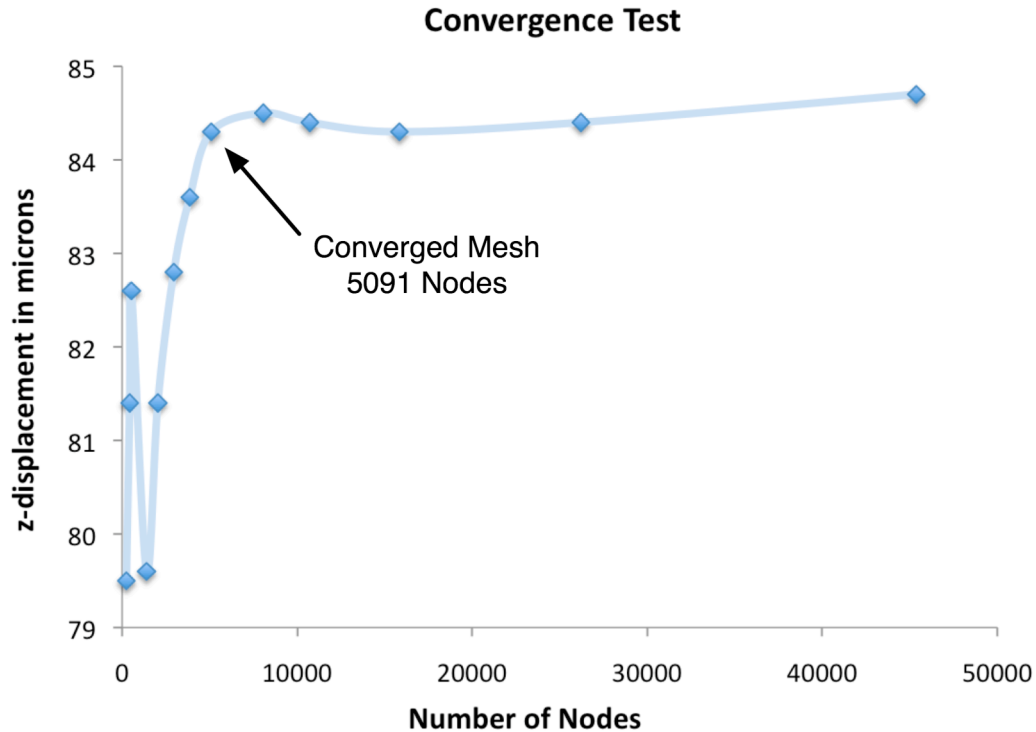
Convergence Test

Figure 5.4.2. A convergence test was performed to estimate the numerical accuracy of the FE approximation. For one eye, the node density of the corresponding FE mesh was increased with the software Eyemesh and FE simulations were performed. The *z*-displacement a node belonging to the scleral canal boundary was tracked and plotted as a function of node density. Adequate numerical accuracy was achieved with 5,091 nodes corresponding to 3,328 elements. Additional convergence tests were performed at other locations within the posterior scleral shell and confirmed this initial finding.

Model Assumptions. In incorporating the fiber-reinforced constitutive theory for ocular soft-tissues developed in Chapter 4 into FE models of the posterior scleral shell, several assumptions were made: 1) The mechanical properties of the collagen fibers are generic and uniform throughout the scleral tissue. 2) The mechanical properties of the ground substance matrix are generic and uniform throughout the scleral tissue. 3) Regional variation in the mechanical response of the scleral shell is principally governed by inhomogeneity of the collagen fiber ultrastructure, which can be quantitatively described using the preferred fiber orientation and the fiber concentration factor. Based on these assumptions, three model parameters (c_1: 1st Mooney-Rivlin coefficient, c_3:

exponential fiber stress coefficient, and c_4: fiber uncrimping coefficient) were uniformly attributed to the entire posterior sclera. Two fiber concentration factors, k_1 and k_2, were attributed to the peripheral sclera (regions 1-4) and peripapillary sclera (regions 5-8), respectively. Individual preferred fiber orientations, θ_{p1} to θ_{p8}, were attributed to each region (Figure 5.4.3). As a consequence, the FE model contained a total number of thirteen model parameters to be determined. In addition, the bulk modulus of the sclera K was fixed at 1 GPa to assure incompressibility, and the ONH was modeled as an incompressible linear isotropic material with an elastic modulus (E_{ONH}) of 1 MPa.
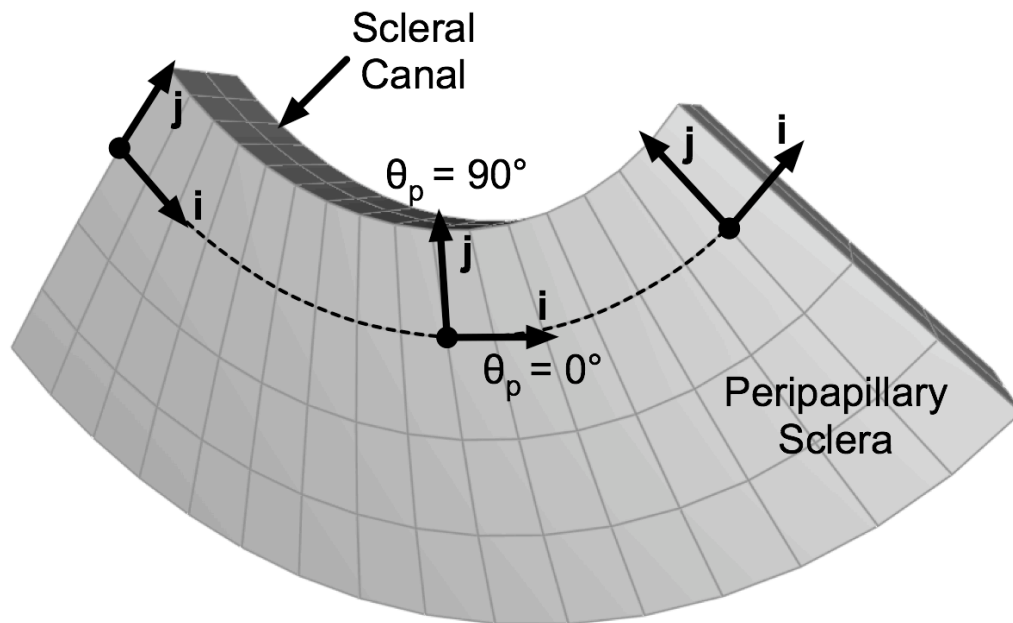
Figure 5.4.3. One sub-region of the peripapillary sclera of a left monkey eye, showing how collagen fiber alignment was defined. For each hexahedral element, the local unit vector **i** was constructed with element edge information. The local unit vector **j** was constructed as being perpendicular to the unit vector **i** and tangent to the scleral surface. Unit vectors **i** and **j** define the plane in which the collagen fibers lie. Although each element of this sub-region share the same preferred fiber orientation θ_p, the unit vector associated with θ_p will be different for each element in the global coordinate system. For example, if the preferred fiber orientation is equal to zero for this sub-region ($\theta_p = 0°$), collagen fibers will be oriented along the unit vector **i** (for $k \neq 0$), corresponding to a circumferential organization.

Boundary and Loading Conditions. For each FE model, IOP was numerically applied to the interior surface of the shell as a uniform pressure load. Nodes belonging to both the peripheral sclera and the clamping boundary were constrained in all three directions in order to maintain consistency with restraints imposed by the clamp in the experimental protocol. For simplicity, the reference geometry generated at 5 mm Hg was assumed to be stress-free.

5.5. Extraction of Scleral Model Parameters: Inverse Finite Element Method

Scleral model parameters were extracted using an inverse FE method, in which an optimization algorithm, *i.e.* differential evolution (Price *et al.* 2005), was coupled with the FE method. The differential evolution algorithm sought to determine the set of thirteen model parameters that yielded the closest match between the FE-simulated and the experimentally-measured displacements. Numerically, the surface node displacements of the FE model were fitted to their colocalized experimental values simultaneously at five IOP levels (7, 10, 20, 30 and 45 mm Hg) by minimizing the following cost function ε :

$$\varepsilon = \frac{1}{N \cdot P} \sum_{n=1}^{N} \sqrt{\sum_{p=1}^{P} \left[\left(x_{n,p}^{e} - x_{n,p}^{m} \right)^2 + \left(y_{n,p}^{e} - y_{n,p}^{m} \right)^2 + \left(z_{n,p}^{e} - z_{n,p}^{m} \right)^2 \right]}. \quad (5.5.1)$$

Here, $\left(x_{n,p}^{e}, y_{n,p}^{e}, z_{n,p}^{e} \right)$ and $\left(x_{n,p}^{m}, y_{n,p}^{m}, z_{n,p}^{m} \right)$ are the three components of the experimental (e) and model (m) displacements, respectively, at surface node n and an IOP level of p; N is the total number of surface nodes and P is the total number of IOP levels. Our preliminary study with the differential algorithm showed that a scale factor F of 0.5, a

crossover probability *CR* of 0.9, and a number of parents *NP* of 50 were well suited for our global optimization problem.

The following initial ranges were used with the differential evolution algorithm for the considered parameters: $0 < c_1 < 1000$ [kPa], $0 < c_3 < 100$ [kPa], $0 < c_4 < 5000$ [-], $0 < (k_1, k_2) < 20$ [-], and $0 < (\theta_{p1},...,\theta_{p8}) < 180$ [°]. Note that the differential evolution algorithm allows the model parameters to evolve beyond their initial ranges, and this was allowed for all model parameters except for the preferred fiber orientations, which were constrained to the range of 0 to 180°.

The inverse FE simulation consisted of 450 iterations of the differential evolution algorithm. Each iteration included 50 FE runs yielding a total of 22,500 ($= 450 \times 50$) FE runs. The simulation was executed on an ION computational server, with 32 GB of RAM and four 64-bit Itanium2 processors (Intel, Santa Clara, CA), using a parallel queuing system written in the script language Perl (The Perl Foundation). One inverse FE simulation typically took two days to obtain full convergence, with each FE run requiring 30 to 50 seconds within Nike3d.

5.6. Measures of Scleral Stiffness

Tangent Modulus. The model parameters c_3 and c_4 as obtained from the inverse FE simulations describe the nonlinearity of the sclera, but do not provide a direct measure of scleral stiffness at each IOP elevations. To provide a relationship between scleral stiffness and IOP, we have isolated components of the spatial elasticity tensor $\mathbb{C}$. In the FE implementation of the constitutive theory, $\mathbb{C}$ was expressed in a fixed global

coordinate system (Chapter 4), and can now be transformed to the local fiber coordinate system as follows

$$\mathbb{C}'_{ijpn} = \mathbf{a}_{iq}\mathbf{a}_{js}\mathbf{a}_{pk}\mathbf{a}_{nm}\mathbb{C}_{qskm} \, , \tag{5.6.1}$$

where $\mathbb{C}'$ is the spatial elasticity tensor in the local fiber coordinate system and $\mathbf{a}$ is the transformation matrix. Accordingly, $\mathbb{C}'_{1111}$ and $\mathbb{C}'_{2222}$ were defined as the tangent moduli along and perpendicular to the preferred fiber orientation, respectively. Both quantities are inhomogeneous, and their directions lie in the plane tangent to the shell surface.

Structural Stiffness. Clinical discussions of the corneo-scleral shell often confuse the effects of its mechanical properties and geometry on its overall mechanical behavior. We therefore attempted to take regional variations in scleral thickness into account by empirically defining the structural stiffnesses S_1 and S_2 at any point in the scleral shell as

$$\begin{aligned} S_1 &= T \cdot \mathbb{C}'_{1111} \\ S_2 &= T \cdot \mathbb{C}'_{2222} \end{aligned} \, , \tag{5.6.2}$$

where T is the local scleral thickness; S_1 and S_2 are the structural stiffnesses along and perpendicular to the preferred fiber orientation, respectively.

5.7. Sensitivity Analyses of the Inverse Finite Element Method

Solution Uniqueness. To examine whether the inverse FE simulation yields a unique solution, pseudo-experimental displacements were generated by the FE model using several predetermined sets of arbitrary model parameters. Inverse FE simulations were then performed to test whether these model parameters could be retrieved.

Effects of Regionalization Pattern. Two different regionalization patterns (Figure 5.4.1) were defined for both eyes to further assess solution uniqueness of the model parameters: c_1, c_3, c_4, k_1 and k_2. Because c_1, c_3, and c_4 were uniformly attributed to the entire posterior sclera, k_1 to the peripheral sclera, and k_2 to the peripapillary sclera, inverse FE simulations are expected to yield comparable values of these model parameters for both regionalization patterns.

Effects of ONH Elastic Modulus. The ONH, which contains the lamina cribrosa and the retinal ganglion cell axons, was considered as a linear isotropic material. To quantify the effects of ONH mechanics on scleral mechanics, inverse FE simulations were performed with ONH elastic moduli E_{ONH} of 0.1, 1, and 5 MPa (Sigal *et al.* 2008) for both eyes.

Effects of Scleral Bulk Modulus. To study the stability of the incompressibility constraint, inverse FE simulations were performed with scleral bulk moduli K of 1.0 and 0.1 GPa for both eyes.

Results. In all studies of solution uniqueness, the inverse FE simulations predicted values for all thirteen model parameters perfectly with a cost function value of zero. Based on these data, the inverse FE method yields unique solutions. Results for all other sensitivity analyses are listed in Table 5.7.1. Overall, changes in the ONH elastic modulus E_{ONH}, scleral bulk modulus K, and scleral regionalization pattern had relatively minor impact on the predicted parameters, of which the mean tangent moduli ($\mathbb{C}'_{1111}$ and $\mathbb{C}'_{2222}$) were particularly less sensitive. For all subsequent analyses, K was fixed to 1 GPa and E_{ONH} to 1 MPa.

	Regionalization Pattern	A	**A**	B	A	A
Input	E_{ONH} [MPa]	0.1	**1**	1	1	5
	K [GPa]	1	**1**	1	0.1	1
Left Eye Output	c_1 [kPa]	249	**193**	178	197	123
	c_3 [kPa]	5.0	**6.8**	9.8	6.2	12.0
	c_4 [-]	631	**563**	621	602	455
	k_1 [-]	2.63	**2.15**	1.41	2.25	1.55
	k_2 [-]	2.33	**2.51**	2.32	2.65	3.15
	ε [μm]	2.44	**2.34**	2.46	2.34	2.29
	c'_{1111} [MPa] 30 mm Hg	10.7	**9.7**	9.5	10.4	8.4
	c'_{2222} [MPa] 30 mm Hg	3.9	**3.9**	5.6	4.0	3.7
Right Eye Output	c_1 [kPa]	156	**99**	86	100	65
	c_3 [kPa]	14.4	**16.5**	16.3	15.6	23.4
	c_4 [-]	487	**475**	457	505	409
	k_1 [-]	1.47	**1.33**	1.00	1.40	1.26
	k_2 [-]	3.51	**4.40**	4.12	4.57	4.99
	ε [μm]	2.39	**2.35**	2.51	2.34	2.42
	c'_{1111} [MPa] 30 mm Hg	9.4	**9.5**	9.0	10.0	9.0
	c'_{2222} [MPa] 30 mm Hg	5.7	**6.3**	6.3	6.6	6.0

Table 5.7.1. Model parameters and mean tangent moduli for the whole sclera (IOP = 30 mm Hg) obtained from inverse FE simulations for both eyes. The regionalization pattern (A: Figure 5.4.1A; B: Figure 5.4.1B), the ONH elastic modulus and the scleral bulk modulus were varied as presented in gray. The data in **bold**, where E_{ONH} = 1 MPa and K = 1 GPa, were selected as the default case for Figures 5.8.1-4 and Table 5.8.1. c'_{1111} and c'_{2222} are the tangent moduli along and perpendicular to the preferred fiber orientation, respectively.

5.8. Inverse Finite Element Results

Figure 5.8.1 depicts both experimentally-measured and model-predicted displacements in left and right eyes as IOP increased from 5 to 10 mm Hg, 10 to 30 mm Hg, and 30 to 45 mm Hg, respectively. The displacements predicted by the model captured the complex displacement patterns of the experimental data well and the maximum cost function value was 2.51 μm for all the cases studied. Displacement

magnitude in all directions was lowest as IOP increased from 30 to 45 mm Hg. This implies that sclera is relatively compliant when IOP is low (5-10 mm Hg), but dramatically stiffens as IOP increases beyond 30 mm Hg.
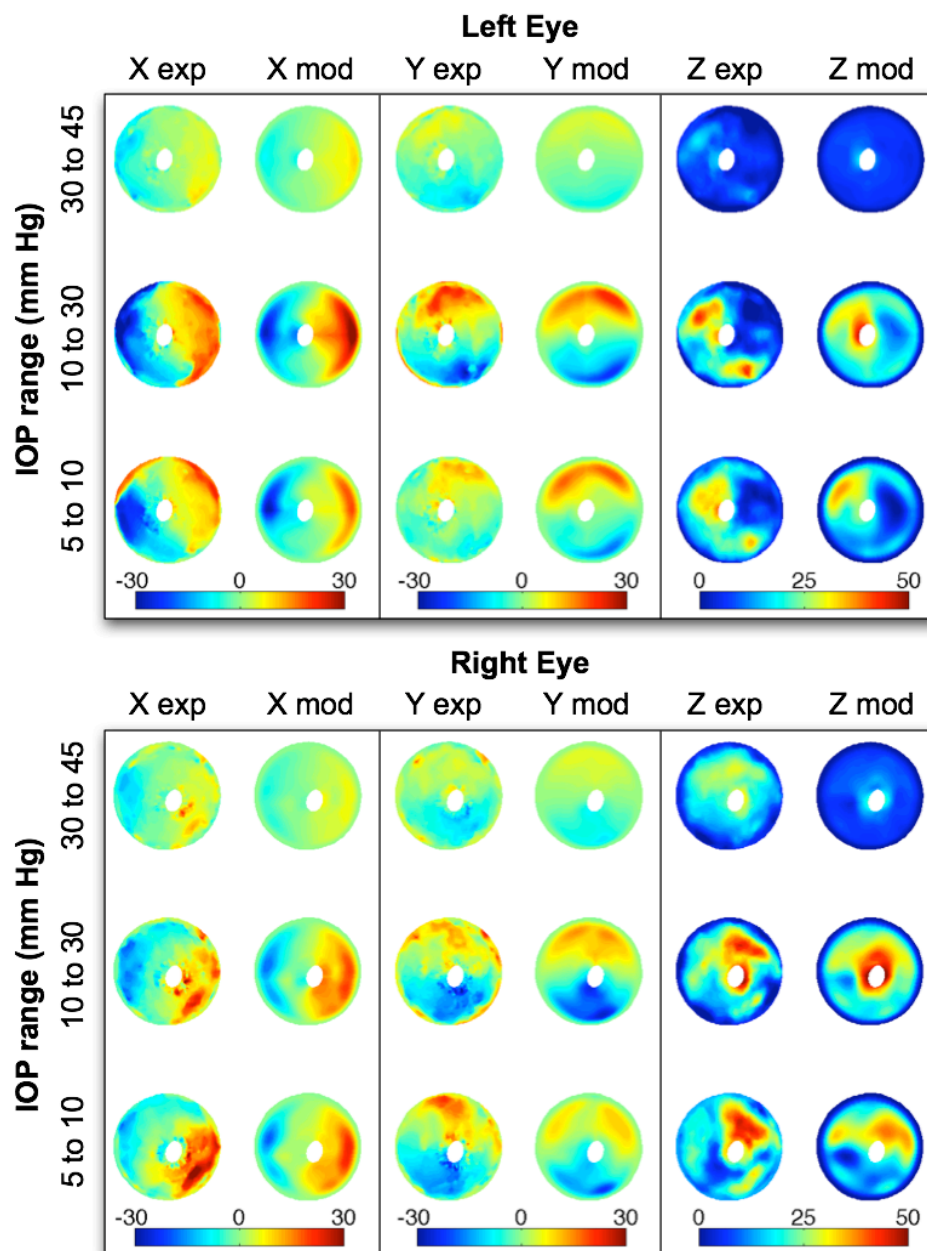
Figure 5.8.1. Comparison of experimentally-measured (exp) and model-predicted (mod) displacements (in μm) for both eyes for three IOP ranges (5 to 10, 10 to 30, and 30 to 45 mm Hg). Model displacements were simultaneously fit to the experimental data obtained at 7, 10, 20, 30 and 45 mm Hg. Both experimental and model displacements are small for the 30-45 mm Hg IOP range, demonstrating a high degree of nonlinearity.
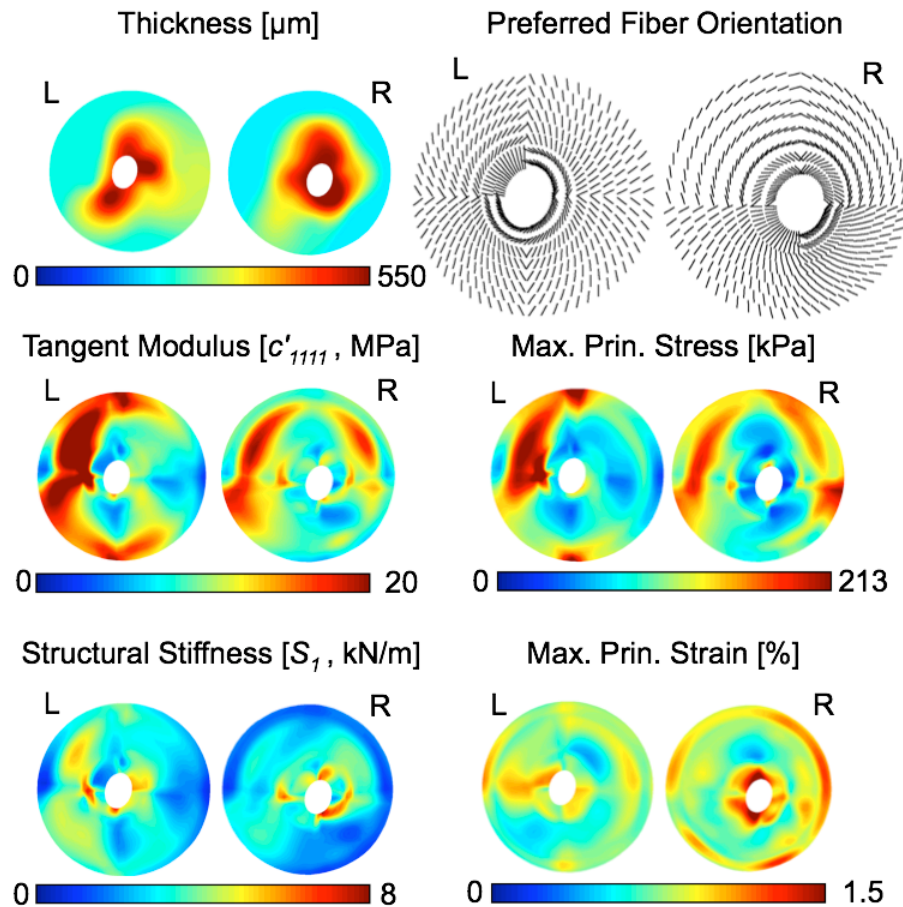
Figure 5.8.2. The main modeling results are shown as color maps for both eyes at an IOP of 30 mm Hg. Scleral thickness maps were derived from experimental ultrasound measurements at 5 mm Hg, and show that the peripapillary sclera is much thicker than the peripheral sclera. An inverse relationship between scleral thickness and scleral tangent modulus c'_{1111} was observed, indicating that thinner sclera is likely to be associated with a higher tangent modulus. The structural stiffness along the preferred fiber orientation, S_1, helps visualize this inverse relationship. Finally, maximum principal strain was concentrated around the scleral canal.

Scleral thickness for both eyes, which was acquired at 5 mm Hg (Table 5.3.1) and interpolated over the entire scleral region, is presented in Figure 5.8.2. In all eyes, the peripapillary sclera was much thicker than the peripheral sclera. Figure 5.8.2 also includes additional results at an IOP of 30 mm Hg obtained from the inverse FE simulations. Note that there is an inverse relationship between scleral tangent modulus and scleral thickness, as depicted in Figure 5.8.3. As a result, the scleral structural

stiffness, the local product of the tangent modulus and thickness, is relatively homogeneous. From Figure 5.8.2, the collagen fibers are generally circumferentially oriented around the ONH in 3 of the 4 sub-regions of the peripapillary sclera. Notice that the fibers from the peripapillary sclera were associated with a higher fiber concentration factor ($k_2 > k_1$ in Table 5.7.1), meaning a stronger anisotropy near the ONH.

Figure 5.8.3. Tangent Modulus c'_{1111} versus scleral thickness for both eyes at an IOP of 30 mm Hg, which illustrates the concept of inverse relationship between two quantities. A thin sclera (the peripheral sclera) has a tendency to be associated with larger c'_{1111}, and a thick sclera (the peripapillary sclera) with smaller c'_{1111}. Notice small R^2 values obtained from linear regression analyses, possibly due to the scatteredness of the data points.

The most critical output quantities ($\mathbb{C}'_{1111}$, $\mathbb{C}'_{2222}$, S_1, S_2, 1st principal strain, and 1st principal stress) for $K = 1$ GPa and $E_{ONH} = 1$ MPa are summarized in Table 5.8.1. for the 5th, 50th (median) and 95th percentiles of their distributions for both the peripheral and peripapillary sclera at IOPs of 10, 30 and 45 mm Hg. They are also displayed (except the structural stiffnesses) for the 25th, 50th (median) and 75th percentiles of their distributions in Figure 5.8.4. As seen in Table 5.8.1, the mean tangent moduli, $\mathbb{C}'_{1111}$ and $\mathbb{C}'_{2222}$, are 3 to

6 times higher at 45 mm Hg than at 10 mm Hg in both eyes. In addition, the mean 1st principal strain is a nonlinear function of IOP. Finally, The mean 1st principal strain is higher in the peripapillary sclera, whereas the mean 1st principal stress is higher in the peripheral sclera.

Percentile			5th			50th			95th		
IOP [mm Hg]			10	30	45	10	30	45	10	30	45
Left Eye	Peripapillary Sclera	c'_{1111} [MPa]	2.1	4.5	6.6	**2.6**	**8.2**	**13.0**	3.4	13.8	22.5
		c'_{2222} [MPa]	0.9	2.1	3.2	**1.0**	**3.8**	**6.7**	1.2	7.1	13.5
		S_1 [kN/m]	0.8	1.7	2.4	**1.1**	**3.4**	**5.3**	1.5	5.8	9.7
		S_2 [kN/m]	0.3	0.9	1.3	**0.4**	**1.6**	**2.9**	0.5	2.8	5.2
		1st Prin. Strain [%]	0.18	0.57	0.70	**0.31**	**0.86**	**1.01**	0.44	1.07	1.25
		1st Prin. Stress [kPa]	5.1	27.3	44.5	**8.4**	**51.9**	**87.2**	13.4	90.9	162
	Peripheral Sclera	c'_{1111} [MPa]	1.9	3.4	4.8	**3.1**	**10.0**	**15.8**	5.0	22.3	36.3
		c'_{2222} [MPa]	0.9	1.5	2.0	**1.2**	**3.9**	**6.3**	1.7	8.0	13.9
		S_1 [kN/m]	0.5	0.8	1.2	**0.9**	**2.8**	**4.5**	1.2	4.9	7.8
		S_2 [kN/m]	0.2	0.4	0.5	**0.3**	**1.1**	**1.7**	0.4	1.9	3.3
		1st Prin. Strain [%]	0.17	0.49	0.61	**0.30**	**0.75**	**0.88**	0.47	1.00	1.20
		1st Prin. Stress [kPa]	3.8	13.4	21.7	**11.3**	**58.9**	**95.7**	25.8	140	226
Right Eye	Peripapillary Sclera	c'_{1111} [MPa]	3.5	4.7	6.0	**4.1**	**7.9**	**11.0**	4.8	12.7	19.5
		c'_{2222} [MPa]	1.0	1.3	1.8	**1.1**	**2.1**	**3.2**	1.3	3.7	7.5
		S_1 [kN/m]	1.5	2.2	2.7	**1.9**	**3.6**	**5.0**	2.5	6.3	9.8
		S_2 [kN/m]	0.4	0.6	0.8	**0.5**	**1.0**	**1.4**	0.7	1.9	3.7
		1st Prin. Strain [%]	0.25	0.79	0.97	**0.35**	**1.06**	**1.28**	0.54	1.57	1.84
		1st Prin. Stress [kPa]	3.6	16.1	26.4	**7.1**	**36.1**	**59.5**	11.3	73.7	136
	Peripheral Sclera	c'_{1111} [MPa]	2.6	4.6	6.4	**3.7**	**9.9**	**14.8**	5.2	17.2	26.3
		c'_{2222} [MPa]	1.3	3.0	4.3	**1.8**	**7.0**	**11.1**	2.7	12.9	20.7
		S_1 [kN/m]	0.5	1.0	1.4	**0.9**	**2.5**	**3.8**	1.5	4.3	6.5
		S_2 [kN/m]	0.3	0.6	0.8	**0.5**	**1.8**	**2.8**	0.7	2.8	4.5
		1st Prin. Strain [%]	0.21	0.55	0.66	**0.35**	**0.79**	**0.94**	0.51	1.19	1.58
		1st Prin. Stress [kPa]	5.4	26.8	43.4	**13.4**	**68.1**	**109**	26.8	132	211

Table 5.8.1. 5th, 50th (median), and 95th percentiles of the tangent moduli, structural stiffnesses, 1st principal strain and 1st principal stress distributions, for IOP = 10, 30 and 45 mm Hg, and for both the peripheral and peripapillary sclera of both eyes. S_1 and S_2 are the structural stiffnesses along and perpendicular to the preferred fiber orientation, respectively.
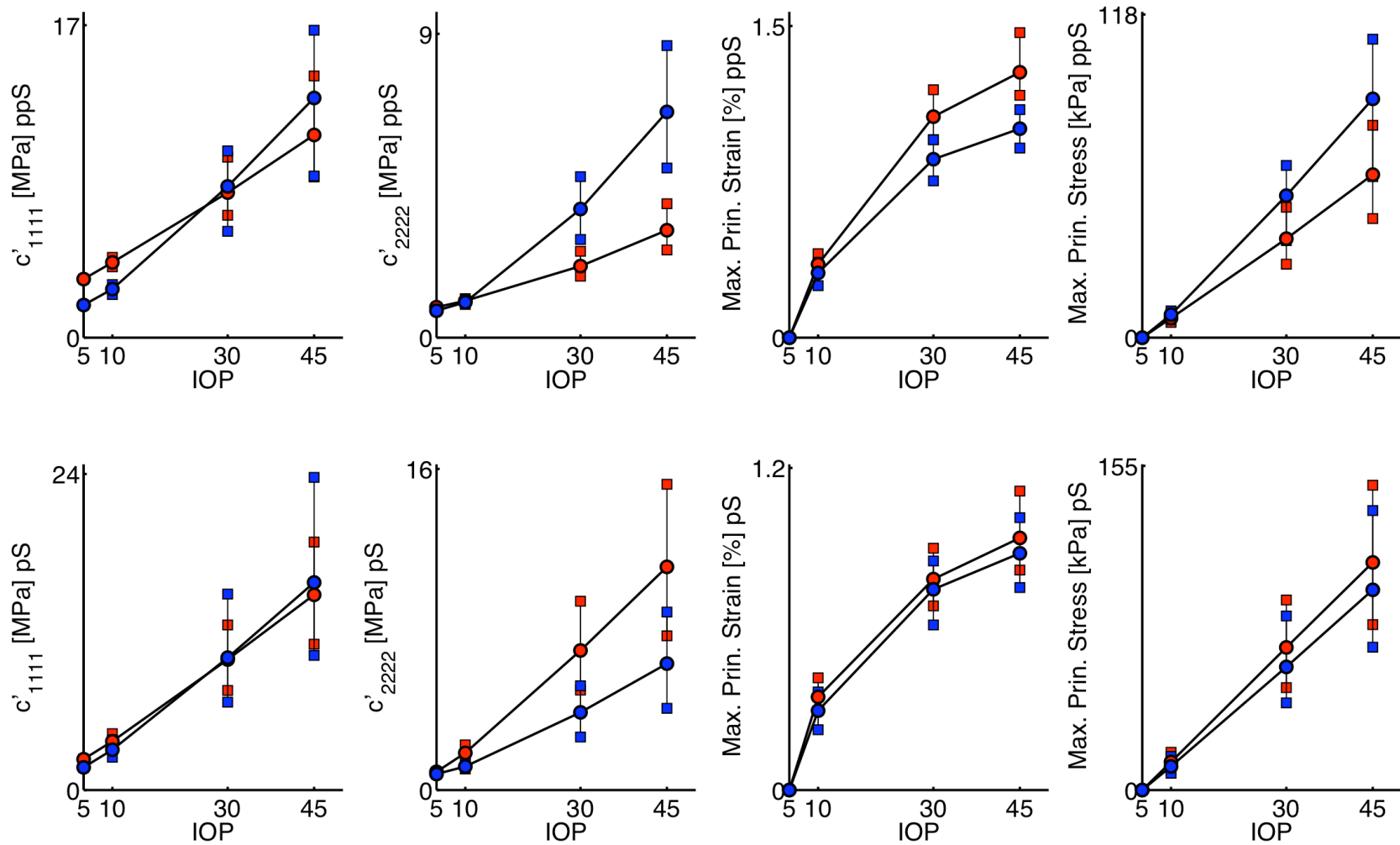
Figure 5.8.4. 25th, 50th (median), and 75th percentiles of the tangent moduli, maximum principal strain and maximum principal stress distributions, for IOP = 5, 10, 30 and 45 mm Hg, and for both the peripheral (pS) and peripapillary (ppS) sclera. The data for the right eye are shown in red and the data for the left eye are shown in blue.

5.9 Deformation Parameters

In Chapter 4, we have quantified four deformation parameters (the scleral canal expansion, the scleral canal twist, the scleral canal z-displacement and the posterior laminar deformation) for an idealized half-spherical shell with a circular scleral canal. To obtain a preliminary estimate of the effects of scleral mechanics on ONH mechanics in monkeys, we computed the four deformation parameters for both eyes based on the FE predictions. Since the ONH shape was approximated by an elliptical cylinder, we computed average values for each of the four deformation parameters for IOP = 10, 30 and 45 mm Hg. Briefly, the scleral canal expansion is a measure of canal opening with IOP. The scleral canal twist represents the amount of rotation that the scleral canal undergoes with IOP. The posterior laminar deformation represents the amount of ONH bowing due to acute elevations of IOP. All four deformation parameters, as predicted from FE modeling, are shown in Table 5.9.1.

	Left Eye			Right Eye		
IOP [mm Hg]	10	30	45	10	30	45
Scleral Canal Expansion [%]	0.30	0.96	1.19	0.26	1.08	1.42
Scleral Canal Twist [°]	0.21	0.53	0.63	0.25	0.37	0.42
Scleral Canal z-Displacement [μm]	22.0	58.2	70.6	25.3	72.1	89.9
Posterior Laminar Deformation [μm]	2.69	16.9	28.7	0.73	11.5	20.4

Table 5.9.1. Scleral canal expansion, scleral canal twist, scleral canal z-displacement and posterior laminar deformation predicted from FE modeling for both eyes at 10, 30, and 45 mm Hg.

From Table 5.9.1, scleral canal expansion, scleral canal twist and scleral canal z-displacement increased with IOP nonlinearly for both eyes, but their rate of increase was smaller at higher IOP. On the other hand, posterior laminar deformation did increase

nonlinearly with IOP for both eyes, but its rate of increase was smaller at lower IOP. Note that scleral canal twist was insignificant (< 1°) in both eyes suggesting that the posterior sclera does not participate in twisting of the ONH tissues (at least for these specific eyes).

5.10. Discussion

In this Chapter, we introduce an experimental method to measure the 3-D displacements of monkey posterior sclera exposed to acute elevations of IOP from 5 to 45 mm Hg, and use the anisotropic hyperelastic model developed in Chapter 4 along with an inverse FE method to extract scleral mechanical properties. Our findings demonstrate that our constitutive model can accurately predict the experimental 3-D displacements of the posterior scleral shell, and that the proposed inverse FE method can estimate a unique set of thirteen model parameters. We have thus captured the inhomogeneous, anisotropic, and nonlinear behavior of the posterior sclera when exposed to acute elevations of IOP.

This study used a pressurization test to measure scleral deformations under pressure load. Unlike traditional biaxial patch tests, the pressurization methodology allowed us to estimate mechanical properties for the entire posterior scleral shell in its physiologic configuration. In addition, the IOP range commonly experienced by normal and glaucomatous eyes was covered in one test set-up. Biaxial testing of an entire posterior scleral shell would require tests of scleral patches excised from many adjacent points, each of which would have to be flattened prior loading.

The models predicted that, in the posterior sclera of monkey eyes, the collagen fibers were generally circumferentially oriented around the ONH in 3 of the 4 sub-

regions of the peripapillary sclera, which is consistent with previous histologic results (Hernandez *et al.* 1987). Furthermore, collagen fibers tended to be more highly concentrated along their preferred orientations in the peripapillary sclera as shown by the higher fiber concentration factor k_2. As seen in Chapter 4, a high fiber concentration factor associated with a circumferential fiber organization will limit scleral canal expansion, and this may help the peripapillary sclera to protect the ONH. Although, it should be noted that small scleral canal expansion is usually associated with large posterior laminar deformation.

In the experimental pressure tests, we observed a high degree of nonlinearity that was manifested by much smaller incremental displacements when IOP was elevated above 30 mm Hg, which was also measured in porcine sclera in our previous study (Girard *et al.* 2008). This nonlinearity was additionally observed in the tangent moduli and structural stiffnesses as they exponentially increased with IOP from 5 to 45 mm Hg.

Physiologically, the sclera is a load bearing structure to resist IOP and yet the eye may need to maintain its shape to preserve focused vision. Thus, it seems to be reasonable to assume that the structural stiffness of the scleral shell should be relatively homogeneous to ensure that the eye expands uniformly with increasing IOP. In this study, we found an inverse relationship between scleral thickness and tangent modulus (Figure 5.8.3), which may contribute to the overall uniform distribution of structural stiffness for the entire posterior sclera (Figure 5.8.2). Further study is necessary to understand the relationship between the ultrastructural characteristics and the overall deformational behavior of the posterior sclera.

The ONH is the primary site of damage in glaucoma (Quigley and Anderson 1976; Quigley and Addicks 1980) and is composed of neural tissues supported by a connective tissue meshwork known as the lamina cribrosa. The mechanical interaction between the scleral shell and ONH at the scleral canal is of vital importance to the understanding of the biomechanical factors influencing glaucomatous susceptibility. Although these experiments and models were not designed to elucidate the mechanical behavior of the scleral canal and ONH, some interesting observations from these models warrant further study. First, the rate of scleral canal expansion was higher at low IOPs, whereas the rate of posterior laminar deformation was higher at high IOPs. This interesting preliminary finding suggests that there is an inverse relationship between scleral canal expansion and posterior laminar deformation as discussed in Chapter 4. The biomechanical behavior of the peripapillary scleral and ONH will need to be explored in future models designed to confirm these findings in a more rigorous setting.

Several limitations should be taken into consideration when viewing this work. First, we have assumed that the collagen fibers were the sole contributors to the nonlinear relationship between IOP and scleral deformations, and that the relative contributions of ground substance and collagen fibers to scleral mechanical properties were uniform throughout the scleral shell. These assumptions are well established when characterizing the mechanical behavior of collagenous soft tissues (Fung 1993), but more work may be needed to characterize the influence of other constituents such as elastin and the effects of regional changes in collagen fiber diameter.

Second, the mechanical deformations for IOPs below 5 mm Hg has not been accounted for in this study because the scleral shells did not acquire their pressurized geometry until approximately 4 mm Hg of IOP was applied. Physiologic IOP for normal monkey eyes is generally above 5 mm Hg, but including information below 5 mm Hg could improve the model's predictions. In the future, one might attempt to resolve this computationally using the inverse elastostatic method (Govindjee and Mihalic 1996; Lu *et al.* 2007) to mathematically recover the initial stress-free configuration of an elastic body. However, this method is only valid on the premise that residual stresses are insignificant, which is not known for monkey posterior sclera.

Third, the boundary of the ONH was represented in the model using an ellipse fitted to the outer aspect of the dural sheath insertion, and was therefore larger than one would expect (~2 mm along the major axis in our model, compared with ~1.5 mm for an anatomic ONH). In addition, the ONH was modeled as a linear elastic plug of the same curvature and thickness of the surrounding sclera, but with its own modulus. Our sensitivity studies showed that the overall model behavior of the posterior sclera was not sensitive to the mechanical properties of the ONH, so these model assumptions have little impact on the reported results. On the contrary, the mechanical behavior of the ONH has been reported to be very sensitive to the mechanical properties of the posterior sclera (Sigal *et al.* 2004). This is consistent with the study conducted in Chapter 4 showing that the distribution of the scleral collagen fibers had large effects on scleral canal expansion and laminar posterior deformation. However, in order to fully understand the interaction between the sclera and the ONH, more accurate data including the geometry of the scleral

canal and the ONH, as well as the mechanical properties of the ONH and the surrounding scleral tissue need to be obtained.

Fourth, the true orientation of the collagen fiber alignment for the whole sclera is still lacking in literature, and we have attempted to predict it in this study (Figure 5.8.2). Due to the relatively coarse discretization of the regions (eight for the whole posterior shell), we could only report an overall estimate of the preferred collagen fiber orientation within each region. Kokott described spatial mapping of collagen fiber orientation in 1934 using standard histology (Kokott 1934). However, given the complex lamellar ultrastructure of the sclera, those data were not used in our study as they did not present the collagen fiber distribution with the reported preferred fiber orientation. Future experimental work will be required to characterize collagen fiber distributions more precisely for entire scleral shells.

Finally, we used eight sub-regions for the posterior sclera to limit the number of model parameters to be extracted with the inverse FE method to thirteen. Using more than thirteen model parameters dramatically increases the computational time for each simulation (Price *et al.* 2005) and can raise a further concern about the uniqueness of the predicted model parameters. As our primary interest is the biomechanics of the scleral canal and its effects on the contained ONH, we have concentrated four of the eight sub-regions to model the peripapillary sclera in the vicinity of the ONH. While we tested several other regionalization patterns with fewer regions and/or parameters (data not shown), the combination of 8 sub-regions with thirteen parameters produced the best fit with the lowest cost function value (Eq. (5.5.1)). Note that the sub-regional discretization of the posterior sclera resulted in discontinuity of the predicted model parameters (*i.e.,*

the preferred fiber orientation and the fiber concentration factor) across the boundaries between the sub-regions, as shown in Figure 5.8.2.

The experimental and computational methodologies presented here have broad applicability to multi-axial mechanical testing and model parameter prediction of thin soft tissues with varying collagen fiber orientations. These methods will be used in Chapters 6 and 7 to characterize the mechanical properties of normal (young and old), and early- and moderate-stage glaucomatous monkey eyes. Mechanical testing and modeling of ocular soft tissues will contribute to our understanding of glaucomatous susceptibility of the ONH (Burgoyne *et al.* 2005), posterior scleral damage (Downs *et al.* 2005), myopia (Rada *et al.* 2006), and a host of other ocular disorders. Since the posterior sclera determines the levels of strain and stress transmitted to the contained ONH and is altered in early experimental glaucoma (Downs *et al.* 2005), it is likely to play an important role in glaucomatous damage to the ONH.

6   Scleral Biomechanics In the Aging Monkey Eye[1]

6.1. Abstract

Custom 3-D experimental and computational tools were developed to investigate the age-related differences in the biomechanical properties of posterior and peripapillary sclera from old (>18 years) and young (<2.1 years) rhesus monkeys following acute elevation of intraocular pressure (IOP) from 5 to 45 mm Hg. The posterior scleral shells from both eyes of eight rhesus monkeys (four young and four old) were individually mounted on a custom-built pressurization apparatus. IOP was incrementally increased from 5 to 45 mm Hg, and the 3-D displacements of each shell were measured using electronic speckle pattern interferometry. The geometry of each scleral shell was reconstructed from data generated by a 3-D digitizer (topography) and a 20 MHz ultrasound transducer (thickness). A fiber-reinforced constitutive model that includes stretch-induced stiffening and a directionality distribution of the collagen fibers was applied to each scleral shell, and a unique set of biomechanical properties was obtained

---

using an inverse finite element (FE) method. Local displacements, thickness, stress and strain, tangent modulus, structural stiffness, and preferred collagen fiber orientation were mapped for each posterior scleral shell. The predictions of the model matched the 3-D experimental displacements well. The posterior sclera exhibited inhomogeneous, anisotropic, nonlinear mechanical behavior in all eyes. The sclera was significantly thinner ($p = 0.038$; multiple linear regression), and tangent modulus and structural stiffness were significantly higher ($p < 0.0001$; generalized estimating equation) in the old monkey group. On average, scleral collagen fibers were circumferentially oriented around the optic nerve head (ONH). Moreover, we found no difference in the preferred fiber orientation and fiber concentration factor between young and old monkey eyes for both scleral regions. Posterior and peripapillary sclera in old monkeys is significantly stiffer than that from young monkeys and is therefore subject to higher stresses but lower strains at all levels of IOP. Age-related stiffening of the sclera should have a large effect on ONH biomechanics, and could therefore play a role in age-related susceptibility to glaucomatous vision loss.

6.2. Introduction

Glaucomatous vision loss occurs at both normal and elevated levels of IOP and is the second leading cause of blindness worldwide (Resnikoff *et al.* 2004; Foster and Resnikoff 2005). The ONH has been shown to be the principal site of damage in glaucomatous optic neuropathy (Quigley and Anderson 1976; Quigley and Addicks 1980), and is a biomechanically compliant tissue in an otherwise strong pressure vessel (Bellezza *et al.* 2000; Sigal *et al.* 2004) – the corneo-scleral envelope. While damage to

the visual system in glaucoma is multi-factorial, ONH and peripapillary scleral biomechanics provides a logic by which the principal pathologic mechanisms in glaucoma can be understood to result in the clinical appearance and behavior of a glaucomatous optic disc (Burgoyne *et al.* 2005; Ethier 2006).

The ONH contains the lamina cribrosa, a fenestrated connective tissue meshwork that spans the scleral portion of the neural canal and provides structural and functional support to the retinal ganglion cell axons as they exit the eye on their path to the brain. The sclera is the principal load bearing tissue of the eye, and is composed primarily of collagen. Ninety percent of the collagen fibers in the sclera are Type I (Edelhauser and Ubels 2003), which provide the eye with the necessary biomechanical strength to resist IOP. Scleral collagen fibers have a large variation in their diameters (Quigley *et al.* 1991) and are formed into irregularly arranged, multi-layered lamellae of varying thickness (Rada *et al.* 2006). Within each lamella, the fibrils run tangent to the scleral shell and are oriented in a preferred orientation to varying degrees (Watson and Young 2004).

The periphery of the lamina cribrosa inserts deeply into the sclera at the canal wall, and studies have indicated that scleral collagen fiber organization (Girard *et al.* 2008c) and scleral stiffness (Sigal *et al.* 2005) have a large impact on ONH biomechanics. In order to study ONH biomechanics as a potential driving mechanism in glaucoma, computational biomechanical models based on the FE method should incorporate accurate geometries and biomechanical properties for both the ONH and posterior scleral shell.

A variety of data suggest that the ONH becomes more susceptible to progressive glaucomatous damage as it ages. These data can be summarized as follows. First, in most

(Klein *et al.* 1992a; Nomura *et al.* 1999; Weih *et al.* 2001; Nomura *et al.* 2002; Rochtchina *et al.* 2002), but not all (Leske *et al.* 1997; Wu and Leske 1997), population based studies, either IOP does not increase with age or if it does, the magnitude of increase is not likely to be clinically important. Second, normal pressure glaucoma is most commonly a disease of the elderly (Drance *et al.* 1973; Chumbley and Brubaker 1976; Levene 1980; Goldberg *et al.* 1981; Klein *et al.* 1992b) and by most measures exists only rarely in the young (Geijssen 1991). Third, age is an independent risk factor for both the prevalence (Tielsch *et al.* 1991) and progression of the neuropathy at all stages of damage (Gordon *et al.* 2002; Heijl *et al.* 2003; Nouri-Mahdavi *et al.* 2004).

It is reasonable to hypothesize that age-related changes in ONH biomechanics, blood supply, and other factors may underlie the increased susceptibility to glaucomatous damage in the elderly. There is substantial evidence that the connective tissues of the lamina and sclera are altered with age, which in turn alters their biomechanical behavior. Age-related changes in the human lamina cribrosa have been associated with increased collagen and elastin content as well as increased collagen and elastin cross-links (Hernandez *et al.* 1989; Albon *et al.* 1995; Albon *et al.* 2000a). Collagen cross-linking is a characteristic of aging soft-tissues (Bailey *et al.* 1998), which result in an increase of stiffness at the tissue or macroscopic level (Spoerl *et al.* 2005). Several studies using uniaxial tensile testing of scleral strips from tree shrew (Siegwart and Norton 1999) and human (Curtin 1969; Avetisov *et al.* 1983; Friberg and Lace 1988) eyes concluded that the stiffness of the sclera increases with age.

To our knowledge, aging effects on the biomechanical properties of normal monkey posterior sclera have not been investigated. In our previous studies, we measured

the 1-D (Downs *et al.* 2003; Downs *et al.* 2005; Girard *et al.* 2007), 2-D (Girard *et al.* 2008a), and 3-D (Girard *et al.* 2008b) deformation patterns of rabbit, monkey and porcine peripapillary sclera with *ex-vivo* experimental protocols. In the present report, we use our latest *ex-vivo* method to experimentally measure the 3-D deformation pattern and thickness of posterior sclera from both eyes of four young and four old monkeys following IOP elevation from 5 to 45 mm Hg (Girard *et al.* 2008b). We then model the posterior sclera as a nonlinear, anisotropic, inhomogeneous soft-tissue using a fiber-reinforced constitutive theory that includes stretch-induced stiffening and multi-directionality of the collagen fiber (Driessen *et al.* 2003; Pinsky *et al.* 2005; Gasser *et al.* 2006; Girard *et al.* 2008c; Kroon and Holzapfel 2008; Nguyen *et al.* 2008), so as to derive shell-specific sets of biomechanical properties based on the experimental observations using an inverse FE method (Girard *et al.* 2008b).

6.3. Experimental Setup and Testing Protocol

All experiments adhered to the ARVO statement for the Use of Animals in Ophthalmic and Vision Research. In this study, we tested eight rhesus monkeys, without any apparent ocular abnormality, classified into two age groups: four were younger than 2.1 years and four were older than 18 years. Note that rhesus monkey age is considered to be approximately equivalent to one third of human age (Tigges *et al.* 1988). For this study, we used an experimental protocol for 3-D scleral testing that has been fully documented in Chapter 5. Briefly, all monkeys were anesthetized with an intramuscular injection of ketamine/xylazine, and sacrificed with an intravenous injection of sodium

pentobarbital. The eyes were enucleated immediately after death and all extra-orbital tissues were removed. Each globe was sectioned approximately 3 mm anterior to the equator and the retina and choroid were dissected away from the posterior scleral shell except for a 7-mm diameter patch centered on the ONH, which was left intact to prevent fluid leakage from the ONH during pressurization. After dissection, the posterior scleral shells were individually mounted on a custom-built pressurization apparatus as shown in Figure 6.3.1.
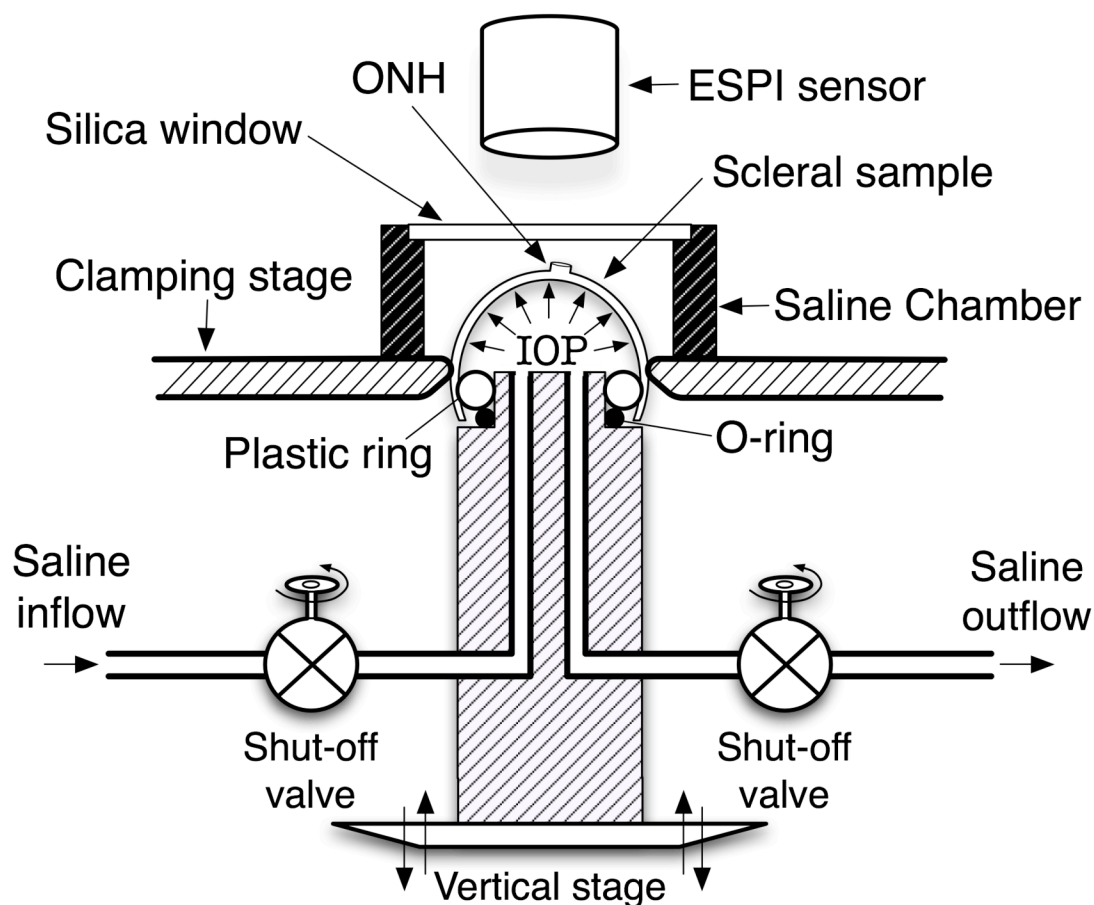
Figure 6.3.1. Schematic of the scleral shell pressurization apparatus. The posterior scleral shell was first mounted onto the plastic ring, and then clamped slightly above the equator by moving the vertical stage toward the clamping stage. Saline outflow was interrupted after saline filled the posterior shell cavity and IOP reached 5 mm Hg. The scleral surface was imaged with an electronic speckle pattern interferometry (ESPI) sensor as IOP increased from 5 to 45 mm Hg in 0.2 mm Hg increments.

After mounting, each shell was blotted dry, covered with a contrast medium (ProCAD, Ivoclar, Schaan, Lichtenstein), and immediately immersed in isotonic saline at 22°C. IOP was incrementally increased from 5 to 45 mm Hg and an electronic speckle pattern interferometry sensor (Erne *et al.* 2005; Kessler *et al.* 2006) (Q100, Ettemeyer AG, Germany) was used to record the full-field 3-D displacements of each shell surface at a resolution of 0.1 μm. Following the pressurization experiment, IOP was reset to 5 mm Hg and scleral topography was measured with a 3-D digitizer arm (MicroScribe G2X, Immersion, San Jose, CA). Scleral thickness was also measured at twenty predetermined locations with a 20 MHz ultrasound transducer (PacScan 300P, Sonomed, Inc., Lake Success, NY). The topography and thickness data were combined to reconstruct the reference geometry of each posterior scleral shell as shown in Figure 6.3.2. The reference geometry was divided into 9 regions, where regions 1-4 encompass the peripheral sclera, regions 5-8 the peripapillary sclera, and region 9 the ONH.
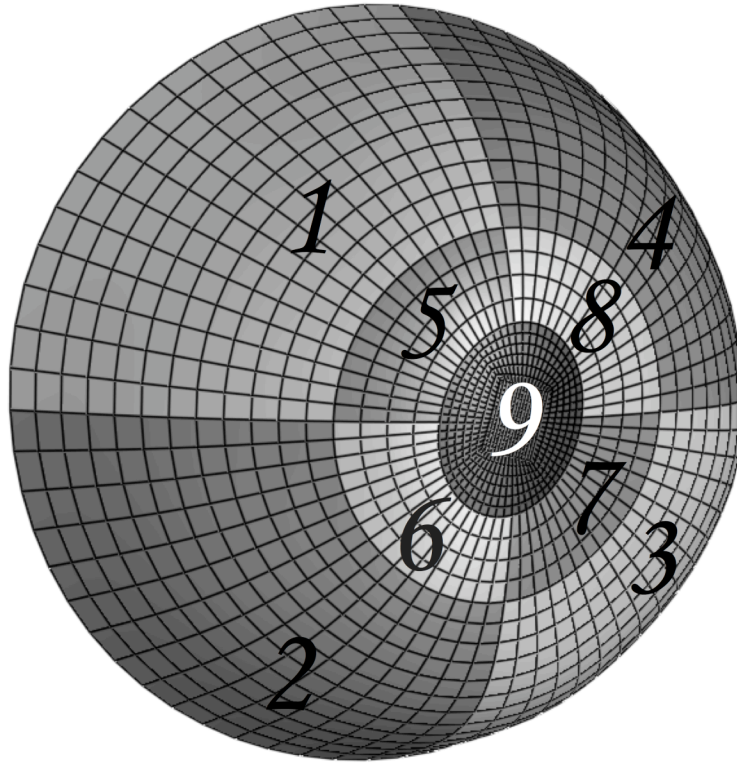
Figure 6.3.2. Anatomically-accurate geometry of one posterior scleral shell that was reconstructed from experimental topography and thickness measurements. Regions 1-4 encompass the peripheral sclera, Regions 5-8 the peripapillary sclera and Region 9 the ONH.

6.4. A Constitutive Theory for the Posterior Sclera

In the field of continuum solid mechanics, constitutive theories are developed to mathematically characterize the deformations (*e.g.* strain) and internal forces (*e.g.* stress) of any mechanically loaded material, including biological soft-tissues. As part of our ongoing effort to understand scleral biomechanics and its potential impact on the ONH, we aim to provide a constitutive theory for the posterior sclera that will be validated with experimental observations from state-of-the-art imaging technologies (*e.g.* electronic speckle pattern interferometry in this study). In our constitutive theory, collagen – organized into long and dense fibrous bundles – is considered the primary biomechanical

element as it provides most of the tensile strength necessary for the sclera to resist IOP. Accordingly, the posterior sclera can be represented as a fiber-reinforced composite structure, in which the collagen fibers are (1) responsible for two important biomechanical characteristics (anisotropy and nonlinearity) and (2) embedded within a ground substance matrix. The following is a brief summary of our constitutive theory, which is fully described in Chapter 4.

Anisotropy

Anisotropy, as opposed to isotropy, is the property by which materials exhibit different stiffnesses along different orientations. Anisotropy in thin soft tissues is generally determined by the organization of their collagen fibers, which run tangent to the tissue surface (Watson and Young 2004). For our constitutive theory, a semi-circular Von Mises distribution (Fisher 1993) is used to describe planar anisotropy of the posterior sclera, in which θ_p is an angle that defines the preferred fiber orientation and k is the fiber concentration factor (Figure 6.4.1). Figure 6.4.1 illustrates the different degrees of collagen fiber alignment for varying k values and $\theta_p = 0°$ described by this distribution. When $k = 0$, the fibers are unorganized and their orientations are random. As k increases, the fibers become increasingly more aligned along the preferred fiber orientation, θ_p.
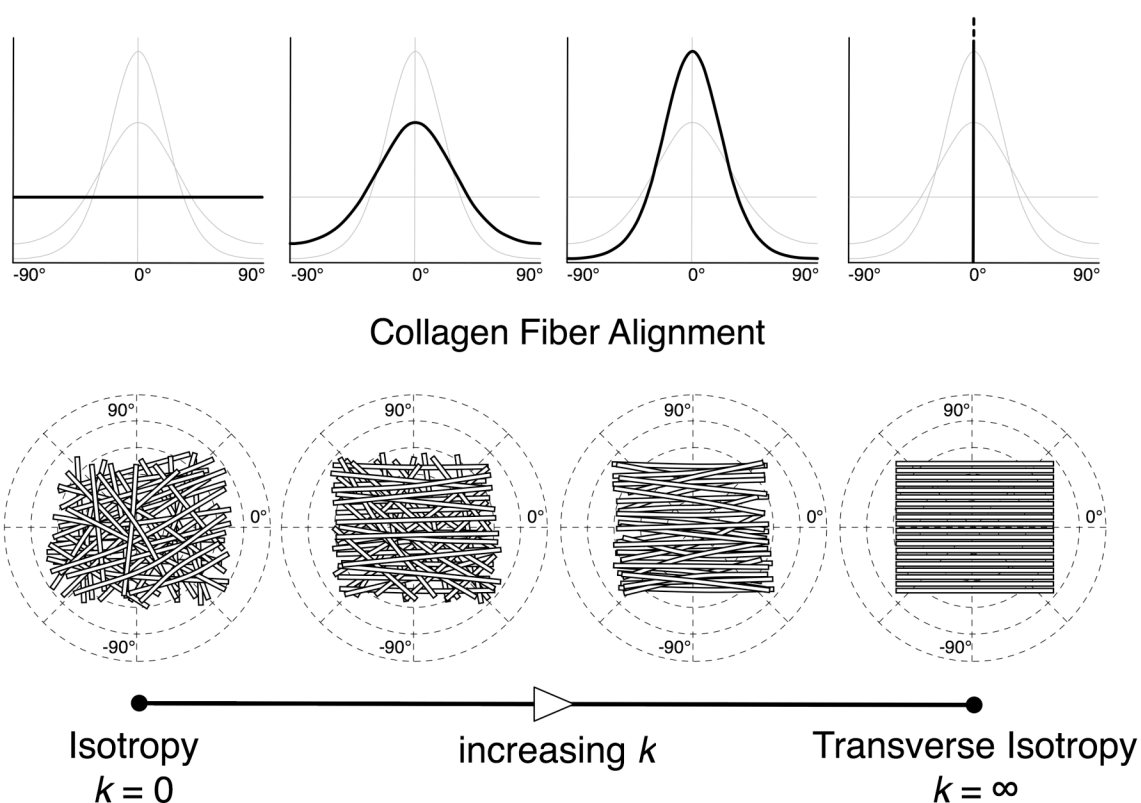
Figure 6.4.1. Semi-circular Von Mises distribution describing local collagen fiber alignment. As the fiber concentration factor k increases, collagen fibers become more aligned along the preferred fiber orientation ($\theta_p = 0°$ in this example). When $k = 0$, collagen fibers are randomly organized, resulting in equal stiffness in all orientations (relevant to skin tissue). This material symmetry is known as isotropy. When $k = \infty$, collagen fibers are all oriented in a particular preferred orientation, which creates high stiffness along θ_p and high compliance perpendicular to θ_p (relevant to tendons and ligaments). This material symmetry is known as transverse isotropy.

Nonlinearity

Collagen fibers uncrimp with stretch (Fung 1993), which results in tissues that are initially compliant at low stretch but increase in stiffness at higher levels of stretch (Figure 6.4.2). This property is known as nonlinearity, and it has been experimentally observed in the posterior sclera (Curtin 1969; Woo *et al.* 1972; Phillips and McBrien 1995; Siegwart and Norton 1999; Wollensak and Spoerl 2004; Spoerl *et al.* 2005; Olesen *et al.* 2007; Girard *et al.* 2008a; Girard *et al.* 2008b; Schultz *et al.* 2008; Weiyi *et al.* 2008). An increase of stiffness is known to protect soft-tissues from undergoing large deformations, which could disrupt the tissue's mechanical integrity at the cellular level (Curtin 1969). For our constitutive theory, IOP-induced stiffening of the sclera is described by specifying the collagen fiber stress as an exponential function of the collagen fiber stretch. Within this relationship, two model parameters govern the degree of nonlinearity of the posterior sclera (c_3: exponential fiber stress coefficient, and c_4: uncrimping rate of the collagen fibers) (Weiss *et al.* 1996; Girard *et al.* 2008c). Note that the product of c_3 and c_4 dominates the scleral response at low IOP, but c_4 alone dominates the scleral response at high IOP.

Collagen Fiber Nonlinearity
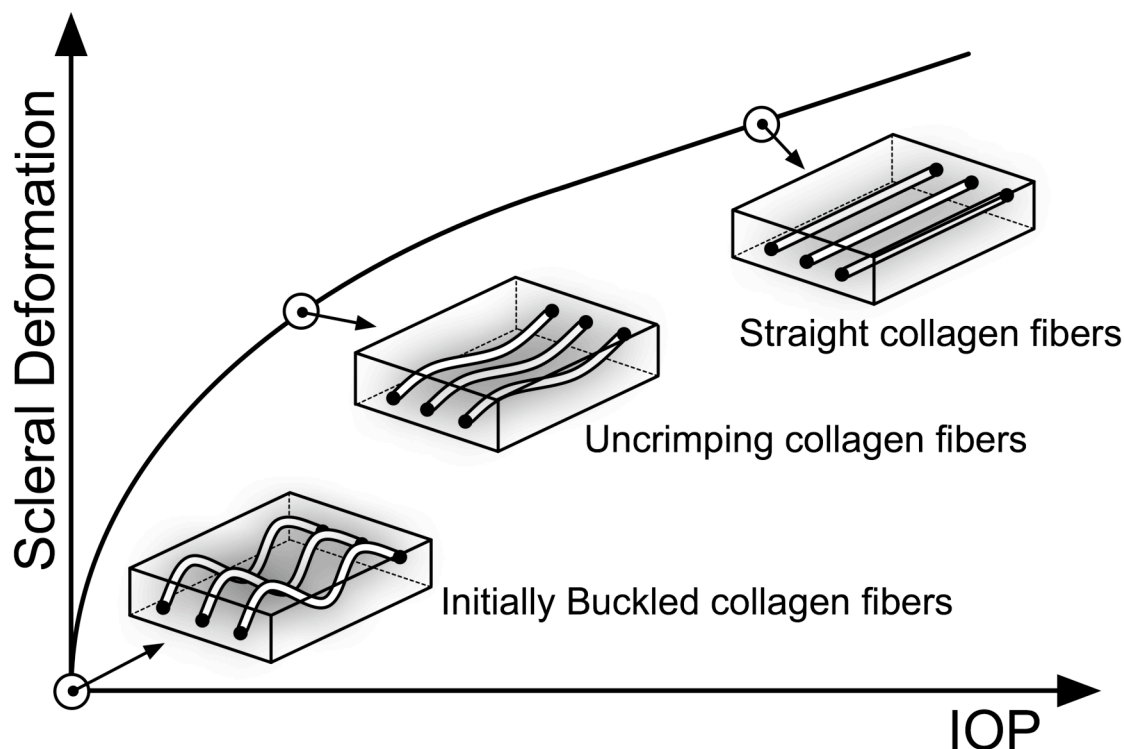
Figure 6.4.2. Uncrimping of the collagen fibers induces scleral stiffening at the macroscopic level. Initially the collagen fibers are buckled, then uncrimp and eventually become straight due to acute elevations of IOP, thus limiting scleral deformations at high IOP values. Note that the parameters c_3 and c_4 govern the degree of nonlinearity of each scleral shell.

Ground Substance Matrix

In our formulation, the ground substance matrix - not to be confused with the extracellular matrix - contains all non-collagenous tissue components (*e.g.* elastin, glycosaminoglycans, proteoglycans, fibroblasts, tissue fluid). The ground substance matrix is assumed to be isotropic, and hence its mechanical behavior can be described with a single intrinsic parameter (c_1, the 1st Mooney-Rivlin coefficient) (Weiss *et al.* 1996; Girard *et al.* 2008c).

6.5. Model Assumptions

The model assumed that stiffness of the ground substance matrix (c_1) and the nonlinear stiffness of the collagen fibers (c_3, c_4) were uniformly attributed to the entire scleral shell (Regions 1-8; Figure 6.3.2). It further assumed that regional variations of the scleral biomechanical response were governed by the local alignment of the collagen fibers. Accordingly, fiber concentration factors, k_1 and k_2, were attributed to the peripheral sclera (Regions 1-4; Figure 6.3.2) and to the peripapillary sclera (Regions 5-8; Figure 2), respectively. Finally, a total of eight preferred fiber orientations, θ_{p1} to θ_{p8}, were attributed to each of the eight scleral regions, respectively (Figure 6.3.2). For simplicity, the ONH was assumed to be an incompressible, linear elastic material with an elastic modulus of 1 MPa for all eyes.

6.6. Estimation of Model Parameters: Inverse Finite Element Method

For each posterior scleral shell, we estimated a set of thirteen model parameters (c_1, c_3, c_4, k_1, k_2, θ_{p1} to θ_{p8}) from the experimental data using an inverse FE method that is described in our previous report (Girard *et al.* 2008b). Briefly, the inverse FE method allows the thirteen model parameters to be determined from the experimentally-measured displacements by simultaneously varying their values until the FE-predicted displacements (x, y, and z) closely match the experimentally-measured displacements for all IOP levels (7, 10, 20, 30 and 45 mm Hg). The inverse FE method is driven by a genetic optimization algorithm (*i.e.* differential evolution (Price *et al.* 2005; Olberding

and Suh 2006)) and yields a unique set of thirteen model parameters for each scleral shell (Girard *et al.* 2008b). Notice that a good agreement was obtained between the FE-predicted and experimentally-measured displacements according to an error criterion defined in Chapter 5 (Girard *et al.* 2008b).

6.7. Additional Measures of Scleral Stiffness

Tangent Modulus

The model parameters c_3 and c_4 describe the stretch-induced stiffening of the collagen fibers, but do not represent a direct measure of scleral stiffness at each IOP. To capture scleral tissue stiffness, two additional quantities were calculated and mapped: the tangent modulus along the preferred fiber orientation and the tangent modulus perpendicular to the preferred fiber orientation. Both tangent moduli represent estimates of local scleral tissue stiffness (a bulk tissue property), can be computed at each IOP, and are functions of the model parameters and the local collagen fiber stretch.

Structural Stiffness

Clinical discussions concerning the observable mechanical behavior of the corneo-scleral shell often confuse the separate contributions of the tissues' biomechanical properties and their geometry. We calculated and continuously mapped structural stiffness – defined as the product of local scleral thickness and local values for each tangent modulus – to capture the mechanical behavior of the scleral shell as a structure in response to acute IOP elevations.

6.8. Statistical Analysis and Results

Statistical Analysis

Regional distributions of tangent moduli and structural stiffnesses were compared between age groups (young and old) for both the peripapillary and peripheral sclera using the generalized estimating equation method. Thickness measurements were compared between age groups using a multiple linear regression.

Results Common to all Eyes and Monkeys

The predicted model parameters (except the eight preferred fiber orientations), as well as monkey age and sex information are reported in Table 6.8.1 for each eye. The maps of scleral thickness, experimentally-measured and FE-predicted displacements, tangent modulus, structural stiffness, maximum principal stress and strain, and the eight predicted preferred fiber orientations are presented in Figure 6.8.1 for each eye. The pooled distributions of preferred fiber orientation are shown in Figure 6.8.2. Finally, the pooled distributions (25th, 50th and 75th percentiles) of maximum principal stress and strain as well as tangent moduli are presented in Figure 6.8.3.

Scleral thickness, experimentally measured at an IOP of 5 mm Hg at twenty locations and interpolated over each scleral shell, is shown in Figure 6.8.1 (first row). In all eyes, the peripapillary sclera was much thicker than the peripheral sclera. Among all regions (*i.e.* inferior, infero-nasal, nasal, supero-nasal, superior, supero-temporal, temporal, infero-temporal), the sclera was considerably thicker in the temporal region for all sixteen eyes ($p < 0.0001$).

For each eye, good agreement (according to a criterion defined in Chapter 5) was obtained between FE-predicted and experimentally-measured displacements at all IOPs (second and third rows of Figure 6.8.1). Figure 6.8.1 also shows that the results obtained for the two eyes of each monkey are remarkably similar for all measures, but vary more substantially between monkeys.

Regional variations (inhomogeneity) in tangent modulus and structural stiffness along the preferred fiber orientation, and in maximum principal strain and stress at an IOP of 30 mm Hg were present and consistent within the eyes of each monkey (Figure 6.8.1). In all eyes, we observed that tangent modulus was higher in the peripheral sclera than in the peripapillary sclera, which suggests that tangent modulus is inversely related to scleral thickness. As a result, the structural stiffness, the local product of the tangent modulus and scleral thickness, was more homogeneously distributed when compared to scleral thickness and tangent modulus. From Figure 6.8.1, we consistently observed tangent modulus, structural stiffness, strain and stress concentrations near the scleral canal.

Maps of the predicted preferred fiber orientation for all eight regions of each eye are shown in Figure 6.8.1, where ⊥ (white) indicates a preferred fiber orientation perpendicular to the scleral canal, and ∥ (black) a preferred fiber orientation tangent to the scleral canal. Figure 6.8.2 shows the pooled distributions of the preferred fiber orientation for all sixteen eyes in both the peripapillary and peripheral sclera. In general, the mean preferred fiber orientation for all tested eyes was tangent to the scleral canal in both scleral regions. However, the pooled distribution in the peripheral sclera was slightly more uniform than in the peripapillary sclera.

Separate from the above results, the fiber concentration factor in the peripapillary sclera (k_2) was higher than that in the peripheral sclera (k_1) for fourteen of the sixteen eyes studied (Table 6.8.1). This result suggests that the collagen fibers are more aligned along the preferred fiber orientation (as explained in Figure 6.4.1) in the peripapillary sclera compared to the peripheral sclera. Note that non-zero fiber concentration factors suggest that the sclera is anisotropic (Figure 6.4.1).

Overall distributions of the tangent moduli in both the peripapillary and peripheral sclera are shown on Figure 6.8.3. Tangent moduli dramatically increased from 5 to 45 mm Hg in both regions of all scleral shells. This finding confirms that the posterior sclera is highly nonlinear and becomes stiffer as IOP increases. Also note that the tangent moduli were higher in the thin peripheral sclera than in the thick peripapillary sclera. In all eyes, maximum principal strain (a local measure of tensile deformations) was a nonlinear function of IOP and relatively low even at IOP = 45 mm Hg (1.1 % and 0.5 % on average, in the peripapillary sclera from young and old monkeys, respectively). Maximum principal stress (a local measure of internal forces) was a linear function of IOP and considerably higher than IOP (17 and 24 × IOP on average in the peripapillary sclera from young and old monkeys, respectively).

Age-related Changes in Scleral Biomechanics

The posterior sclera was significantly thinner in the eyes from old monkeys compared to that from young monkeys ($p = 0.038$).

The parameters c_1 and c_4 (Table 6.8.1) were generally higher in the eyes from the old monkeys, which suggests that the aged eyes have a stiffer ground substance matrix

and a higher collagen fiber uncrimping rate (*i.e.* the fibers stiffen more quickly as IOP increases) than eyes from younger monkeys. Accordingly, the scleral tangent moduli from old monkeys increased by a factor of approximately 7 to 8 for IOPs from 5 to 45 mm Hg, compared to a factor of approximately 4 to 5 in sclera from young monkeys, as illustrated in Figure 6.8.3. Scleral tangent moduli and structural stiffnesses (along and perpendicular to the preferred fiber orientation) were significantly higher for the old monkey eyes in both the peripheral and peripapillary sclera at all levels of IOP ($p < 0.001$ for all comparisons). Figure 6.8.3 also shows that posterior sclera from old monkeys exhibited less strain but higher stress than that from young monkeys at all levels of IOP for both the peripheral and peripapillary sclera regions. Note that even though our results show that young monkeys exhibited significantly lower scleral tangent moduli and structural stiffnesses, one pair of eyes (monkey 2) was in the same range as the old group (Figure 5).

We did not detect age-related changes in the fiber concentration factor ($p > 0.05$) or in the preferred fiber orientation ($p > 0.05$) in any regions.

	Monkey	1		2		3		4	
Young Sclera	Sex	M		M		M		M	
	Age [years]	0.5		1.7		1.7		2.1	
	Eye	os	od	os	od	os	od	os	od
	c_1 [kPa]	116	63	782	629	200	192	197	100
	c_3 [kPa]	26.6	19.4	3.42	2.16	14.8	21.2	6.19	15.6
	c_4 [-]	280	273	1344	1574	325	362	602	505
	k_1 [-]	1.56	1.37	1.98	1.65	1.28	2.67	2.25	1.40
	k_2 [-]	1.67	3.14	1.49	2.99	1.84	3.61	2.65	4.57
Old Sclera	Monkey	5		6		7		8	
	Sex	M		F		M		F	
	Age [years]	18.0		20.3		23.0		30.3	
	Eye	os	od	os	od	os	od	os	od
	c_1 [kPa]	1290	1191	2039	964	1520	2722	643	232
	c_3 [kPa]	61.9	7.41	2.38	1.60	6.19	4.16	4.21	5.82
	c_4 [-]	463	1236	1703	1583	1717	2934	1345	1390
	k_1 [-]	1.40	1.15	4.99	1.62	1.20	2.04	1.50	2.10
	k_2 [-]	2.67	1.49	0.39	4.99	3.84	3.00	2.23	5.78

Table 6.8.1. Estimated model parameters (c_1, c_3, c_4, k_1 and k_2) from inverse FE simulations. Data are shown for both eyes of each monkey in both the young and old groups. Note that all eight other model parameters for each eye (the preferred fiber orientations) are shown in the last row of Figure 5.
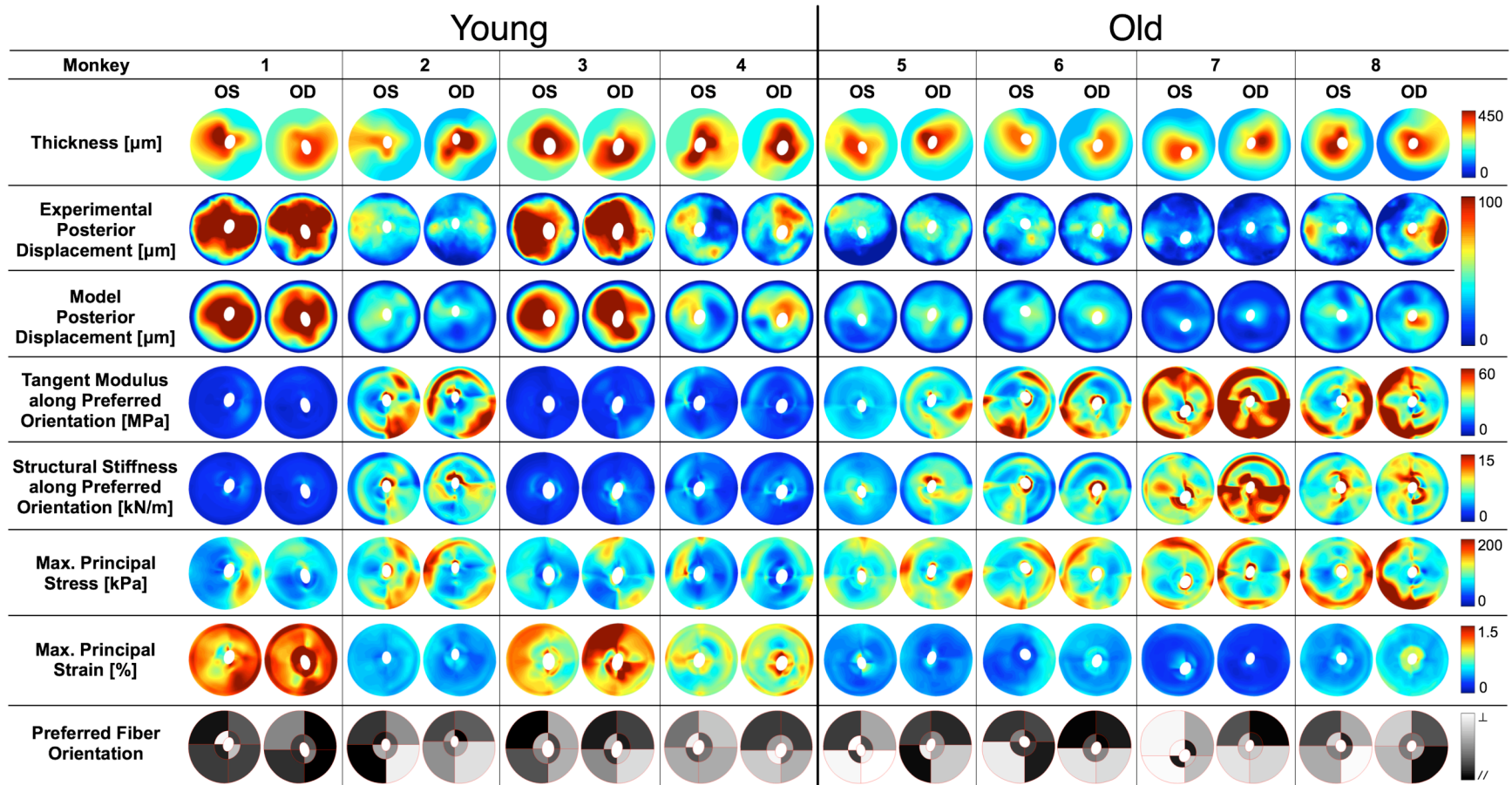
Figure 6.8.1. Individual results for all posterior scleral shells as viewed from the back of the eye (Superior is up). Scleral thickness was experimentally measured at IOP = 5 mm Hg and interpolated to obtain continuous thickness maps. Tangent modulus, structural stiffness, maximum principal stress and strain are shown for all eyes at a single IOP of 30 mm Hg. Good agreement is observed between FE-predicted and experimentally measured posterior displacements (plotted for an IOP range of 5-30 mm Hg). Finally the preferred fiber orientation is shown for all eight regions of each eye, where // (black) corresponds to a collagen fiber organization tangent to the scleral canal (circumferential, $\theta_p = 0°$) and ⊥ (white, $\theta_p = 90°$) corresponds to a fiber organization that is perpendicular to the scleral canal (meridional). Note that the data for the two eyes of each monkey are much more similar than between monkeys, and there are clear age-related differences in all measures except for preferred collagen fiber orientation.
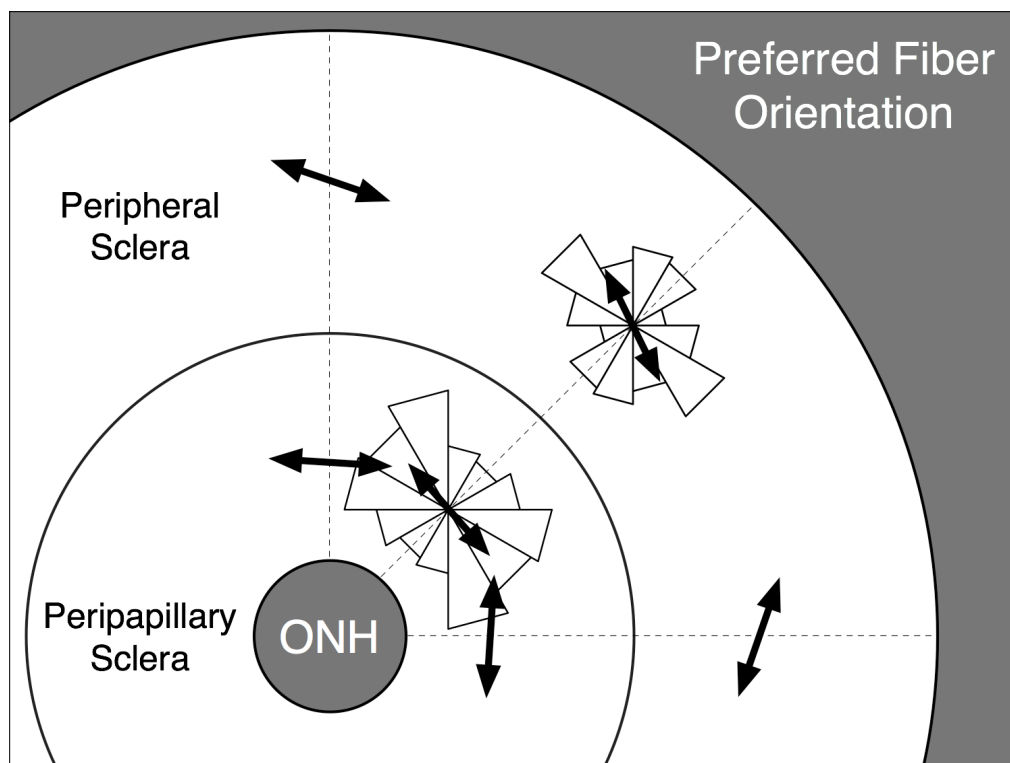
Figure 6.8.2. Pooled Distributions (all eyes) of the preferred fiber orientation in both the peripapillary and peripheral scleral regions are shown as two symmetric rose diagrams, in which larger triangles indicate the most commonly predicted orientations. Mean preferred fiber orientations were calculated from the distributions (black arrows) and suggest a circumferential organization of the collagen fibers around the scleral canal in both the peripapillary and the peripheral sclera.
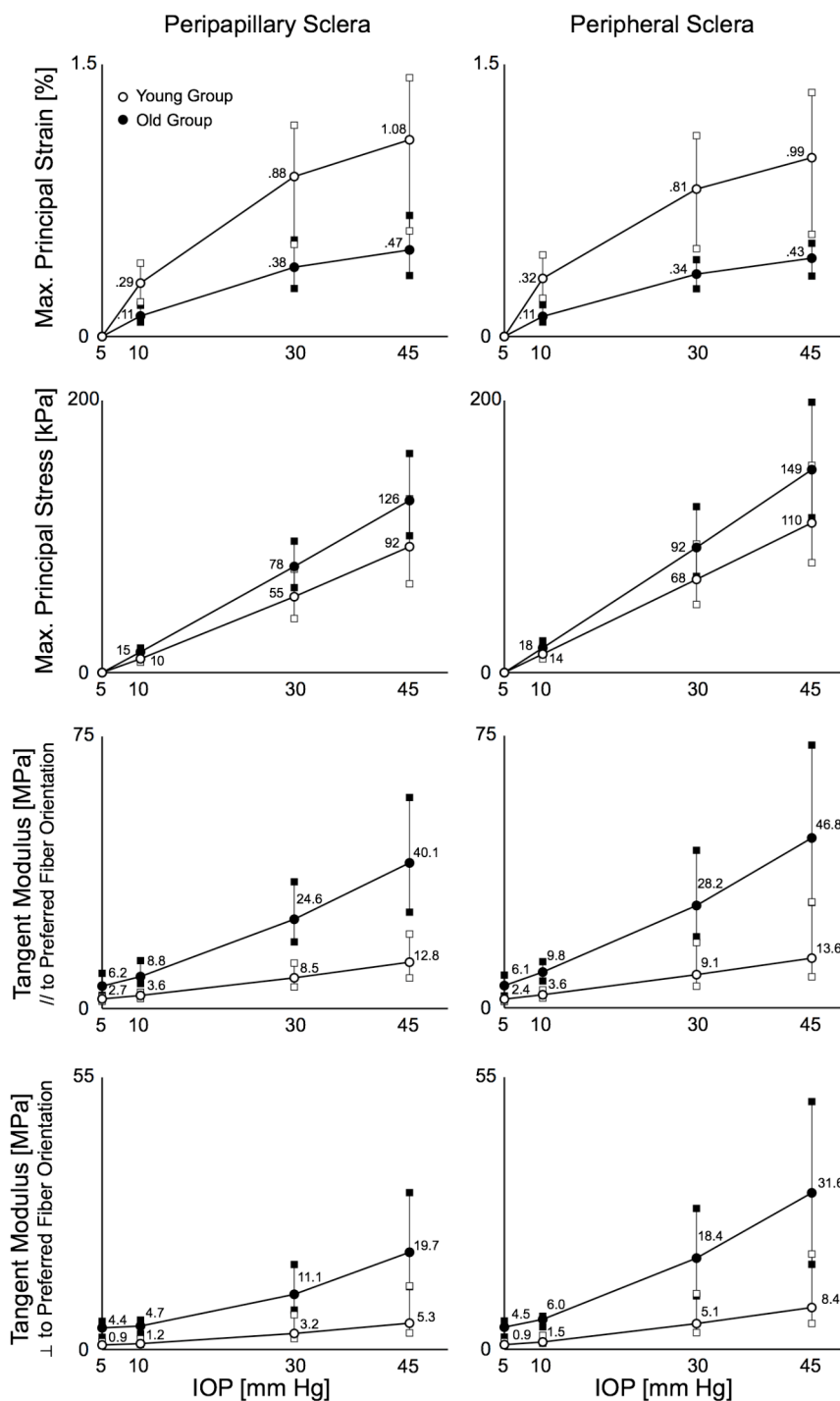
Figure 6.8.3. Maximum principal strain, maximum principal stress, and tangent moduli distributions (error bars show the 25th, 50th, and 75th percentiles) plotted by age group for both scleral regions (peripapillary and peripheral) at the following IOPs: 5, 10, 30 and 45 mm Hg. On average, sclera from the old monkeys exhibited higher tangent moduli and stress, but lower strain than that from the young monkeys. Note the nonlinear relationship between IOP and strain, which is due to the exponential increase of tangent moduli with IOP (the sclera stiffens as IOP increases).

6.9. Discussion

In this report, we measured 3-D displacements of the posterior scleral shell from both eyes of 4 young and 4 old monkeys exposed to acute elevations of IOP from 5 to 45 mm Hg, and estimated inhomogeneous, anisotropic, nonlinear biomechanical properties for each individual shell using an inverse FE method. Our principal findings are as follows. First, peripapillary and posterior sclera is significantly thinner in aged eyes. Second, the monkey posterior sclera is a highly nonlinear, anisotropic, and inhomogeneous soft-tissue. Third, inverse FE simulations predicted that collagen fibers were, on average, circumferentially oriented around the scleral canal in both the peripapillary and peripheral sclera (Figure 6.8.2), as well as more aligned along the preferred fiber orientation in the peripapillary sclera (Table 6.8.1). Fourth, monkey peripapillary and posterior sclera stiffens significantly with age by all measures considered in this study. Fifth, peripapillary concentrations of tangent modulus, structural stiffness, strain and stress (adjacent to the scleral canal) were present at high IOP in each eye. Sixth, apart from their concentrations, the magnitude of peripapillary and posterior scleral stress were substantially higher than IOP at all levels of IOP. Seventh, the magnitude of strain in the peripapillary and posterior sclera of both the young and old eyes was surprisingly low.

On average, the sclera was thickest in the peripapillary region overall and in the temporal region specifically (Figure 6.8.1), which is in agreement with our previous study on thickness characterization of monkey posterior sclera using traditional histology (Downs *et al.* 2001). We also observed a significant thinning of the sclera with age ($p = 0.038$). Jackson and coworkers (Jackson *et al.* 2006) also reported a decreasing trend in

human scleral thickness with age but their finding was not significant (p = 0.122). In addition to these age-related effects, we previously reported significant scleral thinning in response to early experimental glaucoma in a separate group of monkey eyes (Downs *et al.* 2001).

Figure 6.8.3 shows that monkey posterior sclera exhibited a highly nonlinear response to acute IOP elevation from 5 to 45 mm Hg as demonstrated by the dramatic increase in tangent moduli with IOP. This behavior was observed in all eyes in both age groups, and has been previously discussed in Chapters 3 and 5. Interestingly, the rate of scleral stiffening with IOP was higher in the posterior sclera from old monkeys (7 to 8 fold) compared to that from young monkeys (4 to 5 fold). This finding suggests that aged eyes are likely to exhibit a reduction in their ability to absorb transient IOP elevations, which may expose the aged ONH to additional transient biomechanical insults. The accumulated exposure to IOP spikes over a period of years may contribute to age-related glaucomatous susceptibility, which has been previously proposed (Burgoyne and Downs 2008; Downs *et al.* 2008).

The maps of preferred fiber orientation show that monkey posterior sclera is highly anisotropic and inhomogeneous, which manifests most prominently as non-zero fiber concentration factors (Table 6.8.1) and as inhomogeneous tangent modulus fields (Figure 6.8.1). It is interesting to note that as a mechanical structure, structural stiffness is relatively more homogeneous than scleral thickness and tangent modulus. This indicates that these eyes are likely to expand relatively uniformly as IOP increases, and that the eye's mechanical response is optimized to maintain the constant retinal curvature necessary for focused vision.

In all eyes, inverse FE simulations predicted that the collagen fibers were, on average, circumferentially oriented around the scleral canal in both the peripapillary and peripheral sclera (Figure 6.8.2), which is consistent with previous histologic results for the peripapillary sclera (Kokott 1934; Hernandez *et al.* 1987). Moreover, in 14 of 16 eyes, the collagen fibers tended to be more highly aligned along their preferred orientations in the peripapillary sclera compared with the peripheral sclera as shown by the higher peripapillary fiber concentration factor (k_2; Table 6.8.1). Our computational study of posterior scleral biomechanics in Chapter 4 suggests that the presence of highly aligned, circumferential fibers in the peripapillary sclera reduces IOP-induced scleral canal expansion considerably, and this arrangement may be biologically optimized to protect the contained ONH from biomechanical damage.

Although sclera was thinner in old monkey eyes, their tangent moduli were higher, and the resulting structural stiffness was higher than that measured in young monkey eyes ($p < 0.001$). In fact, aging effects were measured in all parameters, in which posterior sclera from old eyes was thinner, yet exhibited higher tangent moduli, structural stiffness and stress but lower strain, compared to eyes from young monkeys.

In all eyes, we observed high tangent modulus, structural stiffness, strain and stress at the scleral canal boundary. Since the lamina cribrosa inserts deeply into the peripapillary sclera and is a highly compliant tissue, it is reasonable for the sclera to be reinforced with high tangent modulus and structural stiffness at the scleral canal boundary in order to resist potential high strain insults. As for the secondary effects of peripapillary scleral connective tissue stress, it is currently unknown if it is correlated with cellular behavior or altered blood flow within the posterior ciliary arteries. Future

efforts will assess its role as a risk factor for, and its contributions to, glaucomatous damage within the ONH and peripapillary sclera.

Our reported stress values within the peripapillary sclera were considerably higher than IOP at all IOP levels (17 and $24 \times$ IOP on average but rising as high as 24 and $32 \times$ IOP in the 75th percentiles) for both young and old monkeys, respectively. These stress values are significantly higher than those initial hypothesized by Greene and coworkers (Greene 1980) and comparable to the ranges reported by Bellezza and coworkers (Bellezza *et al.* 2000) in idealized FE models of the human eye (11 to $27 \times$ IOP in the peripapillary sclera) and by Sigal and coworkers (Sigal *et al.* 2004) in idealized FE models of the human eye (9 to $12 \times$ IOP in the posterior sclera). Our stress estimates were obtained based on anatomically-accurate posterior scleral geometries, 3-D experimental deformation measurements and a highly-improved constitutive theory, which were missing in both aforementioned FE studies and are therefore likely to be the most accurate estimates to date for the monkey eye.

Our reported strain values were consistently low (2.4% was the highest peak strain detected) as opposed to strains experienced by other thin collagenous soft-tissues such as arteries and ligaments (Weiss and Gardiner 2001; Zulliger *et al.* 2004). A variety of previous studies have reported that mechanical strain on scleral fibroblasts resulted in the suppression of TIMP-1 (0.45 % cyclic strain in humans (Yamaoka *et al.* 2001)), in changes in gene expression (4 % constant strain in humans (Cui *et al.* 2004)), in the production of MMP-2 and suppression of TIMP-2 (15 % cyclic strain in humans (Shelton and Rada 2007)), and in enhanced expression of both MMP-2 and TIMP-2 mRNA (20 % cyclic strain in chicks (Fujikura *et al.* 2002)). According to these studies, a wide range of

strain levels has the capacity to trigger remodeling of the scleral extracellular matrix which could result in scleral thinning or thickening, and/or scleral softening or stiffening. Our data do not suggest that the monkey peripapillary and posterior sclera achieves the levels of strain in these previous reports, except for one (0.45 % strain). Further studies will be needed to characterize how the scleral extra-cellular matrix is affected by the levels of strain that we report.

Considered together, the results of this study raise important clinical questions regarding the role of age-related peripapillary and posterior scleral stiffening in the susceptibility to glaucomatous damage and clinical behavior of the aged eye (Burgoyne and Downs 2008). Understood in its simplest terms, if all other components of ONH biomechanics are equal, an isolated increase in scleral stiffness (that is not accompanied by an increase in lamina cribrosa beam stiffness) should limit scleral canal expansion-induced tightening of the lamina cribrosa at elevated IOP. In this scenario the lamina will be left exposed to the direct action of IOP on the ONH surface leading to more (rather than less) laminar deformation at all levels of IOP.

However, the aged lamina is more likely to have stiff connective tissues (Quigley 1982; Hernandez *et al.* 1989; Morrison *et al.* 1989b; Albon *et al.* 1995; Albon *et al.* 2000a; Albon *et al.* 2000b; Kotecha *et al.* 2006; Albon *et al.* 2007) and a compromised blood supply (Grunwald *et al.* 1993; Harris *et al.* 2000). Age-related increases in laminar beam thickness (Hernandez *et al.* 1989; Morrison *et al.* 1989a; Hernandez *et al.* 1991; Albon *et al.* 1995; Kotecha *et al.* 2006), laminar astrocyte basement membrane thickness (Hernandez *et al.* 1989; Hernandez *et al.* 1991), and laminar extracellular matrix hardening (Hernandez *et al.* 1989; Morrison *et al.* 1989a; Hernandez *et al.* 1991; Albon *et*

al. 1995) should not only increase laminar beam stiffness, but should also diminish nutrient diffusion from the laminar capillaries through the laminar extracellular matrix, across the astrocyte basement membranes, and into the adjacent axons.

In general, for a given magnitude of IOP insult, the aged ONH should demonstrate less deformation due to the presence of a stiffer lamina and a stiffer peripapillary sclera. But as can be seen by the above discussion, the effects of scleral stiffness alone, without knowing the biomechanical properties or behavior of the lamina, will be difficult to predict. Whether a stiff sclera is always associated with a stiff lamina and whether a stiff lamina is more or less prone to axon loss for a given form of IOP insult, are core issues in the study of ONH susceptibility. These studies and the devices necessary to carry them out are under development in our own (Burgoyne *et al.* 2008) and other's (Srinivasan *et al.* 2008) laboratories. We are currently using biomechanical FE modeling to study the interactions between scleral and ONH biomechanics and their contributions to the susceptibility of the aged monkey and human eye. This work will be the topic of future reports.

Several limitations should be considered when viewing this work. While the general limitations of the method have been discussed at length in Chapter 5, we will briefly revisit them and focus only on those inherent to this study. First, we have assumed that collagen was the primary fibrous element (Fung 1993) of the sclera, and we have lumped all other tissue constituents into the ground substance matrix. This is a common practice in soft-tissue FE modeling (Weiss *et al.* 1996; Holzapfel *et al.* 2000). As such, our formulation assumes that inhomogeneity of the sclera is solely dependent on the orientation of the collagen fibers. For simplicity we have ignored the regional-variations

in collagen fiber diameter and elastin content that are known to exist within the posterior sclera (*e.g.* relatively large collagen fiber diameter and almost no elastin in the peripheral sclera of human eyes (Quigley *et al.* 1991)). Adding such information to a constitutive theory is not a straightforward task and further experimental and theoretical work will be needed to address how these components influence scleral biomechanics. In total, these limitations should not alter the results or conclusions of this study.

Second, we did not characterize scleral biomechanics between 0 and 5 mm Hg in the tested eyes, because the scleral shells required an IOP of approximately 4 mm Hg to sustain their shape. The inherent 'floppiness' of monkey sclera is an indication that residual scleral stress is minimal and can be neglected. IOPs in the range of 0-5 mm Hg are rarely measured in monkey eyes, so ignoring the initial IOP loading should not compromise the clinical importance of our results.

Third, the ONH tissues were assumed to be linearly elastic, with a common elastic modulus of 1 MPa assigned to the ONH region for both young and old monkey eyes. As previously mentioned, evidence suggests that ONH tissues (especially the lamina cribrosa) become considerably stiffer with age and therefore we could have assigned a lower elastic modulus for the younger eyes. In the absence of reported data on age-dependent laminar moduli in monkeys, we felt it was cautious to assign a common laminar modulus to all eyes to facilitate comparison of scleral biomechanics between age groups. Our previous sensitivity study showed that ONH elastic moduli in the range of 0.1 - 5 MPa did not affect the results of our scleral biomechanical property fitting as shown in Chapter 5. This agrees with several studies that have shown that ONH biomechanics has only a slight impact, if any, on scleral biomechanics (Sigal *et al.* 2004;

Sigal *et al.* 2005; Girard *et al.* 2008c) (the inverse being untrue). Hence, our assumption of using the same ONH modulus for both young and old eyes should not impact the results presented herein.

Fourth, the ONH was represented as an elliptical cylinder, with its external boundary located at the outer aspect of the dural sheath insertion (as measured with the 3-D digitizer) and was therefore larger than one would expect (~2 mm along the major axis in our model, compared with ~1.5 mm for an anatomic ONH). A better characterization of ONH biomechanics that incorporates accurate ONH geometries and inhomogeneous, anisotropic biomechanical properties is currently underway in our laboratory (Downs *et al.* 2007; Roberts *et al.* 2007). When combined with the present work on scleral biomechanics, we should gain an enhanced understanding of the complex interactions between scleral and ONH biomechanics.

Fifth, we divided each reconstructed scleral shell into eight regions to preliminarily asses regional variations in predicted collagen fiber orientation (θ_{p1} to θ_{p8}). Specifying more regions, and therefore more model parameters, would dramatically increase the computational time required for each inverse FE simulation and raise concerns about solution uniqueness (*i.e.* a unique set of model parameters for each eye). Our preliminary study confirmed that a combination of eight regions and thirteen model parameters was the minimum requirement to obtain good agreement between the FE-predicted and experimentally-measured displacements (Figure 6.8.1) while also ensuring a unique set of model parameters (data not shown). Note that dividing the posterior sclera into eight regions resulted in strain, stress, tangent modulus, and structural stiffness discontinuities in the vicinity of the regional boundaries (Figure 6.8.1). This limits

accuracy of the models at those boundaries and introduces artificially high stress and strain in those areas. We were careful to ignore these artificially high values in the presentation of results in Figure 6.8.3, in which we reported the 25th, 50th, and 75th percentile values of each parameter.

Finally, collagen fiber alignment was not measured directly, but was predicted using the models' fits to experimentally-measured scleral deformations (Figure 6.8.2). Due to the relatively coarse discretization of the regions (discussed above) we could only report an overall approximation of the preferred collagen fiber orientation within each region. Future inclusion of experimentally-derived collagen fiber orientation maps as an input parameter will allow for finer regional discretization for the remaining fitted parameters, and improve our characterization of scleral anisotropy.

In summary, new experimental and computational methodologies, as described in Chapters 4 and 5, have been applied to the study of scleral biomechanics in the aging monkey eye. These methods can be applied to other thin soft tissues with multi-directional collagen fibers and will now be used to characterize scleral biomechanics in glaucomatous monkey eyes. The long-term goal of this work is to establish the pathophysiologic links between connective tissue stress/strain within the peripapillary sclera and lamina cribrosa and retinal ganglion cell axon damage and death. Given the determining role of scleral biomechanics on both the neural and connective tissues of the ONH, new strategies for the clinical study (visualization and measurement) of peripapillary and posterior scleral biomechanics are indicated.

7   Scleral Biomechanics in the Glaucomatous Monkey Eye[1]

7.1. Abstract

Custom 3-D experimental and computational tools were developed to investigate the differences in biomechanical properties of posterior sclera between normal and glaucomatous monkey eyes. Experimental glaucoma was achieved in one eye of eight rhesus monkeys, which resulted in ocular hypertension with various degrees of intraocular pressure (IOP) insult. The posterior scleral shells from contralateral normal and glaucomatous eyes of each monkey were individually mounted on a custom-built pressurization apparatus. IOP was incrementally increased from 5 to 45 mm Hg, and the 3-D displacements of each shell were measured using speckle interferometry. The geometry of each scleral shell was reconstructed from data generated by a 3-D digitizer (topography) and a 20 MHz ultrasound transducer (thickness). A fiber-reinforced constitutive model that includes stretch-induced stiffening and multi-directionality of the collagen fibers was applied to each scleral shell, and a unique set of biomechanical

---

properties was obtained using an inverse finite element (FE) method. For all eyes, the posterior sclera exhibited inhomogeneous, anisotropic, nonlinear biomechanical behavior as previously reported. Scleral biomechanical changes caused by chronic IOP elevation were complex, individual-specific and likely the result of extracellular matrix remodeling. Specifically, we observed (1) an insignificant trend toward scleral thinning in glaucomatous eyes, (2) that sclera with initially large tangent modulus or thickness were less prone to biomechanical changes, (3) that a decrease in tangent modulus (possibly due to elastin damage) occurred with low IOP insult, (4) that an increase in tangent modulus (possibly associated with collagen) occurred with large IOP insult, and (5) that fiber reorientation did not occur in glaucomatous eyes. Since the sclera drives the IOP-induced stress and strain levels transmitted to the optic nerve head (ONH), a change in the biomechanical environment of the posterior sclera through remodeling will inevitably disturb that of the ONH.

7.2. Introduction

Open angle glaucoma occurs at both normal (*i.e.* normal-tension glaucoma) and elevated (*i.e.* high-tension glaucoma) levels of IOP with no distinctive etiology (Quigley 2005; Leske 2007; Drance 2008). Open-angle glaucoma is the second leading cause of blindness worldwide (Resnikoff *et al.* 2004; Foster and Resnikoff 2005) and is characterized by connective tissue and axonal damage at the ONH (Quigley and Anderson 1976; Quigley and Addicks 1980). While open-angle glaucoma is most likely a multi-factorial disease, some researchers have theorized that the biomechanics of the ONH and scleral shell plays a central role in driving several pathologic mechanisms that are central to the neuropathy (Burgoyne *et al.* 2005; Ethier 2006).

The ONH is a biomechanically compliant tissue in an otherwise strong pressure vessel – the corneo-scleral envelope (Bellezza *et al.* 2000; Sigal *et al.* 2004). The ONH contains the lamina cribrosa, a fenestrated connective tissue meshwork that spans the scleral canal and provides structural and functional support to the retinal ganglion cell axons as they exit the eye and continue their journey to the brain. The lamina cribrosa inserts deeply into the sclera, which is the principal load bearing tissue of the eye and primarily composed of collagen. Ninety percent of the collagen fibers in the sclera are Type I (Edelhauser and Ubels 2003), which provide the eye with the necessary biomechanical strength to resist IOP. Scleral collagen fibers have a large variation in their diameters (Quigley *et al.* 1991b) and are formed into irregularly arranged, multi-layered lamellae of varying thickness (Rada *et al.* 2006). Within each lamella, the collagen fibers run perpendicular to the transmural direction of the sclera and are oriented along a preferred orientation to varying degrees (Watson and Young 2004).

Recent studies have indicated that scleral collagen fiber organization (Girard *et al.* 2008c) and scleral stiffness (Sigal *et al.* 2005) likely have a large impact on IOP-induced ONH deformations. In order to study ONH biomechanics as a potential driving mechanism in glaucoma, computational biomechanical models based on the FE method should incorporate accurate geometries and biomechanical properties for both the ONH and posterior scleral shell.

Using the monkey model of glaucoma, in which one eye is exposed to chronic IOP elevation, we have shown significant remodeling of the scleral and ONH connective tissues at the earliest stage of glaucomatous damage. In the load-bearing tissues of the monkey eye, morphologic changes were observed such as permanent deformation of the lamina cribrosa (Burgoyne *et al.* 2004), thickening of the lamina cribrosa and mild thinning of the peripapillary sclera (Yang *et al.* 2007a; Yang *et al.* 2007b), increases in both connective tissue volume and total number of beams in the lamina cribrosa (Roberts *et al.* 2008), and a significant thinning of the posterior sclera (Downs *et al.* 2001). These changes likely occur due to an increased cellular activity within the load-bearing tissues of the eye that correlates with increased IOP-induced strain and stress levels. Remodeling will alter the biomechanical properties of the load-bearing tissues of the eye, which in turn might precipitate retinal ganglion cell axon death either directly or indirectly. Knowledge and quantification of ONH and scleral tissue remodeling is therefore crucial to understand the development and progression of glaucomatous optic neuropathy.

This study primarily focuses on the posterior scleral shell, and we have previously shown that the biomechanical properties of the peripapillary sclera are altered in experimental glaucoma using uniaxial testing and linear viscoelastic theory (Downs *et al.*

2003; Downs *et al.* 2005). In the present report, we refine our experimental and computational techniques to characterize peripapillary and posterior scleral biomechanics in 3D in the normal monkey eyes and those with early and moderate glaucomatous damage. Specifically, we experimentally measure the 3-D deformation pattern of posterior sclera from both eyes of eight monkeys (one eye normal and one eye glaucomatous in each monkey) following acute IOP elevation from 5 to 45 mm Hg. Using experimentally measured geometric profile (*i.e.*, surface profile and thickness data) of each posterior sclera, we then model the posterior sclera as a nonlinear, anisotropic, inhomogeneous soft-tissue using a fiber-reinforced constitutive theory (Green 1970; Spencer 1974) that includes stretch-induced stiffening (Weiss and Gardiner 2001) and multi-directionality of the collagen fibers (Lanir 1983; Billiar and Sacks 2000; Freed *et al.* 2005; Pinsky *et al.* 2005; Gasser *et al.* 2006; Boyce *et al.* 2007; Girard *et al.* 2008c; Nguyen *et al.* 2008). We then derive shell-specific sets of biomechanical properties based on the experimental observations using an inverse FE method. These experimental and computational techniques have been previously described in Chapters 4 and 5, and applied to characterize peripapillary and posterior scleral biomechanics in the aging monkey eye in Chapter 6.

7.3. Experimental Setup and Testing Protocol

Experimental Glaucoma and Cumulative IOP Insult

All experiments adhered to the ARVO statement for the Use of Animals in Ophthalmic and Vision Research. In this study, experimental glaucoma was induced in one eye of eight rhesus monkeys without initial ocular abnormality. Our protocol for

generating experimental glaucoma has been fully described in previous reports (Burgoyne *et al.* 2004; Downs *et al.* 2007b; Yang *et al.* 2007a; Yang *et al.* 2007b). Briefly, the trabecular meshwork was photocoagulated using laser in one eye of each monkey in order to elevate IOP. After the initial photocoagulation, IOP was monitored with a TonoPen (Reichert, Depew, NY) over time in both eyes of each monkey (Figure 7.3.1). After the first IOP elevation was confirmed, all eight monkeys were maintained for different time periods in order to create different stages of scleral biomechanical changes due to elevated IOP. Here, we defined the cumulative IOP insult as an IOP insult accumulated over the time period, which can be represented as the difference in area under the IOP-time curve between the glaucomatous (in red; Figure 7.3.1) and the normal (in blue; Figure 7.3.1) eye. In Figure 7.3.1, monkey specimen were arranged in order of increasing cumulative IOP insult, where monkey 1 received the lowest cumulative IOP insult and monkey 8, the highest. Note that the stage of early glaucoma, confirmed by a change in ONH compliance as measured by confocal scanning laser tomography (Burgoyne *et al.* 2004; Downs *et al.* 2007b; Yang *et al.* 2007a; Yang *et al.* 2007b), was at least achieved in each of the eight glaucomatous monkey eyes.
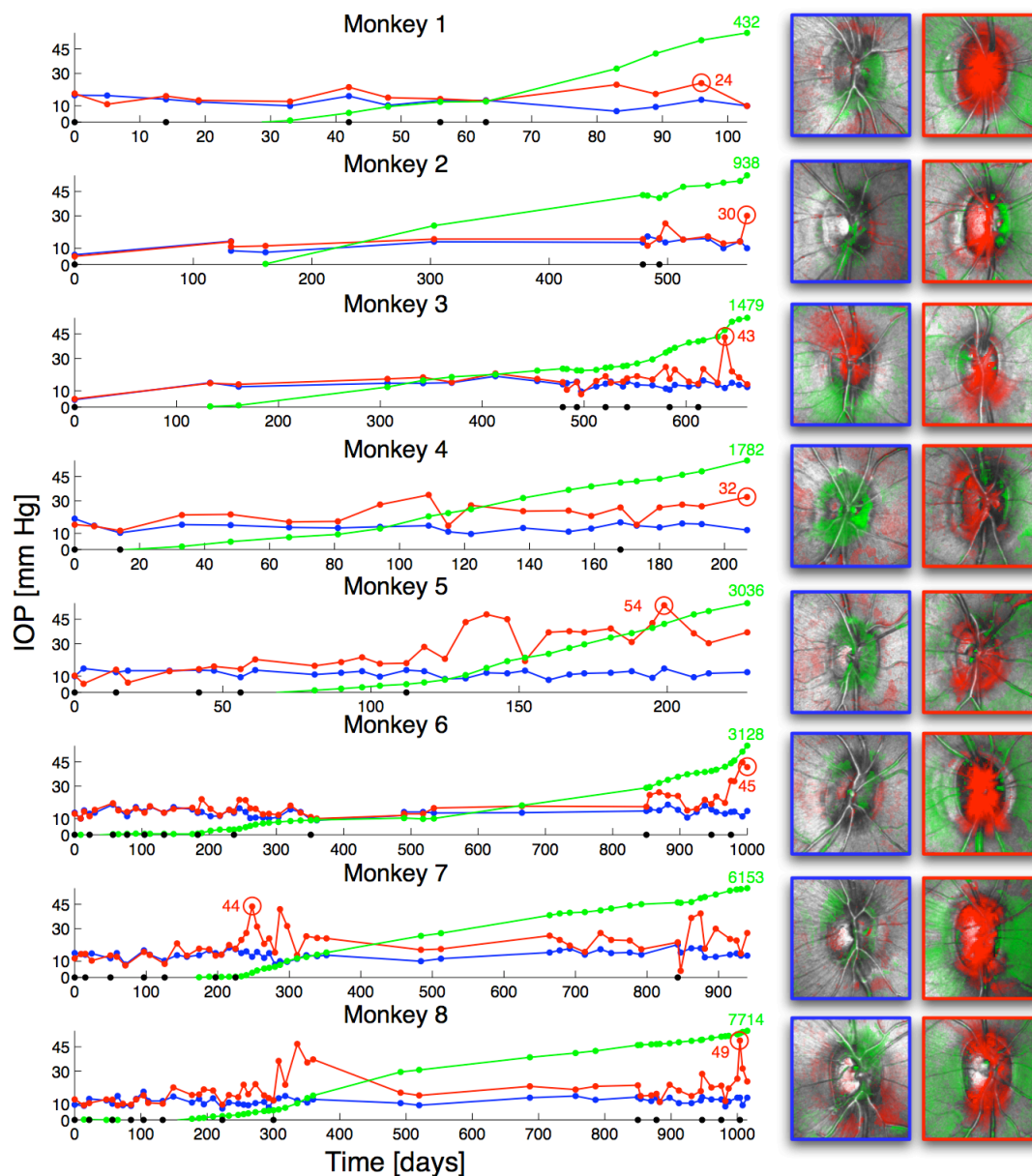
Figure 7.3.1. For each monkey, IOP was monitored over time in both eyes (blue: normal, red: glaucomatous). Cumulative IOP insult was defined as the difference in area under the IOP-time curve between the glaucomatous and normal eye. Monkey 1 received the lowest cumulative IOP insult, and monkey 8 the highest. For each graph, the first day corresponds to the first lasering of the glaucomatous eye, and the last day corresponds to the sacrifice of the monkey. The maximum IOP magnitude in glaucomatous eyes is shown with a red circle. Cumulative IOP insult is shown as a green curve, as well as its maximum value at the day of sacrifice. Black dots represent the days during which photocoagulation was performed. Topographic change analysis maps (OD configuration; last day compared to first day baseline; red and green: posterior and anterior deformation of the retinal surface respectively) are shown on the right for both eyes of each monkey (blue: normal, red: glaucomatous).

Specimen Preparation and Pressurization Apparatus

For this study, we used an experimental protocol for 3-D scleral testing that has been fully documented in Chapter 5. Briefly, the posterior scleral shells from both eyes of each monkey were cleaned from intra- and extra-orbital tissues and individually mounted on a custom-built pressurization apparatus (see Chapter 5 for a detailed schematic of the pressurization apparatus). After mounting, each shell was blotted dry, covered with a contrast medium, and immediately immersed in isotonic saline at room temperature. IOP was incrementally increased from 5 to 45 mm Hg and an electronic speckle pattern interferometry sensor (Erne *et al.* 2005; Kessler *et al.* 2006) (Q100, Ettemeyer AG, Germany) was used to record the full-field 3-D displacements of each shell surface at a resolution of 0.1 μm. IOP was then reset to 5 mm Hg and scleral topography was manually measured with a 3-D digitizer arm (MicroScribe G2X, Immersion, San Jose, CA). Scleral thickness was also measured at twenty predetermined locations with a 20 MHz ultrasound transducer (PacScan 300P, Sonomed, Inc., Lake Success, NY). The topography and thickness data were combined into a reference geometry of each posterior scleral shell.

7.4. A Constitutive Theory for the Posterior Sclera

In the field of continuum solid mechanics, constitutive theories are developed to mathematically characterize the deformations (strain) and internal forces (stress) of any mechanically loaded material, including biological soft-tissues. In our constitutive theory, collagen – organized into long and dense fibrous bundles – is considered the primary biomechanical element as it provides most of the tensile strength necessary for the sclera

to resist IOP. Accordingly, the posterior sclera can be represented as a fiber-reinforced composite structure, in which the collagen fibers are embedded within a ground substance matrix, and responsible for two important biomechanical characteristics (anisotropy and nonlinearity) of the tissue. The following is a brief summary of our constitutive theory, which is fully described in Chapter 4.

Anisotropy

Anisotropy is the property by which materials exhibit different stiffnesses along different orientations. Anisotropy in thin soft tissues is generally determined by the organization of their collagen fibers, which run perpendicularly to the transmural direction (Watson and Young 2004). For our constitutive theory, a semi-circular von Mises distribution (Fisher 1993) is used to describe planar anisotropy of the posterior sclera, in which θ_p is the preferred fiber orientation and k is the fiber concentration factor (Figure 7.4.1).

Nonlinearity

Collagen fibers uncrimp with stretch (Fung 1993), which results in an increase in stiffness at the tissue level (Figure 7.4.1). This property is known as nonlinearity, and has been experimentally observed in the posterior sclera (Curtin 1969; Woo *et al.* 1972; Phillips and McBrien 1995; Siegwart and Norton 1999; Wollensak and Spoerl 2004; Spoerl *et al.* 2005; Olesen *et al.* 2007; Girard *et al.* 2008a; Girard *et al.* 2008b; Schultz *et al.* 2008; Weiyi *et al.* 2008). An increase in stiffness is known to protect soft-tissues from undergoing large deformations, which could otherwise disrupt the tissue's mechanical

integrity at the cellular level (Curtin 1969). For our constitutive theory, IOP-induced stiffening of the sclera is described by specifying the collagen fiber stress as an exponential function of the collagen fiber stretch. Within this relationship, two model parameters govern the degree of nonlinearity of the posterior sclera (c_3: exponential fiber stress coefficient, and c_4: uncrimping rate of the collagen fibers; Chapters 4 and 5). Note that the product of c_3 and c_4 dominates the scleral response at low IOP, but c_4 alone dominates the scleral response at high IOP.

Ground Substance Matrix

In our formulation, the ground substance matrix - not to be confused with the extracellular matrix - contains all non-collagenous tissue components (*e.g.* elastin, glycosaminoglycans, proteoglycans, fibroblasts, tissue fluid) and provides mechanical resistance at low stretch. The ground substance matrix is assumed to be isotropic and linearly elastic, and its mechanical behavior is hence modeled with a single intrinsic parameter (c_1, the 1st Mooney-Rivlin coefficient; Chapters 4 and 5).
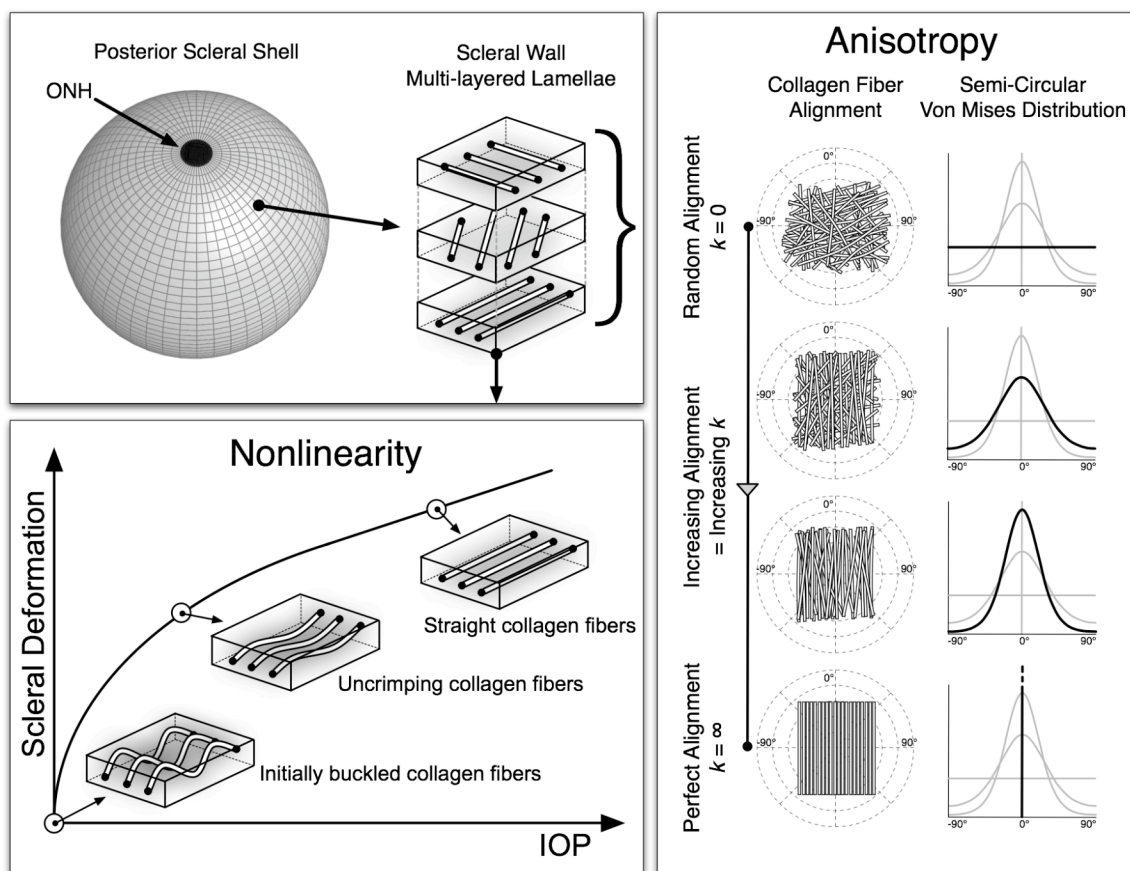
Figure 7.4.1. Nonlinearity and Anisotropy are two biomechanical features that arise from the presence and organization of the scleral collagen fibers that run tangent to the scleral surface. Both features were mathematically transcribed into our constitutive model. **(Anisotropy)** A semi-circular von Mises distribution was used to describe local collagen fiber alignment. As the fiber concentration factor k increases, collagen fibers become more aligned along the preferred fiber orientation (here $\theta_p = 0°$). When $k = 0$, collagen fibers are randomly organized, resulting in equal stiffness along all orientations (relevant to skin tissue). This material symmetry is known as planar isotropy. When $k = \infty$, collagen fibers are all oriented along a unique preferred orientation, which creates high stiffness along θ_p and high compliance perpendicular to θ_p (relevant to tendons and ligaments). This material symmetry is known as transverse isotropy. **(Nonlinearity)** Uncrimping of the collagen fibers induces scleral stiffening at the macroscopic level. Initially the collagen fibers are buckled, then uncrimp and eventually become straight due to acute elevations of IOP, thus limiting scleral deformations at high IOP values. Note that the parameters c_3 and c_4 govern the degree of nonlinearity of each scleral shell.

7.5. Model Assumptions

Each reconstructed scleral shell geometry was sub-divided into 9 regions, in which regions 1-4 represent the peripheral sclera, regions 5-8 the peripapillary sclera, and region 9 the ONH (Figure 7.5.1A). Our model assumed that the stiffness of the ground substance matrix (c_1) and the nonlinear stiffness of the collagen fibers (c_3, c_4) were uniform throughout the entire scleral shell (Regions 1-8; Figure 7.5.1B). It further assumed that regional variations of the scleral biomechanical response are governed by the local alignment of the collagen fibers. Accordingly, fiber concentration factors, k_1 and k_2, were attributed to the peripheral sclera (Regions 1-4; Figure 7.5.1C) and to the peripapillary sclera (Regions 5-8; Figure 7.5.1C), respectively. Finally, a total of eight preferred fiber orientations, θ_{p1} to θ_{p8}, were attributed to each of the eight scleral regions, respectively (Figure 7.5.1D). For simplicity, the ONH was assumed to be an incompressible, linear elastic material with an elastic modulus of 1 MPa for all normal and glaucomatous monkey eyes.
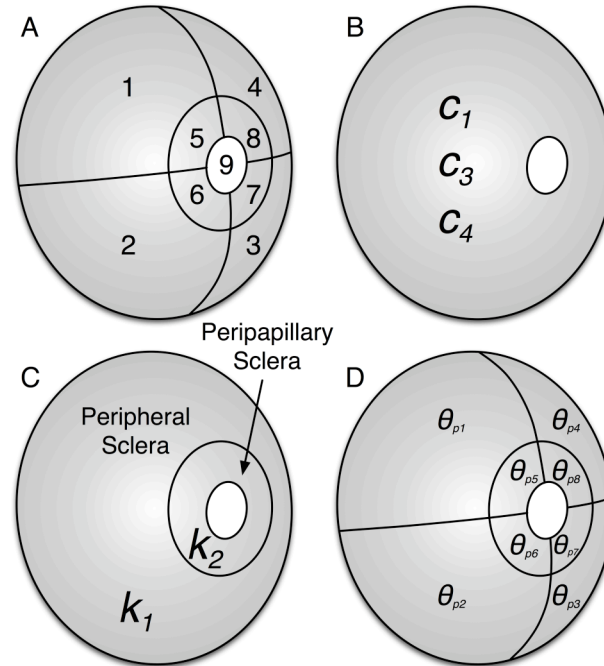
Figure 7.5.1. (A) Each reconstructed posterior scleral geometry was sub-divided into 9 regions. Regions 1-4 represent the peripheral sclera, regions 5-8 the peripapillary sclera, and region 9 the ONH. **(B)** Three stiffness parameters were uniformly attributed to the entire scleral shell (c_1: 1st Mooney-Rivlin coefficient; c_3: exponential fiber stress coefficient; c_4: uncrimping rate of the collagen fibers). **(C)** Two structural parameters, *i.e.* fiber concentration factors k_1 and k_2, were attributed to the peripapillary and peripheral sclera respectively. **(D)** Eight other structural parameters, *i.e.* preferred fiber orientations θ_{p1} to θ_{p8}, were attributed to each of the eight scleral regions respectively. Note that the ONH was assumed linear isotropic with an elastic modulus fixed to 1 MPa for all normal and glaucomatous monkey eyes.

7.6. Estimation of Model Parameters: Inverse Finite Element Method

For each posterior scleral shell, we estimated a set of thirteen model parameters (c_1, c_3, c_4, k_1, k_2, θ_{p1} to θ_{p8}) from the experimental data using an inverse FE method that was fully documented in Chapter 5. Briefly, the inverse FE method allowed the thirteen model parameters to be determined by simultaneously varying their values until the FE-predicted displacements (x, y, and z) closely matched those observed experimentally for

all IOP levels (7, 10, 20, 30 and 45 mm Hg). The inverse FE method is driven by a genetic optimization algorithm (*i.e.* differential evolution (Price *et al.* 2005; Olberding and Suh 2006)) and yields a unique set of thirteen model parameters for each scleral shell (Chapter 5).

7.7. Additional Measures of Scleral Stiffness

Tangent Modulus

The model parameters c_3 and c_4 describe the stretch-induced stiffening of the collagen fibers, but do not represent a direct measure of scleral stiffness as a function of IOP. To capture scleral tissue stiffness, the tangent modulus along the preferred fiber orientation was calculated and mapped. The tangent modulus is an estimate of local scleral tissue stiffness, can be computed at each IOP, and is a function of the model parameters and the local collagen fiber stretch.

Structural stiffness

Clinical discussions concerning the observable mechanical behavior of the corneo-scleral shell often confuse the separate contributions of the tissues' biomechanical properties and their geometry. We calculated and continuously mapped structural stiffness – defined as the local product of scleral thickness and tangent modulus – to capture the mechanical behavior of the scleral shell as a structure in response to acute IOP elevations.

7.8. Statistical Analysis and Results

Statistical Analysis

Regional distributions of maximum principal stress, maximum principal strain, tangent modulus and structural stiffness were compared between normal and glaucomatous eyes of each monkey for three IOP values (10, 30 and 45 mm Hg) using paired t-tests. Note that, initially, each distribution was not normally-distributed. Therefore, for each quantity, the distribution of 3000 means (each of 300 randomly selected values) was used instead. This had the advantage to strictly deal with normal distributions. For each t-test, the t-statistic value was reported. For each quantity, we defined alterations due to chronic IOP elevation as statistically significant when the t-statistic value from comparing the normal and glaucomatous eye of each monkey exceeded the t-statistic values from comparing bilaterally normal eyes of eight monkeys, used in Chapter 6. Thickness differences between normal and glaucomatous eyes were compared to the thickness differences between bilaterally normal eyes of eight monkeys using a multiple linear regression. Finally, we compared tangent modulus and structural stiffness data by age groups using the generalized estimating equation method as described in Chapter 6.

Results Common to all Eyes and Monkeys

The predicted model parameters (except the eight preferred fiber orientations), maximum IOP and IOP before death are reported in Table 7.8.1 for each eye, as well as IOP insult, sex, age and weight for each monkey. The maps of scleral thickness, experimentally-measured and FE-predicted posterior z-displacements, tangent modulus,

structural stiffness, maximum principal stress and strain, and the eight predicted preferred fiber orientations are presented in Figure 7.8.1 for each eye. Tangent modulus (25th, 50th and 75th percentiles) for both eyes and both peripapillary and peripheral regions are shown in Figure 7.8.2, maximum principal stress and strain in the peripapillary sclera in Figure 7.8.3, and structural stiffness in the peripapillary sclera in Figure 7.8.6. Pooled distributions of preferred fiber orientations are shown in Figure 7.8.4. Thickness data are presented in Figure 7.8.5. Finally, Table 7.8.2 presents age-related tangent modulus and structural stiffness data.

Monkey	1		2		3		4	
CIOP insult [mmHg × day]	432		938		1479		1782	
Sex	F		F		F		F	
Age [years]	17.9		22.7		23.0		19.3	
Weight [kg]	8.1		11.3		13.3		8.6	
Eye	os	**od**	**os**	od	**os**	od	**os**	od
IOP Exp. [mm Hg × day]	1236	**1668**	**7731**	6793	**10332**	8853	**4599**	2816
Maximum IOP [mmHg]	17	**24**	**30**	17	**43**	19	**34**	19
IOP at Sacrifice [mmHg]	10	**10**	**30**	10	**14**	12	**32**	12
c_1 [kPa]	1940	**744**	**165**	191	**1607**	1010	**1669**	482
c_3 [kPa]	15.1	**0.90**	**27.9**	35.7	**5.84**	24.0	**1.41**	3.30
c_4 [-]	876	**1200**	**548**	413	**1938**	1169	**2517**	913
k_1 [-]	2.15	**2.28**	**0.49**	1.66	**4.99**	1.32	**1.30**	1.64
k_2 [-]	3.54	**2.46**	**2.25**	1.93	**1.58**	4.03	**1.41**	0.64

Monkey	5		6		7		8	
CIOP insult [mmHg × day]	3127		3128		6153		7714	
Sex	F		F		F		M	
Age [years]	21.0		12.9		11.9		9.8	
Weight [kg]	8.9		5.9		10.0		9.2	
Eye	os	**od**	os	**od**	os	**od**	os	**od**
IOP Exp. [mm Hg × day]	2693	**5820**	13545	**16674**	12909	**19061**	12012	**19726**
Maximum IOP [mmHg]	15	**54**	19	**45**	18	**44**	17	**49**
IOP at Sacrifice [mmHg]	12	**37**	15	**42**	13	**27**	14	**24**
c_1 [kPa]	951	**853**	419	**723**	65.8	**262**	651	**1253**
c_3 [kPa]	4.31	**9.69**	76.5	**13.5**	9.42	**6.09**	2.71	**0.20**
c_4 [-]	915	**1209**	413	**1309**	618	**689**	1850	**2309**
k_1 [-]	1.75	**1.57**	1.14	**3.43**	0.89	**1.91**	3.07	**4.99**
k_2 [-]	1.78	**3.13**	1.09	**3.14**	4.48	**4.52**	0.72	**0.69**

Table 7.8.1. Estimated model parameters (c_1, c_3, c_4, k_1 and k_2) from inverse FE simulations. Data are shown for both eyes of each monkey. The column in **bold** corresponds to the glaucomatous eye. IOP Exp is the IOP exposure for each eye (area under the IOP-time curve) and CIOP insult is the cumulative IOP insult (change in area between the glaucomatous and normal eyes of each monkey). Note that all eight other model parameters for each eye (the preferred fiber orientations) are shown in the last row of Figure 7.8.1.

Scleral Thickness. Scleral thickness, experimentally measured at an IOP of 5 mm Hg at twenty locations and interpolated over each scleral shell, is shown in Figure 7.8.1 (first row). In all eyes, the peripapillary sclera was much thicker (276 to 498 µm on average in the normal eyes) than the peripheral sclera (157 to 252 µm on average in the normal eyes) ($p < 0.0001$). Among all considered regions (*i.e.* inferior, infero-nasal, nasal, supero-nasal, superior, supero-temporal, temporal, infero-temporal), the sclera was significantly thicker in the temporal region for all sixteen eyes ($p < 0.001$).
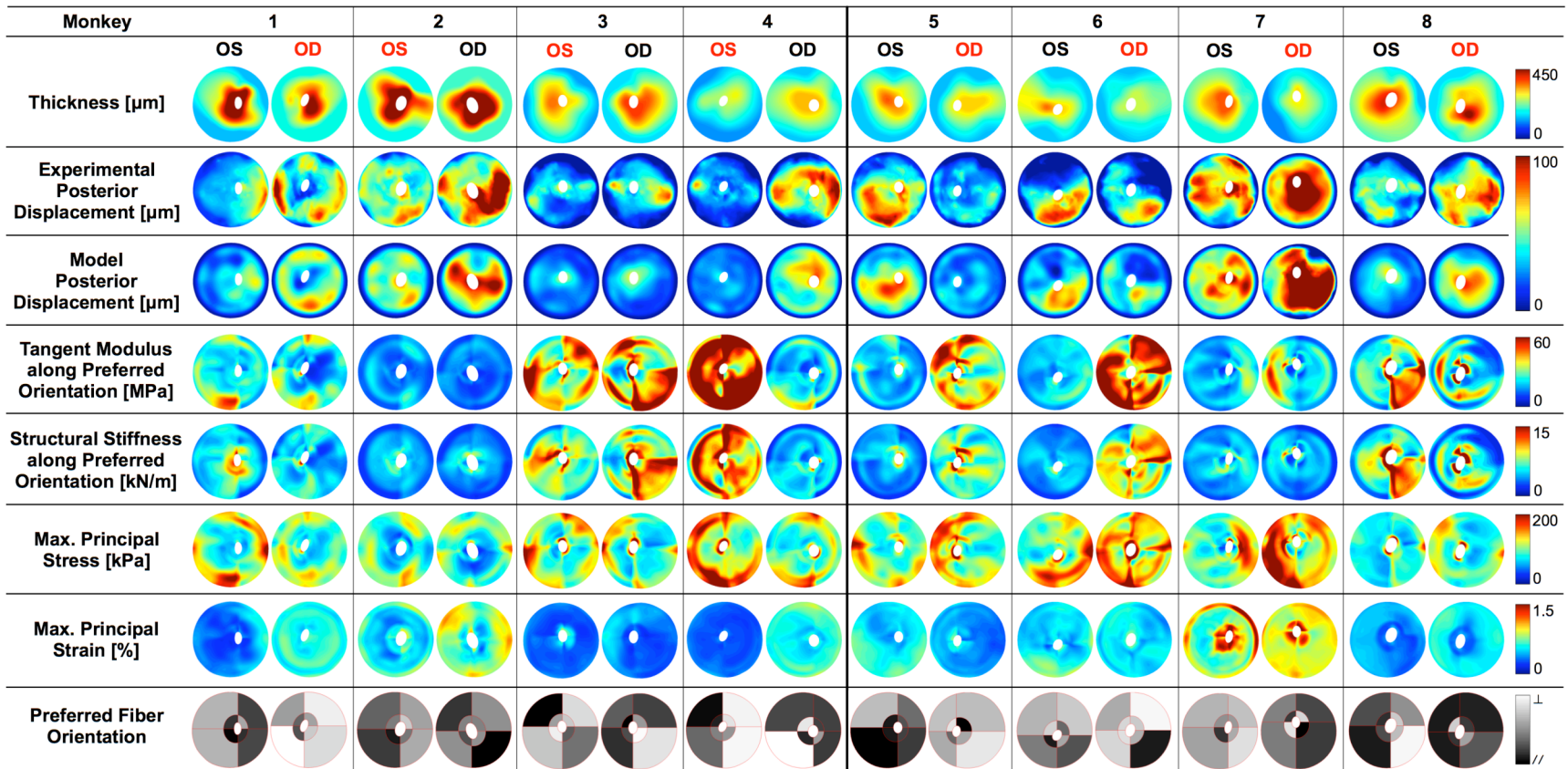
Figure 7.8.1. Individual results for all posterior scleral shells as viewed from the back of the eye (Superior is on top). For each monkey, the glaucomatous eye is shown in red. Scleral thickness was experimentally measured at IOP = 5 mm Hg and interpolated to obtain continuous thickness maps. Tangent modulus, structural stiffness, maximum principal stress and strain are shown for all eyes at a single IOP of 30 mm Hg. Good agreements are observed between FE-predicted and experimentally-measured posterior z-displacements (plotted for an IOP range of 5-30 mm Hg). Finally the preferred fiber orientation is shown for all eight regions of each eye, where // (black) corresponds to a collagen fiber organization tangent to the scleral canal (circumferential, $\theta_p = 0°$) and $\perp$ (white) corresponds to a fiber organization that is perpendicular to the scleral canal (meridional, $\theta_p = 90°$).

Finite Element Predictions. For each eye, good agreement was obtained between the FE-predicted and experimentally-measured posterior displacements between 5 and 30 mm Hg (second and third rows of Figure 7.8.1). Although all not included in Figure 7.8.1, good agreement was also obtained for each IOP range (*i.e.* 5-7, 5-10, 5-20, 5-30, 5-45 mm Hg) and for all displacement components, implying that our constitutive model was able to accurately capture the complex 3-D deformations of the monkey peripapillary and posterior sclera following acute elevation of IOP.

Nonlinearity. For each eye, the sclera stiffened considerably as IOP increased as demonstrated by the large increase in tangent modulus (2.2 to 7.7 fold increase from 10 to 45 mm Hg in the peripapillary sclera from normal eyes; Figure 7.8.2) and by the nonlinear relationship between maximum principal strain and IOP (Figure 7.8.3). Note that maximum principal strain values were consistently low in the normal eyes, as shown in blue in Figure 7.8.3, and varied between 0.32 and 1.49% on average in the peripapillary sclera at 45 mm Hg. Conversely, maximum principal stress was a linear function of IOP (Figure 7.8.3) and was considerably higher than IOP (16 to $30 \times$ IOP on average in the peripapillary sclera from normal eyes, which is valid at all IOP levels due to stress linearity).
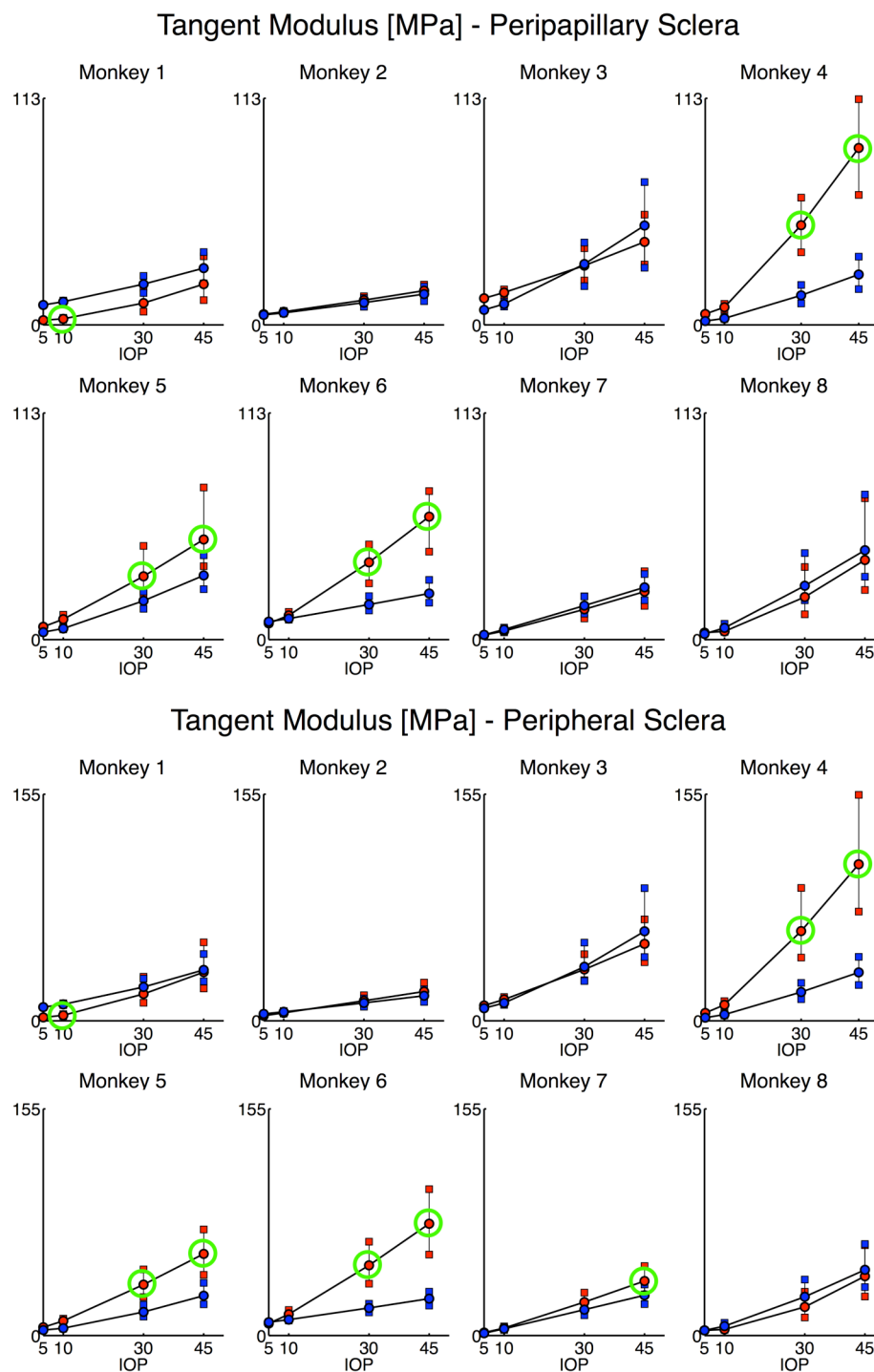
Figure 7.8.2. Tangent modulus in both eyes (blue: normal, red: glaucomatous) and for both the peripapillary (top) and peripheral (bottom) scleral regions of each monkey as a function of IOP. A green circle represents a significant difference between the normal and glaucomatous eye that exceeds the inter-eye differences from eight normal monkeys.
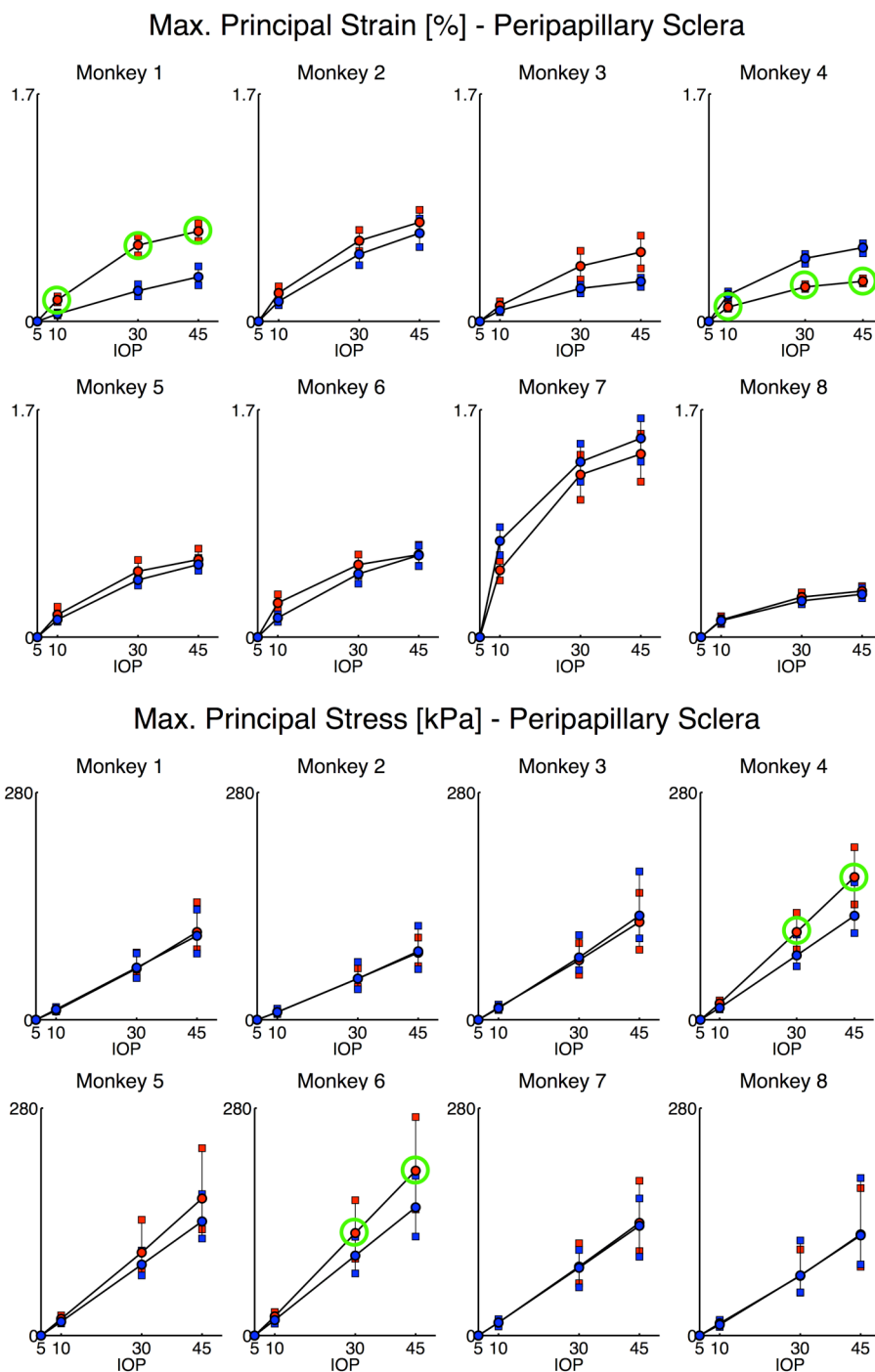
Figure 7.8.3. Maximum principal strain (top) and stress (bottom) in the peripapillary sclera in both eyes (blue: normal, red: glaucomatous) of each monkey as a function of IOP. A green circle represents a significant difference between the normal and glaucomatous eye that exceeds the inter-eye differences from eight normal monkeys. Note that the maximum principal strain is a nonlinear function of IOP, and that the maximum principal stress is a linear function of IOP.

Inhomogeneity. For each eye, the sclera was highly inhomogeneous as demonstrated by the regional variations in tangent modulus. On average, the tangent modulus was higher in the peripheral sclera (17 to 60 MPa in the normal eyes) than in the peripapillary sclera (15 to 50 MPa in the normal eyes).

Anisotropy. For each eye, the sclera was highly anisotropic as demonstrated by the non-zero fiber concentration factors (see Table 7.8.1 and Figure 7.4.1). The fiber concentration factor in the peripapillary sclera (k_2) was higher than that in the peripheral sclera (k_1) for ten of the sixteen eyes studied (Table 7.8.1). Maps of the predicted preferred fiber orientation for all eight regions of each eye are shown in Figure 7.8.1, where $\perp$ (white) indicates a preferred fiber orientation perpendicular to the scleral canal (meridional, $\theta_p = 0°$), and $\parallel$ (black) a preferred fiber orientation tangent to the scleral canal (circumferential, $\theta_p = 90°$). Figure 7.8.4 shows the pooled distributions of the preferred fiber orientation for all sixteen eyes in both the peripapillary and peripheral sclera. In general, the mean preferred fiber orientation for all tested eyes was tangent to the scleral canal in both scleral regions, but this effect was more pronounced in the peripapillary sclera.
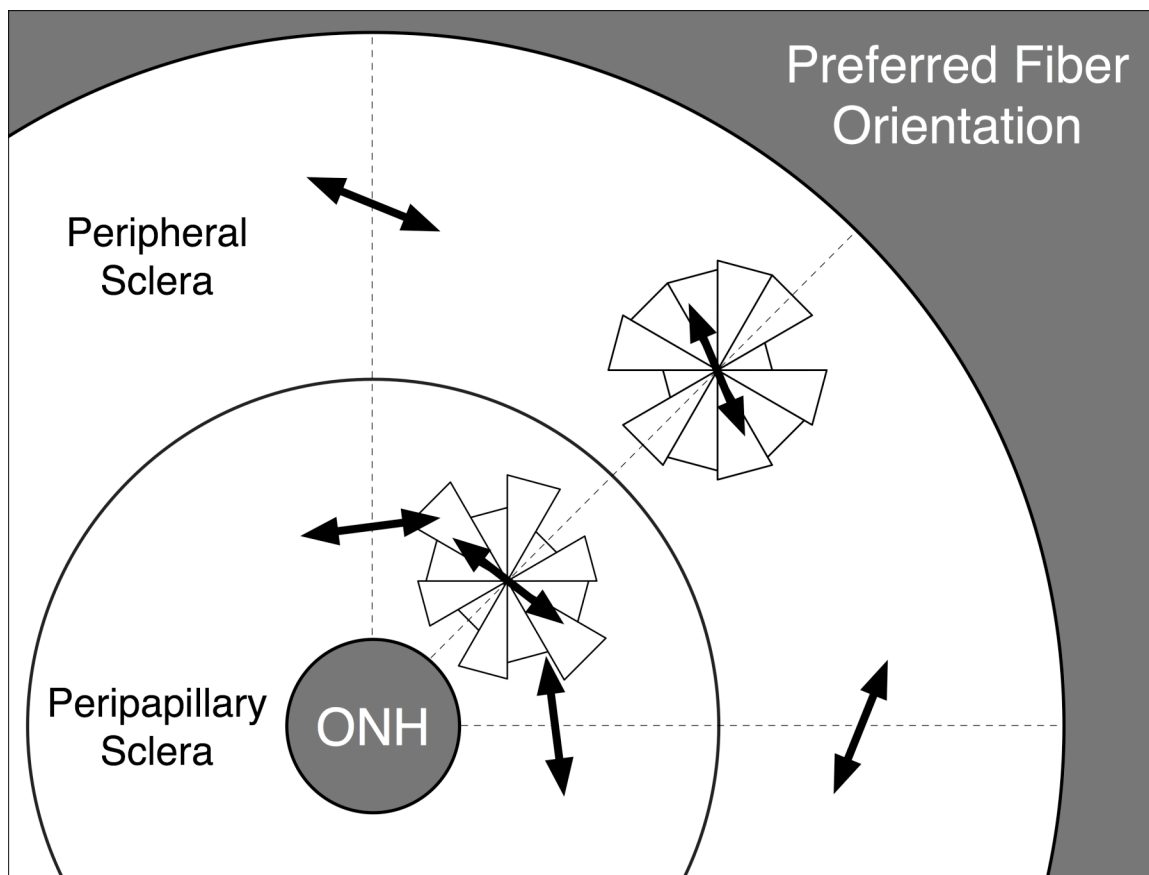
Figure 7.8.4. Pooled distributions (all eyes) of the preferred fiber orientation for the peripapillary and peripheral scleral regions are shown as two symmetric rose diagrams with 30° segment, respectively, in which larger triangles indicate the most commonly predicted orientations. Mean preferred fiber orientations (black arrows) were calculated from the distributions. It suggests a circumferential organization of the collagen fibers around the scleral canal in both the peripapillary (stronger) and the peripheral sclera (weaker).

Age-related Changes in Scleral Biomechanics

We considered all eight normal eyes from this study as being part of one age group (group 2: 17.3 ± 5.1 yrs). Note that monkey lifespan is about a third of human lifespan (Tigges *et al.* 1988). We compared tangent modulus and structural stiffness distributions from that group to that of two other age groups (group 1: 1.5 ± 0.7 yrs; group 3: 22.9 ± 5.3 yrs). Data from groups 1 and 3 were obtained in Chapter 6. We found significant differences in the peripapillary scleral tangent modulus and structural stiffness between age groups using the generalized estimating equation method (Table 7.8.2). Using a multiple linear regression, we found that eyes from group 3 were significantly thinner than eyes from group 2 ($p < 0.05$) but found no significant differences in thickness between eyes from group 1 and group 2 ($p > 0.05$).

Age Group	1			2			3		
Age (mean ± std)	1.5 ± 0.7			17.3 ± 5.1			22.9 ± 5.3		
IOP [mm Hg]	**10**	**30**	**45**	**10**	**30**	**45**	**10**	**30**	**45**
Modulus	3.6***	8.3***	12.5***	6.5	17.9	26.6	8.8*	24.6**	40.1**
Struct. Stiffness	1.4*	3.4**	5.1**	2.8	6.5	9.6	3.3	8.8*	14.4*

Table 7.8.2. Mean (50th percentile) of tangent modulus and structural stiffness distributions in the peripapillary sclera. Groups 1 and 3 were used in Chapter 6. Distributions from group 1 and group 3 were compared to that of group 2 using the generalized estimating equation method (* $p < 0.05$, ** $p < 0.01$, *** $p < 0.001$). Significant differences between the young and adult groups, and between the adult and old groups were found in all but one comparison.

Scleral Biomechanical Changes Attributed to Chronic IOP Elevation

Overall, glaucomatous eyes exhibited lower scleral thickness in both the peripapillary and peripheral regions. However this change of thickness was not overall and regionally significant when compared to the physiologic inter-eye difference from eight normal monkey eyes ($p > 0.05$). Scleral thickness (mean ± standard deviation) is shown in Figure 7.8.5 in both eyes and both regions of each monkey. Note that there is more overlap in the peripheral sclera between scleral thickness in glaucomatous (in red) and normal (in blue) eyes.
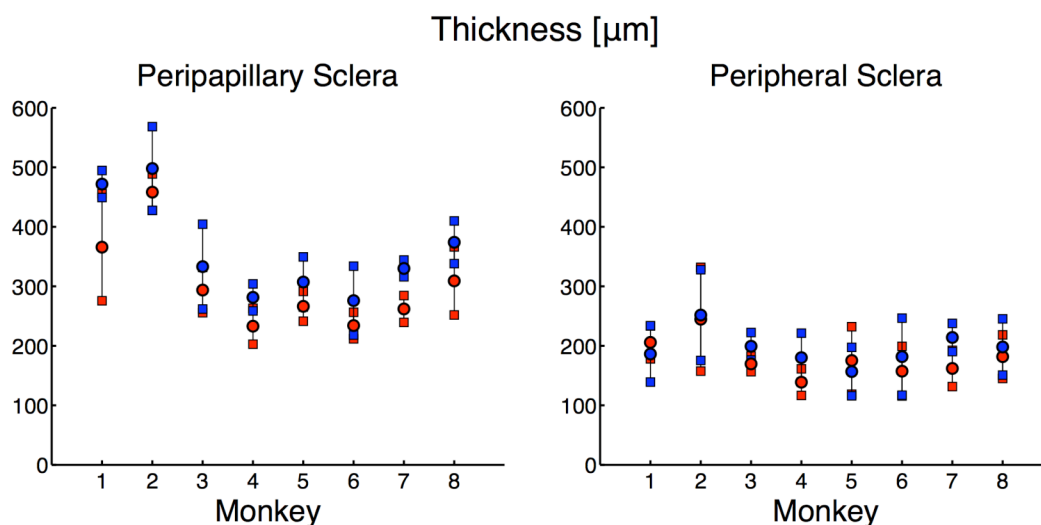
Figure 7.8.5. Peripapillary and peripheral scleral thickness (mean ± standard deviation) in both normal (blue) and glaucomatous (red) eyes of each monkey. Overall, a decreasing trend in monkey scleral thickness was observed in glaucomatous eyes. However, this trend was not overall and regionally significant when compared to inter-eye thickness differences from eight normal monkeys ($p > 0.05$).
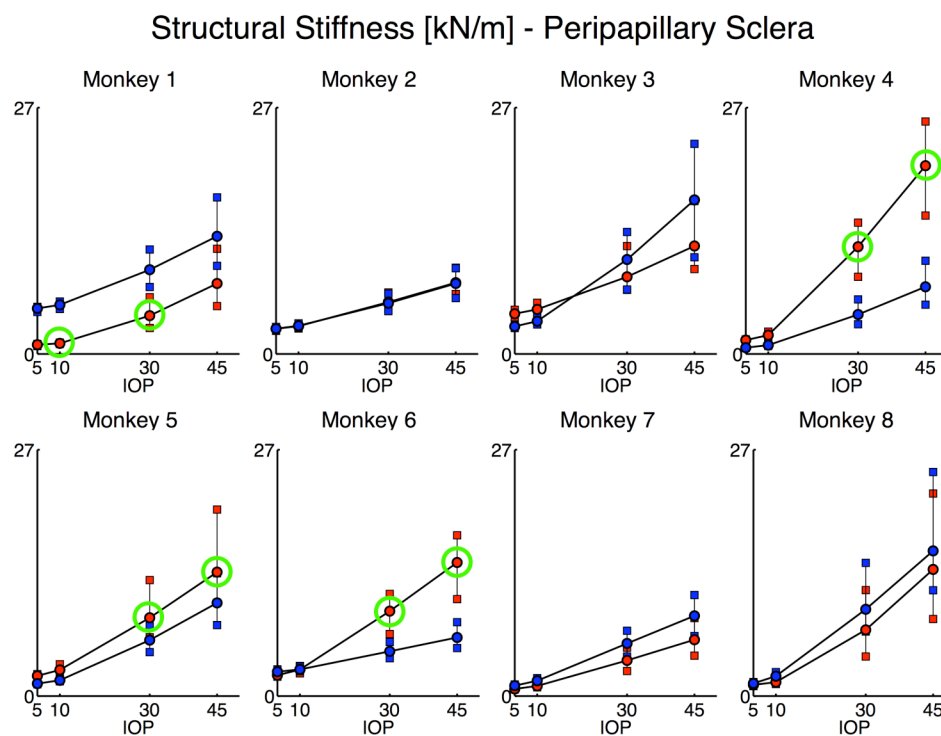
Figure 7.8.6. Structural stiffness (thickness × tangent modulus) in the peripapillary sclera in both eyes (blue: normal, red: glaucomatous) of each monkey as a function of IOP. A green circle represent a significant difference between the normal and glaucomatous eye that exceeds the inter-eye differences from eight normal monkeys.

We observed no significant changes (exceeding the physiologic inter-eye difference of normal monkeys) in tangent modulus (Figure 7.8.2) and structural stiffness (Figure 7.8.6) between the normal and glaucomatous eyes of monkeys 2, 3, and 8.

We observed significant changes (exceeding the physiologic inter-eye difference of normal monkeys) in tangent modulus (Figure 7.8.2) and structural stiffness (Figure 7.8.6) between the normal and glaucomatous eyes of monkeys 1, 4, 5, 6 and 7. The glaucomatous eye in monkey 1 exhibited a significant decrease in tangent modulus (10 mm Hg) and structural stiffness (10 and 30 mm Hg). Note that monkey 1 received the lowest cumulative IOP insult. The glaucomatous eyes in monkeys 4, 5 and 6 exhibited a significant increase in tangent modulus and structural stiffness (30 and 45 mm Hg).

Monkey 7 exhibited a significant increase in tangent modulus (45 mm Hg) in the peripheral sclera only.

We observed significant changes (exceeding the physiologic inter-eye difference of normal monkeys) in maximum principal strain in two monkeys only (1 and 4; Figure 7.8.3) and in maximum principal stress in two monkeys only (4 and 6; Figure 7.8.3).

Finally, we did not detect changes in the fiber concentration factor ($p > 0.05$) or in the preferred fiber orientation ($p > 0.05$) in either the peripapillary or peripheral regions between normal and glaucomatous eyes.

7.9. Discussion

In this study, we characterized changes in scleral biomechanical behavior induced by experimental glaucoma in the monkey. Specifically, for each eye, we measured the 3-D displacements of the posterior scleral shell exposed to acute elevations of IOP from 5 to 45 mm Hg, and estimated the inhomogeneous, anisotropic, and nonlinear biomechanical properties of the shell using an inverse FE method. In addition, we compared tangent modulus and structural stiffness of the normal eyes to age-related data from Chapter 6.

Previously Reported Findings

Some of our findings in this study were reported and discussed in Chapters 4, 5, and 6. These are briefly mentioned as follows. First, the monkey posterior sclera is thicker in the peripapillary and temporal region. Second, the monkey posterior sclera is a highly nonlinear, anisotropic, and inhomogeneous soft-tissue. Third, concentrations of

tangent modulus, structural stiffness, and maximum principal stress were evident adjacent to the scleral canal in each eye. Fourth, maximum principal stress magnitude was substantially higher than IOP. Fifth, maximum principal strain magnitude was low.

In addition, we considered the eight normal eyes of this study as one age group (group 2: 17.3 ± 5.1 yrs) and compared tangent modulus and structural stiffness to those of two other age groups (group 1: 1.5 ± 0.7 yrs and group 3: 22.9 ± 5.3 yrs) from Chapter 6. We found a clear increase in tangent modulus and structural stiffness with age (Table 7.8.2) that likely correlates with increased cross-links within the aging posterior sclera (Bailey 1987; Bailey *et al.* 1998). A detailed discussion on this topic can also be found in Chapter 6. Note that we previously reported a decrease in scleral thickness with age (groups 1 and 3). However, in this study, we found no significant differences in scleral thickness between group 1 and group 2 ($p > 0.05$), but group 3 exhibited significantly thinner sclera than group 2 ($p < 0.05$). This implies that changes in scleral thickness are more likely to occur in older eyes.

Scleral Biomechanical Changes Attributed to Chronic IOP elevation

The main goal of this study was to assess scleral biomechanical changes attributed to chronic IOP elevation. The major findings are as follows. First, there was a decreasing trend in monkey posterior scleral thickness between normal and glaucomatous eyes. Second, tangent modulus and structural stiffness changes attributed to chronic IOP elevation were apparent between normal and glaucomatous eyes in some, but not all, monkeys. Third, changes in scleral anisotropy were not observed between normal and glaucomatous monkey eyes.

On average, we found that all glaucomatous eyes exhibited thinner peripapillary sclera than their contralateral normals (Figure 7.8.5). However, thickness differences between glaucomatous and normal eyes did not exceed the inter-eye physiologic differences of eight normal monkeys from Chapter 6. Using traditional histology, we previously reported significant thinning of the posterior (Downs *et al.* 2001) and peripapillary sclera (Yang *et al.* 2007a; Yang *et al.* 2007b) in monkey eyes subjected to chronic IOP elevation. Recently, Phillips and coworkers measured *in-vivo* axial length changes due to short-term IOP elevations (IOP increased to 100 mm Hg and maintained for one hour) (Phillips and McBrien 2004). They found that the axial length increased in chick eyes, but decreased in tree shrew eyes. Scleral morphologic changes should be assessed in future studies to understand if scleral thinning due to chronic IOP elevation exists and is a consequence of axial elongation, fluid exudation, tissue loss, or a combination of the three.

In this study, we observed no significant changes (*i.e.* exceeding the physiologic inter-eye difference of eight normal monkeys) in scleral tangent modulus (Figure 7.8.2) and structural stiffness (Figure 7.8.6) between the normal and glaucomatous eyes in three monkeys (2, 3 and 8). This result suggests that peripapillary scleral biomechanical changes due to chronic IOP elevation did not occur in the glaucomatous eyes of these monkeys. Since monkey 8 received the highest cumulative IOP insult (7714 mm Hg $\times$ day), we would have expected to observe the largest changes in the glaucomatous eye of this monkey. Interestingly, at IOPs of 30 and 45 mm Hg, the normal eye of monkeys 8 and 3 had the two highest mean tangent modulus and structural stiffness in the peripapillary sclera. Assuming that prior to IOP insult, the glaucomatous eyes in monkeys

3 and 8 were as stiff as their contralateral normals, these results suggest that stiffer scleral shells will be less prone to biomechanical changes when exposed to chronic IOP elevation. A variety of previous studies have reported that mechanical strain applied to scleral fibroblast can trigger a remodeling response of the scleral tissue by releasing MMPs and TIMPs (Yamaoka *et al.* 2001; Fujikura *et al.* 2002; Cui *et al.* 2004; Shelton and Rada 2007). In a stiff sclera, an additional increase in IOP would result in a strain increase, but the latter may be too small to elicit a response from the scleral fibroblasts. Note that mean strain levels at 45 mm Hg in monkeys 3 and 8 were 0.30 and 0.32% respectively, which were smaller than all the reported values in the aforementioned studies on scleral fibroblasts (a minimum of 0.45%). The third monkey in which we did not observe scleral biomechanical changes was monkey 2. A closer examination in monkey 2 reveals that its glaucomatous eye exhibited the largest scleral thickness (Figure 7.8.5), and lowest tangent modulus (Figure 7.8.2) among all normal eyes. Thus its mean structural stiffness was comparable to the mean structural stiffness of all normal eyes. It is possible that the mean structural stiffness may not be a sufficient index to evaluate the degree of scleral biomechanical changes, or that a thicker sclera is less sensitive to biomechanical changes.

We observed significant changes in scleral tangent modulus (Figure 7.8.2) and structural stiffness (Figure 7.8.6) between the normal and glaucomatous eyes of monkeys 1, 4, 5, 6 and 7. The glaucomatous eye in monkey 1 exhibited smaller tangent modulus at 10 mm Hg (Figure 7.8.2) and structural stiffness at 10 and 30 mm Hg (Figure 7.8.6) than those of its contralateral normal. Burgoyne and coworkers have reported hypercompliance of the ONH surface within four to eight weeks of chronic IOP elevation

in monkeys and suggested that weakening of the load-bearing structures of the eye (lamina cribrosa and peripapillary sclera) through connective tissue damage might be responsible for this phenomenon at the earliest stage of glaucomatous optic neuropathy (Burgoyne *et al.* 1995). Moreover, a computational modeling study by Downs and coworkers reported weakening of the lamina cribrosa structure at the earliest stage of glaucomatous optic neuropathy (Downs *et al.* 2007a). It is interesting to note that weakening of the sclera is only present in the glaucomatous eye of monkey 1 – the eye that received the smallest cumulative IOP insult (432 mmHg × day) and had the lowest maximum measured IOP (24 mm Hg). It should also be noted that the decrease in tangent modulus in the glaucomatous eye of monkey 1 was only significant at low IOP (10 mm Hg). In 1957, Roach and Burton studied the roles of elastin and collagen in arteries (Roach and Burton 1957). They found that elastin alone was responsible for resisting pressure-induced arterial deformations at low pressure, and that collagen alone was responsible for resisting pressure-induced arterial deformations at high pressure. These results were recently confirmed by Fonck and coworkers (Fonck *et al.* 2007). Based on these studies, it could be that only damage to elastin occurred in the glaucomatous eye of monkey 1.

We observed a significant increase in tangent modulus at 30 and 45 mm Hg in both the peripapillary and peripheral regions in monkeys 4, 5 and 6, and a significant increase in tangent modulus at 45 mm Hg in the peripapillary region in monkey 7 (Figure 7.8.2). The glaucomatous eyes in monkey 4, 5, and 6 also exhibited larger structural stiffness in the peripapillary sclera at IOPs of 30 and 45 mm Hg (Figure 7.8.6). These findings suggest that at higher levels of cumulative IOP insult in the range of the

chronically elevated IOPs in those eyes, the posterior sclera will stiffen possibly through extracellular matrix remodeling. This is consistent with our previous uniaxial study on scleral biomechanics in glaucomatous monkey eyes (Downs *et al.* 2005), and may be a protective mechanism that limits scleral canal expansion and related deformation of the ONH. Burgoyne and coworkers suggested that the ONH connective tissues could become more rigid with a more advanced stage of glaucoma based on clinical measurements of the ONH surface (Burgoyne *et al.* 1995). This hypothesis was also confirmed by Zeimer and Ogura who reported that human ONHs became more rigid with severe glaucoma (Zeimer and Ogura 1989). Roach and Burton, also demonstrated that collagen alone was responsible for limiting arterial deformations at high pressure (Roach and Burton 1957), which suggests that the observed increase in tangent modulus in glaucomatous eyes at high IOPs is due to collagen remodeling only.

Even though scleral biomechanical changes (through changes in tangent modulus) occurred in five monkeys (1, 4, 5, 6 and 7), significant changes in maximum principal strains in the peripapillary sclera were only observed in two monkeys (1 and 4; Figure 7.8.3), and significant changes in maximum principal stress in the peripapillary sclera were only observed in two monkeys (4 and 6; Figure 7.8.3). This result suggests that overall changes in scleral thickness (generally lower in the glaucomatous eyes) and tangent modulus (generally higher in the glaucomatous eyes) interact so as to maintain the normal homeostasis of the scleral tissue.

In this study, we did not observe significant differences in scleral anisotropy (preferred fiber orientation and fiber concentration factor) between normal and glaucomatous monkey eyes. Such result was recently reported for the monkey lamina

cribrosa (Roberts *et al.* 2008), suggesting that remodeling of the peripapillary and posterior sclera must be accompanied with changes in elastin/collagen content and/or fiber diameter, but not fiber reorientation. This is consistent with work from Quigley and coworkers who reported glaucomatous changes in collagen/elastin content and collagen fiber diameter in the peripapillary sclera in human and monkey eyes (Quigley *et al.* 1991a).

Overall, our results suggest that significant changes in the biomechanical behavior of the sclera are associated with chronic IOP elevations. These changes are complex, individual-specific, and likely the result of scleral extracellular matrix remodeling. Our findings suggest that scleral thinning potentially occurs in the peripapillary sclera of glaucomatous eyes, that sclera with initially large tangent modulus or thickness are less prone to biomechanical changes, that a decrease in tangent modulus (possibly due to elastin damage) occurs at the earliest stage of glaucoma, that an increase in tangent modulus (possibly associated with collagen) occurs at moderate stages of glaucoma, and that fiber reorientation does not occur in glaucomatous eyes. Since the sclera drives the levels of stress and strain transmitted to the ONH, a change in the biomechanical environment of the posterior sclera through remodeling will inevitably perturb the biomechanics of the ONH. Scleral remodeling may provide a protective mechanism and act to keep stress and strain levels within a normal range. Our future work will study the complex biomechanical interactions between the posterior sclera and ONH in both normal and glaucomatous eyes.

Limitations

Several limitations should be considered when viewing this work. While the general limitations of the method have been discussed at length in Chapters 5 and 6, we will briefly revisit them and additionally discuss those inherent to this study. First, IOP was measured in both eyes of each monkey over time (Figure 7.3.1), but we did not characterize the diurnal and nocturnal IOP fluctuations that are known to exist in monkeys. Diurnal IOP fluctuations have been shown to be large in monkeys, especially in glaucomatous eyes, in which they are highly individual-specific and can largely exceed 10 mm Hg (Ollivier *et al.* 2004). Therefore our definition of cumulative IOP insult (change in area under the IOP/time curve) should be taken with caution and was only used here to provide a first estimate of the cumulative insult from IOP. An implantable telemetric IOP transducer is currently being developed for monkeys that should allow for continuous measurements of diurnal and nocturnal IOP fluctuations and more accurate characterization of IOP insult (Downs *et al.* 2008).

Second, we have assumed that collagen was the primary fibrous element (Fung 1993) of the sclera, and we have lumped all other tissue constituents into the ground substance matrix, a common practice in soft-tissue FE modeling (Weiss *et al.* 1996; Holzapfel *et al.* 2000). Because our study suggests that both elastin and collagen may play important roles in glaucomatous damage, further experimental and theoretical work will be needed to address how these components influence scleral biomechanics.

Third, we did not characterize scleral biomechanics between 0 and 5 mm Hg in the tested eyes, because the scleral shells required an IOP of approximately 4 mm Hg to sustain their shape. IOPs in the range of 0-5 mm Hg are rarely measured in monkey eyes,

so ignoring the initial IOP loading should not compromise the clinical importance of our results.

Fourth, the ONH tissues were assumed to be linearly elastic, with a common elastic modulus of 1 MPa assigned to the ONH region for both normal and glaucomatous monkey eyes. Our previous sensitivity study showed that ONH elastic moduli in the range of 0.1 - 5 MPa did not affect the results of our scleral biomechanical property fitting (Chapter 5), hence, our assumption should not impact the results presented herein.

Fifth, the ONH was represented as an elliptical cylinder, with its external boundary located at the outer aspect of the dural sheath insertion (as measured with the 3-D digitizer) and was therefore larger than one would expect.

Sixth, we divided each reconstructed scleral shell into eight regions to preliminarily assess regional variations in predicted collagen fiber orientation (θ_{p1} to θ_{p8}). Our preliminary study confirmed that a combination of eight regions and thirteen model parameters was the minimum requirement to obtain good agreement between the FE-predicted and experimentally-measured displacements (Figure 7.8.1) while also ensuring a unique set of model parameters.

Finally, collagen fiber alignment was not measured directly, but was predicted using the models' fits to experimentally-measured scleral deformations (Figure 7.8.1). Due to the relatively coarse discretization of the regions, we could only report an overall approximation of the preferred collagen fiber orientation within each region. Future inclusion of experimentally-derived collagen fiber orientation maps as an input parameter will allow for finer regional discretization for the remaining fitted parameters, and improve our characterization of scleral anisotropy.

Summary

In summary, new experimental and computational methodologies were used in this study to characterize scleral biomechanics in normal and glaucomatous monkey eyes. These methods have broad applicability and can be applied to other thin soft tissues with multi-directional collagen fibers. The long-term goal of this work is to establish the pathophysiologic links between connective tissue stress/strain within the peripapillary sclera and lamina cribrosa and retinal ganglion cell axon damage and death. Given the large role of scleral biomechanics on both the neural and connective tissues of the ONH, new strategies for the clinical study (visualization and measurement) of peripapillary and posterior scleral biomechanics are indicated.

8 Conclusions and Future Directions

8.1. Conclusions

The objective of this work was to investigate the role of the peripapillary and posterior sclera in glaucoma by characterizing peripapillary and posterior scleral biomechanics in the normal, glaucomatous and aging monkey eye. Four Specific Aims were accomplished to achieve this goal. A summary of the results and conclusions under each Specific Aim is presented in this section.

Specific Aim 1: To evaluate the effects of post-mortem storage time on the mechanical properties of rabbit peripapillary sclera after enucleation, using uniaxial testing and linear viscoelastic theory.

This Aim was accomplished with a combination of experimental and computational tools including uniaxial testing of excised scleral strips from rabbit eyes and a new constitutive model based on linear viscoelastic theory. As described in Chapter 2, twenty-four scleral samples were stored in phosphate buffered saline and divided into six groups according to the time separating sacrifice from scleral testing (post-mortem times of 3, 8, 24, 36, 48, and 72 hours). The main finding was that there were no

significant differences in the viscoelastic properties of rabbit peripapillary sclera from each group, which indicates that rabbit sclera can be stored in phosphate buffered saline at 4 °C for up to 72 hours without undergoing any detectible change in its mechanical properties. Since human and rabbit sclera have similar organic composition, this finding suggests that mechanical testing of peripapillary sclera from human donor eyes that have been collected and stored in phosphate buffered saline for up to 72 hours should yield reliable material property data. This study should be taken carefully as it did not consider the post-mortem time prior enucleation, and the derived conclusion may not be applicable to other ocular soft-tissues especially those with very high cellular contents (*e.g.* retina, lamina cribrosa), which may contribute to the overall stiffness of these tissues.

Specific Aim 2. To develop experimental methods to measure 2-D and 3-D monkey posterior scleral deformations due to acute elevations in IOP, as well as regional variations in scleral thickness and topography.

In Chapter 3, we developed an optical technique to measure surface deformations of pressurized porcine scleral shells. Polystyrene microspheres were randomly scattered and attached to the scleral surface of each shell and optically tracked with increasing IOP sets of algorithms based on the optical flow equation. With this technique we were able to accurately measure scleral surface deformations for IOPs ranging from 5 to 45 mm Hg. In this study, we found a highly nonlinear relationship between calculated maximum principal strain and IOP for each scleral shell tested. This result implied that scleral stiffness was relatively low between 5 and 10 mm Hg, but dramatically increased continuously for each IOP elevation increment beyond 10 mm Hg. Tissue mechanical nonlinearity can potentially serve to limit large deformations that could disrupt the

mechanical integrity of the tissue at the cellular level. Moreover, we found the maximum principal strain was highest and primarily circumferential immediately adjacent to the scleral canal, which suggests that peripapillary deformation following acute IOP elevations may be governed by the underlying scleral collagen microstructure.

While the usage of the experimental technique developed in Chapter 3 provided some insight into scleral biomechanics, it was limited to 2-D deformations with a small field of view. In Chapter 5, we employed the same pressurization apparatus that was developed in Chapter 3, but used electronic speckle pattern interferometry to experimentally measure 3-D deformation of the entire posterior scleral shell from monkey eyes. We found that 3-D deformations from monkey posterior sclera were inhomogeneous and confirmed that the posterior sclera is a highly nonlinear soft-tissue.

In Chapter 5, we also developed experimental techniques to measure posterior scleral topography and thickness using a 3-D digitizer arm and an ultrasound transducer, respectively, at an initial IOP of 5 mm Hg. Both data sets were successfully combined to mathematically reconstruct the anatomical geometry of each shell, to derive a FE mesh for each specimen using custom-written Matlab subroutines.

Specific Aim 3. To develop a 3-D constitutive model for the posterior sclera based on fiber-reinforced composite theory, and its corresponding FE implementation. The sclera will be modeled as a nonlinear, anisotropic and inhomogeneous material using hyperelasticity.

In Chapter 4, we developed an anisotropic hyperelastic constitutive model in order to simulate the mechanical behavior of the posterior sclera under acute elevations of IOP. The constitutive model was derived from fiber-reinforced composite theory, and

incorporated stretch-induced stiffening of the reinforcing collagen fibers. Collagen fiber alignment was assumed to be multi-directional at local material points, confined within the plane tangent to the scleral surface, and directionally distributed in a semi-circular von-Mises distribution. To develop an initial understanding of our constitutive model, we performed FE simulations of an idealized posterior scleral shell geometry and investigated the effects of scleral collagen fiber alignment on scleral and ONH mechanics. We found that scleral collagen fiber alignment had a large impact on both ONH and scleral deformations. Specifically, we found that a combination of highly aligned and circumferential collagen fibers in the sclera restrained scleral canal expansion but created posterior laminar deformation, whereas the opposite was observed with a combination of highly aligned and meridional collagen fibers. We therefore suggest that collagen fiber organization may play a role in the development and progression of glaucomatous optic neuropathy through the modulation of biomechanical insult to the ONH tissues.

Specific Aim 4. To develop an inverse FE method to extract nonlinear, anisotropic, inhomogeneous mechanical properties (Aim 3) for the posterior sclera based on experimental observations (Aim 2). Scleral biomechanics will be characterized for normal (young and old) monkey eyes and for monkey eyes exposed to chronic IOP elevations (*i.e.* experimental glaucoma).

In Chapter 5, we developed an inverse FE method, driven by the differential evolution algorithm, to derive shell-specific sets of mechanical properties for the posterior sclera based on experimental observations. The reconstructed geometry of each shell was used to which the constitutive model developed in Chapter 4 was applied. For

each shell, material parameters were simultaneously varied until the FE-predicted displacements (x, y, and z components) closely matched those obtained experimentally for all IOP levels simultaneously (7, 10, 20, 30 and 45 mm Hg). We found that our constitutive model was able to accurately capture the complex 3-D deformations of the monkey posterior sclera exposed to acute elevations of IOP from 5 to 45 mm Hg. Results from inverse FE simulations showed that the posterior sclera is a highly nonlinear, anisotropic, inhomogeneous soft-tissue. Nonlinearity was observed from experiments and quantified using parameter fitting as follows. We found that the monkey posterior sclera exhibited a least a five-fold increase in tangent modulus at an IOP of 5 mm Hg compared to that at 45 mm Hg. Anisotropy was especially apparent in the peripapillary sclera, in which the collagen fibers were highly aligned and circumferentially oriented around the ONH. This arrangement may be biologically optimized to protect the ONH from biomechanical damage by limiting scleral canal expansion. Inhomogeneity was apparent in the regional variations in tangent modulus. Interestingly, we found an inverse relationship between scleral thickness (low in the peripheral sclera, high in the peripapillary sclera) and tangent modulus (high in the peripheral sclera, low in the peripapillary sclera). Since both scleral thickness and tangent modulus contribute to the stiffness of the shell as a structure, the finding seems reasonable to ensure the eye expands in a uniform manner, thereby preserving its shape to maintain focused vision.

In Chapter 6, we employed our inverse FE method to characterize scleral biomechanics in the aging monkey eye. We found that posterior sclera from old monkey eyes exhibited higher tangent modulus and lower thickness, but considerably lower strain and higher stress than posterior sclera from young monkey eyes. This result shows that

the monkey posterior sclera becomes considerably stiffer with age, which can be explained by an age-related increase in elastin and collagen cross-links (Bailey *et al.* 1998). Interestingly, we found no age-related changes in scleral anisotropy, which suggests that increased cross-linking did not affect the overall anisotropy of the scleral tissue. The posterior sclera transmits IOP-induced stress and strain to the ONH, and since the prevalence of glaucoma increases exponentially with age, a change in the biomechanical environment of the posterior sclera from older eyes may potentially initiate the development of the disease. For example, if all other aspects of ONH biomechanics remain unchanged, an isolated increase in scleral stiffness that is not accompanied by an increase in lamina cribrosa connective tissue stiffness should limit scleral canal expansion-induced tautening of the lamina cribrosa at elevated IOP. In this scenario, the lamina will be left exposed to the direct action of IOP on the ONH surface leading to more posterior laminar deformation at all levels of IOP. Increased posterior laminar deformation may eventually precipitate retinal ganglion cell death, but this remains to be seen.

In Chapter 7, we employed our inverse FE method to characterize scleral biomechanics in contralateral normal and glaucomatous monkey eyes. We used the monkey model of glaucoma in which one eye of each of eight monkeys was exposed to various levels of chronic IOP elevation. Overall, our results show that scleral biomechanical changes occurred in some, but not all, eyes exposed to chronic IOP elevation. In addition, we found that scleral biomechanical changes in the glaucoma eyes were complex, individual-specific and likely the result of extracellular matrix remodeling. Nonetheless, our findings suggest that 1) scleral thinning occurs in the

peripapillary sclera of glaucomatous eyes, 2) sclera with initially large tangent modulus or thickness are less prone to biomechanical changes, 3) a decrease in tangent modulus at low IOP only, possibly due to elastin damage, occurs at the earliest stage of glaucoma, 4) an increase in tangent modulus at high IOPs, possibly associated with collagen, occurs at moderate stages of glaucoma, and 5) fiber reorientation does not occur in glaucomatous monkey eyes.

Since the sclera drives the levels of stress and strain transmitted to the ONH, a change in the biomechanical response of the posterior sclera through remodeling will inevitably disturb that the biomechanical environment of the ONH. Interestingly, scleral remodeling may provide a protective mechanism toward further retinal ganglion cell loss associated with the progression of glaucoma and act to keep stress and strain levels within a homeostatic range.

8.2. Future Directions

Based on the knowledge gained throughout this thesis research, multiple directions can be taken to further our understanding of scleral and ONH biomechanics in glaucoma. In Chapter 2, I demonstrated that the peripapillary sclera can be stored up to three days in phosphate buffered saline at 4°C without undergoing mechanical deterioration. This has important implications for the mechanical testing of human sclera because they are commonly stored for a finite amount of time before they are available for research. The entire methodology we presented in this thesis could be easily reproduced with human samples to characterize the 3-D mechanical behavior of human posterior and peripapillary sclera. While the monkey model of glaucoma has obvious

advantages over other animal models, it will eventually become important to understand if the same mechanisms for glaucomatous optic neuropathy exist in both human and non-human primates.

While it was the first constitutive model that considered the posterior sclera as an inhomogeneous, anisotropic and nonlinear material (Chapters 4 and 5), the ONH was still considered homogeneous, linear, and elastic (Chapters 4 and 5). Our primary focus is to understand the basic interactions between ONH and scleral biomechanics in glaucoma, thus it is essential to improve the existing constitutive models for the ONH tissues. Recently, the lamina cribrosa was modeled as an inhomogeneous, orthotropic and linear material (Downs *et al.* 2007; Roberts *et al.* 2007). However, these models lack experimental validations and do not incorporate the stretch-induced stiffening exhibited by the collagen fibers.

While it has been attempted, it is challenging to characterize the mechanical behavior of the lamina cribrosa experimentally. Recent techniques, including optical coherence tomography imaging (Guo *et al.* 2005; Burgoyne *et al.* 2008; Kagemann *et al.* 2008; Srinivasan *et al.* 2008), second harmonic imaging microscopy (Brown *et al.* 2007; Lomb 2007), and magnetic resonance imaging (Sadun *et al.* 2002; Rausch *et al.* 2007), appear promising. Ideally, a 1 μm imaging resolution would be needed to gather beam-level laminar deformation data, but this is not yet technically possible. Once the full lamina cribrosa can be imaged experimentally, we will be able to extract lamina cribrosa deformations with the optical flow algorithm, which I used to extract scleral deformations in Chapter 3. Moreover, the constitutive model presented in Chapter 4 can be easily adapted to model the mechanical behavior of the lamina cribrosa, and the inverse FE

method developed in Chapter 5 can be used to extract mechanical properties for any soft-tissue that is loaded in 3-D, including the lamina cribrosa using experimental observations.

Once inhomogeneous, nonlinear and anisotropic mechanical properties are available for the lamina cribrosa, we will be able to study the interactions between ONH and scleral biomechanics and we will better understand if some eyes are more susceptible to glaucomatous optic neuropathy due to their biomechanical features. The results presented in Chapters 6 and 7 suggest that the scleral mechanical behavior due to acute elevation of IOP and the scleral remodeling due to chronic IOP elevation are highly specific to an individual. This raises an extremely important point: it is crucial to simultaneously characterize ONH and scleral mechanics in patients to provide valuable predictions regarding their susceptibility to glaucomatous damage.

In this study, we demonstrated that the scleral collagen fiber organization has a large impact on ONH deformation (Chapter 4) and characterized individual scleral collagen fiber organization in the normal, glaucomatous and aging eye. However, my estimates were based on the observed 3-D deformations of an individual scleral shell and I did not characterize scleral collagen fiber organization experimentally. Future work is necessary to validate these estimates experimentally, which will also serve as refinement of the posterior scleral shell models with improved accuracy. Techniques such as X-ray diffraction (Boote *et al.* 2004) and small angle light scattering (SALS; Sacks *et al.* 1997) have been used by several investigators for spatial mapping of collagen fiber organization in biological soft tissues. These techniques could be easily applied to the anterior and

posterior sclera to provide collagen fiber orientation as a known input to the model rather than a fitted parameter.

In this thesis, we have considered collagen as the primary biomechanical constituent of the posterior sclera. Elastin was lumped with all other non-fibrous constituents to form the ground substance matrix. Elastin is highly expressed in both the peripapillary sclera and lamina cribrosa, but is virtually absent in the peripheral sclera (Quigley *et al.* 1991b). To date, there is no clear explanation for this and it will eventually become important to treat elastin as a separate component in constitutive models for ocular soft-tissues. As presented in Chapter 4, it is fairly straightforward to consider elastin as a separate entity in the constitutive model. This type of modeling approach, combined with appropriate experimental data, may provide critical understanding of the mechanical role of elastin in the ONH and peripapillary sclera.

The data from Chapter 7 suggest that extracellular matrix remodeling occurs when the posterior sclera is exposed to chronic IOP elevation. However, this response also appears to be highly specific to an individual. To obtain a better understanding of scleral remodeling, we could consider conducting scleral tissue culture research, in which the pressurization device designed in Chapter 3 could be put into an incubator. The posterior sclera could then be subjected to cyclic IOP elevations for certain periods of time, and we could measure the matrix metalloproteinase and tissue inhibitor of metalloproteinase levels as well as elastin/collagen content, orientation, and fiber diameter. This type of experimental setup combined with appropriate remodeling theories for soft-tissues (Humphrey 1999; Driessen *et al.* 2003; Hariton *et al.* 2007a; Hariton *et al.* 2007b) could greatly enhance our understanding of scleral remodeling.

A Appendix A
Protocols

A.1. Scleral and Corneal Mechanical Testing

Part I: Preparation for the Experiment

Location: Dr. Michael Bottlang's Lab

<u>Things to do with the Laptop computer the day before the experiment:</u>

1) Turn on the laptop.

2) For the sclera, create the following two folders: /Desktop/Sclera/s_m1a_od_txt and /Desktop/Sclera/s_m1a_os_txt. For the cornea, create the following two folders: /Desktop/ Sclera/c_m1a_od_txt and /Desktop/Cornea/c_m1a_os_txt. Remember that each monkey can be specified with a set of three characters (e.g. m1a) also called lab ID. Use the appropriate lab ID for your experiment. "od" and "os" refer to right and left eye.

3) Empty the following files that are located on the Desktop. Make sure these files have been copied and backed up to their appropriate folder as mentioned in Step 35.

File	
geometry_od.txt	geometry_os.txt
clamp_od.txt	clamp_os.txt
canal_od.txt	canal_os.txt
USdata_od.txt	USdata_os.txt
XYaxes_od.txt	XYaxes_os.txt

You then need to open them with Notepad. These files will be used with the 3D-digitizer.

4) Launch the 3-D digitizer software (Immersion MicroScribe Utility Software) located on the Desktop. The 3-D digitizer should be connected to the laptop with a USB port. Make sure that the foot pedal is linked to the 3-D digitizer. The target format is MikePad, which is the default format.
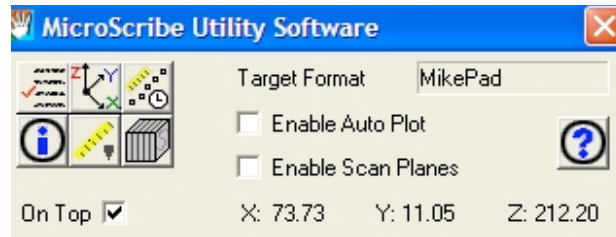
Figure A.1.1. Graphical user interface of the MicroScribe utility software.

5) Make sure that the following files exist in the folder /My Documents/. If not, please create them. They will be used for thickness measurements at twenty different locations at 10 mm Hg.

File_____
10_1_od.txt,   10_1_os.txt
10_2_od.txt,   10_2_os.txt
....
10_19_od.txt,   10_19_os.txt
10_20_od.txt,   10_20_os.txt

Preliminary explanations about the above file naming scheme:

"10" corresponds to 10 mm Hg. "1" to "20" correspond to the 20 measurement sites. "od" is for the right eye. "os" is for the left eye.

The following files will be used to estimate scleral thickness change as a function of IOP at four locations (Inferior, Superior, Nasal, Temporal) in the peripapillary sclera region.

File_____
peri_10_1_od.txt,   peri_10_11_od.txt,   peri_10_111_od.txt,   peri_10_1_os.txt,   peri_10_11_os.txt,
peri_10_111_os.txt,   peri_10_2_od.txt,   peri_10_22_od.txt,   peri_10_222_od.txt,   peri_10_2_os.txt,
peri_10_22_os.txt,   peri_10_222_os.txt,   peri_10_3_od.txt,   peri_10_33_od.txt,   peri_10_333_od.txt,

peri_10_3_os.txt, peri_10_33_os.txt, peri_10_333_os.txt, peri_10_4_od.txt, peri_10_44_od.txt, peri_10_444_od.txt, peri_10_4_os.txt, peri_10_44_os.txt, peri_10_444_os.txt, peri_30_1_od.txt, peri_30_11_od.txt, peri_30_111_od.txt, peri_30_1_os.txt, peri_30_11_os.txt, peri_30_111_os.txt, peri_30_2_od.txt, peri_30_22_od.txt, peri_30_222_od.txt, peri_30_2_os.txt, peri_30_22_os.txt, peri_30_222_os.txt, peri_30_3_od.txt, peri_30_33_od.txt, peri_30_333_od.txt, peri_30_3_os.txt, peri_30_33_os.txt, peri_30_333_os.txt, peri_10_4_od.txt, peri_30_44_od.txt, peri_30_444_od.txt, peri_30_4_os.txt, peri_30_44_os.txt, peri_30_444_os.txt, peri_45_1_od.txt, peri_45_11_od.txt, peri_45_111_od.txt, peri_45_1_os.txt, peri_45_11_os.txt, peri_45_111_os.txt, peri_45_2_od.txt, peri_45_22_od.txt, peri_45_222_od.txt, peri_45_2_os.txt, peri_45_22_os.txt, peri_45_222_os.txt, peri_45_3_od.txt, peri_45_33_od.txt, peri_45_333_od.txt, peri_45_3_os.txt, peri_45_33_os.txt, peri_45_333_os.txt, peri_45_4_od.txt, peri_45_44_od.txt, peri_45_444_od.txt, peri_45_4_os.txt, peri_45_44_os.txt, peri_45_444_os.txt

Preliminary explanations about the above file naming scheme:

"peri" corresponds to peripapillary sclera. "10", "30" and "45" correspond to 10, 30 and 45 mm Hg, respectively. "1", "2", "3" and "4" correspond to the four different locations in the peripapillary sclera where thickness changes will be detected. For a right eye (od), "1" is temporal, "2" is superior, "3" is Nasal and "4" is inferior. For a left eye (os), "1" is nasal, "2" is superior, "3" is temporal and "4" is inferior. For data repeatability, measurements will be performed 3 times at each location, therefore "1", "11" and "111" correspond to the first, second and third measurement at the first location respectively. "od" is for the right eye and "os" is for the left eye.

6) Make sure that the oscilloscope is connected to the port **COM2** from the laptop. The oscilloscope is also connected to the pulser/receiver and the 20 MHz ultrasound probe is connected to the pulser/receiver. Voltage echo signals will be observed on channel 1, with a resolution of 250 ns/div (default setting). Turn off the oscilloscope and pulser/receiver during the night.

7) Make sure that the stage motor is connected to the port **COM1** from the laptop. Turn on the motor controller and open the executable file ScleraTissueTesting.bat located on the Desktop.
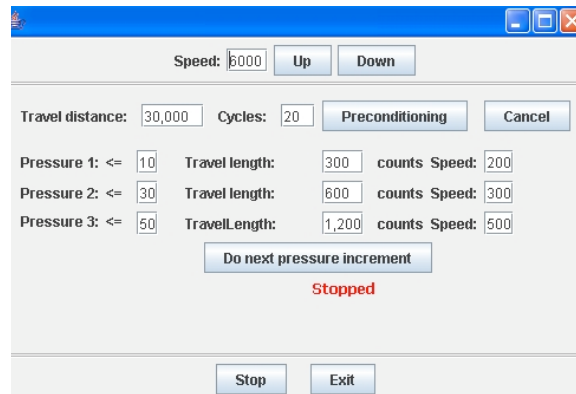
Figure A.1.2. Graphical user interface of the scleral tissue testing software.

The settings to be used are:

Speed for preconditioning: 6,000 (maximum value)

Travel distance for preconditioning: 30,000 (equivalent to a 10 mm Hg pressure increase).

For porcine eyes

Pressure 1: 10 mm Hg, travel length 1: 500, counts speed 1: 300

Pressure 2: 30 mm Hg, travel length 2: 700, counts speed 2: 400

Pressure 3: 50 mm Hg, travel length 3: 1500, counts speed 3: 600

For Monkey eyes

Pressure 1: 10 mm Hg, travel length 1: 500, counts speed 1: 300

Pressure 2: 30 mm Hg, travel length 2: 1500, counts speed 2: 700

Pressure 3: 50 mm Hg, travel length 3: 2000, counts speed 3: 900

Keep the motor controller on during the night.

8) The pressure transducer is always connected to the port **COM3** from the laptop. Reset the probe at 0 mm Hg for atmospheric pressure.

<u>Things to do with the desktop computer "ISTRAM ESPI" the day before the experiment:</u>

1) Create two folders on the J drive (in J:/Sclera/). It is very important to save the data on this drive and not on the C drive. Name the folders with 3 Letters (lab ID) plus "os" or "od" (e.g. m1a_od_espi and m1a_os_espi). You should now have access to the folders J:/Sclera/m1a_od_espi/ and J:/Sclera/m1a_os_espi/.

2) Create two folders on the J drive (in J:/Cornea/). Keep the same names as for the sclera, therefore you should have J:/Cornea/m1a_od_espi/ and J:/Cornea/m1a_os_espi/ available.

3) Create two "Images" folders (if they do not exist) as J:/Sclera/Images/ and J:/Cornea/Images/. These two folders will store all initial scleral and corneal pictures, respectively.

<u>Things to prepare the day before the experiment:</u>

1) One bottle of Saline (1 L). For each litter of saline, use one pack of SIGMA P3813 10 mM phosphate buffered saline, pH 7.4 with one litter of deionized water.

2) One bottle of fixative (5% glut). Please find recipe in the lab notebook under the folder /protocols/.

3) 60 mL syringe filled with 50 mL of saline, attached to the external saline chamber. The saline chamber window should be extremely clean, which is very important to avoid noise in the data. Remember that you always fill the saline chamber from the bottom, which avoids creating air bubbles.

Figure A.1.3. 60 mL syringe attached to the saline chamber.

4) Fill one of the bottle attached to the vertical stage with saline until the level reaches the line. Fill the other bottle with fixative solution (5% glut). Make sure valves are closed to avoid leaks.

5) Attach the ESPI sensor to its support using four M3 hex bolts.

6) Attach the black anodized dock to the stainless steel bread board with four 1/4"-20 hex bolts right next to the 3-D digitizer arm. This dock will be used to obtain geometry and thickness data.
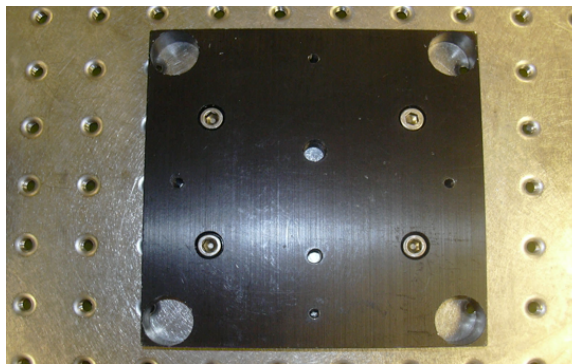
Figure A.1.4. Black anodized dock for the pressurization device.

7) Use the correct clamping module & ring sizes for the experiment and attach them to the pressurization apparatus. Use a 0.8" or 0.9" in diameter clamping module (size 3 or 4, respectively) for porcine eyes + its matching ring. Use 0.6", 0.7" or 0.8" in diameter

clamping module (size 1, 2 or 3, respectively) for monkey eyes + its matching ring. Use a

0.6" or 0.7" in diameter clamping module (size 1 or 2, respectively) for monkey anterior

chambers. 0.6" (size 1) might be good for rabbit sclera. Size 5 has never been used so far.
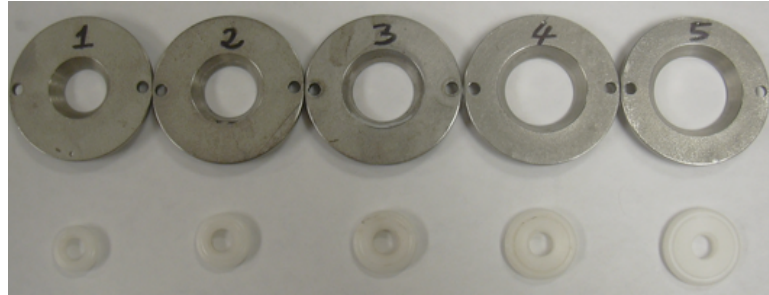
Figure A.1.5. Different clamping modules and matching rings.

8) Put the pressure transducer in its "low" position. It has 2 positions: "high" and "low"

that you can choose from the small vertical stage that carries the probe. Keep the pressure

transducer's valve open, as shown on this picture:

Figure A.1.6. Pressure transducer with open valve.

9) Turn off the small pressure regulator valve. Below is a picture of the "small pressure

regulator".

Figure A.1.7. Pressure regulator.

10) Put a small amount of white titanium powder into a petri dish. 1 or 2 grams should be

enough.

11) About 5 mL of 100 % ethanol

12) **Pulser/receiver set up:**

PRF: 10 kHz
Energy Level: 1 (acoustic energy)
Damping: 1 (signal damping)
Gain: +39 dB
Mode: 1 (T/R)
High Pass Filter (HPF): out
Low Pass Filter (LPF): Full Bandwidth

13) **Oscilloscope set up:**

Sync Out (Pulser/Receiver) is connected to external trigger of the oscilloscope. RF-Signal

(Pulser/Receiver) is connected to channel 1 of the oscilloscope.

Channel 1:

Vertical setting: 5 Volts / division
Horizontal setting: 500 or 250 nanoseconds / division
Probe: 10X

Channel 2:

Never used

External Trigger:

Slope: rising
Level: ~ 200 mV

Devices to protect the day before the experiment (Only in case of primate and human

tissues):

1) Cover the keyboards and mice of the laptop and desktop computers with plastic films

+ lab tape (use simple food plastic wrap).

2) Cover the Oscilloscope with plastic wrap + lab tape.

3) Cover the pressure gage with plastic wrap + lab tape.

4) Cover the pulser/receiver with plastic wrap + lab tape.

Wearing equipment to prepare the day before the experiment:

1) 1 box of S, M or L size gloves.

2) 1 lab coat.

3) 1 protection lab suit.

4) 1 dust mask for mouth protection.

5) 1 splash shield for face protection.

Other equipments you may need:

1) Surgical tools: curved scissors, forceps.

2) 4"x4" gauze pads.

3) Petri dishes.

4) SIGMA P3813 10 mM phosphate buffered saline, pH 7.4.

5) Q-tips.

6) Permanent black marker.

7) Quatricide: 1 concentrated bottle and 1 diluted spray bottle.

8) Plastic pipettes

9) 10 mL & 60 mL syringes.

10) 500 mL empty beaker.

Part II: Lab Notebook, Experiment Files and Fixed Tissue Vial Numbers (FTVN) – Preparation the Day Before the Experiment

If you are about to start mechanical testing on monkey or human eyes, proceed to the following steps:

1) Has the animal been identified in the lab database?

If yes: memorize the animal lab ID (e.g. m1a). This will be used as a prefix for most of the text file names that will be generated.

If no: consider entering this animal within the lab database system.

2) Create two experiment files for this animal. The first file will contain notes about both posterior scleral shells and the second will contain notes about both anterior chambers. Everything related to mechanical testing, ESPI fringes analysis, pre-processing finite element (mesh generation), material property fitting simulation, and post-processing finite element will be commented in these 2 files. For posterior scleral shells, consider using the file mg.exp01474.doc as a template file. For anterior chambers, consider using the file mg.exp01475.doc as a template file. These files are located in the folder .../Exp logs by exp number/ in the lab Notebook. Fill out all the information needed including

Fixed Vial Tissue Numbers (FTVN). You will need six FTVN: one for the right posterior scleral shell, one for the left posterior scleral shell, one for the right anterior chamber, one for the left anterior chamber, and one for the remaining optic nerve and extra orbital tissues for the right eye, and one for the remaining optic nerve and extra orbital tissues for the left eye.

3) Prepare six small vials with tops with the FTVN labeled on the top.

4) Create a sacrifice file for the monkey to be sacrificed.

5) Note that the file exp01479 contains ORA data for monkey corneas.

Part III: Monkey Sacrifice

Location: Necropsy room

1) Gather supplies on a small tray. You will need:

Drugs:

Pentobarbitol or Sleep Away

Syringes and Needles:

For each animal you'll need:

1 - 10cc syringes

1 - 21Gauge, 1" needles

Surgical Instruments:

Large Westcott scissors

0.3 forceps

0.12 forceps

Muscle hook

Hemastats (5 pair)

Enucleation scissors

2 straight razor blades

Miscellaneous:

Fiber-optic light

Tray

Lab tape

Nitrile gloves

Surgical tape

4"x4" gauze pads

Weck cells

Counter Paper (1 piece ~6' long, 1 piece ~36" long, 1 piece ~6" long)

2 large glass (or plastic) vials with tops half filled with PBS, one labeled with OD and one labeled with OS - These are used to store right and left eyes, just after enucleation.

Squirt bottle filled with isotonic saline (PBS, pH 7.4)

Styrofoam head support block

Blue surgical 'diapers'

Large sacrifice bag

2) Prepare your syringe: Attach the 21G1 needle to it. Mark the syringe with lab tape: with a sharpie, make one colored lab tape label - "PENTO". Fill your syringe with 10 mL of pentobarbitol.

When taking drugs from a bottle, first swab the bottle top with alcohol, inject the bottle with air (the same amount as you plan to draw), and draw the drug (turn bottle upside down) making sure there is no air in the syringe.

3) Cover the counter in the surgery suite with counter paper. Using the largest piece of counter paper, cover the counter from end to end. With the medium-sized piece, drape one end over the back of the counter and the other end over the front edge of the counter. Secure the paper to the counter at all four corners with lab tape. Put a blue surgical diaper down on the center of the counter. Set up the fiber optic light on the left rear of the counter for later use.

4) Cover the styrofoam head block with counter paper. Using the small piece of counter paper, wrap the block and secure with lab tape. Wrap the block in such a way that the taped seam is on the underside of the block.

5) Catheterize the animal. This will be conducted under Animal Care guidelines.

6) Inject proper dosage of Pentobarbitol into the catheter tube to induce death.

7) Place the head on the head support block.

8) Cut the lids in the nasal and temporal corners to the bone. Beginning nasally (at the tear duct), use the forceps and Westcott scissors to separate Tenon's capsule from the globe at the limbus. Proceed around inferiorly, temporally, and finally superiorly, separating the capsule and musculature from the globe. Proceed very carefully! As Tenon's and the musculature become separated from the globe, use hemastats to keep the tissues out of the way. Cut Tenon's capsule anterior to posterior as far into the orbit as possible at the nasal and temporal axes. Using the enucleation scissors reach under the globe, pressing the scissors to the orbital wall prior to each cut (VERY IMPORTANT)

and cut away the remaining attachments, being careful to get as much of the optic nerve as possible.

10) Place the enucleated globe in the proper large vial of PBS, cap it, and shake it to remove excess clotted blood.

11) Folding a 4"x4" gauze pad into fourths, place the corner of the folded gauze into the orbit and tape it in place with lab tape. This will absorb any blood from cut vessels.

12) Turn the animal over and repeat steps 9), 10), and 11) for the other eye.

13) Optional: Have an assistant remove the brain of the monkey and place it in fixative (10% formalin). To do so, first remove skin and muscle tissue to expose the skull. Using a bone saw, make cuts into the skull, across the brow bone, just above the ear insertion, and the nape of the neck. Pry off the skull cap using Rongers or another sturdy scissor-like instrument. Once, the brain is exposed, pull away overlying membrane using a hemostat and scalpel. This membrane continues underneath the cerebral cortex, and should be pulled back from there as well. While carefully pulling the brain up, use a scalpel to cut away nerve bundles underneath. Finally, make a vertical cut along the posterior base of the brain, severing the spinal cord. This is a blind cut. The entire brain can then be carefully pulled from the cranial cavity.

14) Place the animal in a sacrifice bag, then twist and tape the bag shut. Place the bag in the biohazard bin in the cold room.

Part IV: Monkey Tissue Preparation

Location: Dissection room, near the cutting room

You need:

Both large vials that contain monkey whole globes you just enucleated

6 vials with tops with FTVN labeled on them.

- 2 of them will be filled with isotonic saline at room temperature (~ 22 degree Celsius). These 2 vials will be later filled with 5% glut fixative at the end of the experiment to store posterior shells.

- 2 of them will be filled with exactly 7 mL of corneal preservation medium (Optisol GS) at 4 degree Celsius. These 2 vials will be later filled with 5% glut fixative at the end of the experiment to store anterior chambers.

- 2 of them will be filled with fixative (5% glut) (for remaining optic nerves)

Squirt bottle filled with isotonic saline (PBS, pH 7.4)

4"x4" gauze pads

2 glass petri dishes

Forceps

Scissors

1 biohazard bag

1 box

1) Bring both large vials containing the globes to the dissecting room. Remove all extra-orbital tissues and clean the scleral shell with great care for the right eye. Perform two nasal cuts and one superior cut along the length of the retrobulbar optic nerve to preserve orientation for subsequent axon counting. This should be done while the nerve is still

attached to the eye. Section the optic nerve (leave ~ 2 to 3 mm of optic nerve stump). Place remaining nerve in one vial filled with glut fixative with FTVN on top. Place extra-orbital tissues in the biohazard bag.

3) Section (a small cut is enough) the right eye below the equator (using a razor blade). Make sure to keep the retina and choroid intact. Separate the anterior chamber from the posterior shell by cutting along a line parallel to the equator. Create a small notch to later distinguish the superior quadrant of the anterior chamber.

Important Note: it appears that if the retina and choroid are removed near the ONH, it will likely create leaks at the sclera/nerve junction. It is best to carefully dissect the retina and the choroid, except for a 7-mm diameter patch centered on the ONH.

4) Place the right anterior chamber in a vial filled with 7 mL of corneal preservation medium (Optisol GS) at 4 degree Celsius with FTVN indicated on the top. Place the right posterior scleral shell in a vial filled with isotonic saline with its FTVN mentioned on top at room temperature.

5) Repeat all steps for the left eye.

6) Place both anterior chambers labeled with FTVN in a refrigerator at 4 degree Celsius.

Part V: 3-D Scleral and Corneal Mechanical Testing

Location: Dr. Michael Bottlang's Lab

At this point you have 1 or 2 sclera ready to be tested, and eventually 1 or 2 anterior chambers.

Explanations will be given for scleral samples first.

1) The valve of the small pressure regulator (0 to 2 psi) must be turned off (see Figure A.1.7). Turn on the valve of the pressure regulator that is attached to the yellow compressed air tank. We want an output pressure that belongs to the range: 20 - 40 psi. **Do not exceed 40 psi**. 30 psi is a good value to choose (the figure below shows 30 psi on the left pressure reading).

Figure A.1.8. Pressure regulator.

Important note: if you do not realize that the compressed air tank is empty and you can not obtain a new one in time, you can simply use a 60 mL syringe filled with air and bypass the compressed air tank line. This is also a very good way to increase air pressure and maintain it constant within the posterior shell or anterior chamber.

2) Put the pressurization apparatus in its black dock. You do not need to attach the pressurization apparatus to the dock.
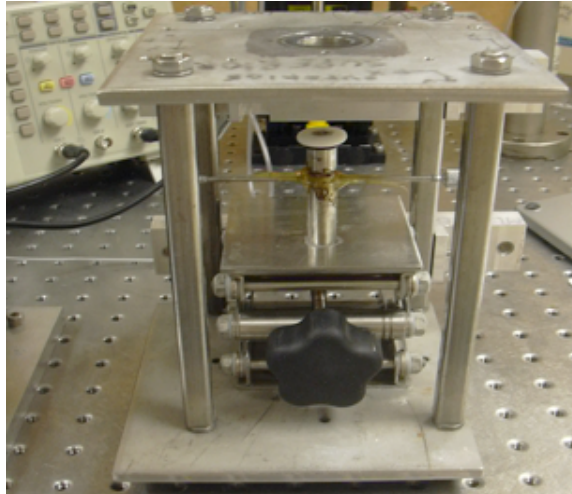
Figure A.1.9. Pressurization apparatus attached to the dock.

3) Remember that yesterday you already attached the clamping module & plastic ring to the pressurization apparatus. Bring down the translation stage to its lowest position, and cover the plastic ring with the scleral shell (always start with a right eye (od) if you are working with a pair).

Figure A.1.10. Pressurization apparatus with balloon sample.

4) With two forceps or with your fingers (wearing gloves), try to orient the shell as best as you can. Superior and inferior are written on the top plate of the apparatus, to avoid any mistakes. Move the specimen upward by using the vertical stage, and bring it close to the clamping region but do not clamp the sample yet. At this point, try to center the optic nerve stump with your forceps and gently pull it upward to maximize the surface area where displacements will be measured. It is important to have a maximum amount of tissue above the clamp to minimize any possible boundary effects around the optic nerve stump. Note that the optic nerve stump cannot be exactly located at the center of the ring because it will not respect the physiological shape of the eye. You may need some practice with porcine eyes (see bottom of the page) before doing any experiments with valuable tissues.

5) Clamp tightly the scleral shell by moving the stage upward to its maximum position. You can now switch fluid and use saline (one valve allows you to switch from air pressure to saline pressure). You can increase the pressure by turning the valve of the small pressure regulator (0 to 2 psi). Once there is eventually no more air to get rid of, you can shut down the system (turn off the pressure regulator valve) and switch from pressure regulator pressurizing to column of saline pressurizing by simply removing the saline bottle cap, and turning a valve.

Note: It may happen that detached retina will block pressure increase because it will get stuck within the holes of the pressure chamber. In this case, you should use a 60 mL syringe and bypass the column of saline. Open the pressure transducer valve and create a saline flow with the syringe that should take care of the problem. Afterward, you can simply close the valve and reestablish the column of saline.

6) Dry the scleral shell with a gauze pad. Use a pipette and add a single drop of 100 %

ethanol into the petri dish that contains white titanium powder and mix it well. Cover the

tissue with this mixture with either a Q-tip or a paintbrush. Spread it uniformly and let it

dry for at least one minute. Do not spread the mixture anywhere else, because it is

extremely difficult to clean or remove. The outer shell surface should be completely

uniform and white. Keep in mind that the whiter it is, the better the ESPI fringes will be.

7) Set up the pressurization apparatus horizontally and attach it to the breadboard near the

ESPI station. Use four 1/4"-20 hex bolts.
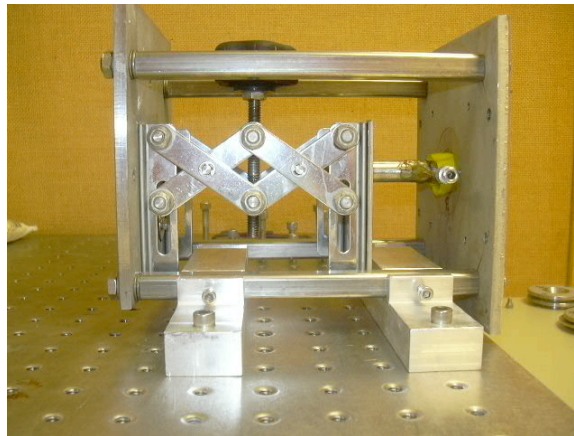
Figure A.1.11. Pressurization apparatus in horizontal position.

8) Attach the external saline chamber to the pressurization apparatus with four M4 hex

bolts. Note: do not tighten too much otherwise you may break the glass window. Use the

syringe filled with 50 mL of saline (prepared the day before) to fill the cavity. Set up the

pressure to approximately 5 mm Hg by using the motorized vertical stage and its mini

pad controller (Up and Down keys).

Figure A.1.12. Mini pad controller.

9) Add the ESPI sensor attached to its support on top of the saline chamber with four M6 hex bolts. Use the correct orientation for the ESPI coordinate systems (X & Y) as shown on the right in the figure below.
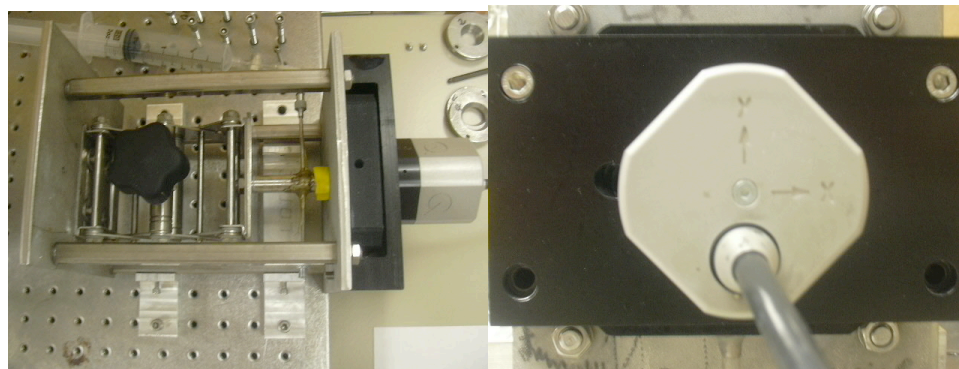
Figure A.1.13. ESPI sensor attached to the pressurization apparatus.

10) The speed of the vertical stage (upper box) has already been set up to 6,000 (no unit), the travel length to 30,000 (no unit) and the number of cycles to 20 by default. Check if this information is correct on the laptop screen. Start the preconditioning cycle by clicking on the "preconditioning" button. This will automatically drive the motorized stage for 20 cycles where the pressure will oscillate between 5 and 15 mm Hg. You will have to wait for about 10 to 15 minutes after the preconditioning period to reach mechanical equilibrium.

11) In the meantime turn on the ESPI desktop computer. Log on as an administrator, and launch the software ISTRA Q100 V2.7 (Start > Programs > Istra > Istra Q100 v2.7). Go to Measurement > Storage Directory and set up the storage directory (created the day before) on the J drive (in J:/Sclera/) as e.g. m1a_od_espi if you are working with the right eye. Then insert the two diodes as shown in the figure below and turn the switch on to provide enough light for you to capture an image of the scleral shell.
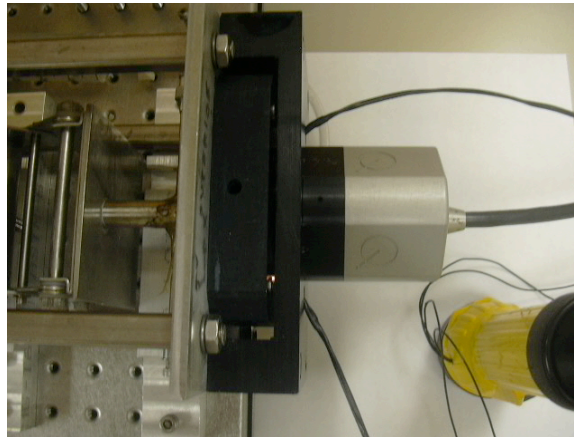
Figure A.1.14. Diodes from the flash light attached to the ESPI support.

Then press F2 for live image, capture the image by clicking on Measurement > Capture Image. Save the image (as shown below) in the "Images" directory located on the J drive (J:/Sclera/Images/) by clicking on Image > Save Image. Save it as e.g. m1a_od.tiff.
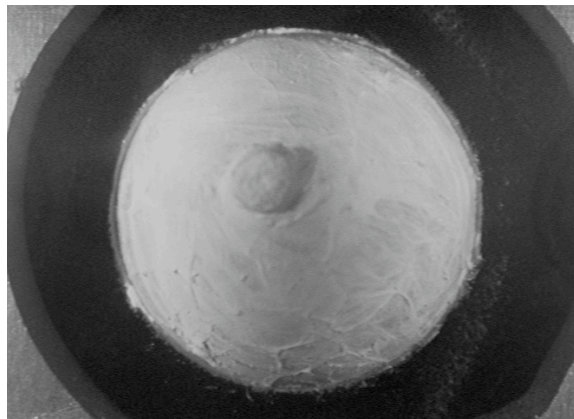
Figure A.1.15. Posterior scleral shell observed with the ESPI sensor.

12) Turn off the light switch and remove the two diodes. Press F3. If you have waited for the equilibrium period (~ 10 to 15 minutes), the screen should appear black. If you observe some movement, you should probably wait a little bit longer to reach equilibrium. You can click F3 every time the image gets saturated. Make sure you are still reading 5 mm Hg on the pressure gage. If not, you can always adjust it with Up and Down keys of the minipad.

13) **Important notes about ScleraTissueTesting software user's interface:**

Note1: You may have noticed that the user can set 3 different speed values and 3 different travel length values. As we know that since soft tissues are primarily made of collagen type I, they get stiffer as the pressure load increases. Because of this nonlinear phenomenon, the user cannot use a single speed and travel length value as the pressure increases from 5 to 45 mm Hg. The speed and travel length need to be changed to adapt to the highly sensitive ESPI sensor. Therefore the user can choose 3 different speeds and 3 different travel lengths in the pressure ranges [-5 mm Hg; 10 mm Hg], [10 mm Hg; 30 mm Hg] and [30 mm Hg; 45 mm Hg]. Some calibrations values are given at the beginning of the protocol, however it is always good to check if those values are suitable for each eye. To incrementally increase the pressure you can press the Right key on the minipad, it will automatically use the speed and travel length values depending on which pressure range the current pressure value lies in.

To calibrate the three speed values and three travel length values, bring the pressure to 5+ mm Hg, press the minipad Right key and find good values (speed 1 & travel length 1) to obtain about 10 fringes on your screen (use F3 on the desktop to see the fringes). Use a fast enough speed to avoid image saturation. Bring the pressure to 10+ mm Hg and repeat

this step to find speed 2 & travel length 2. Bring the pressure to 30+ mm Hg and find speed 3 and travel length 3. Once you have calibrated the system, bring your pressure back to exactly 5 mm Hg and wait for equilibrium.

Note2: The Left key of the minipad will allow you to record the pressure in mm Hg from the pressure transducer. All readings will be saved in the file Pressure.txt located in the folder c:/Temp/. If you exit the software and re-start it this file will be overwritten!

Note3: Every time you press the Right key on the minipad, the stage will move upward immediately. Once the pressure increase is complete, the software will hang and wait for 5 seconds. After 5 seconds you will hear 5 quick consequent beeps, which means that you can record the pressure. Because we want to keep data as close to equilibrium data as possible, it is good to wait for equilibrium after each pressure increase. 5 seconds appears to be a good time to obtain equilibrium and to avoid ESPI image saturation. Note that the pressure increase is extremely small (~ 0.1 mm Hg) which means that viscoelasticity does not have a major effect on the resultant displacement field. If the user is willing to modify the waiting time, it is possible to do so in the lowest box of the user interface. The time is expressed in seconds. However I would recommend keeping the default value, which is currently 5 seconds in order to keep consistency for each experiment.

14) Make sure your pressure is still at 5 mm Hg. If not, adjust it. You are now ready to acquire ESPI fringes. Go to Measurement > Record Series. The default settings with Visible Direction > 1, Illumination Configuration > Q100 all directions and Requested Step Count > 1000 are the settings to use. Then press OK.

15) You are now dealing with two computers at the same time (laptop + desktop). With the mini pad click Left key to record the initial pressure (should be 5 mm Hg if you were

careful), then click the Right key to do a small pressure increase (with the mini pad). Right after the pressure increase, the software will pause for 5 seconds. After 5 seconds you will hear the equilibrium beep. At this time just click Left key with your left hand to record the pressure in <u>Pressure.txt</u> simultaneously with the button <u>capture</u> on the desktop with your right hand, which will save the fringes as 4 separate images. Repeat until the pressure exceeds 45 mm Hg. Below is the user interface of the ISTRA Q100 v2.7 software.
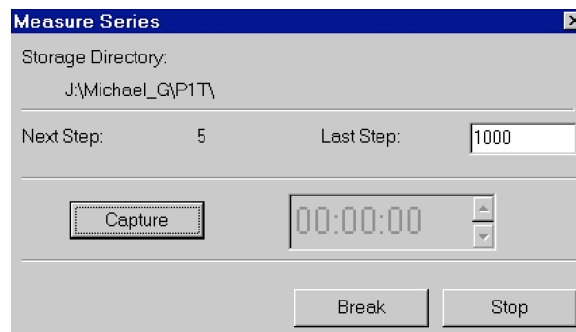
Figure A.1.16. ISTRA Q100 v2.7 graphical user interface.

16) Remove the saline from the external saline chamber with the syringe. Remove the ESPI sensor plus its support. Remove the external saline chamber. Place the pressurization apparatus on the black dock with the inferior quadrant toward yourself. Attach the pressurization apparatus to the dock with two <u>8-32 hex bolts</u>.

17) Put the pressure gage in its "high" position. Set up the speed of the motor to its maximum (6,000 which should always kept unchanged) and bring the pressure back to 30 mm Hg (mini pad, Up & Down keys). Keep the shell hydrated with drops of saline.

18) Launch the Immersion <u>MicroScribe Utilization Software</u> that is located on the Desktop of the laptop computer, which should be already opened if you have followed strictly all the previous steps.

244

19) Reset the digitizer by pressing the white button located on its back. The red diode of the digitizer will turn green.

20) Open the file clamp_od.txt (or clamp_os.txt if you are dealing with the left eye) located on the Desktop of the laptop. You can now start to digitize the clamping area by pressing the foot pedal linked to the 3-D digitizer. Get about 20 to 30 points. Save the file and close it.

21) Open the file canal_od.txt. Digitize the scleral canal as best as you can (limit between the optic nerve stump and the sclera). Generate about 20 to 30 points. Save the file and close it.

22) Open the file geometry_od.txt. Digitize the whole shell with lots of points (~ 1,000 points). Save the file and close it. Do it very carefully, and do not push too hard with the tip.

23) Open the file XYaxes_od.txt. Digitize the following 8 points in order (each of them are in a black circle). Those 8 points have been created to define the digitizer coordinate system with respect to the ESPI coordinate system, so it's very important to get them.
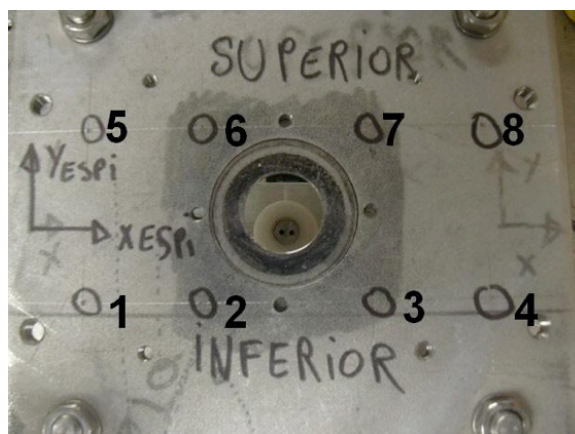
Figure A.1.17. Top plate of the pressurization apparatus.

Save the file and close it. You are done with the digitizer. Brick the tip back to its home position.

24) Draw 20 points on the top of the scleral shell with a sharpie black permanent marker as follows. Always start from the right side and go counter clockwise as shown below. Note that if it is a right eye, points "1", "2" and "3" will belong to the temporal region, and points "11", "12" and "13" will belong to the nasal region. If it is a left eye points "1", "2" and "3" will belong to the nasal region, and points "11", "12" and "13" will belong to the temporal region.
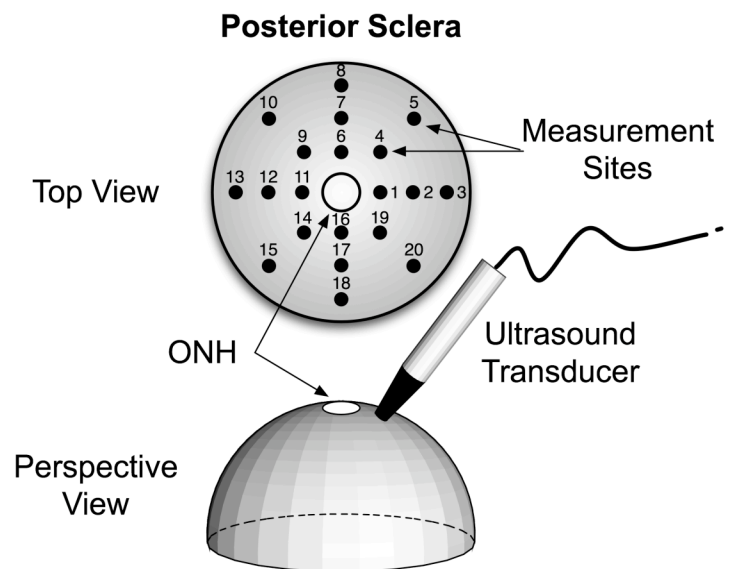
Figure A.1.18. Location of the 20 measurement sites.

Open the file USdata_od.txt. Digitize the 20 points in order (from 1 to 20). It is very important to respect this order for later 3-D shell reconstruction. Save the file and close it.

Important note: The pressure was chosen to be 30 mm Hg to gather all the data from the 3-D digitizer arm. These data are needed for the 3-D finite element reconstruction. However, we need the initial geometry at 5 mm Hg. 30 mm Hg was chosen instead of 5 mm Hg for the following two reasons. First, at 5 mm Hg, it is very difficult to digitize the

shell as there is almost no resistance from the shell, therefore the digitizer tip can push

the tissue too much that the digitizer user will be unaware of. Secondly, displacements

between 5 and 30 mm Hg are probably on the order of 50 microns, which is invisible for

the naked eye, which is also invisible for the 3-D digitizer because it has a resolution of ~

0.23 mm. Moreover at 30 mm Hg, the user will feel the presence of the shell when

touching it with the digitizer tip because of its higher resistance.

25) Turn on the oscilloscope and the pulser/receiver (settings defined above), then launch

the software OpenChoice Desktop (laptop). Go to Select Instrument > COM2 and Select

Channels > Channel 1. To obtain a similar signal as shown below, you just have to click

on Get Data.
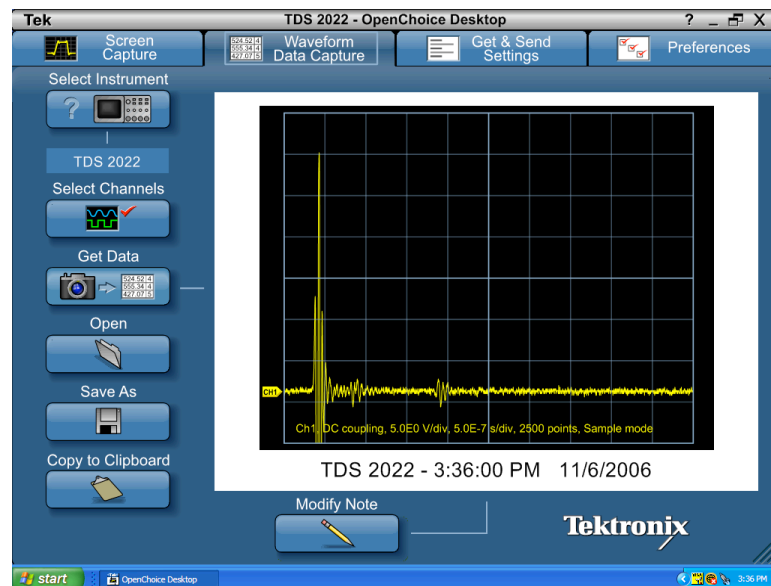
Figure A.1.19. OpenChoice Desktop graphical user interface.

26) Switch from saline pressure to air pressure with the pressure regulator, and bring the

pressure to 10 mm Hg. Air within the cavity will be humid enough to keep the shell

hydrated. Wait for ~ 10 to 15 minutes to reach equilibrium. Again, it is always good to

keep the outer shell hydrated with a few drops of saline. You can do so by dipping the ultrasound transducer into saline and spread saline onto the scleral surface.

27) For each black dot that was drawn onto the scleral surface, we are interested in measuring a corresponding thickness at 10 mm Hg. To do so, try to orient the pachymeter probe perpendicular to the outer scleral surface. You will know that the probe is perpendicular to the surface when you start seeing a good echo signal on the oscilloscope. This means that acoustic energy is reflected from the inner surface of the shell, which will be enough to evaluate the thickness at this spot. An echo should look like that:
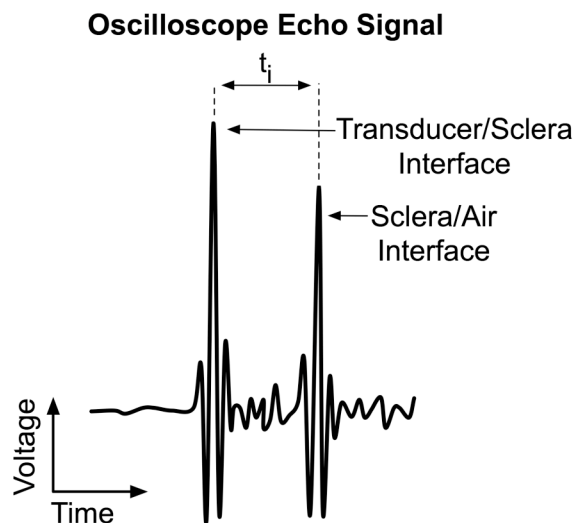
Figure A.1.20. Oscilloscope echo signals.

Note that the first peak represents acoustic energy (transformed into voltage) that is reflected from the ultrasound probe/outer tissue surface interface.

Once you get an echo on the oscilloscope, press the RUN/STOP button of the oscilloscope. This will freeze the signal. With the software OpenChoice Desktop click on Get Data and then Save As to record the signal as a text file (it is important to record it as a "txt" format and not as a "csv" format). For the first point, save the signal in the file

10_1_od.txt that is located in the folder <u>My Documents</u>. Press <u>RUN/STOP</u> to rerun the oscilloscope.

28) Repeat the same step for the other 19 points and try to get good echoes. The better the echoes are, the easier it will be for the 3-D shell reconstructions.

29) This following step will help us to characterize thickness changes as a function of IOP for the peripapillary sclera (Inferior, Superior, Nasal & Temporal regions). Attach the ultrasound transducer to the mechanical positioning arm. Attach the positioning arm to the optical board with the incorporated magnet (<u>switch: ON</u>). Bring the probe tip, still attached to the arm, in contact with point number 1 (temporal for od, nasal for os) and try to obtain an echo signal and make everything stable. Press the <u>RUN/STOP</u> button of the oscilloscope, catch the signal with the laptop and save the signal as a text file: peri_10_1_od.txt. Do not move anything and repeat the measurement two more times and save the signals as peri_10_11_od.txt and peri_10_111_od.txt. This will show that the data are repeatable.

30) Repeat the same thing for point number 6 (always superior region). Save the files as peri_10_2_od.txt, peri_10_22_od.txt, and peri_10_222_od.txt.

31) Repeat the same thing for point number 11 (nasal for od, temporal for os). Save the files as peri_10_3_od.txt, peri_10_33_od.txt, and peri_10_333_od.txt.

32) Repeat the same thing for point number 16. Save the files as peri_10_4_od.txt, peri_10_44_od.txt, and peri_10_444_od.txt.

33) Increase the pressure to 30 mm Hg, make sure you still keep the outer shell hydrated. Repeat steps 29 to 32 for this pressure. Save files as peri_30_1_od.txt...

34) Increase the pressure to 45 mm Hg, make sure you still keep the outer shell hydrated. Repeat steps 29 to 32 for this pressure. Save files as peri_45_1_od.txt...

35) We now want to fix the shell at pressure. Add the white plastic chamber on top of the eye. See the figure below:
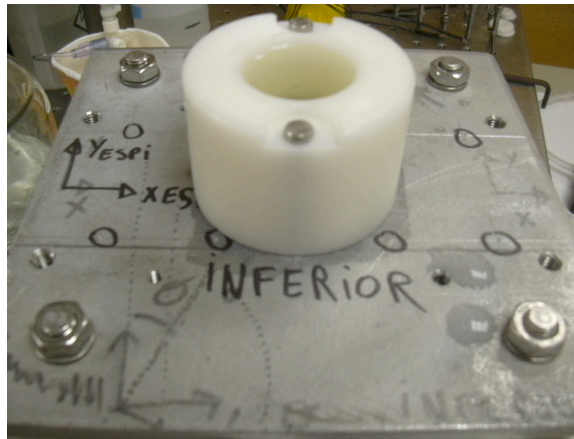
Figure A.1.21. Plastic sealing chamber.

Go back to column of saline pressurizing by opening the pressure transducer valve, by filling the cavity with saline, by closing the pressure transducer valve and by bringing the pressure to 10 mm Hg for a right eye or 45 mm Hg for a left eye (use Up & Down keys of the minipad). You can now close the saline valve and open the fixative valve. The fixative bottle is also located on the motorized vertical stage. Now, open the pressure transducer valve and let the saline go away, it should be pretty clear when fixative will be inside the cavity (use food colorant to color the fixative). Once fixative is fully inside the pressure chamber, fill the white plastic chamber with fixative until it covers the whole half-globe. Make sure the pressure is still at 10 (od) or 45 mm Hg (os). If not, adjust it. Add a gauze pad on top of the white plastic chamber. Wait for about an hour for the tissue to be fixed. In the meantime save all the text files that have been generated in the folder /Sclera/m1a_od_txt located on the Desktop. Files include: Ultrasound text files,

digitizer text files, and pressure reading text file (do not forget this one: it is Pressure.txt in c:/Temp/).

36) After one hour, remove fixative from the white plastic chamber with a small pipette, and discard it in a 500 mL beaker. Open the pressure transducer valve and empty the whole system from its fixative by creating an airflow that bypasses the column of fixative. Unclamp the tissue. Empty the vial with FTVN on top that has been filled with saline (or Optisol, for anterior chambers) with a pipette (discard in the 500 mL beaker) and fill it with 5% glut fixative. Take the fixed tissue out of its clamp using a forceps (the tissue may get stuck a little bit because the scleral portion that was not immersed is likely to be dry) and drop it in its corresponding vial filled with fixative, then cap the vial.

37) After one hour do a saline flush of the saline bottle and the pressurization apparatus, use a half-balloon if you have any or simply cut a glove finger.

38) Repeat step 1 to 37 with the left eye (os).

39) Clean: add concentrated quatricide to all saline solutions that have been in contact with the specimen. Use the spray bottle to disinfect tools and device. Use a quatricide flow within the whole system (use a balloon) and flush everything after with water. Glut is a good alternative to quatricide with similar disinfecting purposes, as quatricide seems to damage the luer ends of each tube and makes silicon brittle (the transparent silicon that seals the glass window of the external saline chamber).

Corneal, anterior chamber testing (The following day)

Make sure that you have prepared everything as mentioned at the beginning of the protocol. Follow all Steps from 1 to 39 for both anterior chambers with exceptions for steps listed in the following Differences section.

Use folders /Desktop/Cornea/m1a_od_txt on the laptop and J:/Cornea/m1a_od_espi on the ESPI computer.

Differences:

Step 21: Digitize sclera/cornea boundary (limbus) instead. Keep the name canal_od.txt, as those files are constantly overwritten.

Steps 24 to 34: Do not go through. Instead, measure central corneal thickness at 10, 30 & 45 mm Hg. Save files as central_10_od.txt, central_30_od.txt and central_45_od.txt. Then continue to Step 35 until Step 39.

A.2. Extraction of 3-D Scleral Displacements

The following protocol will describe the steps needed to extract 3-D full-field displacements for each scleral shell.

1) After completion of one experiment, copy the folders /s_m1a_od_espi/ and /s_m1a_od_txt/ (for animal m1a, eye od) to your desktop.

2) Create the folder /s_m1a_od_disp/ on your desktop. In this folder, copy the image file **m1a_od.tiff**, as generated during the experiment, as well as both files **rec.ber** and **reccircle.ber** that can be found in the folder /ESPI/Borders/ from the attached DVD.

3) Launch the software istraMS (DVD location: ESPI/IstrQ100/**istrams.exe**). The following image should appear on your screen.
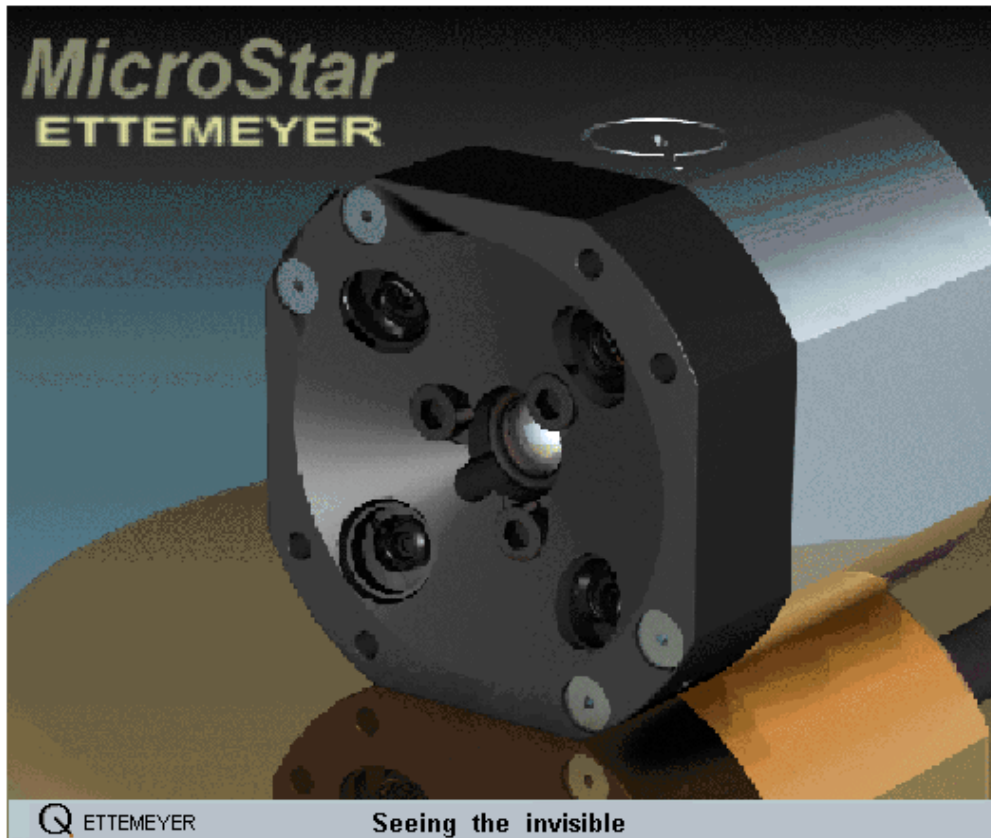
Figure A.2.1. ESPI software to extract 3-D full-field displacements.

4) Go to <u>Image > Load Image</u> and select /s_m1a_od_disp/**m1a_od.tiff** (Figure A.2.2).
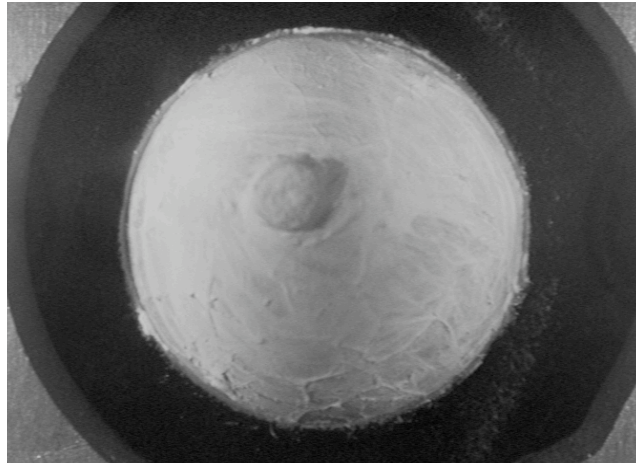
Figure A.2.2. Posterior scleral shell observed with the ESPI sensor.

5) Go to <u>Image > Load Border</u> and select /s_m1a_od_disp/**rec.ber**. The file **rec.ber** serves as a border and delimitates the field of view in which the 3-D displacements will be computed. It is strongly recommended to always use the same border file for all analyses.

6) Go to <u>Settings > Storage Directory</u> and select the folder /s_m1a_od_espi/ that is located on your desktop.

7) Open the file **Pressure.txt** from the folder /s_m1a_od_txt/ with Crimson Editor (http://www.crimsoneditor.com). This file contains all IOP levels from 5 to 45 mm Hg. We are interested in computing 3-D full-field displacements for the following IOP ranges: 5-7, 5-10, 5-20, 5-30, and 5-45 mm Hg and therefore we need to evaluate the total number of IOP steps for each IOP range.

Here is an example of what was recorded in one file **Pressure.txt**.

```
Line #        IOP value
1             4.98
2             5.13
3             5.29
4             5.42
5             5.59
6             5.74
7             5.92
8             6.09
9             6.23
10            6.38
11            6.55
12            6.72
13            6.89
14            7.07
15            7.23
16            7.39
17            7.6
...           ...
30            9.77
31            9.93
32            10.1
33            10.45
...           ...
58            19.42
59            19.68
60            19.91
61            20.63
62            20.82
...           ...
82            29.29
83            29.47
84            30.35
85            30.61
86            30.86
...           ...
110           44.44
111           45.32
112           45.57
113           46.45
```

In this file, 4.98 mm Hg corresponds to the initial IOP. For this experiment, the first IOP

step was performed from 4.98 to 5.13 mm Hg. To extract 3-D displacements between 5

and 7 mm Hg, we will first locate the closest value to 7 mm Hg, which is on line 14 (7.07

mm Hg). We will then compute the real IOP interval which is (7.07 - 4.98 = 2.09 mm

Hg) and convert this value from mm Hg to Pa (2.09 mm Hg = 278.64 Pa). The value

expressed in Pa is the one that will be used as loading for inverse finite element simulations. Since 7.07 mm Hg is located on Line 14, it required 13 IOP steps to reach that value during the experiment. All these information should be entered in the file **Pressure.txt** as follows, and repeated for all other IOP intervals (*i.e.* 5-10, 5-20, 5-30 and 5-45 mm Hg):

```
Line #          IOP value
1               4.98  Initial IOP
2               5.13
3               5.29
4               5.42
5               5.59
6               5.74
7               5.92
8               6.09
9               6.23
10              6.38
11              6.55
12              6.72
13              6.89
14              7.07  Step 13: 7.07 – 4.98 = 2.09 mm Hg = 278.64 Pa
15              7.23
16              7.39
17              7.6
…               …
30              9.77
31              9.93  Step 30: 9.93 – 4.98 = 4.95 mm Hg = 659.95 Pa
32              10.1
33              10.45
…               …
58              19.42
59              19.68
60              19.91 Step 59: 19.91 – 4.98 = 14.93 mm Hg = 1990.50 Pa
61              20.63
62              20.82
…               …
82              29.29
83              29.47
84              30.35 Step 83: 30.35 – 4.98 = 25.85 mm Hg = 3446.38 Pa
85              30.61
86              30.86
…               …
110             44.44
111             45.32 Step 110: 45.32 – 4.98 = 40.34 mm Hg = 5378.22 Pa
112             45.57
113             46.45
```

8) With the software istraMS, go to <u>Measurement > Evaluate Series</u> and enter <u>Evaluation Range, First:</u> 1, <u>Last:</u> 13. This will start the ESPI fringe analysis algorithm so as to extract 3-D displacements for the IOP range: 5 to 7 mm Hg. For each step, you will visualize four different fringe patterns, corresponding to the four laser illumination directions. After the fringe analysis is performed, you should click on the "User Control Window" icon.

9) Click on the "x" icon, then <u>Data > Other File Operations > ASCII export > all</u> and export the x-component of the displacement field as **x1_57.txt** in the folder /s_m1a_od_disp/.

10) Click on the "y" icon, then <u>Data > Other File Operations > ASCII export > all</u> and export the y-component of the displacement field as **y1_57.txt** in the folder /s_m1a_od_disp/.

11) Click on the "z" icon, then <u>Data > Other File Operations > ASCII export > all</u> and export the z-component of the displacement field as **z1_57.txt** in the folder /s_m1a_od_disp/.

12) Repeat steps 8) to 11) for the IOP range: 5 to 10 mm Hg. Export the x-, y- and z-components of the displacement field as **x1_510.txt**, **y1_510.txt**, **z1_510.txt** in the folder /s_m1a_od_disp/.

13) Repeat steps 8) to 11) for the IOP range: 5 to 20 mm Hg. Export the x-, y- and z-components of the displacement field as **x1_520.txt**, **y1_520.txt**, **z1_520.txt** in the folder /s_m1a_od_disp/.

14) Repeat steps 8) to 11) for the IOP range: 5 to 30 mm Hg. Export the x-, y- and z-components of the displacement field as **x1_530.txt**, **y1_530.txt**, **z1_530.txt** in the folder /s_m1a_od_disp/.

15) Repeat steps 8) to 11) for the IOP range: 5 to 45 mm Hg. Export the x-, y- and z-components of the displacement field as **x1_545.txt**, **y1_545.txt**, **z1_545.txt** in the folder /s_m1a_od_disp/.

16) After extraction of all displacements, go to <u>Image > Load Image</u> and select /s_m1a_od_disp/**m1a_od.tiff**.

17) Go to <u>Image > Load Border</u> and select a different border file /s_m1a_od_disp/**reccircle.ber**. This file is needed to locate the clamp boundary so as to align finite element meshes and 3-D displacement fields in later anatomical reconstructions.
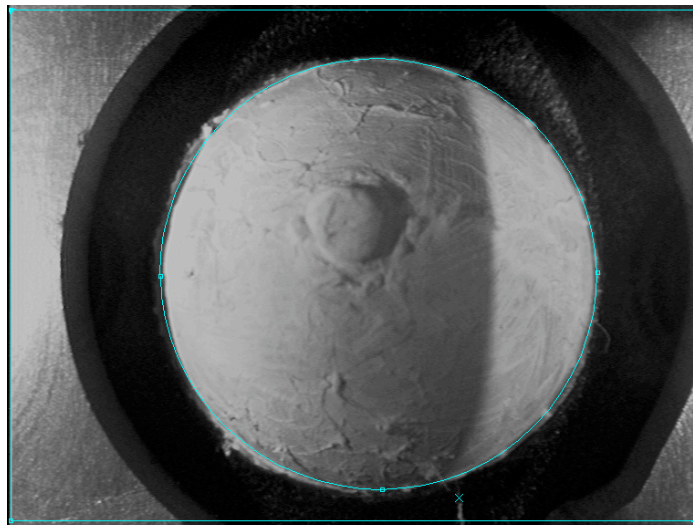
Figure A.2.3. Delineated Clamping boundary.

Define the clamping boundary (green circle in Figure A.2.3) using the "Modify" icon. Make sure the reference point (green cross in Figure A.2.3) is inside the green rectangle but outside the green circle. Go to <u>Measurement > Evaluate Series</u>, choose <u>First: 1 Last:</u>

10, and click OK. Click on the "User Control Window" icon then "x". Go to <u>Data ></u>
<u>Other File Operations > ASCII export > all</u> and export the x-component of the
displacement field as **recminuscircle.txt** in the folder /s_m1a_od_disp/.

A.3. Extraction of Scleral Mechanical Properties

1) Copy all files from the folder /s_m1a_od_disp/ into the folder /s_m1a_od_txt/. Copy
all files from the folder /Code/Eyemesh/ (attached DVD) into the folder /s_m1a_od_txt/.

2) Open Matlab and set the path to /s_m1a_od_txt/. Run the commands *rvs od 1, …, rvs
od 20* in order to extract twenty scleral thickness values as measured experimentally.
Record all twenty thickness values and manually enter them in the file
gennerateinnersurface.m (see Appendix B.1 for more explanations).

3) Enter all five IOP values, as calculated in Appendix A.2 (*e.g.* 278.64, 659.95, 1990.50,
3446.38, 5378.22 Pa) in the file **nike3dinputdeck.m**. This five values will be used as
loading for all finite element simulations.

4) In Appendix A.2, displacements were calculated for the entire field of view of the
ESPI sensor (~ 35×25 mm^2) and reported in a 256×256 matrix. Now, we would like to
restraint that field of view and consider the displacements that are only pertinent to the
posterior sclera. To do so, open the file **recminuscircle.txt** with Excel or with any
software that will display this file in a matrix format. As shown in Figure A.3.1, extract
the parameters *imin*, *imax*, *jmin* and *jmax*. Enter the obtained values in the file **ESPI.m**.
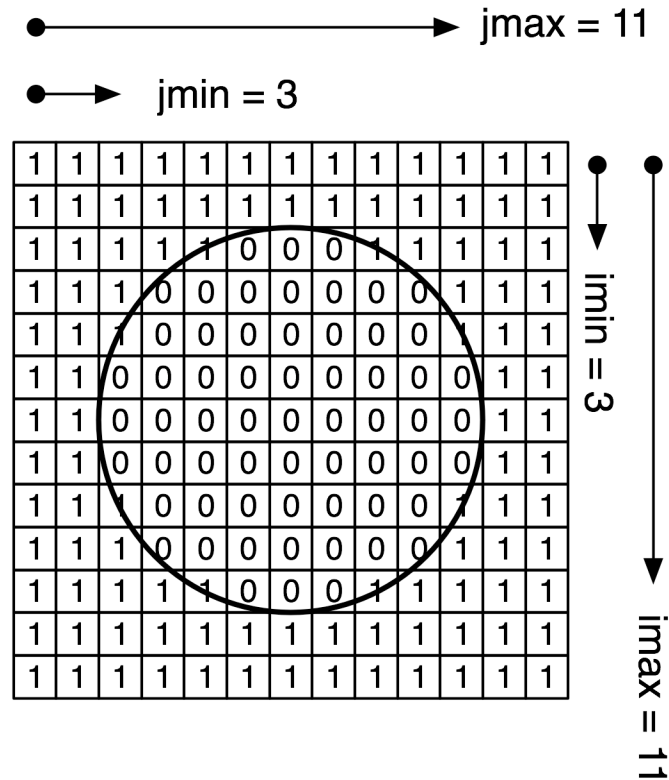
Figure A.3.1. Displacements reported in a 256×256 matrix format. Here, a 13×13 matrix is shown for illustration. The parameters *imin, imax, jmin* and *jmax* delimitate the scleral field of view (filled with zero's in the file **recminuscircle.txt**).

5) Type Eyemesh in the Matlab command window, and press enter. In the Eyemesh GUI,

choose the following parameters:

Tissue
      Sclera/Lamina
      prefix, m1a_od
      clamp size, choose from 1 to 5 according to the experiment
Tissue Thickness
      ultrasound data
      sound speed, 1600 m/s.
Exp ESPI Data
      Available
      number of measurement, 1
      measurement considered, 1
Mesh Parameters
      np12, 17
      np34, 17
      npt, 3

        nper, 7
        nr, 8
        nelb, 12
        cutangle, 0
B-Spline Parameters
        nelx, 80
        smooth, 0.008
        factor, 0.55

Then press the "Start Meshing" button. Two files will be created: The Nike3d input deck,

m1a_od.nk, and the experimental file **m1a_od.exp**. The user's manual for Eyemesh can

be found in Appendix B.1.

6) Copy both files to the ION computational server in the /scratch/ folder using the

commands:

    `scp /s_m1a_od_txt/`**`m1a_od.nk`**` mgirard@192.168.7.207:/scratch/`

    `scp /s_m1a_od_txt/`**`m1a_od.exp`**` mgirard@192.168.7.207:/scratch/`

Then execute the inverse finite element simulation with this command:

    `nohup perl `**`runfast.pl m1a_od`**` 2>/dev/null >`**`m1a_od.out`**` &`

More explanations about the inverse finite element method can be found in Appendix

B.3.

7) To visualize results, use Eyeview as explained in Appendix B.4.

B

Appendix B,
User's Manuals

B.1. Finite Element Preprocessing Software, Eyemesh v1.02

Introduction

Eyemesh was written in Matlab version R2007a (Matlab, The Mathworks, Nattick, MA) and is a preprocessing software intended to generate 8-noded hexahedral meshes from posterior scleral geometries. All meshes produced by Eyemesh are in the Nike3d format (*.nk). The following Matlab files are needed to execute Eyemesh:

File_____
circlefit.m
cutboundaries.m
cutplane.m
ellipse_fitting_1.m
ellstuff.m
ESPI.m
eyemesh.fig
eyemesh.m
fit_ellipse_hy.m
generateinnersurface.m
localmax.m
meshinnerquadrant.m
meshouterquadrant.m
nike3dinputdeck.m
plane_fit.m
rsv.m
scleramesh.m
transform.m

Eyemesh consists of approximately 5,000 lines of Matlab code, and therefore the code has not been printed in this Appendix. However, All files can be found in the attached DVD in the folder */Code/Eyemesh/.*

Execution

To execute Eyemesh, the user needs to copy the Eyemesh folder to his local hard drive and run Matlab version 2007a or higher (preferably on a Mac as it was not tested with Windows). Note that Eyemesh requires the Matlab B-Spline toolbox to be installed. Within Matlab, select the path to the folder Eyemesh with the command *path(path,'/../../Eyemesh/')*. In the Matlab command window, type "eyemesh" and press Enter. A graphical user interface should appear on your screen as shown below
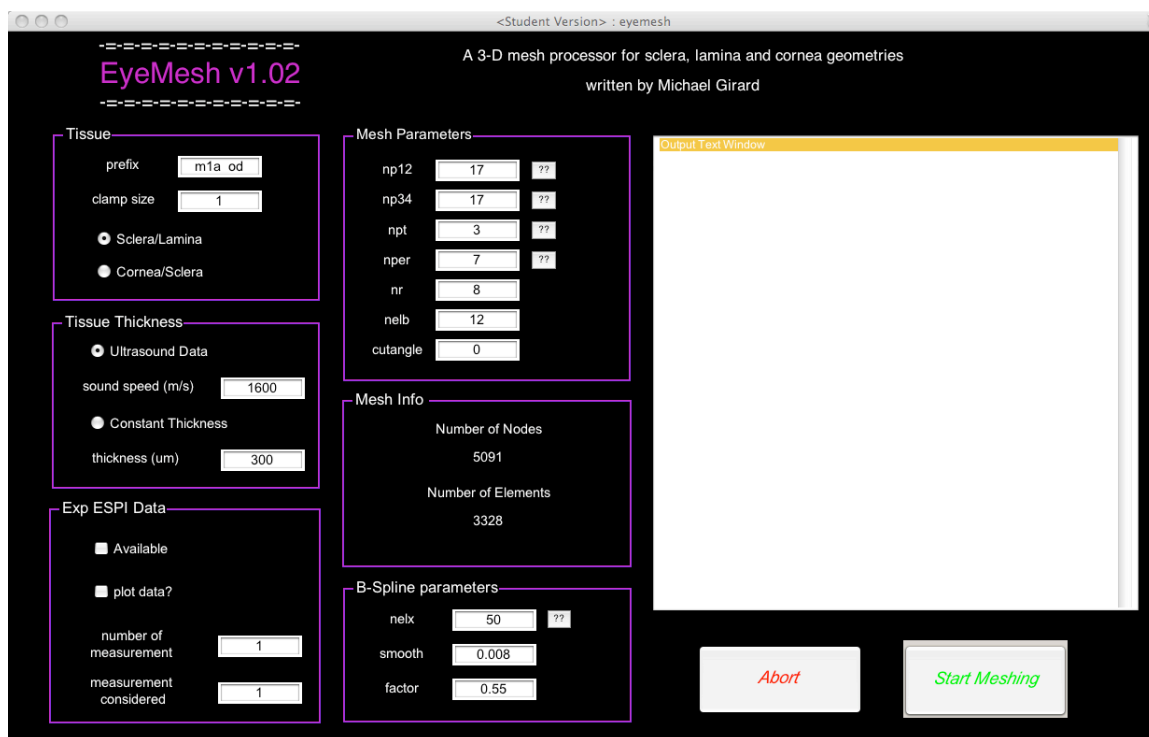
Figure B.1.1. Graphical user interface of Eyemesh.

The minimum requirement to execute Eyemesh is to provide the following files:

File

canal_od.txt
clamp_od.txt
geometry_od.txt
USdata_od.txt
XYaxes_od.txt

These files, which were obtained from experiment as explained in Appendix A.1, need to be copied in the folder Eyemesh. To execute Eyemesh, the user needs to click on the "Start Meshing" green button located at the bottom right corner of the window.

Tissue Type

Eyemesh allows the user to either mesh posterior scleral geometries (Sclera/Lamina option) or anterior chamber geometries (Cornea/Sclera option). Note that the latter option is at an experimental stage and may require more investigation to be fully operational.
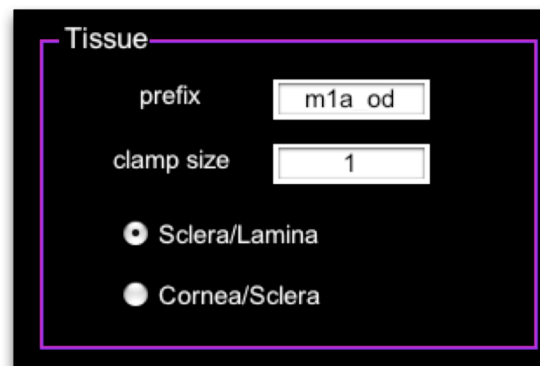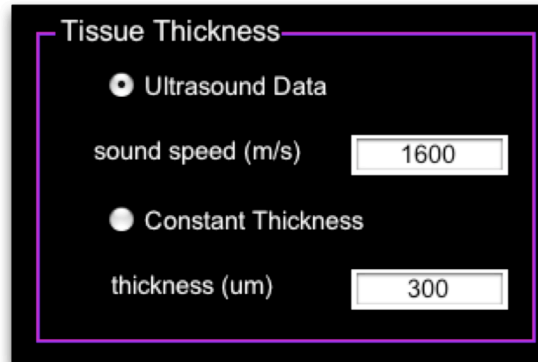
Figure B.1.2. Tissue type options.

As shown in Figure B.1.2, prefix (m1a_od) is a string of characters which contains the animal lab ID (m1a) and information on whether the specimen is from a left (os) or right (od) eye. The clamp size was decided during the experiment (see Appendix A.1) and is an integer that varies between one and five.

Tissue Thickness

Figure B.1.3. Tissue thickness options.

If the ultrasound data option is selected, Eyemesh allows the user to provide the speed of sound in m/s of the tissue being considered (default value: 1600 m/s). Alternatively, Eyemesh allows the user to provide a constant thickness value in μm. Note that if the ultrasound data option is selected, the user needs to provide further information. First, all ultrasound text files (see Appendix A.1) need to be copied within the Eyemesh folder. Second, within the Matlab command window the user needs to execute the command *rsv od 1*, which will calculate the scleral thickness obtained at the first measurement location (i.e. *1*) for a right eye (i.e. *od*). A Matlab figure will appear showing the ultrasound signal and its corresponding thickness value in mm as shown below.
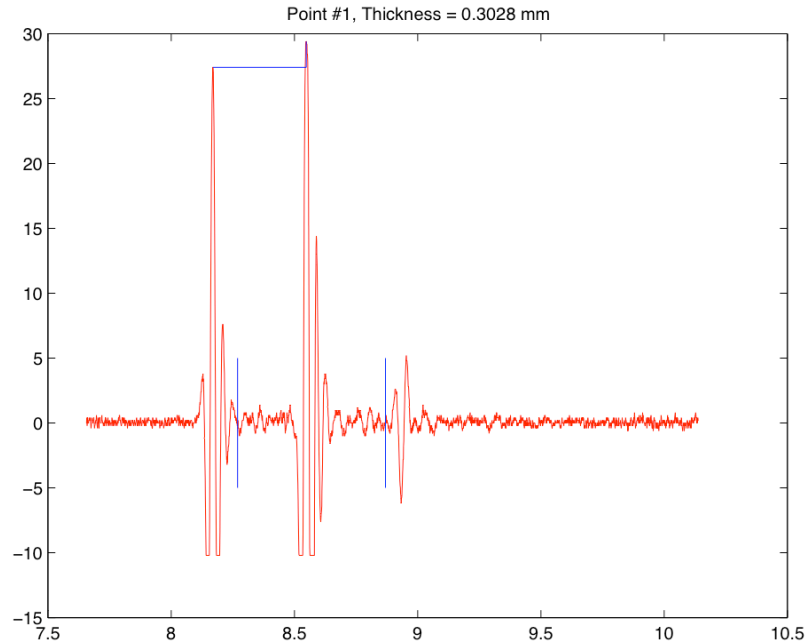
Figure B.1.4. Ultrasound echo signal (mV) as a function of time (µsec) for one measurement location. Scleral thickness is half the product of peak-to-peak time difference and scleral speed of sound (here 302.8 µm).

On Figure B.1.4, a blue line links both echo signals, meaning that the thickness was successfully calculated. However, executing the command *rsv od 1* can eventually results in a warning message due to the low intensity of the second echo signal (Sclera/Air interface). In this case, the user can modify the parameters *xlim*, *xtemp1*, and *xtemp2* in the file **rvs.m**, which will provide new boundaries for the peak signal detection. For each of the twenty measurement locations, thickness information which were collected using the function *rsv*, need to be manually entered in the array *closest* within the Matlab file **gennerateinnersurface.m**. Additional information can be found in the Matlab file **gennerateinnersurface.m**.

Experimental ESPI Data

Figure B.1.5. Experimental ESPI data options.

By clicking on the availability check box, the user needs to provide the number of ESPI measurements for this sample and the measurement being considered for this analysis. All displacement files, as generated in Appendix A.2 need to be copied in the Eyemesh folder. The needed files are:

File (x component)	File (y component)	File (z component)
x1_57.txt	y1_57.txt	z1_57.txt
x1_510.txt	y1_510.txt	z1_510.txt
x1_520.txt	y1_520.txt	z1_520.txt
x1_530.txt	y1_530.txt	z1_530.txt
x1_545.txt	y1_545.txt	z1_545.txt

By providing ESPI experimental files, Eyemesh will automatically generate an experimental file (*i.e.* **m1a_od.exp**) which will contain experimental nodal displacement values. This file will be important to solve inverse FE problems. The plot data check box allows the user to visualize the 3-D displacement data superimposed with nodes from the mesh being generated.

Mesh Parameters

There are four parameters which control the size of the mesh: $np12$, $np34$, npt, and $nper$. $np12$ controls the node density along the meridional orientation of the sclera (orientation perpendicular to the scleral canal). $np34$ controls the node density along the circumferential orientation of the sclera (orientation tangent to the scleral canal), npt controls the node density along the tissue thickness, and $nper$ controls the node density within the ONH.

Figure B.1.6. Mesh parameter options.

The three other parameters (nr, $nelb$, and $cutangle$) control the mesh configuration in terms of regionalization. nr is the total number of scleral sub-regions of the mesh (1, 4 or 8), $nelb$ controls the size of the peripheral sclera in terms of elements along the meridional orientation and $cutangle$ (0 or 45 degrees) controls the orientation of the regions. Based on anatomical geometry reconstruction of monkey posterior sclera, it is recommended to use the values shown in Figure B.1.6 for all discussed parameters.
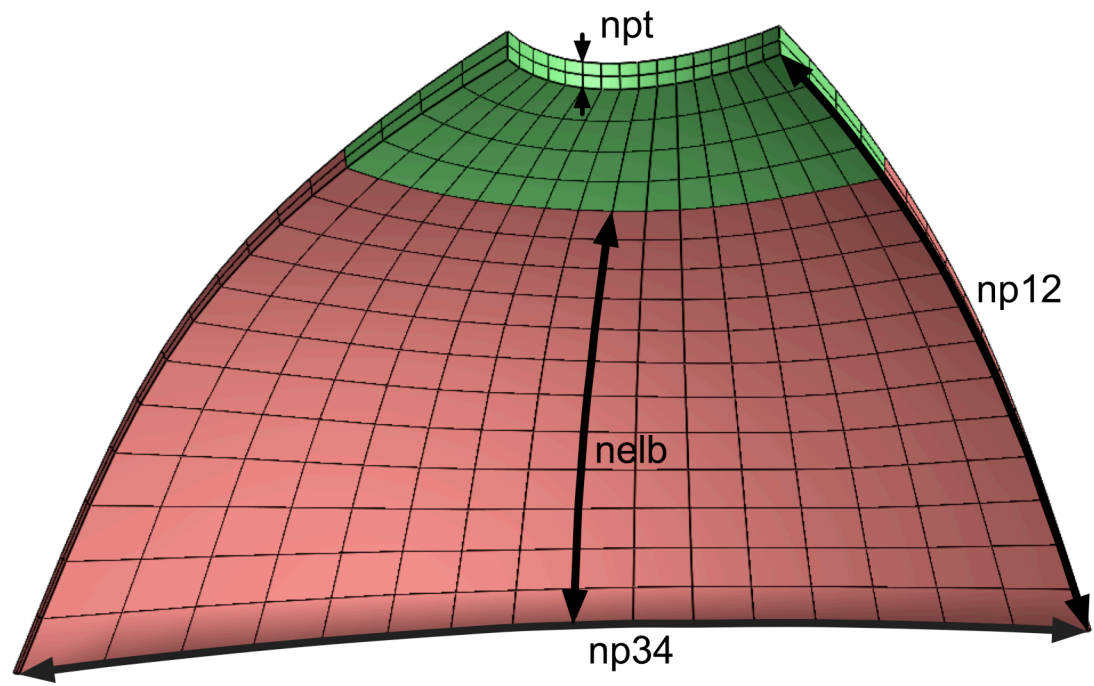
Figure B.1.7. One quadrant of the scleral mesh showing the parameters *np12*, *np34*, *npt*, and *nelb*. Here, *npt* = 3, *np12* = *np34* = 17, and *nelb* = 12. Note that *np12*, *np34*, and *npt* are node quantities, whereas *nelb* is an element quantity. For this figure, the mesh has been visualized with the software Postview.

Mesh Information

Figure B.1.8. Mesh Information.

The total number of nodes in the mesh, $NUMNP$, is calculated according to the following equation (for more information see file **scleramesh.m**)

$$NUMNP = npt \cdot \left[np34^2 + 4 \cdot (np34 \cdot np12 - np12) \right. \\ \left. + (nper - 2) \cdot (4 \cdot np34 - 4) \right]$$

(B.1.1)

The total number of elements in the mesh, $NUMEL$, is calculated according to the following equation

$$NUMEL = (npt - 1) \cdot \left[(np34 - 1)^2 + (4 \cdot np34 - 4) \cdot (nper - 1) \right. \\ \left. + 4 \cdot (np34 - 1) \cdot (np12 - 1) \right]$$

(B.1.2)

Both quantities $NUMNP$ and $NUMEL$ are automatically updated when the parameters they depend upon are changed.

B-Spline Parameters
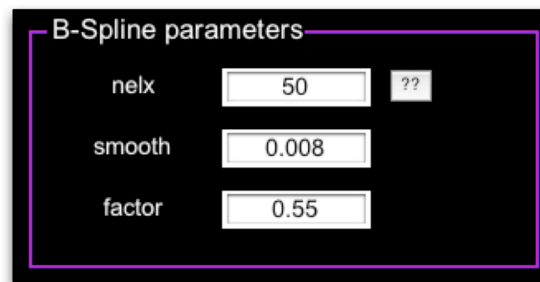
Figure B.1.9. B-Spline parameter options.

The outer scleral surface is generated within Eyemesh by fitting a thin-plate B-Spline to the experimental data available in the file **geometry_od.txt** (or **geometry_os.txt** for a left eye). The parameter $nelx$ controls the grid density of the thin-plate B-Spline. It is recommended to use $nelx = 80$. The parameter $smooth$ is a real expected to vary between 0 and 1. $smooth$ controls the roughness of the outer scleral

surface, where $smooth = 1$ provides the roughest outer scleral surface. It is recommended to use $smooth = 0.008$. Finally the parameter *factor* modifies the extent of the grid being used for data smoothing. In the event that the warning message *"??? qhull precision warning"* appears in the Matlab command window, it is recommended to use $factor = 0.65$ or higher instead of $factor = 0.55$. More information can be obtained by typing *help tpaps* in the Matlab command window or by looking at the main Matlab file **scleramesh.m**.

Pressure Loading

The pressure step values need to be manually added to the Matlab file **nike3dinputdeck.m**. Pressure values for each eye were determined during the ESPI fringe analysis (see Appendix A.2) and can be found in the file **Pressure.txt**.

ESPI Field of View

The field of view of the ESPI sensor is 35×25 mm^2. ESPI displacements are typically reported in a 256×256 matrix format that covers this field of view. To locate the eye boundaries within this field of view, four parameters can be changed (*i.e.* imin, imax, jmin and jmax) in the Matlab file **ESPI.m**. The determination of these four parameters is explained in Appendix A.2.

Output Text Window

Figure B.1.10. Output Text Window.

The output text window located on the right side of Eyemesh provides information for the user during the meshing process as shown on Figure B.1.10.

Abort Execution

There are two possibilities to abort the execution of Eyemesh. The user can click on the "Abort" button located in the bottom right corner of the graphical user interface, which will close the Eyemesh window and all other displayed figures. Alternatively, the user can type "ctrl+c" in the Matlab command window.

Files Generated by Eyemesh

For a given animal ID (*e.g.* m1a, right eye), the two principal files generated by Eyemesh are **m1a_od.nk** and **m1a_od.exp**. The file **m1a_od.nk** is a Nike3d input deck and contains control information (control deck), material information (material deck), the node coordinate table (node point deck), the element connectivity table (hexahedron

element deck), the IOP levels (load curve deck) and the IOP facet table (pressure boundary condition deck). For more information about Nike3d input decks, please refer to the Nike3d user's manual (*/Manuals/Nike3d.pdf*).

The file **m1a_od.exp** is referred to as the experimental file. It contains node numbers (from file **m1a_od.nk**) and their co-localized x-, y-, and z-displacement values that were obtained from experiment. Displacements are reported for the following IOP ranges: 5-7 mm Hg (step 1), 5-10 mm Hg (step 2), 5-20 mm Hg (step 3), 5-30 mm Hg (step 4) and 5-45 mm Hg (step 5).

A third file is generated by Eyemesh. This file is named **closest** and contains a 20 by 4 matrix. The 4th column contains all twenty thickness values obtained from experiment. The first, second and third columns contain the corresponding spatial coordinates (x, y and z) of each thickness measurement location.

Eyemesh Flow Chart
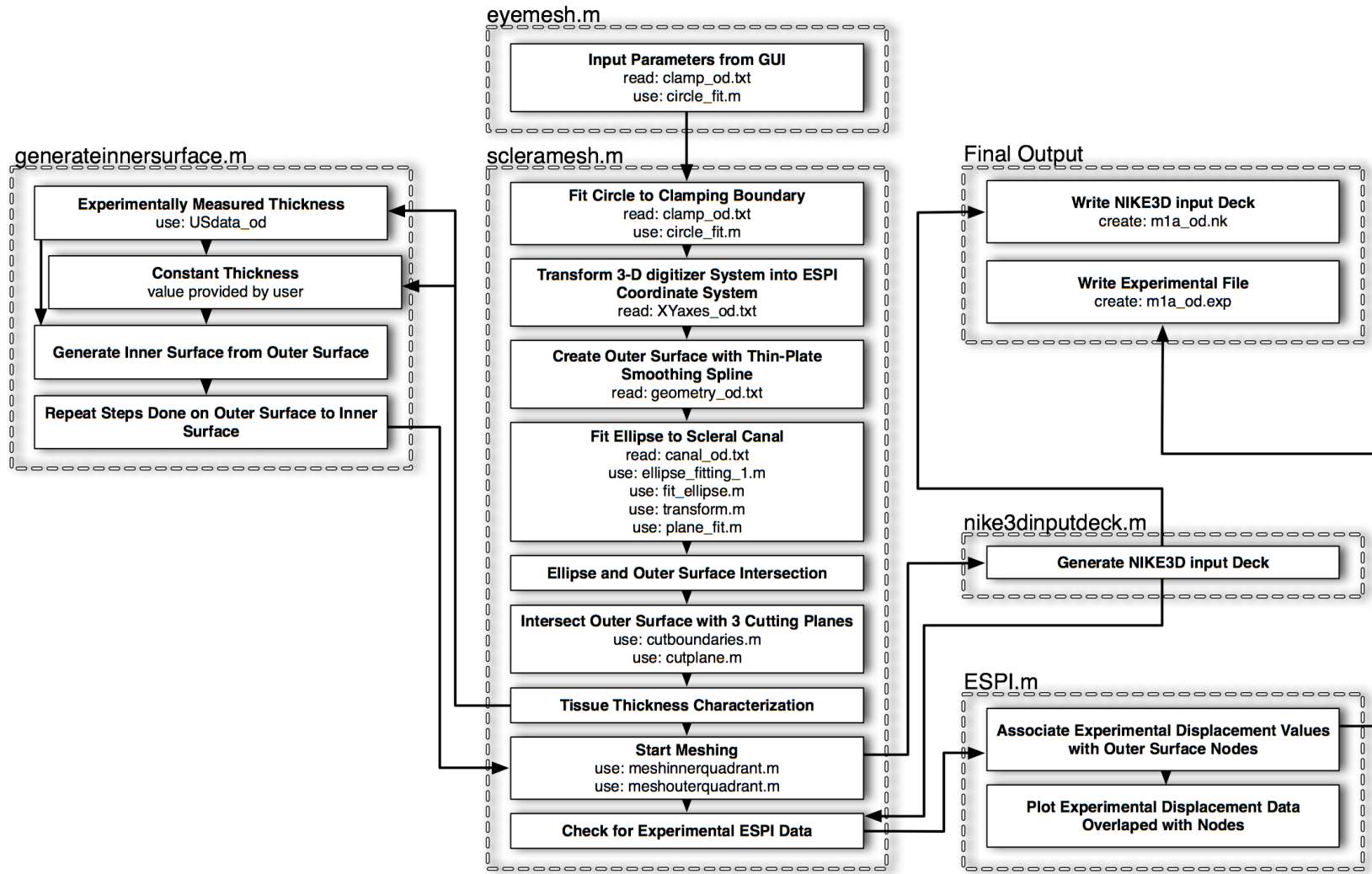
Figure B.1.11. Eyemesh flow chart. The two output files generated (format: *.nk and *.exp) can be used for inverse FE simulations.

Typical Eyemesh Execution

This section is presenting the major figure outputs when a typical Eyemesh simulation is run. The eye considered has for animal ID m4g_os.
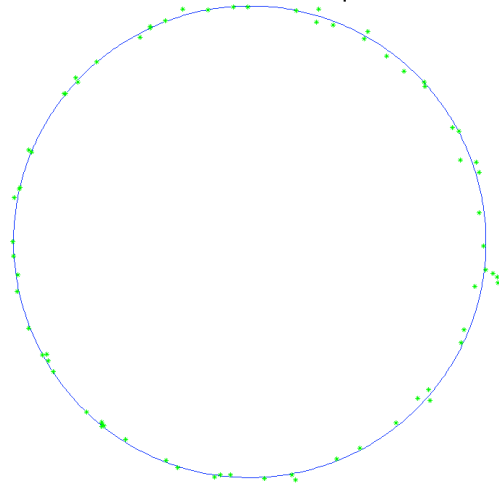
Figure B.1.12. Best fit of the clamping boundary. The green dots are obtained from the file **clamp_os.txt**, which are best fitted with a circle as shown in blue.
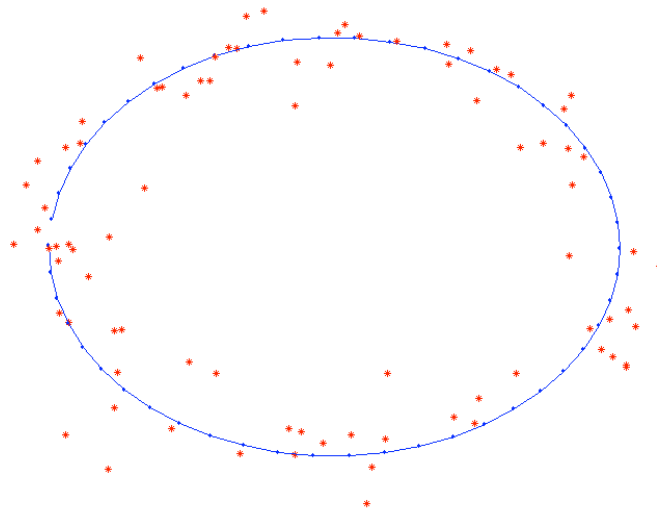
Figure B.1.13. Best fit of the scleral canal. The red dots are obtained from the file **canal_os.txt**, which are best fitted with an ellipse as shown in blue.
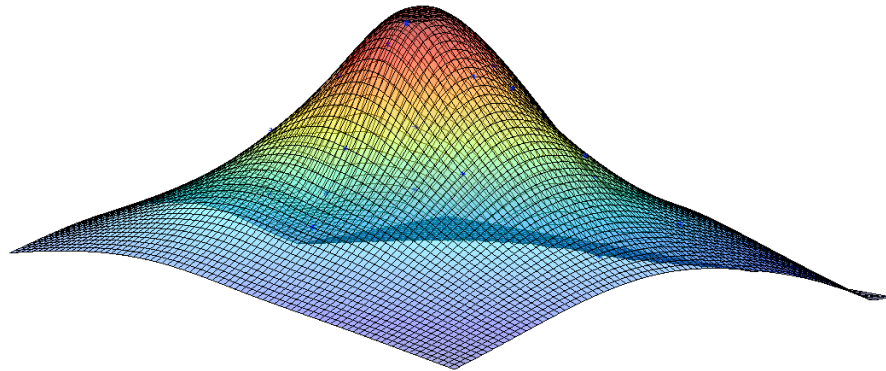
Figure B.1.14. Thickness data used in the file gennerateinnersurface.m are interpolated over the whole scleral field of view with a thin-plate B-spline.
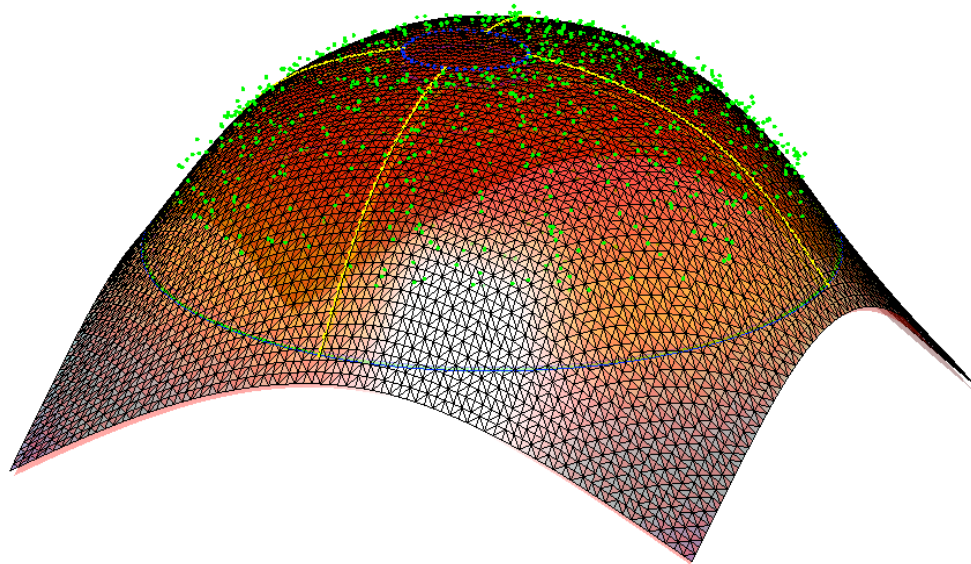
Figure B.1.15. The outer surface of the shell is obtained with a thin-plate B-spline. The green dots are the raw data as digitized and saved in the file **geometry_os.txt**. The scleral canal and clamping boundaries (shown in blue) are used to reconstruct the anatomical geometry of the shell. A set of four yellow curves that run from the clamping boundary to the scleral canal boundary are used to divide the outer surface of the shell into four quadrants.
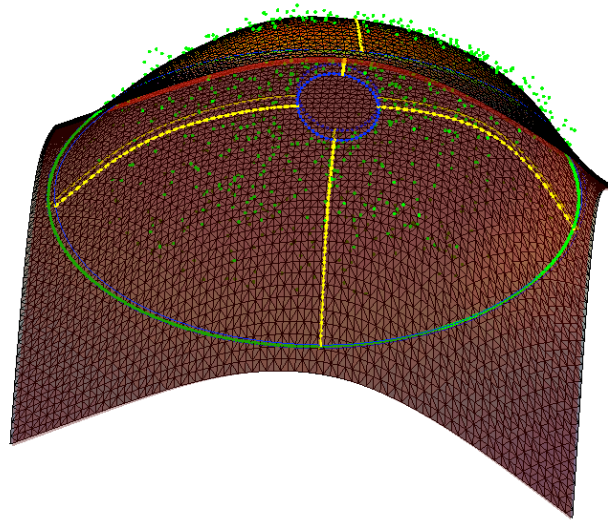
Figure B.1.16. The inner surface of the shell is derived from the outer shell surface and thickness information. The scleral canal and clamping boundaries (shown in blue) are projected onto the inner surface of the shell. A set of four yellow curves that run from the clamping boundary to the scleral canal boundary are used to divide the inner surface of the shell into four quadrants. The two sets of yellow curves allow the user to appreciate the thickness of the scleral shell, with large thickness observed near the ONH.
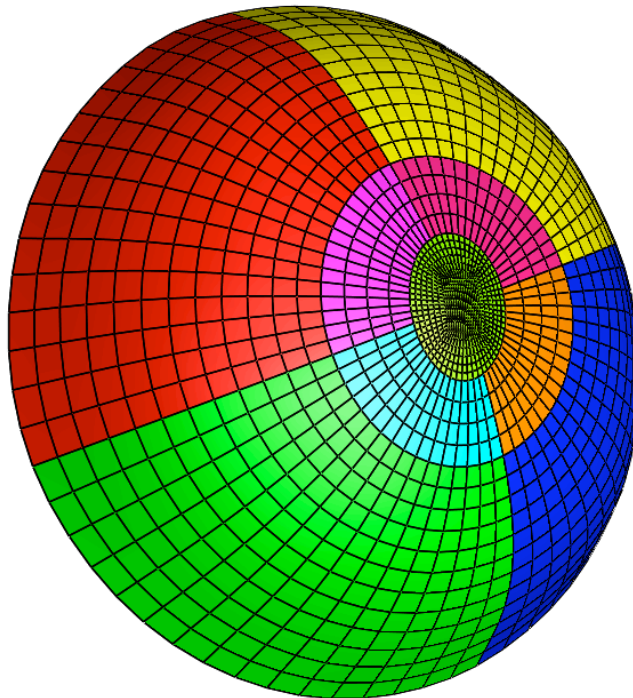
Figure B.1.17. FE mesh of the posterior sclera as generated with Eyemesh. The user can recognized the 8 sub-regions in the posterior sclera. The mesh was visualized with the software Postview.
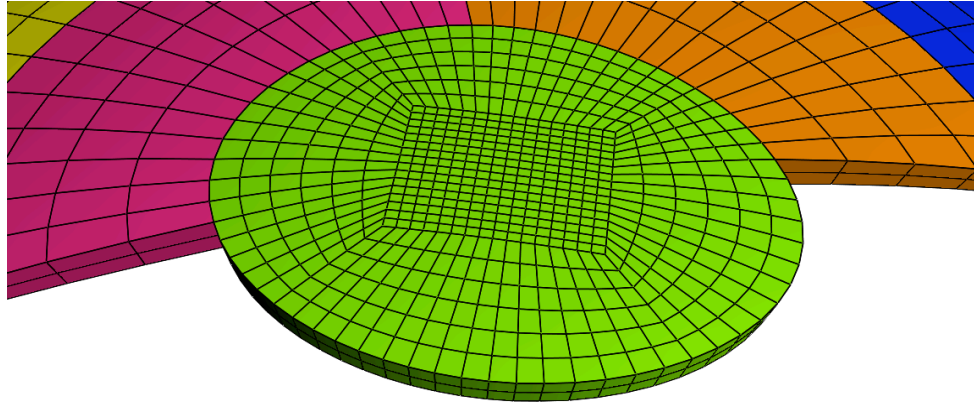
Figure B.1.18. Close-up view of the ONH.
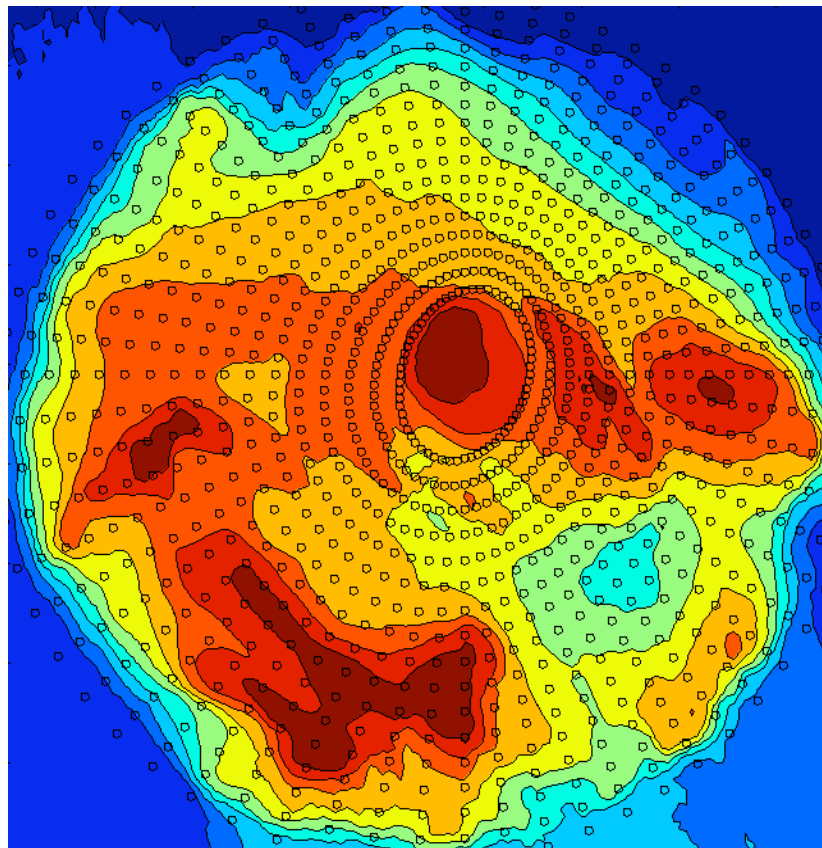
Figure B.1.19. The z-displacement map, saved in the file z1_545.txt, is projected onto the outer surface nodes of the mesh. Each outer surface node is associated with an experimental value for the z-component of the displacement field. Here, we observe the displacements along the z-direction for an IOP elevation from 5 to 45 mm Hg. This step is repeated for all pressure elevations (*i.e.* 5 to 7, 5 to 10, 5 to 20, 5 to 30 and 5 to 45 mm Hg) and all displacement component (*i.e.* x, y and z).

B.2. Finite Element Software, Nike3d, Material Type 18

Introduction

The anisotropic hyperelastic constitutive model developed in Chapter 4 was implemented within the FE software Nike3d. To use this model, the user needs to be familiar with Nike3d and should refer to its user's manual that can be found in the attached DVD as */Manuals/Nike3d.pdf*. The constitutive model includes multi-directionality of the collagen fibers at local material points as described by the semi-circular Von-Mises distribution. The constitutive model was implemented as Material 18 on top of Weiss' implementation of transversely isotropic hyperelasticity (Weiss, 1994). In this implementation, Weiss' model can be retrieved when the fiber concentration factor k is large (see Chapter 4).

Nike3d Implementation – Material Type 18

Fortran Subroutine s18mn.f

The 2nd Piola-Kirchhoff stress tensor, the Cauchy stress tensor, and the spatial elasticity tensor (Chapter 4) were implemented within the Fortran subroutine **s18mn.f**, where all integrals were computed with Gaussian quadrature rules. In **s18mn.f**, the following model parameters were defined in the variable *prop* as follows:

Model Parameter	Description	Position
c_1	1st Mooney-Rivlin coefficient	*prop(1)*
c_3	Exponential stress coefficient	*prop(3)*
c_4	Fiber uncrimping coefficient	*prop(4)*
K	Bulk modulus	*prop(9)*
θ_p	Preferred fiber orientation	*prop(42)*
k	Fiber concentration factor	*prop(43)*

Additionally, since the calculation of the semi-circular Von-Mises distribution involves the modified Bessel function of the first kind and zeroth order, the function *besi0* was added at the end of this subroutine. Because the modified subroutine **s18mn.f** contains 2,400 lines of Fortran code, it was not printed within this Appendix. Instead, it can be found in the folder */Code/Nike3d New Material 18/* from the attached DVD. Note that this file should not be redistributed as it contains in part original Nike3d code.

Fortran Subroutine s18int.f

This subroutine specifically defines the plane of the collagen fibers for each element. The model was tested for option *AOPT* = 0 (see Nike3d user's manual), meaning that the local material x- and y-axes are given by three nodes for each element (Figure B.2.1).
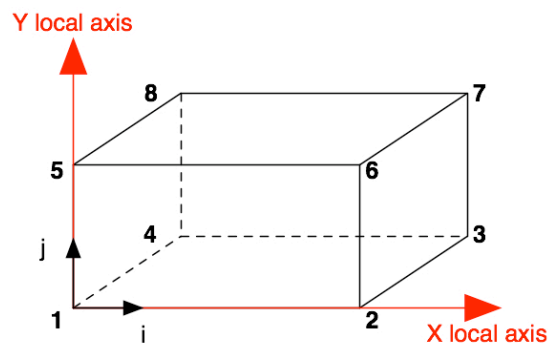
Figure B.2.1. Local element nodes used to define local material axes (here nodes 1, 2 & 5) for one 8-noded hexahedral element. Note that for elements that were obtained with Eyemesh the nodes 4, 3 & 1 are used due to a different node ordering convention.

If the local x- and y-axes are not initially perpendicular, we define the local z-axis to be associated with the unit vector $\mathbf{k} = \mathbf{i} \times \mathbf{j}$ and redefine the local y-axis to be associated with the unit vector $\mathbf{j} = \mathbf{k} \times \mathbf{i}$. Both local x- and y-axes describe the plane of the fibers. Therefore a fiber orientation defined by θ will be obtained as $\mathbf{a}_0(\theta) = \cos(\theta)\mathbf{i} + \sin(\theta)\mathbf{j}$.

Nike3d Material Deck – Material Type 18

For our new definition of Material 18, the material deck shown next page is needed for any Nike3d input file (*.nk) as generated with Eyemesh. Notice that **Card 8** was used to add the preferred fiber orientation θ_p, and the fiber concentration factor k as defined in Chapter 4.

Material Type 18 (Hyperelasticity with Multi-Directional Fibers)

Columns		Quantity	Format
1-10	**Card 3**	1st Mooney-Rivlin Coefficient (Pa), c_1	E10.0
11-20		2nd Mooney-Rivlin Coefficient (Pa), c_2 EQ. 0.0: default value for posterior sclera	E10.0
21-30		Exponential Stress Coefficient (Pa), c_3	E10.0
31-40		Fiber Uncrimping Coefficient (dimensionless), c_4	E10.0
1-10	**Card 4**	Bulk Modulus (Pa), K .EQ. 1.E+08/09: default values for posterior sclera	E10.0
11-20		NA	E10.0
1-10	**Card 5**	NA	E10.0
21-30		Augmented Lagrangian Flag .EQ. 1.0: activate augmented Lagrangian method	E10.0
31-40		Tolerance for augmented Lagrangian iterations, TOL .GT. 0.0: converge when volume strain norm $< TOL$ .LT. 0.0: augment exactly (-TOL) times per step	E10.0
1-10	**Card 6**	Material axes option, $AOPT$ EQ. 0.0: local material axes are given by local element nodes specified on Card 7 below. This is the default value for posterior sclera	E10.0
1-30	**Card 7**	AOPT .EQ. 0.0: local element nodes (default: 4, 3, 1) the nodes 4-3 defines the local x-axis the nodes 4-1 defines the initial local y-axis the local z-axis is the cross-product of x and y the final local y-axis is the cross-product of z and x	3E10.0
1-10	**Card 8**	2D semi-circular Von-Mises distribution function, P .EQ. 1.0: activate multi-directionality of the fibers	E10.0
11-20		Preferred fiber orientation (degrees), θ_p .EQ. 0.0: circumferential orientation (tangent to canal) .EQ. 90.0: meridional orientation (perpendicular to canal)	E10.0
21-30		Fiber concentration factor (dimensionless), k .EQ. 0.0: isotropic distribution of the fibers .EQ. 1.E+09: transverse isotropy (Weiss' model)	E10.0

B.3. Inverse Finite Element Method

Introduction

An inverse FE method was developed to extract model parameters for the posterior sclera. For a common FE analysis in continuum solid mechanics, the geometry and mechanical properties of an elastic body are known, but the deformations and stresses are to be determined. Conversely, for an inverse FE analysis, the geometry and deformations of an elastic body are known, but the mechanical properties and stresses are to be determined. Here, we used an inverse FE method, in which a global optimization algorithm (*i.e.* differential evolution) was coupled with the nonlinear FE method (*i.e.* Nike3d) to fit model-predicted to experimentally-measured displacements (see Chapter 5). The inverse FE method was implemented on a Linux server (32GB of RAM and four 64-bit Itanium2 processors) with the programming languages Fortran77, Fortran90 and Perl. It requires the following files:

File	Type
runfast.pl	Perl
denike3d_0.f90	Fortran90
denike3d_1.f90	Fortran90
denike3d_2.f90	Fortran90
denike3d_3.f90	Fortran90
read_input.f90	Fortran90
read_n3dhsp.f	Fortran77
nike3d.lnx	Executable file

The inverse FE method contains 1,575 lines of code (excluding Nike3d) and all files are provided in the attached DVD under the folder */Code/Inverse FE/*. The inverse FE method is driven by the differential evolution algorithm, which is a relatively simple genetic optimization algorithm. More information about differential evolution can be

found in the excellent book from Price (Price, Storn et al., 2005). The Fortran version of differential evolution was obtained from *http://www.icsi.berkeley.edu/~storn/code.html*, then adapted for our application.

Execution

To run an inverse FE element simulation, the user needs to provide the Nike3d input file (*e.g.* **m1a_od.nk** for animal m1a, right eye) and the experimental file (*e.g.* **m1a_od.exp** for animal m1a, right eye) that were generated by Eyemesh (Appendix B.1). Both files need to be copied in the same folder as all the other files. This is typically done in the */scratch/* folder, when working with the ION computational server. To execute an inverse FE simulation (for **m1a_od**), the user needs to enter the following Unix command in a terminal shell window

```
nohup perl runfast.pl m1a_od 2>/dev/null >m1a_od.out &
```

Control Parameters

For all inverse FE simulations, the following parameters may be changed. However, it is recommended to keep the default values as presented here.

File	Parameters		Default
runfast.pl			
	Dim_XC	Number of model parameters to be determined	13
	NP	Number of parents	50
	XCmin	Minimum initial bounds for $[c_1, c_3, c_4, k_1, k_2, \theta_{p1} \dots \theta_{p8}]$	
	XCmax	Maximum initial bounds for $[c_1, c_3, c_4, k_1, k_2, \theta_{p1} \dots \theta_{p8}]$	
	restartflag	.EQ. 1: restart a stopped inverse FE simulation	0
	numprocess	Number of processors used	7
	itermax	Maximum number of iterations	2000
denike3d_2.f90			
	CR_XC	Crossover factor for differential evolution	0.9
	F_XC	Mutation factor for differential evolution	0.5-0.8
	strategy	Strategy of the mutation operations	2

Main Outputs

For a given animal ID (*e.g.* m1a, right eye), the files generated during an inverse FE simulation are **m1a_od.out**, **tempbestm1a_od** and **n3dhspbestm1a_od**. The file **m1a_od.out** is considered as an output file and contains information about differential evolution convergence. It is constantly updated during an inverse FE simulation and contains the best population member (*i.e.* set of model parameters) for each iteration of the differential evolution algorithm. As an example, the following text is printed within the file **m1a_od.out** for each iteration of the differential evolution algorithm:

```
iteration # 30, Time = 2.335 h = 0.0972916666666667 d, it is 18:41:15
1234567891011121314151617181920212223242526272829303132333435363738394041424344454647484950
X:     440215.590586961         55147.8617661679          1153.55719668110
    2.16401840436387          4.45561120928580         104.577995016475
    160.030511800075         32.7932206268644          68.8410055074403
    31.1746664741380        101.130243202663          75.8739866949899
    132.040346839200
Error:    2.56698700000000
```

The first line indicates the iteration number, the time spent so far and the current time. On the second line, we can observe the parent numbers ranging from 1 to *NP* (here *NP* = 50). For each parent, one FE simulation is run with Nike3d. On the third line is the best population member, which is the set of model parameters that provides the smallest error between the FE-predicted and experimentally-measured displacements for this iteration. This set of parameters contains thirteen numbers, which corresponds to the following model parameters (in order): $c1$, $c3$, $c4$, $k1$, $k2$, θ_{p1}, θ_{p2}, θ_{p3}, θ_{p4}, θ_{p5}, θ_{p6}, θ_{p7}, θ_{p8}. Finally, the last line displays the cost function (in µm), which is a measure of the differences between the FE-predicted and experimentally-measured displacements as explained in Chapter 5. It is highly recommended to look for convergence by opening the file **m1a_od.out** when an inverse FE simulation is running (located in */scratch/*).

An inverse FE element simulation typically requires 450 iterations of the differential evolution algorithm (approximately two days of computational time). However, it is recommended to stop an inverse FE simulation (see next section) when the difference in cost functions from two different iterations is equal to 0.000001 μm. Once an inverse FE simulation is stopped, two important files need to be considered: **tempbestm1a_od** and **n3dhspbestm1a_od**. The file **tempbestm1a_od** is the Nike3d input deck (eye: m1a_od) with the best set of model parameters. The file **n3dhspbestm1a_od** is the corresponding Nike3d output file and contains FE-predicted displacements that best match those experimentally measured. Both files will be generated in the folder */home/mgirard/global/* from the ION computational server.

Abort Execution

To abort an inverse FE simulation, the user needs to type the following Unix commands in a terminal: *killall perl*, followed by *killall nike3d*. The user can check if the inverse FE simulation was effectively killed with the following Unix command: *ps -ef*.

Restart

If an inverse FE simulation was stopped by mistake or if the ION computational server crashed, it is possible to restart it. In the file **runfast.pl**, the user needs to activate the restart flag by replacing *$restartflag = 0* with *$restartflag = 1*. The inverse FE simulation can now be executed with the Unix command:

```
nohup perl runfast.pl m1a_od 2>/dev/null >m1a_od.out &
```

Stress, Strain and Tangent Modulus Files

FE-predicted displacements are located in the file **n3dhspbest_m1a**, but this file does not contain other FE results such as stress, strain, and tangent modulus. To extract these quantities the user needs to run the following Unix command *perl strainstress.pl* in the folder */home/mgirard/n3user/*. After execution of this script, three files will be created: **n3strainm1a_od**, **n3stressm1a_od**, and **n3elastim1a_od**. The files **n3strainm1a_od** and **n3stressm1a_od** contain all six components of the strain and stress tensors, respectively. The file **n3elastim1a_od** contains two components of the spatial elasticity tensor. These components are referred to as the tangent moduli along and perpendicular to the preferred fiber orientation (see Chapters 4 and 5). Note that the Perl script *strainstress.pl* is located in the attached DVD in the folder */Code/Inverse FE/*.

Backup

Everytime an inverse FE simulation is run, all files from the */scratch/* folder are copied to */home/mgirard/backup_scratch/*.

Inverse Finite Element Flow Chart
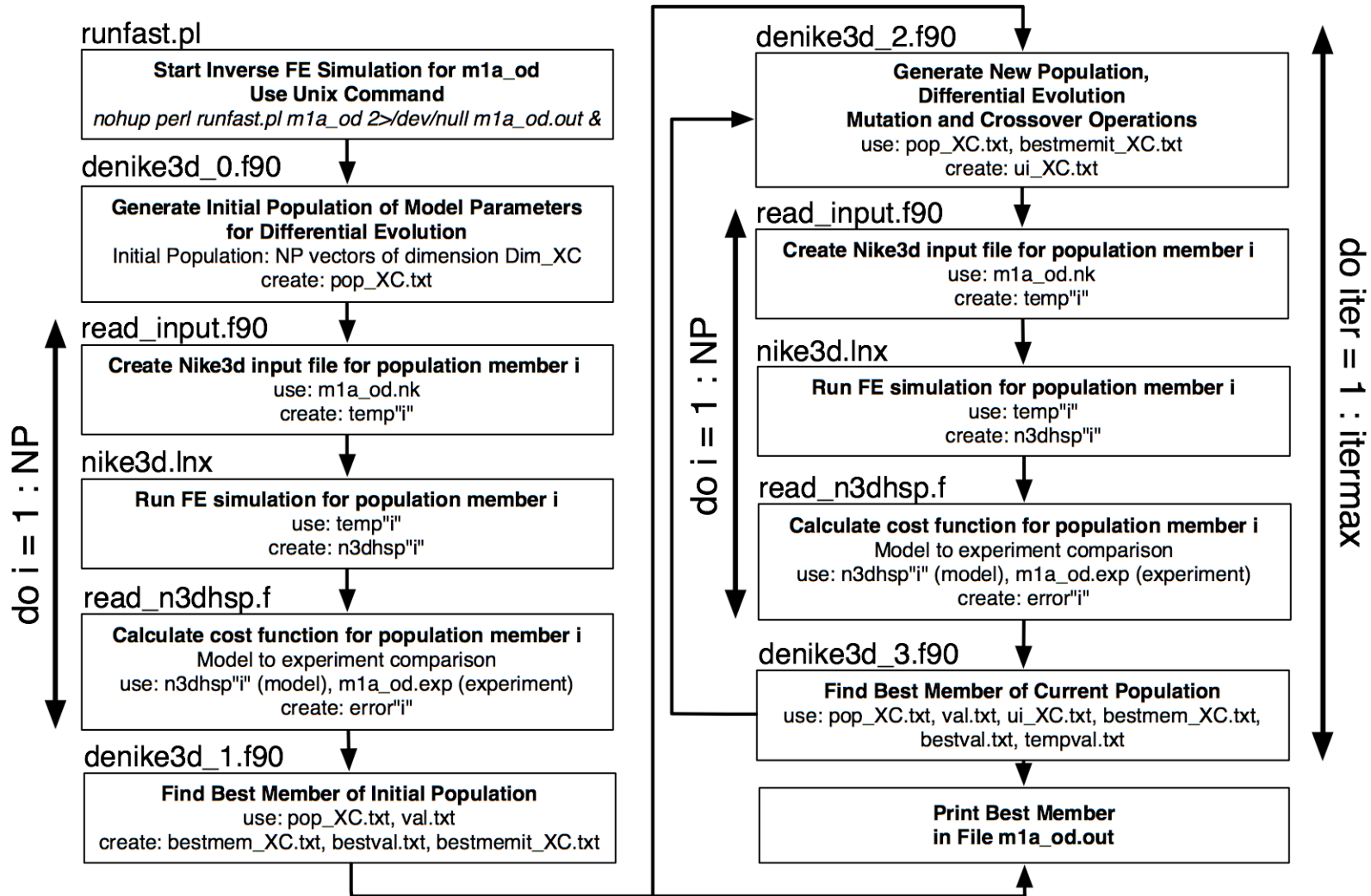
Figure B.3.1. Inverse FE flow chart. The output file generated (format: *.out) keeps a record of the best population member obtained for each iteration.

B.4. Finite Element Postprocessing Software, Eyeview v1.01

Introduction

Eyeview was written in Matlab version R2007a (Matlab, The Mathworks, Nattick, MA) and is a postprocessing software intended to visualize experimentally-measured scleral displacements, experimentally-measured scleral thickness, and output results from FE simulations that were run with Nike3d. FE Results that can be visualized include: FE-predicted displacements, principal strain magnitudes and orientations, principal stress magnitudes and orientations, tangent moduli, and structural stiffnesses. Eyeview has an advantage over other postprocessing softwares that were designed for nonlinear analyses: it allows the user to display results for several IOP levels simultaneously. Examples will be shown in later sections to illustrate this point. The following Matlab files are needed to execute Eyeview:

File
cellwrite.m
elastimodule.m
eyeview.m
myrandit.m
stressmodule.m
surfature.m

Eyeview consists of approximately 3,200 lines of Matlab code, and therefore the code has not been printed in this Appendix. However, All files can be found in the attached DVD in the folder */Code/Eyeview/*.

Execution

To execute Eyeview, the user needs to copy the Eyeview folder to his local hard drive and run Matlab version 2007a or higher. Note that Eyeview requires the Matlab Statistics toolbox to be installed. Within Matlab, select the path to the folder Eyeview with the command *path(path,'/../../Eyemesh/')*. In the Matlab command window, the user needs to type "eyeview m1a_od" (for animal m1a) and press Enter. The minimum requirement to execute Eyeview is to provide the following files

File	Type	Code
m1a_od.exp	Experimental file	Eyemesh (Appendix B.1)
closestm1a_od	Thickness data file	Eyemesh (Appendix B.1)
tempbestm1a_od	Nike3d input deck	Inverse FE (Appendix B.3)
n3dhspbestm1a_od	Nike3d output file	Inverse FE (Appendix B.3)
n3stressm1a_od	Nike3d stress file	Inverse FE (Appendix B.3)
n3strainm1a_od	Nike3d strain file	Inverse FE (Appendix B.3)
n3elastim1a_od	Nike3d tangent modulus file	Inverse FE (Appendix B.3)

Eyeview will not run properly if these files are not provided. Note that the file **closest**, as generated with the software Eyemesh, needs to be renamed to **closestm1a_od**.

Typical Eyeview Execution

After entering "eyeview m6u_od" (for animal m6u_od) the following text will appear in the Matlab command window:

```
=-=-=-=-=-=-=-=-=-=-=-=-=-=-=-=-=-=-=-=-=-=-=-=-=-=-=-=
Welcome To Eyeview v1.01
The best postprocessing soft ever to visualize scleral data
It is intended to work with the nonlinear FE code NIKE3D
Written by miikkee@gmail.com
=-=-=-=-=-=-=-=-=-=-=-=-=-=-=-=-=-=-=-=-=-=-=-=-=-=-=-=

VISUALIZATION FOR ANIMAL m6u_od

>>>>>>>>>>>>>>>>>>>>>>>>>>
Reading NIKE3D input file
done
>>>>>>>>>>>>>>>>>>>>>>>>>>
Element Volume Calculations
Tetrakis Hexahedron volume method selected
done
>>>>>>>>>>>>>>>>>>>>>>>>>>
Computing Surface Curvature
done
>>>>>>>>>>>>>>>>>>>>>>>>>>
Reading thickness data
done
Do Stats? y/n
>>>
```

By answering "y" to the above question, Eyeview will compute the 25th, 50th (median) and 75th percentiles of the thickness, tangent moduli, structural stiffnesses, principal stresses and principal strains distributions at IOP = 10, 30 and 45 mm Hg in the peripapillary and peripheral scleral regions. Percentiles will be saved in the file **m6u_od.stat**. The following text will be displayed:

```
>>>>>>>>>>>>>>>>>>>>>>>>>>
Starting Thickness Stat
step #1
step #2
step #3
step #4
step #5
>>>>>>>>>>>>>>>>>>>>>>>>>>
Starting Cijkl Stat
step #1
step #2
step #3
step #4
step #5
```

```
>>>>>>>>>>>>>>>>>>>>>>>>>
Starting SS Stat
step #1
step #2
step #3
step #4
step #5
>>>>>>>>>>>>>>>>>>>>>>>>>
Starting Stress Stat
step #1
step #2
step #3
step #4
step #5
>>>>>>>>>>>>>>>>>>>>>>>>>
Starting Strain Stat
step #1
step #2
step #3
step #4
step #5
saving stats in *.stat file
Save stat data as .csv file? y/n
>>>
```

The user has the option to save all distributions in a csv format if the data need to be imported to the software Excel. Note that during a statistical analysis, all distributions will also be saved in different files in the Matlab binary format (*.mat). All files will be named as **m6u_od_Region_Quantity_IOP.mat**, where "Region" can either be replaced with "ppS" (peripapillary sclera) or "pS" (peripheral sclera). "Quantity" can be replaced with "C1" (tangent modulus along the preferred fiber orientation, "C2" (tangent modulus perpendicular to the preferred fiber orientation), "S1" (structural stiffness along the preferred fiber orientation), "S2" (structural stiffness perpendicular to the preferred fiber orientation), "stra1" (first principal strain), "stra2" (second principal strain), "stre1" (first principal stress), "stre2" (second principal stress) or "T" (Thickness). "IOP" can be replaced with "10" (10 mm Hg), "30" (30 mm Hg) or "45" (45 mm Hg).

The next question that will appear in the Matlab command window is:

```
Cijkl Visualization? y/n
>>>
```

By entering "y", Matlab will display the tangent moduli along and perpendicular to the preferred fiber orientation.
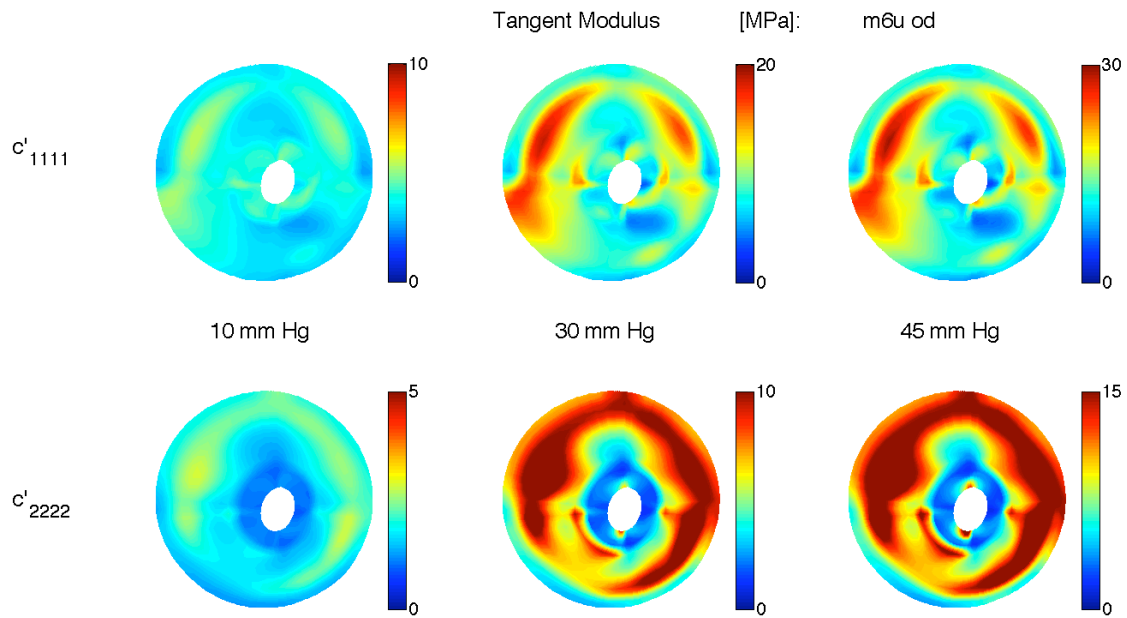
Figure B.4.1. Tangent modulus in MPa along (c'_{1111}) and perpendicular (c'_{2222}) to the preferred fiber orientation at IOP = 10, 30 and 45 mm Hg.

For each of the following questions, figures will be displayed.

```
Structural Stiffness Visualization? y/n
>>>
```

Structural Stiffness   [kN/m]:   m6u od
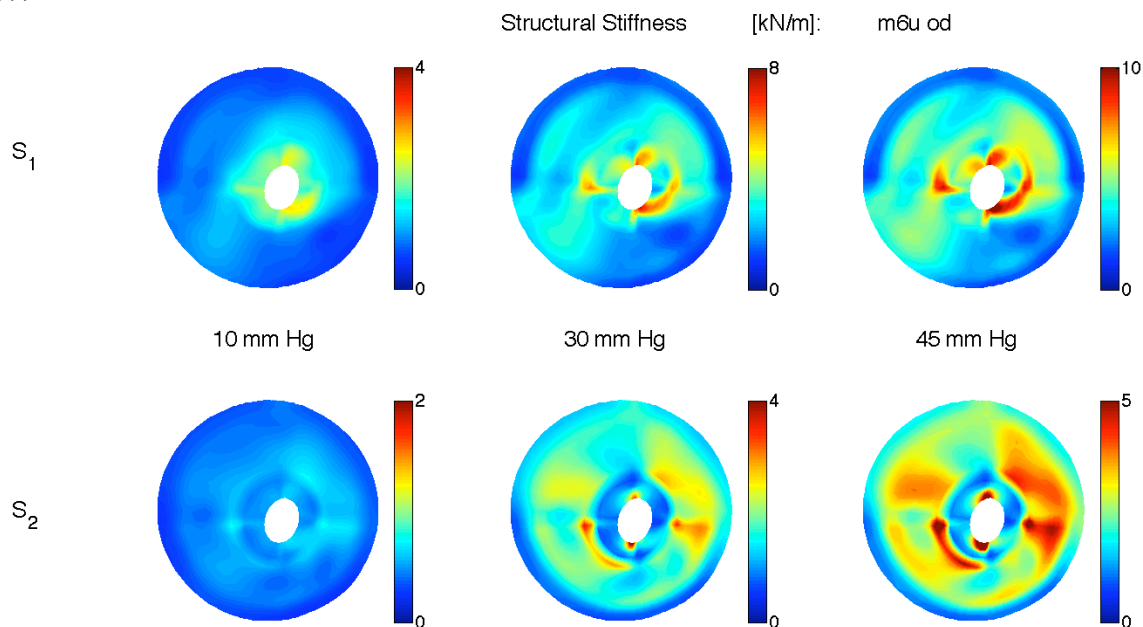
Figure B.4.2. Structural stiffness in kN/m along (S_1) and perpendicular (S_2) to the preferred fiber orientation at IOP = 10, 30 and 45 mm Hg.

```
Stress Visualization? y/n
>>>
```

Principal Stress [kPa]:   m6u od
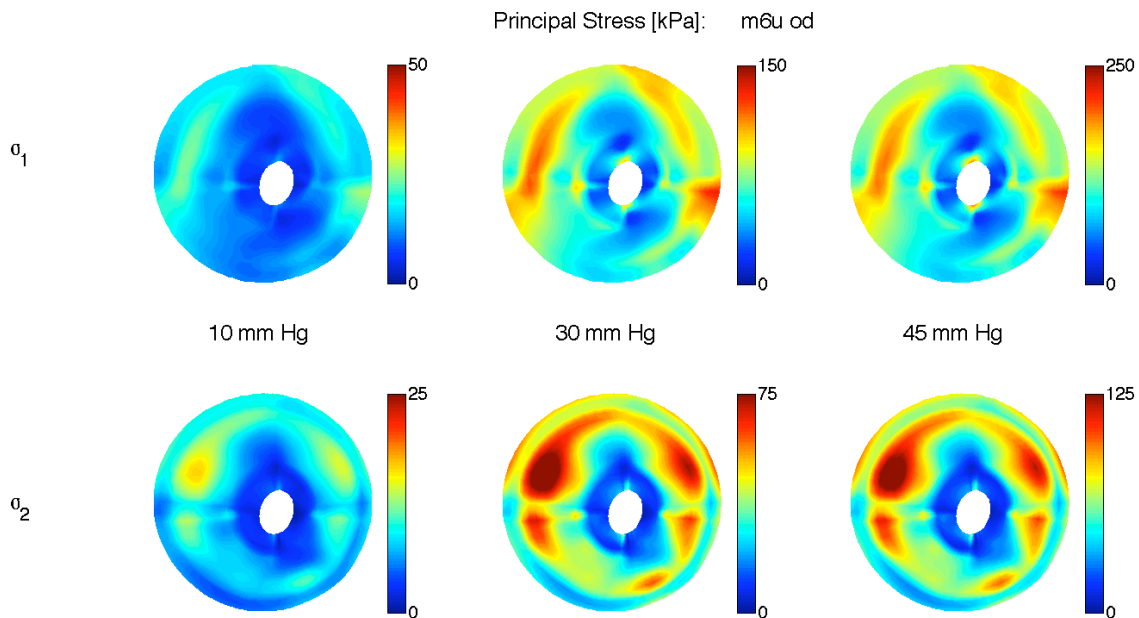
Figure B.4.3. First (σ_1) and second (σ_2) principal stresses in kPa at IOP = 10, 30 and 45 mm Hg.
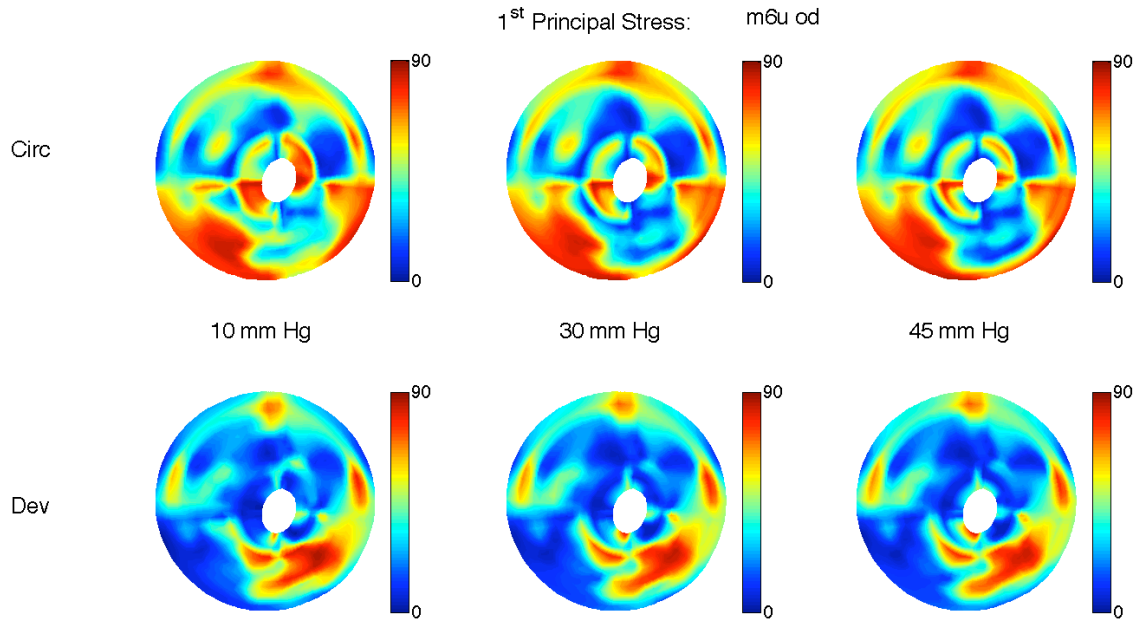
Figure B.4.4. Circumferentiality (Circ) and deviation (Dev) of the maximum principal stress orientation at IOP = 10, 30 and 45 mm Hg. Circ is a scalar angle, that varies between 0 and 90°. If Circ is equal to 0°, the orientation of the maximum principal stress is tangent to the scleral canal (*i.e.* circumferential orientation with respect to the ONH). If Circ is equal to 90°, the orientation of the maximum principal stress is perpendicular to the scleral canal (*i.e.* meridional orientation). Dev is defined as the angular deviation between the preferred fiber orientation and the maximum principal stress orientation. It is an angle that varies between 0 and 90°. If Dev is equal to 0°, the preferred fiber orientation and the maximum principal stress orientation are parallel. If Dev is equal to 90°, the preferred fiber orientation and the maximum principal stress orientation are perpendicular. Notice that the orientation of the maximum principal stress is tangent to the scleral canal at IOP = 45 mm Hg (top-right map), and that the orientation of the maximum principal stress is mainly parallel to the preferred fiber orientation (second row).

```
Strain Visualization? y/n
>>>
```

Principal Strain [%]:   m6u od
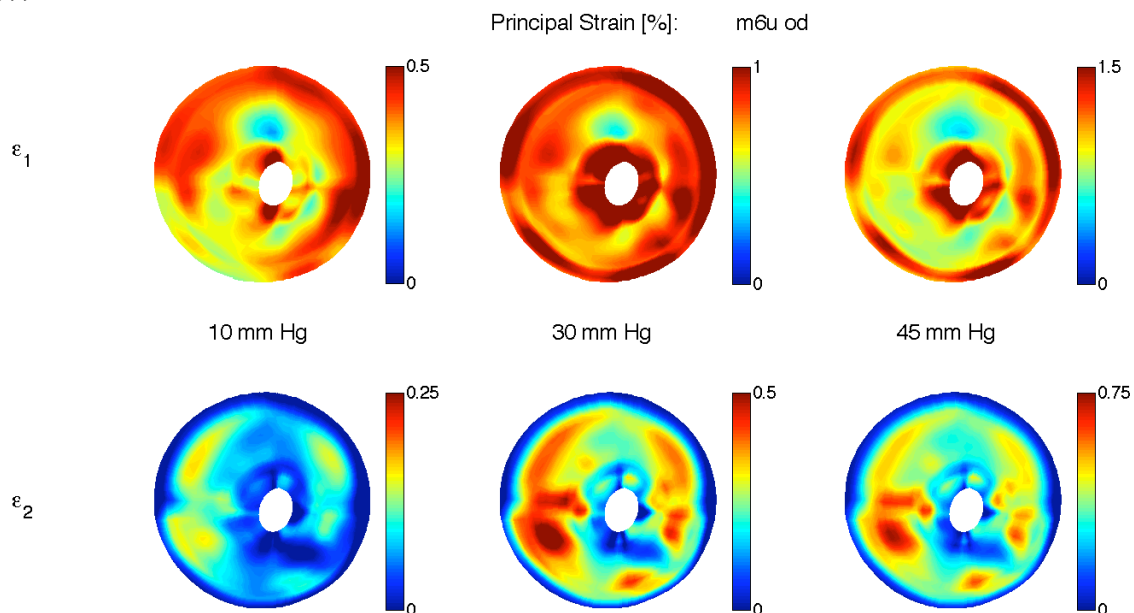
Figure B.4.5. First (ε_1) and second (ε_2) principal strains in % at IOP = 10, 30 and 45 mm Hg.

1st Principal Strain: m6u od
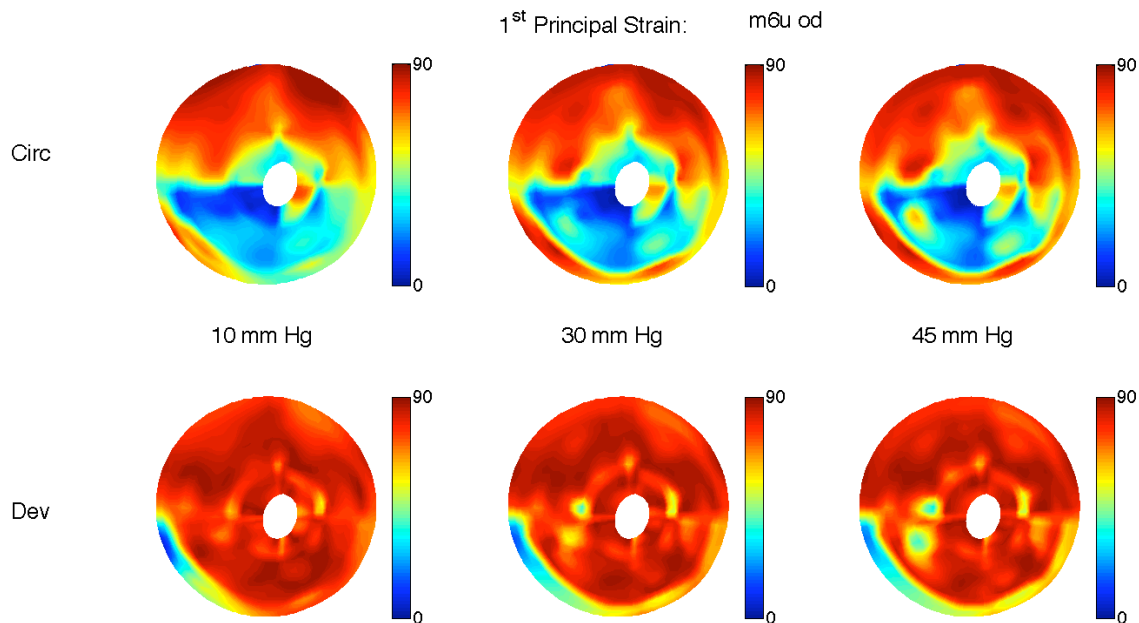
Figure B.4.6. Circumferentiality (Circ) and deviation (Dev) of the maximum principal strain orientation at IOP = 10, 30 and 45 mm Hg. See Figure B.4.4 for detailed explanations about Circ and Dev. Notice that the orientation of the maximum principal strain is tangent to the scleral canal at IOP = 45 mm Hg (top-right map), and that the orientation of the maximum principal strain is mainly perpendicular to the preferred fiber orientation (second row).

```
DISP Visualization? y/n
>>>
```
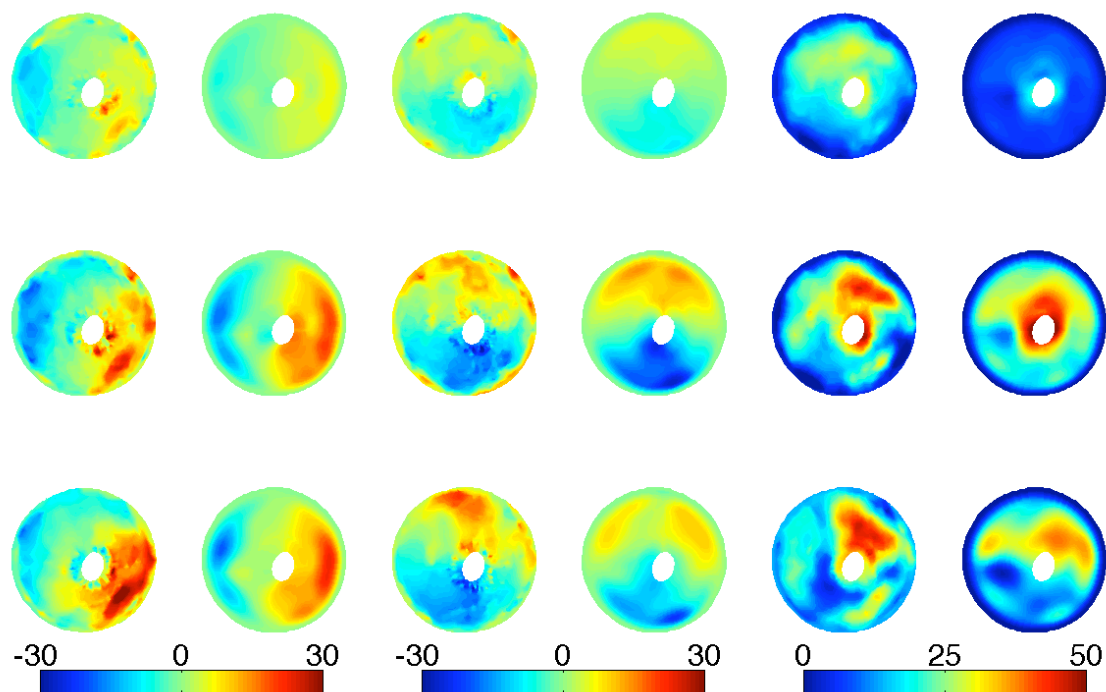

Figure B.4.7. Comparison of experimentally-measured (x, first column; y, third column; z, fifth column) and model-predicted (x, second column; y, fourth column; z, sixth column) displacements (in μm) for three IOP ranges (first row, 30 to 45 mm Hg; second row, 10 to 30 mm Hg; third row, 5 to 10 mm Hg). Note that model displacements were simultaneously fit to the experimental data obtained at 7, 10, 20, 30 and 45 mm Hg (see Chapter 5). Both experimental and model displacements are small for the 30-45 mm Hg IOP range, demonstrating a high degree of nonlinearity.

The following additional plots will also be generated.
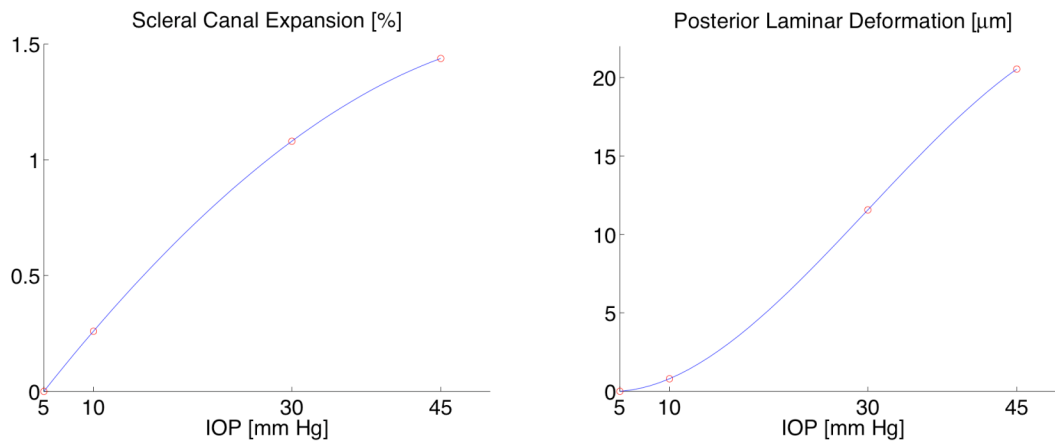
Figure B.4.8. Scleral canal expansion in % (left) and posterior laminar deformation in μm (right) as functions of IOP.
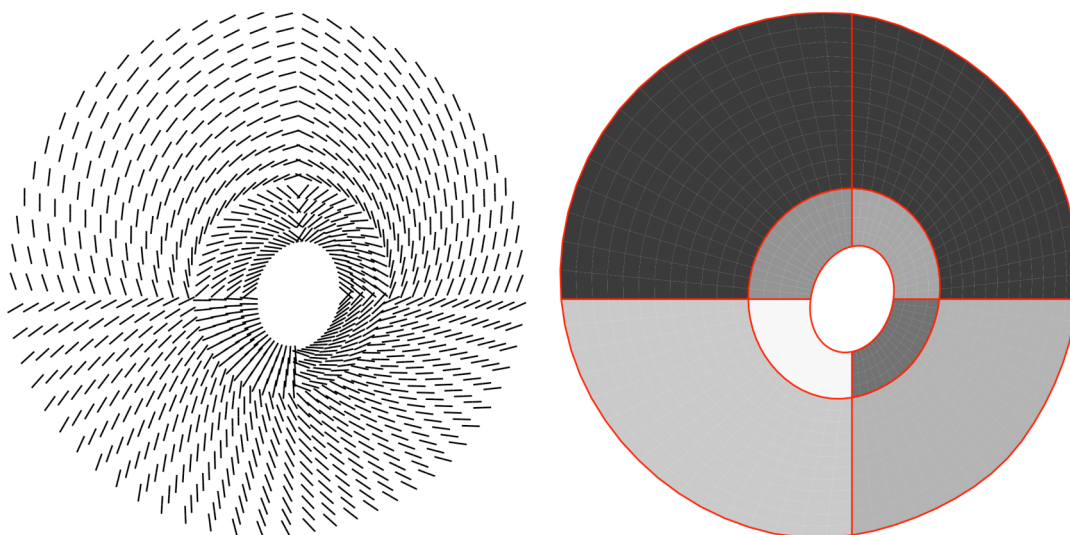
Figure B.4.9. Predicted preferred fiber orientation displayed as a vector map (left) and as a contour map (right) where black color corresponds to fibers perpendicular to the scleral canal (*i.e.* meridional orientation), and white color to fibers parallel to the scleral canal (*i.e.* circumferential orientation).
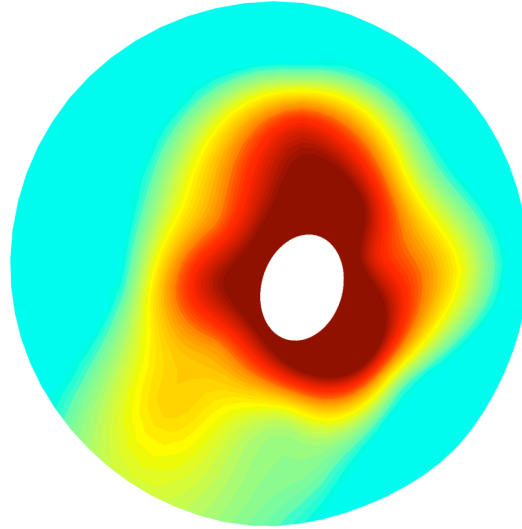
Figure B.4.10. Thickness map. Data were interpolated over the entire scleral field based on the twenty experimental thickness measurements (see Chapter 5).

Other Postprocessing Software

The user can use a different postprocessing software to visualize Nike3d output binary files. This software is called Postview and is currently being developed by Steve Maas and Jeffrey Weiss (Musculoskeletal Research Laboratories, The University of Utah, Salt Lake City, USA). It can be downloaded at this address *http://mrl.sci.utah.edu/* and can be installed on Windows, Linux or Mac workstations. To generate Postview files, a different Nike3d executable needs to be used (file **nike3d.lnxn3plot** located in /Code/Inverse FE/ from the attached DVD). The Unix command line to use is

```
./nike3d.lnxn3plot I=input_file.nk G=postview_file.pv
```

List of References

Abolmaali, A., R. A. Schachar and T. Le (2007). "Sensitivity study of human crystalline lens accommodation." Comput Methods Programs Biomed **85**(1): 77-90.

Alberts, B., A. Johnson, J. Lewis, M. Raff, K. Roberts and P. Walter (2008). Molecular Biology of the Cell, Garland Science, Taylor & Francis Group, LLC, an informa business.

Albon, J., S. Farrant, S. Akhtar, R. Young, M. E. Boulton, G. Smith, M. Taylor, J. Guggenheim and J. E. Morgan (2007). "Connective tissue structure of the tree shrew optic nerve and associated ageing changes." Invest Ophthalmol Vis Sci **48**(5): 2134-44.

Albon, J., W. S. Karwatowski, N. Avery, D. L. Easty and V. C. Duance (1995). "Changes in the collagenous matrix of the aging human lamina cribrosa." Br J Ophthalmol **79**(4): 368-75.

Albon, J., W. S. Karwatowski, D. L. Easty, T. J. Sims and V. C. Duance (2000a). "Age related changes in the non-collagenous components of the extracellular matrix of the human lamina cribrosa." Br J Ophthalmol **84**(3): 311-7.

Albon, J., P. P. Purslow, W. S. Karwatowski and D. L. Easty (2000b). "Age related compliance of the lamina cribrosa in human eyes." Br J Ophthalmol **84**(3): 318-23.

Anderson, D. R. and A. Hendrickson (1974). "Effect of intraocular pressure on rapid axoplasmic transport in monkey optic nerve." Invest Ophthalmol **13**(10): 771-83.

Ault, H. K. and A. H. Hoffman (1992a). "A composite micromechanical model for connective tissues: Part I--Theory." J Biomech Eng **114**(1): 137-41.

Ault, H. K. and A. H. Hoffman (1992b). "A composite micromechanical model for connective tissues: Part II--Application to rat tail tendon and joint capsule." J Biomech Eng **114**(1): 142-6.

Avetisov, E. S., N. F. Savitskaya, M. I. Vinetskaya and E. N. Iomdina (1983). "A study of biochemical and biomechanical qualities of normal and myopic eye sclera in humans of different age groups." Metab Pediatr Syst Ophthalmol **7**(4): 183-8.

Avetisov, S. A., V. R. Mamikonian and G. V. Voronin (2003). "An evaluation of the biomechanical parameters of the corneoscleral eye coating in kerato-refractive surgery." Vestn Ross Akad Med Nauk(2): 8-15.

Bailey, A. J. (1987). "Structure, function and ageing of the collagens of the eye." Eye **1 (Pt 2)**: 175-83.

Bailey, A. J., R. G. Paul and L. Knott (1998). "Mechanisms of maturation and ageing of collagen." Mech Ageing Dev **106**(1-2): 1-56.

Barron, J. L., D. J. Fleet and S. S. Beauchemin (1994). "Performance of optical flow techniques." Int J Comput Vis **12**(1): 43-77.

Barron, J. L. and R. Klette (2002). "Quantitative Color Optical Flow." Proceedings of ICPR.

Battaglioli, J. L. and R. D. Kamm (1984). "Measurements of the compressive properties of scleral tissue." Invest Ophthalmol Vis Sci **25**(1): 59-65.

Bellezza, A. J., R. T. Hart and C. F. Burgoyne (2000). "The optic nerve head as a biomechanical structure: initial finite element modeling." Invest Ophthalmol Vis Sci **41**(10): 2991-3000.

Bellezza, A. J., C. J. Rintalan, H. W. Thompson, J. C. Downs, R. T. Hart and C. F. Burgoyne (2003a). "Anterior scleral canal geometry in pressurised (IOP 10) and non-pressurised (IOP 0) normal monkey eyes." Br J Ophthalmol **87**(10): 1284-90.

Bellezza, A. J., C. J. Rintalan, H. W. Thompson, J. C. Downs, R. T. Hart and C. F. Burgoyne (2003b). "Deformation of the lamina cribrosa and anterior scleral canal wall in early experimental glaucoma." Invest Ophthalmol Vis Sci **44**(2): 623-37.

Bengtsson, B. (1981). "The prevalence of glaucoma." Br J Ophthalmol **65**(1): 46-9.

Bereiter-Hahn, J. (1995). Probing biological cells and tissues with acoustic microscopy. Advances in acoustic microscopy. Berlin, Germany Springer.

Billiar, K. L. and M. S. Sacks (2000a). "Biaxial mechanical properties of the native and glutaraldehyde-treated aortic valve cusp: Part II--A structural constitutive model." J Biomech Eng **122**(4): 327-35.

Billiar, K. L. and M. S. Sacks (2000b). "Biaxial mechanical properties of the natural and glutaraldehyde treated aortic valve cusp--Part I: Experimental results." J Biomech Eng **122**(1): 23-30.

Bonet, J. and R. D. Wood (1997). Nonlinear continuum mechanics for finite element analysis. Cambridge, UK, Cambridge University Press.

Boote, C., S. Dennis and K. Meek (2004). "Spatial mapping of collagen fibril organisation in primate cornea-an X-ray diffraction investigation." J Struct Biol **146**(3): 359-67.

Boyce, B. L., R. E. Jones, T. D. Nguyen and J. M. Grazier (2007). "Stress-controlled viscoelastic tensile response of bovine cornea." J Biomech **40**(11): 2367-76.

Bron, A. J., R. C. Tripathi and B. J. Tripathi (1997). Wolff's anatomy of the eye and orbit, Hodder Arnold Publication.

Brown, D. J., N. Morishige, A. Neekhra, D. S. Minckler and J. V. Jester (2007). "Application of second harmonic imaging microscopy to assess structural changes in optic nerve head structure ex vivo." J Biomed Opt **12**(2): 024029.

Buhrmann, R. R., H. A. Quigley, Y. Barron, S. K. West, M. S. Oliva and B. B. Mmbaga (2000). "Prevalence of glaucoma in a rural East African population." Invest Ophthalmol Vis Sci **41**(1): 40-8.

Burgoyne, C. F. and J. C. Downs (2008). "Premise and Prediction-How Optic Nerve Head Biomechanics Underlies the Susceptibility and Clinical Behavior of the Aged Optic Nerve Head." J Glaucoma **17**(4): 318-328.

Burgoyne, C. F., J. C. Downs, A. J. Bellezza and R. T. Hart (2004). "Three-dimensional reconstruction of normal and early glaucoma monkey optic nerve head connective tissues." Invest Ophthalmol Vis Sci **45**(12): 4388-99.

Burgoyne, C. F., J. C. Downs, A. J. Bellezza, J. K. Suh and R. T. Hart (2005). "The optic nerve head as a biomechanical structure: a new paradigm for understanding the role of IOP-related stress and strain in the pathophysiology of glaucomatous optic nerve head damage." Prog Retin Eye Res **24**(1): 39-73.

Burgoyne, C. F., H. A. Quigley, H. W. Thompson, S. Vitale and R. Varma (1995). "Early changes in optic disc compliance and surface position in experimental glaucoma." Ophthalmology **102**(12): 1800-9.

Burgoyne, C. F., G. Williams and B. Fortune (2008). "Posterior Bowing of the Lamina Cribrosa and Peripapillary Sclera Are Clinically Detectable Within Heidelberg Spectralis 3D OCT Volumes of the Non-Human Primate (NHP) Optic Nerve Head (ONH) Following Acute and Chronic IOP Elevation." Invest. Ophthalmol. Vis. Sci. **49**(5): 3655-.

Cahane, M. and E. Bartov (1992). "Axial length and scleral thickness effect on susceptibility to glaucomatous damage: a theoretical model implementing Laplace's law." Ophthalmic Res **24**(5): 280-4.

Charette, P. G., I. W. Hunter and P. J. Hunter (1997). "Large deformation mechanical testing of biological membranes using speckle interferometry in transmission. I: Experimental apparatus." Appl Opt **36**(10): 2238-45.

Chumbley, L. C. and R. F. Brubaker (1976). "Low-tension glaucoma." Am J Ophthalmol **81**(6): 761-7.

Collaborative Normal-Tension Glaucoma Study Group (1998). "Comparison of glaucomatous progression between untreated patients with normal-tension glaucoma and patients with therapeutically reduced intraocular pressures." Am J Ophthalmol **126**(4): 487-97.

Cui, W., M. R. Bryant, P. M. Sweet and P. J. McDonnell (2004). "Changes in gene expression in response to mechanical strain in human scleral fibroblasts." Exp Eye Res **78**(2): 275-84.

Curtin, B. J. (1969). "Physiopathologic aspects of scleral stress-strain." Trans Am Ophthalmol Soc **67**: 417-61.

David, T., S. Smye, T. Dabbs and T. James (1998). "A model for the fluid motion of vitreous humour of the human eye during saccadic movement." Phys Med Biol **43**(6): 1385-99.

Downs, J., C. F. Burgoyne, Y. Liang and V. L. Sallee (2008a). "A New Implantable System for Telemetric IOP Monitoring in Nonhuman Primates (NHP)." Invest. Ophthalmol. Vis. Sci. **49**(5): 2043-.

Downs, J. C. (2002). Experimental and computational Modeling of the posterior scleral shell of the normal and glaucomatous monkey eye. Department of Biomedical Engineering New Orleans Tulane University **PhD:** 221.

Downs, J. C., R. A. Blidner, A. J. Bellezza, H. W. Thompson, R. T. Hart and C. F. Burgoyne (2002). "Peripapillary scleral thickness in perfusion-fixed normal monkey eyes." Invest Ophthalmol Vis Sci **43**(7): 2229-35.

Downs, J. C., M. E. Ensor, A. J. Bellezza, H. W. Thompson, R. T. Hart and C. F. Burgoyne (2001). "Posterior scleral thickness in perfusion-fixed normal and early-glaucoma monkey eyes." Invest Ophthalmol Vis Sci **42**(13): 3202-8.

Downs, J. C., M. D. Roberts and C. F. Burgoyne (2008b). "Mechanical environment of the optic nerve head in glaucoma." Optom Vis Sci **85**(6): 425-35.

Downs, J. C., M. D. Roberts, C. F. Burgoyne and R. T. Hart (2007a). Finite element modeling of the lamina cribrosa microarchitecture in the normal and early glaucoma optic nerve head Proceedings of the ASME, Summer Bioengineering Conference Keystone, Colorado, USA.

Downs, J. C., J. K. Suh, K. A. Thomas, A. J. Bellezza, C. F. Burgoyne and R. T. Hart (2003). "Viscoelastic characterization of peripapillary sclera: material properties by quadrant in rabbit and monkey eyes." J Biomech Eng **125**(1): 124-31.

Downs, J. C., J. K. Suh, K. A. Thomas, A. J. Bellezza, R. T. Hart and C. F. Burgoyne (2005). "Viscoelastic material properties of the peripapillary sclera in normal and early-glaucoma monkey eyes." Invest Ophthalmol Vis Sci **46**(2): 540-6.

Downs, J. C., H. Yang, C. Girkin, L. Sakata, A. Bellezza, H. Thompson and C. F. Burgoyne (2007b). "Three-dimensional histomorphometry of the normal and early glaucomatous monkey optic nerve head: neural canal and subarachnoid space architecture." Invest Ophthalmol Vis Sci **48**(7): 3195-208.

Drance, S. M. (1972). "Some factors in the production of low tension glaucoma." Br J Ophthalmol **56**(3): 229-42.

Drance, S. M. (2008). "What can we learn from the disc appearance about the risk factors in glaucoma?" Can J Ophthalmol **43**(3): 322-7.

Drance, S. M., V. P. Sweeney, R. W. Morgan and F. Feldman (1973). "Studies of factors involved in the production of low tension glaucoma." Arch Ophthalmol **89**(6): 457-65.

Driessen, N. J., M. A. Cox, C. V. Bouten and F. P. Baaijens (2008). "Remodelling of the angular collagen fiber distribution in cardiovascular tissues." Biomech Model Mechanobiol **7**(2): 93-103.

Driessen, N. J., G. W. Peters, J. M. Huyghe, C. V. Bouten and F. P. Baaijens (2003). "Remodelling of continuously distributed collagen fibres in soft connective tissues." J Biomech **36**(8): 1151-8.

Edelhauser, H. F. and J. L. Ubels (2003). The cornea and the sclera. Adler's physiology of the eye, Clinical applications. St. Louis, Missouri, Mosby.

Elsheikh, A., D. Alhasso and P. Rama (2008). "Biomechanical properties of human and porcine corneas." Exp Eye Res **86**(5): 783-90.

Erne, O. K., J. B. Reid, L. W. Ehmke, M. B. Sommers, S. M. Madey and M. Bottlang (2005). "Depth-dependent strain of patellofemoral articular cartilage in unconfined compression." J Biomech **38**(4): 667-72.

Ethier, C. R. (2002). "The inner wall of Schlemm's canal." Exp Eye Res **74**(2): 161-72.

Ethier, C. R. (2006). "Scleral biomechanics and glaucoma--a connection?" Can J Ophthalmol **41**(1): 9-12, 14.

Ethier, C. R., M. Johnson and J. Ruberti (2004). "Ocular biomechanics and biotransport." Annu Rev Biomed Eng **6**: 249-73.

Fechtner, R. D. and R. N. Weinreb (1994). "Mechanisms of optic nerve damage in primary open angle glaucoma." Surv Ophthalmol **39**(1): 23-42.

Fisher, N. I. (1993). Statistical analysis of circular data Cambridge, UK, Cambridge University Press.

Foster, A. and S. Resnikoff (2005). "The impact of Vision 2020 on global blindness." Eye **19**(10): 1133-5.

Freed, A. D., D. R. Einstein and I. Vesely (2005). "Invariant formulation for dispersed transverse isotropy in aortic heart valves: an efficient means for modeling fiber splay." Biomech Model Mechanobiol **4**(2-3): 100-17.

Friberg, T. R. and J. W. Lace (1988). "A comparison of the elastic properties of human choroid and sclera." Exp Eye Res **47**(3): 429-36.

Friedman, D. S., R. C. Wolfs, B. J. O'Colmain, B. E. Klein, H. R. Taylor, S. West, M. C. Leske, P. Mitchell, N. Congdon and J. Kempen (2004). "Prevalence of open-angle glaucoma among adults in the United States." Arch Ophthalmol **122**(4): 532-8.

Fujikura, H., Y. Seko, T. Tokoro, M. Mochizuki and H. Shimokawa (2002). "Involvement of mechanical stretch in the gelatinolytic activity of the fibrous sclera of chicks, in vitro." Jpn J Ophthalmol **46**(1): 24-30.

Fung, Y. C. (1993). Biomechanics: Mechanical properties of living tissues. New York, NY, Springer-Verlag.

Gaasterland, D. and C. Kupfer (1974). "Experimental glaucoma in the rhesus monkey." Invest Ophthalmol **13**(6): 455-7.

Gaasterland, D., T. Tanishima and T. Kuwabara (1978). "Axoplasmic flow during chronic experimental glaucoma. 1. Light and electron microscopic studies of the monkey optic nervehead during development of glaucomatous cupping." Invest Ophthalmol Vis Sci **17**(9): 838-46.

Gasser, T. C., R. W. Ogden and G. A. Holzapfel (2006). "Hyperelastic modelling of arterial layers with distributed collagen fibre orientations." J. R. Soc. Interface **3**: 15–35.

Geijssen, H. C. (1991). Studies on normal pressure glaucoma. Amstelveen, Kugler Publications.

Girard, M., J. K. Suh, R. T. Hart, C. F. Burgoyne and J. C. Downs (2007). "Effects of storage time on the mechanical properties of rabbit peripapillary sclera after enucleation." Curr Eye Res **32**(5): 465-70.

Girard, M. J., J. C. Downs, C. F. Burgoyne and J. K. Suh (2008a). "Experimental surface strain mapping of porcine peripapillary sclera due to elevations of intraocular pressure." J Biomech Eng **130**(4): 041017.

Girard, M. J. A., J. C. Downs, M. Bottlang, C. F. Burgoyne and J.-K. F. Suh (2008b). "Peripapillary and Posterior Scleral Mechanics, Part II - Experimental and Inverse Finite Element Characterization." J Biomech Eng. Under revision.

Girard, M. J. A., J. C. Downs, C. F. Burgoyne and J.-K. F. Suh (2008c). "Experimental surface strain mapping of porcine peripapillary sclera due to elevations of intraocular pressure." J Biomech Eng. In Press.

Girard, M. J. A., J. C. Downs, C. F. Burgoyne and J.-K. F. Suh (2008d). "Peripapillary and Posterior Scleral Mechanics, Part I - Development of an Anisotropic Hyperelastic Constitutive Model." J Biomech Eng. Under revision.

Girard, M. J. A., J.-K. F. Suh, M. Bottlang, C. F. Burgoyne and J. C. Downs (2008). "Scleral biomechanics in the aging monkey eye " IOVS. In preparation.

Goldberg, I., F. C. Hollows, M. A. Kass and B. Becker (1981). "Systemic factors in patients with low-tension glaucoma." Br J Ophthalmol **65**(1): 56-62.

Gordon, M. O., J. A. Beiser, J. D. Brandt, D. K. Heuer, E. J. Higginbotham, C. A. Johnson, J. L. Keltner, J. P. Miller, R. K. Parrish, 2nd, M. R. Wilson and M. A. Kass (2002). "The Ocular Hypertension Treatment Study: baseline factors that predict the onset of primary open-angle glaucoma." Arch Ophthalmol **120**(6): 714-20; discussion 829-30.

Govindjee, S. and P. A. Mihalic (1996). "Computational methods for inverse finite elastostatics." Comput Methods Appl Mech Engrg **136**: 47-57.

Green, A. E. (1970). Large elastic deformations. Oxford, UK, Clarendon Press.

Greene, P. R. (1980). "Mechanical considerations in myopia: relative effects of accommodation, convergence, intraocular pressure, and the extraocular muscles." Am J Optom Physiol Opt **57**(12): 902-14.

Greene, P. R. and T. A. McMahon (1979). "Scleral creep vs. temperature and pressure in vitro." Exp Eye Res **29**(5): 527-37.

Grunwald, J. E., J. Piltz, N. Patel, S. Bose and C. E. Riva (1993). "Effect of aging on retinal macular microcirculation: a blue field simulation study." Invest Ophthalmol Vis Sci **34**(13): 3609-13.

Guo, L., V. Tsatourian, V. Luong, A. G. Podoleanu, D. A. Jackson, F. W. Fitzke and M. F. Cordeiro (2005). "En face optical coherence tomography: a new method to analyse structural changes of the optic nerve head in rat glaucoma." Br J Ophthalmol **89**(9): 1210-6.

Hallquist, J. O. (1984). NIKE3D: an implicit, finite-deformation, finite element code for analyzing the static and dynamic response of three-dimensional solids. University of California, Lawrence Livermore National Laboratory

Hariton, I., G. de Botton, T. C. Gasser and G. A. Holzapfel (2007a). "Stress-driven collagen fiber remodeling in arterial walls." Biomech Model Mechanobiol **6**(3): 163-75.

Hariton, I., G. deBotton, T. C. Gasser and G. A. Holzapfel (2007b). "Stress-modulated collagen fiber remodeling in a human carotid bifurcation." J Theor Biol **248**(3): 460-70.

Harris, A., M. Harris, J. Biller, H. Garzozi, D. Zarfty, T. A. Ciulla and B. Martin (2000). "Aging affects the retrobulbar circulation differently in women and men." Arch Ophthalmol **118**(8): 1076-80.

Hayreh, S. S. (1969). "Blood supply of the optic nerve head and its role in optic atrophy, glaucoma, and oedema of the optic disc." Br J Ophthalmol **53**(11): 721-48.

Hayreh, S. S. (2001). "The blood supply of the optic nerve head and the evaluation of it - myth and reality." Prog Retin Eye Res **20**(5): 563-93.

Heijl, A., M. C. Leske, B. Bengtsson, B. Bengtsson and M. Hussein (2003). "Measuring visual field progression in the Early Manifest Glaucoma Trial." Acta Ophthalmol Scand **81**(3): 286-93.

Heijl, A., M. C. Leske, B. Bengtsson, L. Hyman, B. Bengtsson and M. Hussein (2002). "Reduction of intraocular pressure and glaucoma progression: results from the Early Manifest Glaucoma Trial." Arch Ophthalmol **120**(10): 1268-79.

Hernandez, M. R. (2000). "The optic nerve head in glaucoma: role of astrocytes in tissue remodeling." Prog Retin Eye Res **19**(3): 297-321.

Hernandez, M. R., W. M. Andrzejewska and A. H. Neufeld (1990). "Changes in the extracellular matrix of the human optic nerve head in primary open-angle glaucoma." Am J Ophthalmol **109**(2): 180-8.

Hernandez, M. R., X. X. Luo, W. Andrzejewska and A. H. Neufeld (1989). "Age-related changes in the extracellular matrix of the human optic nerve head." Am J Ophthalmol **107**(5): 476-84.

Hernandez, M. R., X. X. Luo, F. Igoe and A. H. Neufeld (1987). "Extracellular matrix of the human lamina cribrosa." Am J Ophthalmol **104**(6): 567-76.

Hernandez, M. R., N. Wang, N. M. Hanley and A. H. Neufeld (1991). "Localization of collagen types I and IV mRNAs in human optic nerve head by in situ hybridization." Invest Ophthalmol Vis Sci **32**(8): 2169-77.

Heys, J. and V. H. Barocas (1999). "Mechanical characterization of the bovine iris." J Biomech **32**(9): 999-1003.

Hoffman, A. H. and P. Grigg (1984). "A method for measuring strains in soft tissue." J Biomech **17**(10): 795-800.

Hogan, M. J. (1971). Histology of the human eye: An atlas and textbook, Saunders.

Holzapfel, G., T. Gasser and R. Ogden (2000). "A New Constitutive Framework for Arterial Wall Mechanics and a Comparative Study of Material Models." Journal of Elasticity **61**(1): 1-48.

Holzapfel, G. A. (2000). Nonlinear solid mechanics. A continuum approach for engineering West Sussex, England John Wiley & Sons Ltd.

Humphrey, J. D. (1999). "Remodeling of a collagenous tissue at fixed lengths." J Biomech Eng **121**(6): 591-7.

Humphrey, J. D. (2001). "Stress, strain, and mechanotransduction in cells." J Biomech Eng **123**(6): 638-41.

Humphrey, J. D., R. K. Strumpf and F. C. Yin (1990). "Determination of a constitutive relation for passive myocardium: I. A new functional form." J Biomech Eng **112**(3): 333-9.

Humphrey, J. D., D. L. Vawter and R. P. Vito (1987). "Quantification of strains in biaxially tested soft tissues." J Biomech **20**(1): 59-65.

Humphrey, J. D. and F. C. Yin (1987). "On constitutive relations and finite deformations of passive cardiac tissue: I. A pseudostrain-energy function." J Biomech Eng **109**(4): 298-304.

Iwase, A., Y. Suzuki, M. Araie, T. Yamamoto, H. Abe, S. Shirato, Y. Kuwayama, H. K. Mishima, H. Shimizu, G. Tomita, Y. Inoue and Y. Kitazawa (2004). "The prevalence of primary open-angle glaucoma in Japanese: the Tajimi Study." Ophthalmology **111**(9): 1641-8.

Jackson, T. L., A. Hussain, A. Hodgetts, A. M. Morley, J. Hillenkamp, P. M. Sullivan and J. Marshall (2006). "Human scleral hydraulic conductivity: age-related changes, topographical variation, and potential scleral outflow facility." Invest Ophthalmol Vis Sci **47**(11): 4942-6.

Jin, B., Z. Ai and M. Rasmussen (2005). "Simulation of eye disease in virtual reality." Conf Proc IEEE Eng Med Biol Soc **5**: 5128-31.

Johnson, M. C. and R. D. Kamm (1983). "The role of Schlemm's canal in aqueous outflow from the human eye." Invest Ophthalmol Vis Sci **24**(3): 320-5.

Jonas, J. B., E. Berenshtein and L. Holbach (2003). "Anatomic relationship between lamina cribrosa, intraocular space, and cerebrospinal fluid space." Invest Ophthalmol Vis Sci **44**(12): 5189-95.

Jonas, J. B., E. Berenshtein and L. Holbach (2004). "Lamina cribrosa thickness and spatial relationships between intraocular space and cerebrospinal fluid space in highly myopic eyes." Invest Ophthalmol Vis Sci **45**(8): 2660-5.

Jonas, J. B. and W. M. Budde (2005). "Optic nerve damage in highly myopic eyes with chronic open-angle glaucoma." Eur J Ophthalmol **15**(1): 41-7.

Jonas, J. B., C. Y. Mardin, U. Schlotzer-Schrehardt and G. O. Naumann (1991). "Morphometry of the human lamina cribrosa surface." Invest Ophthalmol Vis Sci **32**(2): 401-5.

Jonas, J. B., A. M. Schmidt, J. A. Muller-Bergh, U. M. Schlotzer-Schrehardt and G. O. Naumann (1992). "Human optic nerve fiber count and optic disc size." Invest Ophthalmol Vis Sci **33**(6): 2012-8.

Jones, R. and C. Wykes (1989). Holographic and speckle interferometry Cambridge, UK, Cambridge University Press.

Kagemann, L., H. Ishikawa, G. Wollstein, P. M. Brennen, K. A. Townsend, M. L. Gabriele and J. S. Schuman (2008). "Ultrahigh-resolution spectral domain optical coherence tomography imaging of the lamina cribrosa." Ophthalmic Surg Lasers Imaging **39**(4 Suppl): S126-131.

Kastelic, J., A. Galeski and E. Baer (1978). "The multicomposite structure of tendon." Connect Tissue Res **6**(1): 11-23.

Kessler, O., E. Lacatusu, M. B. Sommers, E. Mayr and M. Bottlang (2006). "Malrotation in total knee arthroplasty: effect on tibial cortex strain captured by laser-based strain acquisition." Clin Biomech (Bristol, Avon) **21**(6): 603-9.

Klein, B. E., R. Klein and K. L. Linton (1992a). "Intraocular pressure in an American community. The Beaver Dam Eye Study." Invest Ophthalmol Vis Sci **33**(7): 2224-8.

Klein, B. E., R. Klein, W. E. Sponsel, T. Franke, L. B. Cantor, J. Martone and M. J. Menage (1992b). "Prevalence of glaucoma. The Beaver Dam Eye Study." Ophthalmology **99**(10): 1499-504.

Kokott, W. (1934). "Das spaltlinienbild der sklera. (Ein beitrag zum funktionellen bau der sklera)." Klin Mbl Augen **92**: 177-185.

Komai, Y. and T. Ushiki (1991). "The three-dimensional organization of collagen fibrils in the human cornea and sclera." Invest Ophthalmol Vis Sci **32**(8): 2244-58.

Kotecha, A., S. Izadi and G. Jeffery (2006). "Age-related changes in the thickness of the human lamina cribrosa." Br J Ophthalmol **90**(12): 1531-4.

Kroon, M. and G. A. Holzapfel (2008). "A new constitutive model for multi-layered collagenous tissues." J Biomech.

Lanir, Y. (1983). "Constitutive equations for fibrous connective tissues." J Biomech **16**(1): 1-12.

Lanir, Y. and Y. C. Fung (1974a). "Two-dimensional mechanical properties of rabbit skin. I. Experimental system." J Biomech **7**(1): 29-34.

Lanir, Y. and Y. C. Fung (1974b). "Two-dimensional mechanical properties of rabbit skin. II. Experimental results." J Biomech **7**(2): 171-82.

Le, A., B. N. Mukesh, C. A. McCarty and H. R. Taylor (2003). "Risk factors associated with the incidence of open-angle glaucoma: the visual impairment project." Invest Ophthalmol Vis Sci **44**(9): 3783-9.

Lee, B., M. Litt and G. Buchsbaum (1992). "Rheology of the vitreous body. Part I: Viscoelasticity of human vitreous." Biorheology **29**(5-6): 521-33.

Leske, M. C. (1983). "The epidemiology of open-angle glaucoma: a review." Am J Epidemiol **118**(2): 166-91.

Leske, M. C. (2007). "Open-angle glaucoma -- an epidemiologic overview." Ophthalmic Epidemiol **14**(4): 166-72.

Leske, M. C., A. M. Connell, A. P. Schachat and L. Hyman (1994). "The Barbados Eye Study. Prevalence of open angle glaucoma." <u>Arch Ophthalmol</u> **112**(6): 821-9.

Leske, M. C., A. M. Connell, S. Y. Wu, L. Hyman and A. P. Schachat (1997). "Distribution of intraocular pressure. The Barbados Eye Study." <u>Arch Ophthalmol</u> **115**(8): 1051-7.

Leske, M. C., A. Heijl, M. Hussein, B. Bengtsson, L. Hyman and E. Komaroff (2003). "Factors for glaucoma progression and the effect of treatment: the early manifest glaucoma trial." <u>Arch Ophthalmol</u> **121**(1): 48-56.

Leske, M. C., S. Y. Wu, A. Hennis, R. Honkanen and B. Nemesure (2008). "Risk factors for incident open-angle glaucoma: the Barbados Eye Studies." <u>Ophthalmology</u> **115**(1): 85-93.

Levene, R. Z. (1980). "Low tension glaucoma: a critical review and new material." <u>Surv Ophthalmol</u> **24**(6): 621-64.

Levin, L. A. (2003). Optic Nerve. <u>Adler's physiology of the eye, Clinical applications</u>. St. Louis, Missouri, Mosby.

Levy, N. S. and E. E. Crapps (1984). "Displacement of optic nerve head in response to short-term intraocular pressure elevation in human eyes." <u>Arch Ophthalmol</u> **102**(5): 782-6.

Levy, N. S., E. E. Crapps and R. C. Bonney (1981). "Displacement of the optic nerve head. Response to acute intraocular pressure elevation in primate eyes." <u>Arch Ophthalmol</u> **99**(12): 2166-74.

Lomb, L. (2007). Second harmonic generation imaging of the lamina cribrosa. <u>Kirchhoff Institut der Physik (KIP)</u>, Universitat Heidelberg.

Lu, J., X. Zhou and M. L. Raghavan (2007). "Inverse elastostatic stress analysis in pre-deformed biological structures: Demonstration using abdominal aortic aneurysms." <u>J Biomech</u> **40**(3): 693-6.

Lucas, B. D. and T. Kanade (1981). "An iterative image registration technique with an application to stereo vision " <u>Proceedings of DARPA Image Understanding Workshop</u>: 121-130.

Maier, P. C., J. Funk, G. Schwarzer, G. Antes and Y. T. Falck-Ytter (2005). "Treatment of ocular hypertension and open angle glaucoma: meta-analysis of randomised controlled trials." <u>Bmj</u> **331**(7509): 134.

Mase, G. T. and G. E. Mase (1999). <u>Continuum mechanics for engineers</u>, CRC press.

Mikelberg, F. S., H. M. Yidegiligne, V. A. White and M. Schulzer (1991). "Relation between optic nerve axon number and axon diameter to scleral canal area." <u>Ophthalmology</u> **98**(1): 60-3.

Minckler, D. S., A. H. Bunt and G. W. Johanson (1977). "Orthograde and retrograde axoplasmic transport during acute ocular hypertension in the monkey." <u>Invest Ophthalmol Vis Sci</u> **16**(5): 426-41.

Mitchell, P., F. Hourihan, J. Sandbach and J. J. Wang (1999). "The relationship between glaucoma and myopia: the Blue Mountains Eye Study." <u>Ophthalmology</u> **106**(10): 2010-5.

Mitchell, P., W. Smith, K. Attebo and P. R. Healey (1996). "Prevalence of open-angle glaucoma in Australia. The Blue Mountains Eye Study." <u>Ophthalmology</u> **103**(10): 1661-9.

Morrison, J. C., M. E. Dorman-Pease, G. R. Dunkelberger and H. A. Quigley (1990). "Optic nerve head extracellular matrix in primary optic atrophy and experimental glaucoma." Arch Ophthalmol **108**(7): 1020-4.

Morrison, J. C., J. A. Jerdan, M. E. Dorman and H. A. Quigley (1989a). "Structural proteins of the neonatal and adult lamina cribrosa." Arch Ophthalmol **107**(8): 1220-4.

Morrison, J. C., J. A. Jerdan, N. L. L'Hernault and H. A. Quigley (1988). "The extracellular matrix composition of the monkey optic nerve head." Invest Ophthalmol Vis Sci **29**(7): 1141-50.

Morrison, J. C., N. L. L'Hernault, J. A. Jerdan and H. A. Quigley (1989b). "Ultrastructural location of extracellular matrix components in the optic nerve head." Arch Ophthalmol **107**(1): 123-9.

Nemesure, B., R. Honkanen, A. Hennis, S. Y. Wu and M. C. Leske (2007). "Incident open-angle glaucoma and intraocular pressure." Ophthalmology **114**(10): 1810-5.

Nguyen, T. D., R. E. Jones and B. L. Boyce (2008). "A nonlinear anisotropic viscoelastic model for the tensile behavior of the corneal stroma." J Biomech Eng **130**(4): 041020.

Nomura, H., F. Ando, N. Niino, H. Shimokata and Y. Miyake (2002). "The relationship between age and intraocular pressure in a Japanese population: the influence of central corneal thickness." Curr Eye Res **24**(2): 81-5.

Nomura, H., H. Shimokata, F. Ando, Y. Miyake and F. Kuzuya (1999). "Age-related changes in intraocular pressure in a large Japanese population: a cross-sectional and longitudinal study." Ophthalmology **106**(10): 2016-22.

Nouri-Mahdavi, K., D. Hoffman, A. L. Coleman, G. Liu, G. Li, D. Gaasterland and J. Caprioli (2004). "Predictive factors for glaucomatous visual field progression in the Advanced Glaucoma Intervention Study." Ophthalmology **111**(9): 1627-35.

Nowick, A. S. and B. S. Berry (1961). "Lognormal distribution function for describing anelastic and other relaxation processes I. Theory and numerical computations." IBM J **5**(4): 297-311.

Olberding, J. E. and J.-K. F. Suh (2006). "A dual optimization method for the material parameter identification of a biphasic poroviscoelastic hydrogel: Potential application to hypercompliant soft tissues." J Biomech **39**(13): 2468-75.

Olesen, C. G., I. Tertinegg, A. Eilaghi, G. W. Brodland, C. Horst, J. H. Veldhuis, J. G. Flanagan and C. R. Ethier (2007). Measuring the biaxial stress-strain characteristics of the human sclera. Proceedings of the ASME, Summer Bioengineering Conference Keystone, Colorado, USA.

Ollivier, F. J., D. E. Brooks, M. E. Kallberg, H. L. Sapp, A. M. Komaromy, G. R. Stevens, W. W. Dawson, M. B. Sherwood and G. N. Lambrou (2004). "Time-specific intraocular pressure curves in Rhesus macaques (Macaca mulatta) with laser-induced ocular hypertension." Vet Ophthalmol **7**(1): 23-7.

Olsen, T. W., S. Y. Aaberg, D. H. Geroski and H. F. Edelhauser (1998). "Human sclera: thickness and surface area." Am J Ophthalmol **125**(2): 237-41.

Olsen, T. W., S. Sanderson, X. Feng and W. C. Hubbard (2002). "Porcine sclera: thickness and surface area." Invest Ophthalmol Vis Sci **43**(8): 2529-32.

Papadopoulos, M., N. Cable, J. Rahi and P. T. Khaw (2007). "The British Infantile and Childhood Glaucoma (BIG) Eye Study." Invest Ophthalmol Vis Sci **48**(9): 4100-6.

Pedrigi, R. M., G. David, J. Dziezyc and J. D. Humphrey (2007). "Regional mechanical properties and stress analysis of the human anterior lens capsule." Vision Res **47**(13): 1781-9.

Phillips, J. R. and N. A. McBrien (1995). "Form deprivation myopia: elastic properties of sclera." Ophthalmic Physiol Opt **15**(5): 357-62.

Phillips, J. R. and N. A. McBrien (2004). "Pressure-induced changes in axial eye length of chick and tree shrew: significance of myofibroblasts in the sclera." Invest Ophthalmol Vis Sci **45**(3): 758-63.

Pierscionek, B. K., M. Asejczyk-Widlicka and R. A. Schachar (2007). "The effect of changing intraocular pressure on the corneal and scleral curvatures in the fresh porcine eye." Br J Ophthalmol **91**(6): 801-3.

Pinsky, P. M., D. van der Heide and D. Chernyak (2005). "Computational modeling of mechanical anisotropy in the cornea and sclera." J Cataract Refract Surg **31**(1): 136-45.

Price, K. V., R. M. Storn and J. A. Lampinen (2005). Differential evolution. A practical approach to global optimization. . Berlin, Germany Springer.

Quantock, A. J. and K. M. Meek (1988). "Axial electron density of human scleral collagen. Location of proteoglycans by x-ray diffraction." Biophys J **54**(1): 159-64.

Quigley, H. and D. R. Anderson (1976). "The dynamics and location of axonal transport blockade by acute intraocular pressure elevation in primate optic nerve." Invest Ophthalmol **15**(8): 606-16.

Quigley, H. A. (1982). "Childhood glaucoma: results with trabeculotomy and study of reversible cupping." Ophthalmology **89**(3): 219-26.

Quigley, H. A. (1993). "Open-angle glaucoma." N Engl J Med **328**(15): 1097-106.

Quigley, H. A. (2005). "Glaucoma: macrocosm to microcosm the Friedenwald lecture." Invest Ophthalmol Vis Sci **46**(8): 2662-70.

Quigley, H. A. and E. M. Addicks (1980). "Chronic experimental glaucoma in primates. II. Effect of extended intraocular pressure elevation on optic nerve head and axonal transport." Invest Ophthalmol Vis Sci **19**(2): 137-52.

Quigley, H. A. and E. M. Addicks (1981). "Regional differences in the structure of the lamina cribrosa and their relation to glaucomatous optic nerve damage." Arch Ophthalmol **99**(1): 137-43.

Quigley, H. A., E. M. Addicks, W. R. Green and A. E. Maumenee (1981). "Optic nerve damage in human glaucoma. II. The site of injury and susceptibility to damage." Arch Ophthalmol **99**(4): 635-49.

Quigley, H. A. and A. T. Broman (2006). "The number of people with glaucoma worldwide in 2010 and 2020." Br J Ophthalmol **90**(3): 262-7.

Quigley, H. A., A. Brown and M. E. Dorman-Pease (1991a). "Alterations in elastin of the optic nerve head in human and experimental glaucoma." Br J Ophthalmol **75**(9): 552-7.

Quigley, H. A., M. E. Dorman-Pease and A. E. Brown (1991b). "Quantitative study of collagen and elastin of the optic nerve head and sclera in human and experimental monkey glaucoma." <u>Curr Eye Res</u> **10**(9): 877-88.

Quigley, H. A., R. W. Flower, E. M. Addicks and D. S. McLeod (1980). "The mechanism of optic nerve damage in experimental acute intraocular pressure elevation." <u>Invest Ophthalmol Vis Sci</u> **19**(5): 505-17.

Quigley, H. A. and W. R. Green (1979). "The histology of human glaucoma cupping and optic nerve damage: clinicopathologic correlation in 21 eyes." <u>Ophthalmology</u> **86**(10): 1803-30.

Quigley, H. A., R. M. Hohman, E. M. Addicks, R. W. Massof and W. R. Green (1983). "Morphologic changes in the lamina cribrosa correlated with neural loss in open-angle glaucoma." <u>Am J Ophthalmol</u> **95**(5): 673-91.

Quigley, H. A., S. K. West, J. Rodriguez, B. Munoz, R. Klein and R. Snyder (2001). "The prevalence of glaucoma in a population-based study of Hispanic subjects: Proyecto VER." <u>Arch Ophthalmol</u> **119**(12): 1819-26.

Rada, J. A., S. Shelton and T. T. Norton (2006). "The sclera and myopia." <u>Exp Eye Res</u> **82**(2): 185-200.

Rausch, S., I. A. Sigal, R. E. Norman, C. G. Olesen, I. Tertinegg, K. Morgan, S. Portnoy, J. G. Sled, J. G. Flanagan and C. R. Ethier (2007). "Measurement of Scleral Thickness Distribution in Human Eyes Using Micro-MRI." <u>Invest. Ophthalmol. Vis. Sci.</u> **48**(5): 3306-.

Resnikoff, S., D. Pascolini, D. Etya'ale, I. Kocur, R. Pararajasegaram, G. P. Pokharel and S. P. Mariotti (2004). "Global data on visual impairment in the year 2002." <u>Bull World Health Organ</u> **82**(11): 844-51.

Roach, M. R. and A. C. Burton (1957). "The reason for the shape of the distensibility curves of arteries." <u>Can J Biochem Physiol</u> **35**(8): 681-90.

Roberts, M. D., V. Grau, J. Grimm, J. Reynaud, A. Bellezza, C. F. Burgoyne and J. C. Downs (2008). "Remodeling of the Connective Tissue Microarchitecture of the Lamina Cribrosa Occurs Early in Experimental Glaucoma in the Monkey Eye." <u>Invest Ophthalmol Vis Sci</u>.

Roberts, M. D. and R. T. Hart (2005). "Shape adaptation of long bone structures using a contour based approach." <u>Comput Methods Biomech Biomed Engin</u> **8**(3): 145-56.

Roberts, M. D., R. T. Hart, Y. Liang, A. J. Bellezza, C. F. Burgoyne and J. C. Downs (2007). <u>Continuum-level finite element modeling of the optic nerve head using a fabric tensor based description of the lamina cribrosa</u>. Proceedings of the ASME, Summer Bioengineering Conference Keystone, Colorado, USA.

Rochtchina, E., P. Mitchell and J. J. Wang (2002). "Relationship between age and intraocular pressure: the Blue Mountains Eye Study." <u>Clin Experiment Ophthalmol</u> **30**(3): 173-5.

Sacks, M. S., D. B. Smith and E. D. Hiester (1997). "A small angle light scattering device for planar connective tissue microstructural analysis." <u>Ann Biomed Eng</u> **25**(4): 678-89.

Sadun, A. A., V. Carelli, S. Bose, F. N. Ross-Cisneros, P. Barboni and E. T. Ahrens (2002). "First application of extremely high-resolution magnetic resonance imaging to study microscopic features of normal and LHON human optic nerve." <u>Ophthalmology</u> **109**(6): 1085-91.

Sanchez, R. M., G. R. Dunkelberger and H. A. Quigley (1986). "The number and diameter distribution of axons in the monkey optic nerve." <u>Invest Ophthalmol Vis Sci</u> **27**(9): 1342-50.

Sander, E. A., J. C. Downs, R. T. Hart, C. F. Burgoyne and E. A. Nauman (2006). "A cellular solid model of the lamina cribrosa: mechanical dependence on morphology." <u>J Biomech Eng</u> **128**(6): 879-89.

Saw, S. M., G. Gazzard and D. S. Friedman (2003). "Interventions for angle-closure glaucoma: an evidence-based update." <u>Ophthalmology</u> **110**(10): 1869-78; quiz 1878-9, 1930.

Schultz, D. S., J. C. Lotz, S. M. Lee, M. L. Trinidad and J. M. Stewart (2008). "Structural factors mediating scleral stiffness." <u>Invest Ophthalmol Vis Sci</u>.

Schutte, S., S. P. van den Bedem, F. van Keulen, F. C. van der Helm and H. J. Simonsz (2006). "A finite-element analysis model of orbital biomechanics." <u>Vision Res</u> **46**(11): 1724-31.

Sharma, R. K. and E. J. Ehinger (2003). Development and structure of the retina <u>Adler's physiology of the eye, Clinical applications</u>. St. Louis, Missouri, Mosby.

Shelton, L. and J. S. Rada (2007). "Effects of cyclic mechanical stretch on extracellular matrix synthesis by human scleral fibroblasts." <u>Exp Eye Res</u> **84**(2): 314-22.

Shiose, Y., Y. Kitazawa, S. Tsukahara, T. Akamatsu, K. Mizokami, R. Futa, H. Katsushima and H. Kosaki (1991). "Epidemiology of glaucoma in Japan--a nationwide glaucoma survey." <u>Jpn J Ophthalmol</u> **35**(2): 133-55.

Siegwart, J. T., Jr. and T. T. Norton (1999). "Regulation of the mechanical properties of tree shrew sclera by the visual environment." <u>Vision Res</u> **39**(2): 387-407.

Sigal, I. A., J. G. Flanagan and C. R. Ethier (2005). "Factors influencing optic nerve head biomechanics." <u>Invest Ophthalmol Vis Sci</u> **46**(11): 4189-99.

Sigal, I. A., J. G. Flanagan, I. Tertinegg and C. R. Ethier (2004). "Finite element modeling of optic nerve head biomechanics." <u>Invest Ophthalmol Vis Sci</u> **45**(12): 4378-87.

Sigal, I. A., J. G. Flanagan, I. Tertinegg and C. R. Ethier (2008a). "Modeling individual-specific human optic nerve head biomechanics. Part I: IOP-induced deformations and influence of geometry." <u>Biomech Model Mechanobiol</u>.

Sigal, I. A., J. G. Flanagan, I. Tertinegg and C. R. Ethier (2008b). "Modeling individual-specific human optic nerve head biomechanics. Part II: influence of material properties." <u>Biomech Model Mechanobiol</u>.

Sigal, I. A., M. D. Roberts, M. J. A. Girard, C. F. Burgoyne and J. C. Downs (2009). Biomechancial changes of the optic disc. <u>Ocular disease: mechanisms and management</u>. New York Elvesier.

Simo, J. C. and R. L. Taylor (1991). "Quasi-incompressible finite elasticity in principal stretches. Continuum basis and numerical algorithms " <u>Comput Methods Appl Mech Engrg</u> **85**: 273-310.

Smith, S. W. (1997). <u>The scientist and engineer's guide to digital signal processing</u>, California Technical Publishing.

Smolek, M. (1988). "Elasticity of the bovine sclera measured with real-time holographic interferometry." <u>Am J Optom Physiol Opt</u> **65**(8): 653-60.

Sommer, A., J. M. Tielsch, J. Katz, H. A. Quigley, J. D. Gottsch, J. Javitt and K. Singh (1991). "Relationship between intraocular pressure and primary open angle

glaucoma among white and black Americans. The Baltimore Eye Survey." <u>Arch Ophthalmol</u> **109**(8): 1090-5.

Spencer, A. J. M. (1974). <u>Continuum theory of the mechanics of fibre-reinforced composites</u> New York, NY, Springer-Verlag.

Spencer, A. J. M. (1985). <u>Continuum theory of the mechanics of fibre-reinforced composites</u> New York, NY, Springer-Verlag.

Spoerl, E., A. G. Boehm and L. E. Pillunat (2005). "The influence of various substances on the biomechanical behavior of lamina cribrosa and peripapillary sclera." <u>Invest Ophthalmol Vis Sci</u> **46**(4): 1286-90.

Srinivasan, V. J., D. C. Adler, Y. Chen, I. Gorczynska, R. Huber, J. Duker, J. S. Schuman and J. G. Fujimoto (2008). "Ultrahigh-speed Optical Coherence Tomography for Three-Dimensional and En Face Imaging of the Retina and Optic Nerve Head." <u>Invest Ophthalmol Vis Sci</u>.

Streuli, C. (1999). "Extracellular matrix remodelling and cellular differentiation." <u>Curr Opin Cell Biol</u> **11**(5): 634-40.

Taber, L. A. and J. D. Humphrey (2001). "Stress-modulated growth, residual stress, and vascular heterogeneity." <u>J Biomech Eng</u> **123**(6): 528-35.

Tektas, O. Y. and E. Lutjen-Drecoll (2008). "Qualitative and Quantitative Morphological Changes in the Vasculature and Extracellular Matrix of the Optic Nerve Head in Glaucomatous Eyes." <u>Invest. Ophthalmol. Vis. Sci.</u> **49**(5): 3678-.

Teng, S. W., H. Y. Tan, J. L. Peng, H. H. Lin, K. H. Kim, W. Lo, Y. Sun, W. C. Lin, S. J. Lin, S. H. Jee, P. T. So and C. Y. Dong (2006). "Multiphoton autofluorescence and second-harmonic generation imaging of the ex vivo porcine eye." <u>Invest Ophthalmol Vis Sci</u> **47**(3): 1216-24.

Tielsch, J. M., A. Sommer, J. Katz, R. M. Royall, H. A. Quigley and J. Javitt (1991). "Racial variations in the prevalence of primary open-angle glaucoma. The Baltimore Eye Survey." <u>Jama</u> **266**(3): 369-74.

Tigges, J., T. P. Gordon, H. M. McClure, E. C. Hall and A. Peters (1988). "Survival rate and life span of rhesus monkeys at the Yerkes regional primate research center." <u>American Journal of Primatology</u> **15**(3): 263-273.

Timoshenko, S. (1970). <u>Theory of Elasticity</u>, McGraw-Hill.

Trier, K. and S. M. Ribel-Madsen (2004). "Latanoprost eye drops increase concentration of glycosaminoglycans in posterior rabbit sclera." <u>J Ocul Pharmacol Ther</u> **20**(3): 185-8.

Tsatsos, M. and D. Broadway (2007). "Controversies in the history of glaucoma: is it all a load of old Greek?" <u>Br J Ophthalmol</u> **91**(11): 1561-2.

Varma, R., M. Ying-Lai, B. A. Francis, B. B. Nguyen, J. Deneen, M. R. Wilson and S. P. Azen (2004). "Prevalence of open-angle glaucoma and ocular hypertension in Latinos: the Los Angeles Latino Eye Study." <u>Ophthalmology</u> **111**(8): 1439-48.

Verri, A. and T. Poggio (1987). "Against quatitative optical flow." <u>Proceedings of the First International Conference on Computer Vision</u>: 171-180.

Wagner, K. W. (1913). " Zur theorie der unvoll kommener dielektrika." <u>ann Phys</u> **40**: 817-855.

Watson, P. G. and R. D. Young (2004). "Scleral structure, organisation and disease. A review." <u>Exp Eye Res</u> **78**(3): 609-23.

Weih, L. M., B. N. Mukesh, C. A. McCarty and H. R. Taylor (2001). "Association of demographic, familial, medical, and ocular factors with intraocular pressure." Arch Ophthalmol **119**(6): 875-80.

Weiss, J. A. (1994). "A constitutive model and finite element representation for transversely isotropic soft tissues " Ph. D. Thesis, Department of bioengineering, University of Utah, UT: 111.

Weiss, J. A. and J. C. Gardiner (2001). "Computational modeling of ligament mechanics." Crit Rev Biomed Eng **29**(3): 303-71.

Weiss, J. A., B. N. Maker and S. Govindjee (1996). "Finite element implementation of incompressible, transversely isotropic hyperelasticity." Comput Methods Appl Mech Engrg **135**: 107-28.

Weiyi, C., X. Wang, C. Wang, L. Tao, X. Li and Q. Zhang (2008). "An experimental study on collagen content and biomechanical properties of sclera after posterior sclera reinforcement." Clin Biomech (Bristol, Avon).

Wensor, M. D., C. A. McCarty, Y. L. Stanislavsky, P. M. Livingston and H. R. Taylor (1998). "The prevalence of glaucoma in the Melbourne Visual Impairment Project." Ophthalmology **105**(4): 733-9.

Wolfs, R. C., P. H. Borger, R. S. Ramrattan, C. C. Klaver, C. A. Hulsman, A. Hofman, J. R. Vingerling, R. A. Hitchings and P. T. de Jong (2000). "Changing views on open-angle glaucoma: definitions and prevalences--The Rotterdam Study." Invest Ophthalmol Vis Sci **41**(11): 3309-21.

Wollensak, G. and E. Spoerl (2004). "Collagen crosslinking of human and porcine sclera." J Cataract Refract Surg **30**(3): 689-95.

Woo, S. L., A. S. Kobayashi, W. A. Schlegel and C. Lawrence (1972). "Nonlinear material properties of intact cornea and sclera." Exp Eye Res **14**(1): 29-39.

Wu, S. Y. and M. C. Leske (1997). "Associations with intraocular pressure in the Barbados Eye Study." Arch Ophthalmol **115**(12): 1572-6.

Yamaoka, A., T. Matsuo, F. Shiraga and H. Ohtsuki (2001). "TIMP-1 production by human scleral fibroblast decreases in response to cyclic mechanical stretching." Ophthalmic Res **33**(2): 98-101.

Yan, D. B., F. M. Coloma, A. Metheetrairut, G. E. Trope, J. G. Heathcote and C. R. Ethier (1994). "Deformation of the lamina cribrosa by elevated intraocular pressure." Br J Ophthalmol **78**(8): 643-8.

Yang, H., J. C. Downs, A. Bellezza, H. Thompson and C. F. Burgoyne (2007a). "3-D histomorphometry of the normal and early glaucomatous monkey optic nerve head: prelaminar neural tissues and cupping." Invest Ophthalmol Vis Sci **48**(11): 5068-84.

Yang, H., J. C. Downs, C. Girkin, L. Sakata, A. Bellezza, H. Thompson and C. F. Burgoyne (2007b). "3-D histomorphometry of the normal and early glaucomatous monkey optic nerve head: lamina cribrosa and peripapillary scleral position and thickness." Invest Ophthalmol Vis Sci **48**(10): 4597-607.

Young, R. D. (1985). "The ultrastructural organization of proteoglycans and collagen in human and rabbit scleral matrix." J Cell Sci **74**: 95-104.

Zeimer, R. C. and Y. Ogura (1989). "The relation between glaucomatous damage and optic nerve head mechanical compliance." Arch Ophthalmol **107**(8): 1232-4.

Zulliger, M. A. M. A., P. Fridez, K. Hayashi and N. Stergiopulos (2004). "A strain energy function for arteries accounting for wall composition and structure." Journal of Biomechanics **37**(7): 989-1000.

Biography

Michaël J. A. Girard was born on January 13, 1981 in Nancy, France. He received his Diplôme d'Ingénieur in advanced solid and fluid mechanics from the Institut des Sciences et Techniques de l'Ingénieur de Lyon in 2003. He was then offered a National Institutes of Health research assistantship to pursue a doctoral degree in the Department of Biomedical Engineering at Tulane University under the joint supervision of Drs. J-K. Francis Suh, J. Crawford Downs and Claude F. Burgoyne. In 2005, after hurricane Katrina devastated the city of New Orleans, he relocated with Drs. Downs and Burgoyne to the Devers Eye Institute in Portland, Oregon. He received his Ph.D. in December, 2008. Michaël's research has focused primarily on the biomechanics of the aging and glaucomatous eye characterized by means of experimental and computational techniques. His main finding is that monkey sclera undergoes at least a five-fold increase in stiffness when exposed to intraocular pressure from 5 to 45 mm Hg, a characteristic known as nonlinearity stemming from the presence of collagen fibers. Using idealized eye models, he has demonstrated that the alignment and spatial distribution of scleral collagen fibers have a large impact on optic nerve head biomechanics, suggesting that inter-individual variations in collagen fiber alignment could be a major factor for the development of glaucoma. Moreover, he has shown that monkey posterior sclera from older eyes are considerably stiffer, which suggests that the age-induced stiffening of the sclera may contribute to the development of glaucoma. He has also characterized scleral biomechanical changes in eyes exposed to chronic intraocular pressure elevation.